THE UNIVERSITY *of* EDINBURGH

The Optimisation and Characterisation of Durable Microelectrodes for Electroanalysis in Molten Salt

Ewen O. Blair

A thesis submitted for the degree of Doctor of Philosophy

The University of Edinburgh

Abstract

This work presents microfabricated microelectrodes, capable of quantitative analysis in molten salt (MS). MSs are an electrolytic medium of growing interest, especially in the area of nuclear reprocessing. However, designing sensors for a MS-based nuclear reprocessing system is a challenge, owing to the usually corrosive nature and high operating temperatures (typically 450 - 500°C) of MS.

Microelectrodes are well placed as sensors, with numerous advantages over macro-scale electrodes. As a consequence, there have been previous attempts to utilise microelectrodes in MS. However, these have not been successful and all have suffered disadvantages inherent in traditional microelectrode manufacturing.

The microelectrodes presented in this work were produced using standard microfabrication techniques and characterised in MS. An analysis of failure mechanisms guided a systematic study of material combinations. This resulted in a sensor, which is capable of delivering quantifiable electrochemistry in MS. However, the lifetime and yield of the sensor were determined to only be 46% and 1.4 hours respectively.

Further investigation of the microelectrode failure mechanisms guided several layout changes to the microelectrode design. By reducing critical area, where defects or pinholes could form, these resulted in improvements in performance. This increased the yield to 65%, while the average lifetime increased up to 45 hours.

Test structures were designed to investigate the causes of the continued microelectrode failures and identified shorting between the electrode metal and silicon substrate. This suggests the existence of defects in the underlying insulator are the cause of the 35% of microelectrodes which never functioned. Separate test structures suggested the lifetimes of the microelectrodes could also be improved by removing the need for a metal adhesion layer. Tantalum has been suggested as a replacement electrode metal and a

proof of concept study demonstrated the feasibility of employing thin film tantalum as an electrode metal in LKE.

Using this technology as a platform, several proof-of-concept microelectrode designs are also presented: liquid microelectrodes, microelectrode arrays, and a nanoelectrode. These are targeted at specific sensing applications, and provide an expanded spectrum of measurements in MS.

Declaration of Authorship

I declare that the work presented in this thesis was undertaken by myself at the University of Edinburgh, except in the instances below.

This thesis has not entirely or in part been submitted for any other degree or professional qualification.

The cyclic voltammograms presented in the following figures were recorded by Dr Damion Corrigan: 4.13 (a), (b), (c), 5.2 (a), (c), 5.9 (b), (d).

The photographs presented in the following figures were also taken by Dr Damion Corrigan: 4.16, 4.17, 4.18 (a) and (b).

The super thin track microelectrodes discussed in chapters 6 and 7 were fabricated by Dr Ilka Schmüser.

The schematic presented in figure 1.5 was created by Mr Justin Elliott.

Acknowledgements

This thesis is dedicated to my parents who have never stopped supporting me, although they are under no obliation to read the whole thing.

I'd like to thank my supervisors Professor Anthony Walton and Professor Andy Mount for all they've done and for trying, and occasionally suceeding, to stop me from doing anything too stupid.

A special thanks goes to Dr Damion Corrigan for helping me find my feet and breaking so many of my beautifully made electrodes.

The work in this thesis would not have been posisble without the academics and, especially, technical staff at the Scottish Microelectronic centre: Andy, Jon, Stewart (Smith), Ewan, Brian, Richard, and Stewart (Ramsay).

Thanks to everyone in the Mount group and friends: Richard, Justin, Simon, Kate, Andrew, Ugne, Eva, and Hannah for keeping me sane, ish. Special thanks to Charlotte, who first discovered the joy of putting electrodes into molten salt.

I'm indebted to all those past and present in the SMC who helped me with useful discussion and beer: Ilka, Coinneach, David, Anthony, Mags, Enrico, Yifan, Eldad, Cami, and Andreas.

In the real world, I'm grateful to everyone in G.A.S, The Cool Group, and George Lopez. Especially the support from: Sarah, Hamish, Rob, Greg, and Jahan.

To those who have taken on the molten salt research, I quote the comedian Frankie Boyle:

you have released me, this monster is yours now.

Contents

Contents i

List of Figures vi

List of Tables x

Glossary xi

1 Introduction 1
- 1.1 Nuclear Energy . . . 2
- 1.2 Closing the Nuclear Fuel Cycle . . . 3
  - 1.2.1 PUREX . . . 4
  - 1.2.2 Pyrochemical Reprocessing . . . 5
  - 1.2.3 Outline of This Project . . . 6
- 1.3 Summary . . . 7

2 Background to Online Sensing in Molten Salt 13
- 2.1 Introduction . . . 14
- 2.2 Molten Salts . . . 14
  - 2.2.1 Properties . . . 14
  - 2.2.2 Engineering Challenges . . . 14
- 2.3 Online Monitoring in Molten Salts . . . 15
  - 2.3.1 Spectroscopic Monitoring . . . 15
  - 2.3.2 Electrochemical Monitoring . . . 15
- 2.4 Microelectrodes . . . 16
  - 2.4.1 Definition of a Microelectrode . . . 16
  - 2.4.2 Advantages and Applications of Microelectrodes . . . 17
  - 2.4.3 Methods of Microelectrode Manufacture . . . 21
- 2.5 Microelectrodes in Molten Salt . . . 23

2.5.1 Dropping Electrodes in Molten Salt . . . 23
2.5.2 Solid Microelectrodes in Molten Salt . . . 25
2.5.3 Microfabricated Microelectrodes in Molten Salt . . . 27
2.6 Summary . . . 28

3 Background to Electrochemical Methods 41
3.1 Introduction . . . 42
3.2 Three-Electrode System . . . 42
3.3 Electrochemical Methods Used in this Work . . . 44
3.3.1 Cyclic Voltammetry . . . 44
3.3.2 Chronoamperometry . . . 45
3.4 Electrochemical Response from a Microelectrode . . . 46
3.5 Summary . . . 48

4 The Benchmark Microelectrode 51
4.1 Introduction . . . 52
4.2 The Benchmark Microelectrode Design . . . 52
4.3 Benchmark Microelectrode Materials . . . 53
4.4 Benchmark Microelectrode Fabrication Process . . . 56
4.5 Experimental Set Up . . . 58
4.5.1 High Temperature Equipment . . . 58
4.5.2 Electrical Connection . . . 59
4.5.3 Electrical Noise . . . 61
4.5.4 Salt Preparation . . . 62
4.6 Characterisation of the Benchmark Microelectrode . . . 63
4.6.1 Characterisation Methodology . . . 63
4.6.2 Benchmark Microelectrode Performance . . . 65
4.7 Summary . . . 70

5 Optimisation of Microelectrode Materials 76
5.1 Introduction . . . 77
5.2 Delamination in Thin Films . . . 77
5.2.1 Delamination of the Benchmark Microelectrode . . . 77
5.2.2 Origin of Stress in Thin Films . . . 77
5.2.3 Determining Stress in Thin Films . . . 79
5.3 Determining Stress in the Benchmark Microelectrode . . . 80
5.3.1 Methodology . . . 80

5.3.2 Stress Measurement Results . . . 82
5.3.3 Additional Sources of Stress in the Benchmark Microelectrode . . 82
5.4 Reducing Stress in Thin Films . . . 83
5.4.1 Stress Relief Layer . . . 83
5.4.2 Stress Relief Quantification . . . 83
5.4.3 Stress Relief Performance in LKE . . . 84
5.5 Electrode Metal and Adhesion Layer Loss . . . 86
5.5.1 Titanium Electrodissolution . . . 86
5.5.2 Titanium Nitride Adhesion Layer . . . 88
5.6 Top Insulator Permeability . . . 90
5.6.1 Stoichiometric Silicon Nitride Top Insulator . . . 90
5.6.2 Fabrication of Microelectrodes with a Si_3N_4 Top Insulator . . . 90
5.6.3 Si_3N_4 Top Insulator Performance in LKE . . . 90
5.6.4 Quantifying Stress in the Si_3N_4 Top Insulator . . . 93
5.7 Localised Top Insulator Damage . . . 93
5.7.1 Electrode Metal Edge Spikes . . . 93
5.7.2 New Fabrication Process . . . 94
5.7.3 Platinum Electrode Performance in LKE . . . 95
5.8 Summary . . . 98

6 Characterisation and Optimisation of Microelectrode Yield 106
6.1 Introduction . . . 107
6.2 Change of Operating Temperature . . . 107
6.3 Background to Microelectrode Yield . . . 107
6.3.1 Yield Definition . . . 107
6.3.2 Measuring Yield . . . 108
6.3.3 Yield of the Version Two Microelectrode . . . 108
6.4 Improving Microelectrode Yield . . . 109
6.4.1 Effect of Critical Area . . . 109
6.4.2 Thin Track Microelectrode with Reduced Critical Area . . . 110
6.4.3 Yield of the Thin Track Microelectrodes . . . 111
6.4.4 Super Thin Track Microelectrode with Further Reduced Critical Area . . . 112
6.4.5 Yield of the Super Thin Track Microelectrodes . . . 114
6.5 Investigating Insulator Defectivity . . . 114
6.5.1 Test Structures . . . 114
6.5.2 Test Structure Design . . . 115

6.5.3 Test Structure Results . . . 117
6.6 Summary . . . 123

7 Characterisation of Microelectrode Lifetimes 127
7.1 Introduction . . . 128
7.2 Background Resistance . . . 128
7.3 Methodology . . . 129
7.4 Version Two Microelectrode Lifetime . . . 130
7.5 Thin Track Microelectrode Lifetime . . . 132
7.6 Thin Track Microelectrode Lifetime Failures . . . 133
7.6.1 Failure Mechanism . . . 133
7.6.2 Mechanism of Platinum Loss . . . 136
7.7 Super Thin Track Electrode Lifetime . . . 138
7.8 Tantalum as an Electrode Metal . . . 140
7.8.1 Tantalum Macroelectrode Fabrication . . . 140
7.8.2 Tantalum Characterisation . . . 140
7.9 Summary . . . 141

8 Alternative Microelectrode Architectures for Enhancing Electrode Performance 145
8.1 Introduction . . . 146
8.2 Detecting Species that Reduce at More Negative Potentials using Reactive Electrodes . . . 146
8.2.1 Reactive Electrodes . . . 146
8.2.2 Aluminium Microelectrodes . . . 147
8.2.3 Fabrication of Aluminium Microelectrodes . . . 147
8.2.4 Characterisation of Aluminium Microelectrodes . . . 148
8.2.5 Bismuth Microelectrodes . . . 149
8.2.6 Fabrication of Bismuth Microelectrodes . . . 149
8.2.7 Characterisation of Bismuth Microelectrodes . . . 150
8.2.8 Conclusions and Future Direction . . . 150
8.3 Development of Microelectrode Arrays . . . 151
8.3.1 Microelectrode Arrays . . . 151
8.3.2 Microfabricated Microelectrode Array Design . . . 152
8.3.3 Microelectrode Array Characterisation . . . 153
8.3.4 Conclusions and Future Direction of Microelectrode Arrays . . . 155
8.4 LKE Compatible Nanoelectrodes . . . 156

8.4.1 Advantages of Nanoelectrodes . . . 156
8.4.2 Nanoelectrode Fabrication . . . 156
8.4.3 Nanoelectrode Characterisation . . . 157
8.4.4 Conclusion and Future Direction for LKE Compatible Nanoelectrodes . . . 161
8.5 On-Chip Counter Electrode . . . 161
8.5.1 Design and Fabrication . . . 161
8.5.2 Dual Electrode Characterisation . . . 161
8.6 Summary . . . 162

9 Conclusions and Future Directions 168
9.1 Summary . . . 169
9.2 Future work . . . 171
9.2.1 Microelectrode Design . . . 171
9.2.2 Industrial Deployment . . . 171
9.3 Other Applications of the Microelectrodes . . . 172

A Chemicals and Tools used in Microfabrication 177

B Chemicals and Tools used in High Temperature Measurements 179

List of Figures

1.1 A fission reaction . . . 2
1.2 Open nuclear fuel cycle . . . 3
1.3 Closed nuclear fuel cycle . . . 4
1.4 The PUREX process . . . 5
1.5 The pyrochemical process . . . 6

2.1 Macro- and microelectrode diffusion profiles . . . 16
2.2 Schematic of the Electrochemical Double Layer . . . 18
2.3 Graph of capacitve charging current and Faradaic current versus electrode size . . . 20
2.4 Electrical noise versus electorode area . . . 21
2.5 SEM of commercial microelectrode . . . 22
2.6 The photolithography process . . . 23
2.7 Molten salt electrode and experimental set up used by Heus et. al . . . 24
2.8 Molten salt electrode and experimental set up used by Malinowska et al. 26
2.9 Molten salt electrode and experimental set up used by Heus et al. . . . 27

3.1 Standard three-electrode set up . . . 43
3.2 Typical macroelectrode CV . . . 45
3.3 Typical microelectrode CVs of a solution reaction and a plating and stripping reaction . . . 46
3.4 Common microelectrode geometries . . . 47

4.1 Benchmark microelectrode schematic . . . 52
4.2 Layout of benchmark microelectrodes on wafer . . . 53
4.3 Benchmark microelectrode cross-section . . . 54
4.4 Benchmark microelectrode fabrication process . . . 57
4.5 High temperature set up: crucible and cell . . . 59
4.6 High temperature set up: furnace . . . 60

4.7 High temperature set up: microelectrode connection and full set up . . . 61
4.8 Furnace electrical noise with and without electrical shielding 62
4.9 Ideal CV of the LKE potential window compared to a typical LKE CV . 64
4.10 CV of the LKE potential window after electrochemical cleaning 64
4.11 Ideal cyclic voltammogram of a plating and stripping reaction at a microelectrode (mock-up). 65
4.12 Macroelectrode CV of Ag plating and stripping in LKE 66
4.13 Benchmark microelectrode CVs of Ag plating and stripping in LKE . . . 67
4.14 First and third CV of Ag plating and stripping at a benchmark microelectrode in LKE 68
4.15 Benchmark microelectrode delamination 68
4.16 Benchmark microelectrode metal loss 69
4.17 Ag plating on the benchmark microelectrode top insulator 70
4.18 Benchmark microelectrode top insulator perimeter damage 70

5.1 Substrates under compressive and tensile stress 78
5.2 CVs of Ag plating and stripping on microelectrodes with SiO_2 underlying insulator in LKE 85
5.3 Microelectrode with SiO_2 underlying insulator after removal from LKE . 86
5.4 Electrode metal test structure 87
5.5 CVs of the electrode metal test structure in LKE 87
5.6 The metal test structure after cycling. 88
5.7 CVs of the electrode metal test structure with TiN in LKE 89
5.8 The TiN test structure after cycling in LKE 89
5.9 CVs of Ag plating and stripping on microelectrodes with a Si_3N_4 top insulator in LKE 91
5.10 Microelectrode with Si_3N_4 top insulator after cycling in LKE 92
5.11 Profile of the electrode metal step on a microelectrode. 94
5.12 The ideal lift-off process and what may be happening in reality 95
5.13 The pattern and etch process 96
5.14 CVs of Ag plating and stripping on Pt microelectrodes in LKE 97
5.15 Ag plating and stripping on a Pt microelectrode at different scan rates . 98

6.1 V2M yield against applied potential 109
6.2 CV of a failed V2M 110
6.3 Layout of the TTM 111
6.4 Yield of the TTMs against potential 112

6.5 Layout of the STTM . . . 113
6.6 Layout of the STTM microdisc . . . 114
6.7 Yield of the STTMs against negative potential limit . . . 115
6.8 Schematic of the test structures for determining microelectrode failure . . . 116
6.9 Average currents recorded on the test structures . . . 117
6.10 Currents of three individual test structures . . . 118
6.11 Surface of the test structure top insulator before and after testing . . . 119
6.12 Si perimeter of a test structure before and after testing . . . 120
6.13 Cross-section through the test structure highlighting where the Ag has plated. . . . 121
6.14 The edge of a test structure sectioned using a focused ion beam. . . . 121
6.15 Steps of a comb test structure before and after testing . . . 122
6.16 The yield of each microelectrode layout and their CAs, assuming 10 mm immersion in MS. . . . 123

7.1 Layouts of three microelectrode designs and their CAs, assuming a 10 mm immersion in the salt. . . . 128
7.2 Lifetimes of individual V2Ms. . . . 130
7.3 CVs of a failed, but previously functioning V2M compared to a CV of V2M which never functioned . . . 131
7.4 Two V2Ms after testing in the LKE . . . 131
7.5 Lifetimes of the □TTMs compared with the lifetimes of the V2Ms. . . . 133
7.6 Lifetimes of the ◯TTMs compared with □TTMs and the V2M. . . . 134
7.7 Three TTMs after lifetime experiments . . . 135
7.8 A typical CV of Ag plating and stripping at a TTM vs a CV exhibiting current fluctuations . . . 135
7.9 Growth of current fluctuations in CVs over time . . . 136
7.10 CV after TTM failure . . . 137
7.11 Pt test chips before and after soaking in LKE . . . 138
7.12 Lifetimes of the STTMs and TTMs . . . 139
7.13 Two STTMs after lifetime experiments . . . 140
7.14 CV of LKE potential window with a Ta thin film macroelectrode . . . 141

8.1 Lift off process for patterning Al . . . 148
8.2 Al TTM . . . 149
8.3 Bismuth TTM . . . 150
8.4 Diffusion profile merging over time . . . 152

8.5 Microelectrode array layout . . . 153
8.6 CV of Ag plating and stripping at a microelectrode array in LKE 154
8.7 A microsquare array and a microdisc array after repeated cycling across the LKE potential window . . . 155
8.8 Cross-section of an MNEE . . . 157
8.9 TTM before and after etching to become an MNEE . . . 158
8.10 CV of Ag plating and stripping on the proof of concept MNEE . . . 158
8.11 The nanoband electrode from figure 8.10 post cycling in LKE. . . . 159
8.12 CV of plating and stripping on the proof of concept MNEE after 5 mins . 160
8.13 Layout of the DEs . . . 162
8.14 CV of Zn plating and stripping at an on-chip CE . . . 163

9.1 Transverse cross-section of the microelectrode architecture. . . . 169
9.2 The three microelectrode layouts characterised with their respective CA and yield. . . . 170

List of Tables

4.1 Predicted limiting currents for the CVs in figure 4.13, calculated using equation (3.3) 66

5.1 Parameters used in the calculation of thermal stresses using equation (5.1). 82
5.2 Predicted limiting currents for CVs in figure 5.2, calculated using equation (3.3). 84
5.3 Predicted limiting currents for the CVs in figure 5.9, calculated using equation (3.3), compared with the measured values. 91
5.4 Predicted limiting currents for the CVs in figure 5.14, calculated using equation (3.3), compared with the measured values. 96
5.5 Stress measured for each insulation layer at 21°C and 500°C. 98

8.1 The array spacings, microelectrode sizes, and geometries of the fabricated microelectrode arrays. 152

Glossary

Variables and Constants

V	Voltage
C_d	Capacitance of the electrochemical double layer
i_c	Current due to capacitive charging of the electrochemical double layer
R_s	Solution resistance
t	Time
τ	Charging constant of the electrochemical double layer
ε_0	Permittivity of free space
ε_r	Relative permittivity
A_e	Area of an electrode
d	Thickness of the electrochemical double layer
c	Concentration
D	Diffusion Coefficient
F	Faraday's Constant: 96,485.332 Cmol^{-1}
i_L	Limiting Current
l	Microsquare Electrode Edge Length
n	Number of Electrons Transferred in a Reaction
r	Radius of a Microdisc Electrode

$\sigma_f^e(T)$	Extrinsic stress in a thin film f at a temperature T
σ_f^i	Intrinsic stress in a thin film f
$\sigma_f^t(T)$	Total stress in a thin film f at a temperature T
T	Temperature
R	Wafer Radius
E	Young's Modulus
h_f	Thickness of a substrate f
h_s	Thickness of a substrate s
ν	Poisson's Ratio
α	Linear Thermal Expansion Coefficient
m	Number of Elements in a Microelectrode Array
nD	Microelectrodes Spaced n Times their Critical Dimension on the X and Y Axis

Acronyms / Abbreviations

NFC	Nuclear Fuel Cycle
PUREX	Plutonium Uranium Recovery by EXtraction
TBP	Tributyl Phosphate
UREX	Uranium Extraction
TRUEX	Transuranic Extraction
DIAMEX	Diamide Extraction
MS	Molten Salt
LKE	LiCl-KCl Eutectic
CD	Critical Dimension
WE	Working Electrode

RE	Reference Electrode
CE	Counter Electrode
CV	Cyclic Voltammogram
BM	Benchmark Microelectrode
Si-rich SiN	Silicon-Rich Silicon Nitride
HMDS	Hexamethyldisilazane
LPCVD	Low Pressure Chemical Vapour Deposition
V2M	Version Two Microelectrode
CA	Critical Area
TTM	Thin Track Microelectrode
STTM	Super Thin Track Microelectrode
□TTM	Thin Track Microsquare Electrode
◯TTM	Thin Track Microdisc Electrode
MNEE	Microsquare Nanoband Edge Electrode
DEs	Dual Electrodes

Chapter 1

Introduction

1.1 Nuclear Energy

Nuclear fission is a well-known method of producing energy, with one of the smallest CO_2 by-products of any energy source [1–6]. As one of many alternative energy sources to fossil fuels it supplies around 16% of global electricity annually [4, 7]. Nuclear fission is a process where a heavier atom splits into several lighter atoms, releasing energy and free neutrons [8, 9]. The neutrons released from the event can then collide with other heavy atoms triggering new fission reactions, causing a chain reaction. Nuclear power takes advantage of this process by artificially inducing this in a uranium isotope ^{235}U and using the energy released to generate electricity. Figure 1.1 shows this reaction, where a ^{235}U is struck by a neutron and releases energy and more neutrons to carry on the reaction.

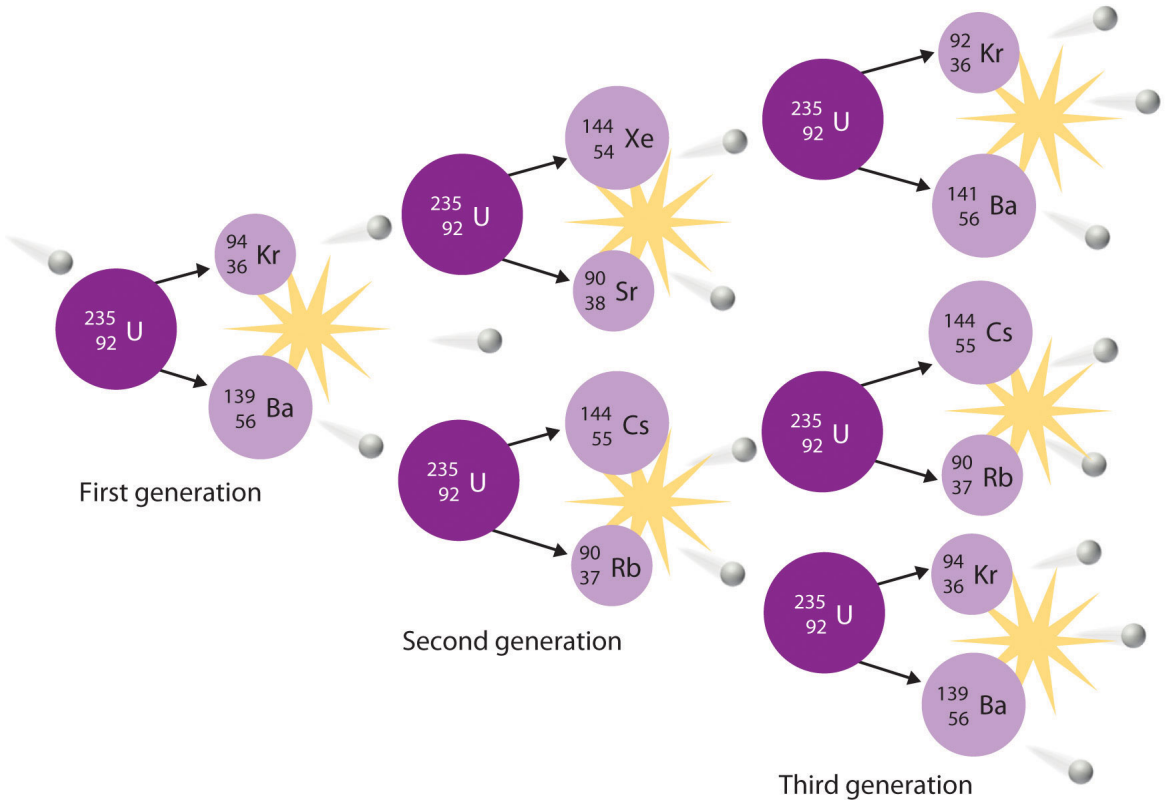

Figure 1.1: A fission reaction where a ^{235}U atom has been struck by a neutron and split into two lighter atoms and three neutrons, which then collide with other ^{235}U atoms, sustaining the reaction [10].

Uranium fuel also contains typically around 95 - 97% ^{238}U which, when fissioned, does not produce fast enough neutrons to cause further reactions. As the ^{235}U is used

up, the relative concentration of ^{238}U increases and eventually becomes large enough that the reaction cannot self-sustain, and the uranium fuel must be replaced.

The disposal of this spent nuclear fuel is complicated by the fact that it is extremely hot and radiotoxic. Handling and disposing of this spent fuel is therefore hazardous and ecologically dangerous, especially as some of the most radioactive elements produced in the fission reaction have half lives of decades and elements such as plutonium have half lives of over 2400 years [11]. As a consequence, many countries simply choose to permanently store spent waste in underground repositories [12]. This presents another challenge, as plutonium that has built up during the fission process is present in the spent fuel and makes nuclear proliferation a concern [13, 14]. An additional motivation to better handle spent fuel is that there is only around a century's worth of mineable uranium predicted to remain; therefore there is a large global effort to developing a sustainable or "closed" nuclear fuel cycle (NFC) [15–18].

1.2 Closing the Nuclear Fuel Cycle

An NFC begins with the mining of uranium ore before the uranium is isolated, usually chemically. This yields U_3O_8 which is then converted into UF_6 for an enrichment process, which increases the concentration of ^{235}U from around 0.7% to 3 - 5%. After this the uranium is converted into solid fuel such as UO_2 to be used in a nuclear reactor. Once the fuel is spent, it is put into interim storage to cool and reduce its radiation levels, and is then put into a long term storage repository. This process is known as an open, or once-through NFC and is shown in figure 1.2.

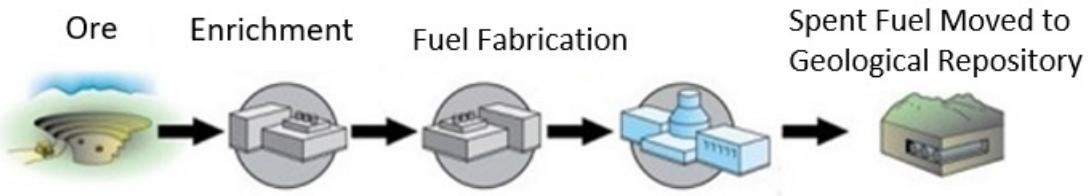

Figure 1.2: The once-through NFC. The uranium is mined, enriched, used, and disposed of in a geological repository [19].

The alternative is a closed NFC presented in figure 1.3, where the spent fuel is recycled back into new fuel. A typical used fuel rod consists of around 96% uranium, 1% plutonium, and 3% other fission products such as americium and strontium. This recycling takes the form of separating the uranium from the minor actinides and lanthanides

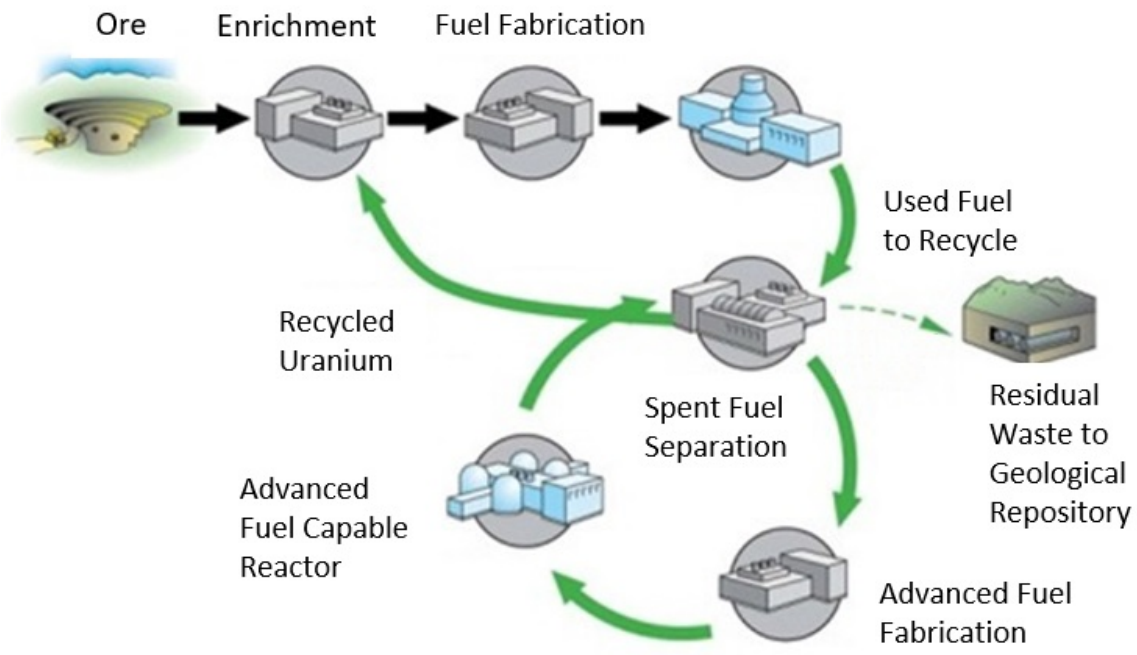

Figure 1.3: A closed NFC, where the uranium is recycled back into the front end of process [19].

which have built up during the fission process. The uranium can then be fabricated into new fuel rods or combined with plutonium and other fission products to create mixed oxide fuel. This yields a large amount of uranium to be reused, possibly multiple times, and leaves behind a much smaller volume of waste that requires disposal. As such, a closed NFC addresses two of the key drawbacks in nuclear power. These benefits make it essential for the future of nuclear power to develop and optimise reprocessing technologies.

1.2.1 PUREX

The PUREX (Plutonium Uranium Recovery by Extraction) process is an established reprocessing system in use by a number of countries [20–22]. The PUREX process is shown in figure 1.4 and uses an aqueous phase, solvent based extraction to separate uranium and plutonium from the rest of the spent fuel. This is achieved by dissolving the spent fuel in hot nitric acid and adding an organic solvent such as tributyl phosphate (TBP), which complexes with the uranium and plutonium. These form a separate phase from the remaining fission products and can be extracted and reused, thus closing the NFC. A drawback with this process is that plutonium can be extracted in isolation, leading to

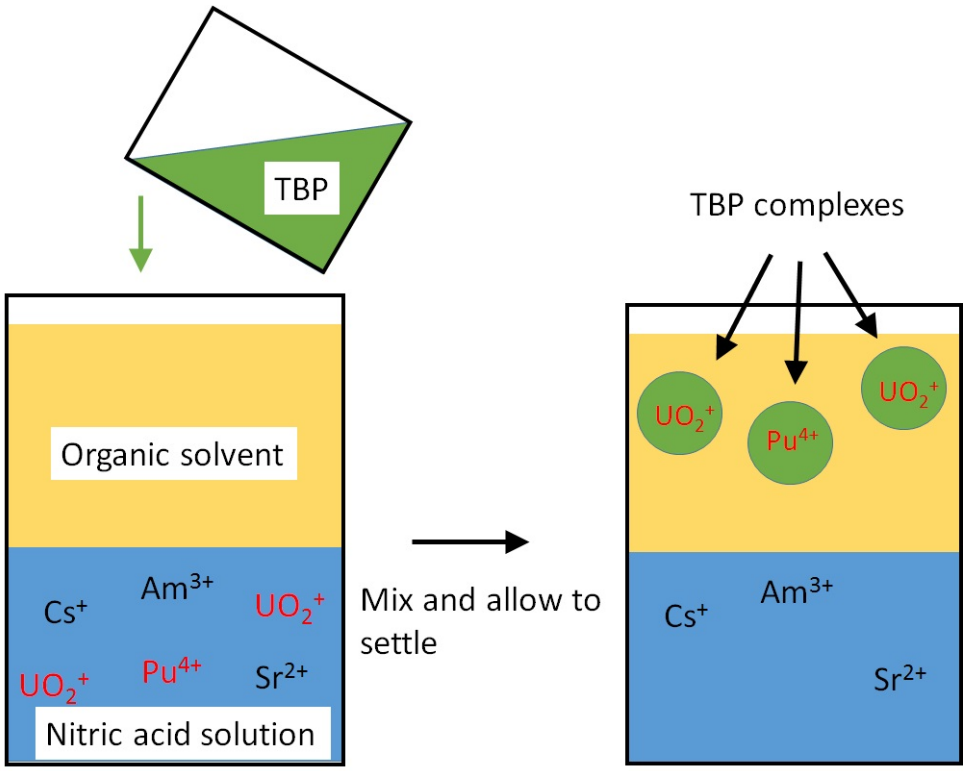

Figure 1.4: The PUREX process for separating uranium and plutonium from spent nuclear waste [23].

concerns about possible nuclear proliferation. In order to address this, the UREX process was developed which differs from PUREX through the addition of acetohydroxamic acid which prevents the separation of plutonium [24]. Other PUREX based methods exist such as TRUEX (Transuranic Extraction) and DIAMEX (Diamide Extraction), which are designed to allow the extraction of other transuranic elements [25, 26].

1.2.2 Pyrochemical Reprocessing

An additional technique to aqueous-based PUREX processes, is pyrochemical reprocessing which takes place in a high temperature molten salt (MS) electrolyte (400 - 800°C) and is shown in figure 1.5 [15, 27–30]. The spent waste is submerged in the MS and dissolved. The uranium can be electroplated onto a solid cathode and then extracted, while the plutonium and other minor actinides are reduced into a liquid cathode and removed from the system. This process enables the extraction of the uranium, while plutonium and other transuranics are collected together in a liquid cathode, which offers improved proliferation resistance as plutonium and the other transuranic elements

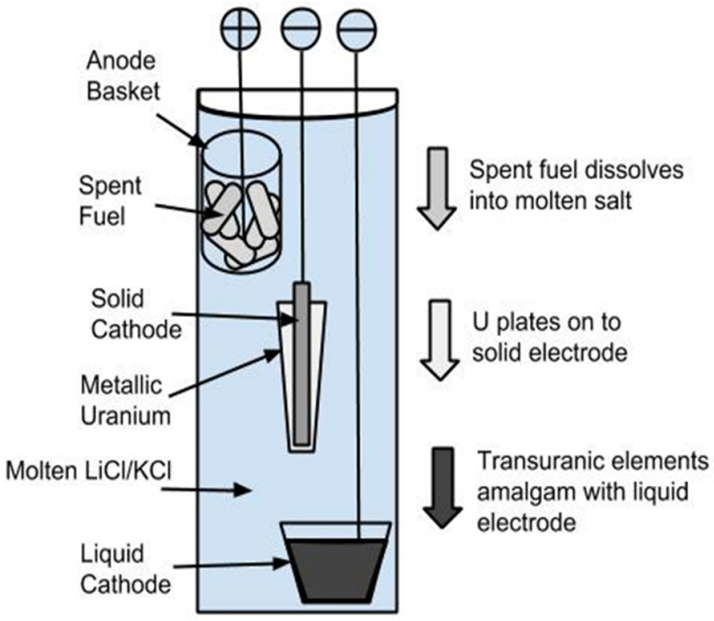

Figure 1.5: The pyrochemical process for separation of spent nuclear fuel.

cannot be isolated [14, 31]. The high operating temperatures and inorganic components make the process more robust to the high heat and radiation levels of the spent fuel, which therefore does not need to spend time cooling in interim storage [14, 28, 32]. This also means that reprocessing can be carried out in very close proximity to the reactor, which results in higher security and a more efficient NFC as spent fuel does not need to be transported or stored for long periods of time [14, 32]. Another benefit is that a wider variety of fuels can be reprocessed such as nitride, metallic or carbide fuels, which could be challenging for aqueous-based processes [32].

While established in theory, the pyrochemical process has not made the transition to industry, owing in part to the technological barriers of working in MS [27, 33–35]. This is due to the high temperature and corrosive properties of MS as well as a lack of fundamental understanding of MS properties. The combination of these challenges means there is still an active literature focusing on the development of in-situ monitoring in MS [36–38].

1.2.3 Outline of This Project

This work documents the development of the first microfabricated sensors that can provide online monitoring of chemical elements within the MS. These sensors take the form of electrochemical microelectrodes, which convey a numerous benefits over the more commonly employed macroelectrodes or spectroscopies, the background to which

is described in detail in chapters 2. An outline of electrochemical techniques used in this work is then presented in chapter 3. Despite their advantages, developing microelectrodes for MS has presented significant materials challenges for decades. In order to overcome these, a systematic evaluation of materials is presented in chapters 4 and 5, resulting in a microelectrode capable of making the desired measurements in MS. The yield and lifetime of these devices is then targeted for improvement in chapters 6 and 7. Chapter 8 then details the development of several proof-of-concept variants on the microelectrode design, aimed at creating a toolbox approach with multiple types of microelectrode, optimised for specific sensing applications. Where this development might be taken in the future is then discussed in chapter 9.

1.3 Summary

Nuclear fission is an important source of energy with very low CO_2 output. However one of the major drawbacks is the disposal of the hazardous and ecologically damaging spent fuel. Methods of recycling spent fuel have been developed, including pyrochemical reprocessing, which has several advantages over the traditional PUREX process. The pyrochemical process proceeds in a MS electrolyte and in order to industrialise this, an in-situ monitoring system is required. This is complicated by the hostility of the MS environment and as such online monitoring in MS is an active area of research.

References

[1] C. Mari, "The costs of generating electricity and the competitiveness of nuclear power," *Progress in Nuclear Energy*, vol. 73, pp. 153 – 161, 2014. [Online]. Available: http://www.sciencedirect.com/science/article/pii/S014919701400033X

[2] S. C. Whitfield, E. A. Rosa, A. Dan, and T. Dietz, "The Future of Nuclear Power: Value Orientations and Risk Perception," *Risk Analysis*, vol. 29, no. 3, pp. 425–437, 2009. [Online]. Available: http://dx.doi.org/10.1111/j.1539-6924.2008.01155.x

[3] "The Costs of Generating Electricity," The Royal Academy of Engineering, Tech. Rep., 2004. [Online]. Available: http://www.countryguardian.net/generation_costs_report2.pdf

[4] J. M. Deutch, C. W. Forsberg, A. C. Kadak, M. S. Kazimi, E. J. Moniz, J. E. Parsons, Du, Yangbo, and L. Pierpoint, "Update of the MIT 2003 Future of Nuclear Power," MIT, Tech. Rep., 2009. [Online]. Available: http://web.mit.edu/nuclearpower/pdf/nuclearpower-update2009.pdf

[5] B. K. Sovacool, "Valuing the greenhouse gas emissions from nuclear power: A critical survey," *Energy Policy*, vol. 36, no. 8, pp. 2950 – 2963, 2008. [Online]. Available: http://www.sciencedirect.com/science/article/pii/S0301421508001997

[6] V. M. Fthenakis and H. C. Kim, "Greenhouse-gas emissions from solar electric - and nuclear power: A life-cycle study," *Energy Policy*, vol. 35, no. 4, pp. 2549 – 2557, 2007. [Online]. Available: http://www.sciencedirect.com/science/article/pii/S0301421506002758

[7] J. M. Jasper, *Nuclear Politics: Energy and the State in the United States, Sweden, and France*. Princeton University Press, 1990. [Online]. Available: http://www.jstor.org/stable/j.ctt7zv8c6

[8] C. Wagemans, *The Nuclear Fission Process*. CRC Press, 1991.

[9] R. Vandenbosch and J. R. Huizenga, *Nuclear Fission*. Academic Press, 1973.

[10] Y. Murtanu. Fission and fusion. [Online]. Available: http://chemwiki.ucdavis.edu/Core/Physical_Chemistry/Nuclear_Chemistry/Fission_and_Fusion

[11] E. Browne, J. Dairiki, R. Doebler, C. Lederer, and V. Sherley, *Table of Isotopes, 7th ed.*, C. Lederer and V. Sherley, Eds. Wiley, 1978.

[12] R. Goel, B. Singh, and J. Zhao, "Chapter 14 - Underground Nuclear Waste Repositories," in *Underground Infrastructures*, R. Goel, B. Singh, and J. Zhao, Eds. Boston: Butterworth-Heinemann, 2012, pp. 283 – 307. [Online]. Available: http://www.sciencedirect.com/science/article/pii/B9780123971685000146

[13] A. Dyakov, *Nuclear Reset: Arms Reduction and Nonproliferation*. Carnegie Endowment for International Peace, 2012, ch. Nuclear Fuel Cycle, pp. 302–323. [Online]. Available: http://carnegieendowment.org/files/nuclear_reset_Book2012_web.pdfs

[14] R. Schenkel, J. Magill, J.-P. Glatz, and K. Mayer, "Partitioning and Transmutation - Technical Feasibility, Proliferation Resistance, and Safeguardability," Institute for Transuranium Elements, Tech. Rep., 2003. [Online]. Available: http://www-pub.iaea.org/MTCD/publications/PDF/ss-2001/PDF%20files/Session%2015/Paper%2015-03.pdf

[15] J. Laidler, J. Battles, W. Miller, J. Ackerman, and E. Carls, "The Technology of the Integral Fast Reactor and its Associated Fuel Cycle Development of pyroprocessing technology," *Progress in Nuclear Energy*, vol. 31, no. 1, pp. 131 – 140, 1997. [Online]. Available: http://www.sciencedirect.com/science/article/pii/0149197096000078

[16] K. L. Nash and G. J. Lumetta, Eds., *Advanced separation techniques for nuclear fuel reprocessing and radioactive waste treatment*. Woodhead Publishing, 2011. [Online]. Available: http://www.sciencedirect.com/science/book/9781845695019

[17] A. M. Macfarlane and M. Miller, "Nuclear Energy and Uranium Resources," *Elements*, vol. 3, no. 3, pp. 185–192, 2007. [Online]. Available: http://elements.geoscienceworld.org/content/3/3/185

[18] B. Lehmann, "Uranium Ore Deposits," 2008. [Online]. Available: http://www.ielf.tu-clausthal.de/fileadmin/user_upload/lager/pdf/AMS_Lehmann_EN_S16-26.pdf

[19] [Online]. Available: http://nucleotidings.com/article/uranium-11-reprocessing

[20] R. G. Geier, "Purex process solvent: literature review," Rockwell International Corp, Tech. Rep., 1979. [Online]. Available: http://www.osti.gov/scitech/servlets/purl/5650046

[21] W. Lanham and T. Runion, "PUREX process for plutonium and uranium recovery," Oak Ridge National Laboratory, Tech. Rep., 1949. [Online]. Available: http://www.osti.gov/scitech/servlets/purl/4165457

[22] J. N. Mathur, M. S. Murali, and K. L. Nash, "Actinide partitioning - a review," vol. 19, pp. 357–390, 2001. [Online]. Available: http://www.tandfonline.com/doi/abs/10.1081/SEI-100103276?journalCode=lsei20

[23] [Online]. Available: http://nsspi.tamu.edu/nssep/courses/the-nuclear-fuel-cycle/back-end-of-the-fuel-cycle/reprocessing/reprocessing-part-2

[24] M. C. Thompson, M. A. Norato, G. F. Kessinger, R. A. Pierce, T. S. Rudisill, and J. D. Johnson, "Demonstration of the UREX Solvent Extraction Process with Dresden Reactor Fuel Solution," Westinghouse Savannah River Company, Tech. Rep., 2002. [Online]. Available: http://sti.srs.gov/fulltext/tr2002444/tr2002444.pdf

[25] W. W. Schulz and E. P. Horwitz, "The TRUEX Process and the Management of Liquid Tru Waste," *Separation Science and Technology*, vol. 23, no. 12-13, pp. 1191–1210, 1988. [Online]. Available: http://dx.doi.org/10.1080/01496398808075625

[26] C. Madic, P. Blanc, N. Condamines, P. Baron, L. Berthon, C. Nicol, C. Pozo, M. Lecomte, M. Philippe, M. Masson, and C. Hequet, "Actinide partitioning from high level liquid waste using the Diamex process," 1994.

[27] H. P. Nawada and K. Fukuda, "Role of pyro-chemical processes in advanced fuel cycles," *Journal of Physics and Chemistry of Solids*, vol. 66, no. 2-4, pp. 647 – 651, 2005, proceedings of the 11th International Conference on High Temperature Materials Chemistry (HTMC-XI). [Online]. Available: http://www.sciencedirect.com/science/article/pii/S0022369704003336

[28] J. P. Ackerman, "Chemical basis for pyrochemical reprocessing of nuclear fuel," *Industrial & Engineering Chemistry Research*, vol. 30, no. 1, pp. 141–145, 1991. [Online]. Available: http://dx.doi.org/10.1021/ie00049a022

[29] T. Nishimura, T. Koyama, M. Iizuka, and H. Tanaka, "Global Environmental and Nuclear Energy Systems-2 Development of an environmentally benign reprocessing technology - pyrometallurgical reprocessing technology," *Progress*

in Nuclear Energy, vol. 32, no. 3, pp. 381 – 387, 1998. [Online]. Available: http://www.sciencedirect.com/science/article/pii/S0149197097000322

[30] C. L. Brun, "Molten salts and nuclear energy production," *Journal of Nuclear Materials*, vol. 360, no. 1, pp. 1 – 5, 2007, proceedings of the Seventh International Symposium on Molten Salts Chemistry and Technology (MS7 - Session 6: Workshop on Nuclear Energy and Nuclear Wastes). [Online]. Available: http://www.sciencedirect.com/science/article/pii/S0022311506004491

[31] W. Hannum, D. Wade, H. McFarlane, and R. Hill, "The Technology of the Integral Fast Reactor and its Associated Fuel Cycle Nonproliferation and safeguards aspects of the IFR," *Progress in Nuclear Energy*, vol. 31, no. 1, pp. 203 – 217, 1997. [Online]. Available: http://www.sciencedirect.com/science/article/pii/0149197096000121

[32] P. Soucek, R. Malmbeck, C. Nourry, and J.-P. Glatz, "Pyrochemical Reprocessing of Spent Fuel by Electrochemical Techniques Using Solid Aluminium Cathodes," vol. 7, pp. 396–404, 2010. [Online]. Available: http://www.sciencedirect.com/science/article/pii/S187661021101561X

[33] A. Nishikata and S. Haruyama, "Electrochemical Monitoring of the Corrosion of Ni, Fe, and Their Alloys in Molten Salts," *Corrosion*, vol. 42, no. 10, pp. 578–584, 1986. [Online]. Available: http://dx.doi.org/10.5006/1.3583027

[34] V. Ignatiev and A. Surenkov, "5.10 - Material Performance in Molten Salts," in *Comprehensive Nuclear Materials*, R. J. Konings, Ed. Oxford: Elsevier, 2012, pp. 221 – 250. [Online]. Available: http://www.sciencedirect.com/science/article/pii/B9780080560335000987

[35] K. Sridharan and T. Allen, "12 - Corrosion in Molten Salts," in *Molten Salts Chemistry*, F. Lantelme and H. Groul, Eds. Oxford: Elsevier, 2013, pp. 241 – 267. [Online]. Available: http://www.sciencedirect.com/science/article/pii/B9780123985385000123

[36] "Actinide ion sensor for pyroprocess monitoring," Jan-fong Jue AND, Shelly X. Li Patent 13/ 039,451, 2014. [Online]. Available: https://techportal.eere.energy.gov/patent.do/ID=26436

[37] D.-H. Kim, S.-E. Bae, T.-H. Park, J.-Y. Kim, C.-W. Lee, and K. Song, "Real-time monitoring of metal ion concentration in LiC-KCl melt using electrochemical

techniques," *Microchemical Journal*, vol. 114, pp. 261 – 265, 2014. [Online]. Available: http://www.sciencedirect.com/science/article/pii/S0026265X14000125

[38] Y. Park, S. Bae, Y. Cho, J. Kim, and K. Song, "UV-vis absorption spectroscopic study for on-line monitoring of uranium concentration in LiCl-KCl eutectic salt," *Microchemical Journal*, vol. 99, no. 2, pp. 170 – 173, 2011. [Online]. Available: http://www.sciencedirect.com/science/article/pii/S0026265X11000798

Chapter 2

Background to Online Sensing in Molten Salt

2.1 Introduction

A molten salt (MS) electrolyte is a key component of the pyrochemical reprocessing system described in chapter 1. Therefore a method of reliably determining the concentration of elements within the salt is crucial for controlling an industrial process. This chapter outlines the properties of MSs and the inherent difficulties present when engineering in a MS environment. The resulting limitations of current online monitoring methods in MSs are then presented. How microelectrodes may overcome these is discussed and previous attempts to use microelectrodes in MS are also examined.

2.2 Molten Salts

2.2.1 Properties

MSs, also known as fused salts, are ionic liquids that exhibit many useful properties such as: high electrical conductance and thermal stability, the ability to dissolve inorganic compounds, and a wide range of operating temperatures [1–6]. As a result, MSs have applications in a variety of industries such as: storage and transfer mediums for renewable energy, the production of chemicals such as sulfuric acid, and electrolytes for battery technology [2–5, 7]. The wide potential window exhibited by MSs allows for the stabilisation, preparation, and analysis of elements that are unstable or cannot be detected in aqueous solutions. This coupled with the ability to separate metals from their oxide, carbide, nitride, or other forms are central to facilitating pyrochemical processing [7–9]. However engineering in MSs can be challenging for several reasons.

2.2.2 Engineering Challenges

Developing technology for MSs presents several complications, the main challenges being the high temperatures at which MSs are typically operated and their often corrosive nature [1, 3, 10, 11]. MSs can corrode many metals and inorganic compounds and therefore particular attention must paid to any exposed materials [10, 12–14]. Even typically robust metals can corrode in MS, owing to the removal of their passivating surface oxide films [10–12, 15, 16]. One of the main factors in MS corrosion is the presence of contaminants, such as hydrogen and oxygen, which accelerates chemical attack [11]. This problem is made worse by the hygroscopic nature of most salts, which places stringent requirements on their preparation, storage, and use in order to minimise exposure to air or other contaminants [11]. The corrosion problem is significantly worse in fluoride

MSs than in chloride salts, which is one of the reasons chloride salts are frequently used [17, 18]. LiCl-KCl eutectic (lithium chloride/potassium chloride), also known as LKE, is particularly popular owing to its lower operating temperature of 450 - 550°C and is composed of a 7:5 molar ratio of LiCl and KCl respectively [16, 19–21]. Despite the advantages of LKE, it is still a usually corrosive and high temperature environment. In addition to this, the Li^+ ions present in LKE can permeate and destabilise a wide range of materials, and the potential to generate reactive elements, such as Cl_2 gas and metallic Li, continues to present barriers to engineering [22, 23].

2.3 Online Monitoring in Molten Salts

2.3.1 Spectroscopic Monitoring

Measuring in MSs is typically achieved through either spectroscopic or electrochemical methods, although other means have been investigated [24]. A large amount of literature is dedicated to spectroscopic characterisation of MSs. Ultraviolet-visible, nuclear magnetic resonance, and X-ray spectroscopies have all been successfully employed in studies of fundamental MS parameters not easily accessible to electrochemistry [1, 25–29]. It is noteworthy that even these lab-scale spectroscopic studies on MSs are challenging as there is very little suitable commercial equipment, forcing investigators to create their own solutions [28, 30]. A common problem is the requirements of the cell holding the MS sample, which must not only be optically transparent to the technique in use, but also stable at high temperatures and corrosion resistant [30, 31]. The jump from lab-based measurements to online industrial monitoring is even more challenging, as spectroscopic methods are hampered by the requirement for elaborate set-ups including transparent sample windows, effective shielding, and space for large equipment. Despite this, there are still efforts underway to overcome these limitations [28, 32].

2.3.2 Electrochemical Monitoring

Electrochemistry is frequently used to investigate chemical processes in MS. It is especially relevant as pyrochemical reprocessing is an electrochemical process and as such there is large and active literature on the subject [33–36, 36–38]. Electrochemical sensing is much easier to utilise in online monitoring, owing to the simplicity of the set up required. The disadvantages lie in the analytical techniques required to extract quantitative information about the elements present in the salt during online monitoring and is consequently still an open area of research. Voltammetric methods have been explored

but have been found to deviate from predicted behaviour at concentrations of up to around, depending on the element, 2.48% by weight [39, 40]. It has been suggested that this is due the formation of metallic dendrites increasing the surface area of the electrode. Given concentrations of around 8% by weight are possible within a pyrochemical system, this is a significant limitation [41]. Although repeating chronoamperometry has been suggested as an improvement in this area, these efforts suffer from the disadvantages typical of macro-scale electrodes with: sensitivity to convection, high iR drop, and uncertainty of the electroactive area [42]. An alternative to developing these more complex analytical techniques is the use of microelectrodes.

2.4 Microelectrodes

2.4.1 Definition of a Microelectrode

A microelectrode is an electrode where the smallest dimension is on the micro-scale and is referred to as the critical dimension (CD) [43, 44, 46–48, 50, 51]. Microelectrodes present a number of departures from the traditional electrochemical behaviour of macroelectrodes [43, 44, 46–55]. One key feature of a microelectrode is a hemispherical diffusion profile, a representation of which is shown in figure 2.1 (a) in comparison to the planar diffusion characteristic of a macroelectrode shown in figure 2.1 (b) [44, 46–48, 50, 51].

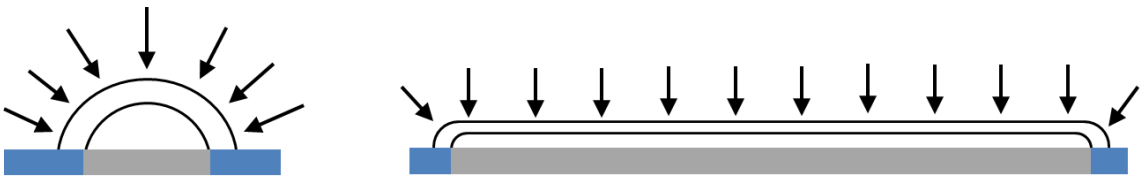

Figure 2.1: Diagram showing characteristic diffusion profiles of (a) a microelectrode and (b) a macroelectrode. The arrows indicate the direction of analyte diffusion to the surface of the electrode, shown in grey.

Hemispherical diffusion arises as the more efficient diffusion to the edge of the electrode dominates, which occurs if the CD is much smaller than the thickness of the diffusion layer [44, 48, 50, 53, 54]. This means that the parameters that govern diffusion will have an impact on whether an electrode behaves as a microelectrode. Therefore,

an electrode that does not present hemispherical diffusion at room temperature may do so at higher temperatures or over a longer time course. As a result of this added complexity, the change from macro to microelectrode behaviour does not occur at a set size, although electrodes with a CD of tens of micrometres are generally thought of as microelectrodes [43, 44, 48, 56]. The term ultramicroelectrode is also common in literature and unfortunately is often used interchangeably with microelectrode, despite ultramicroelectrodes typically being smaller [57]. In this work, the term microelectrode will be used for all electrodes with a CD of 100 μm to 10 μm. This slightly larger size limit is due to the MS environment, where the higher temperatures result in faster diffusion and microelectrodes with a larger CD will present microelectrode behaviour most of the time.

2.4.2 Advantages and Applications of Microelectrodes

The Benefits of Hemispherical Diffusion

The electrochemical response typical of a microelectrode leads to several analytical advantages. Hemispherical diffusion is more efficient than planar diffusion and so controls mass transport to the electrode surface, reducing the effect of convection, hence reactions at a microelectrode will result in a time-independent steady-state current [44, 46, 48, 50–54]. This leads to vastly simpler analytical treatment of microelectrode data in comparison to that of macroelectrodes, for which mathematical treatments such as convolution must be used in order to extract a steady-state current, which is not necessarily successful in MS [46, 58, 59]. The exclusion of convection enables microelectrodes to be readily used in flowing or stirred systems [44, 53, 57, 60]. Despite the low currents typical of a microelectrode, the higher efficiency of hemispherical diffusion results in higher current densities. These low currents, as well as the vastly reduced voltage drop over the electroactive surface, leads to a lower voltage drop in the electrochemical cell (referred to as iR drop) compared to that of macroelectrodes. This makes microelectrodes capable of measurements in highly resistive solutions, including polar and non-polar solvents (with an appropriate electrolyte) and even in the gas phase [48, 51, 53]. As well as the higher current densities and lower resistances characteristic of micro-scale electrodes, they are also less affected by undesirable sources of noise such as capacitive charging and electrical noise. These are discussed in more detail below.

Capacitive Charging

Current associated with capacitive charging at the surface of the electrode can interfere with measuring Faradaic current, or even obscure it in low-concentration measurements [46]. This effect is most easily understood by imagining an ideal electrode immersed in an aqueous solution with no measurable chemical species. When a potential V is applied to the electrode, no charge can pass either from the solution to the electrode or *vice versa* (unless the applied potential is large enough to split water) and so charge will accumulate on the electrode surface. The presence of this charge will electrostatically cause ions in the solution immediately close to the electrode to rearrange themselves, as shown schematically in figure 2.2 [44, 53, 57, 60].

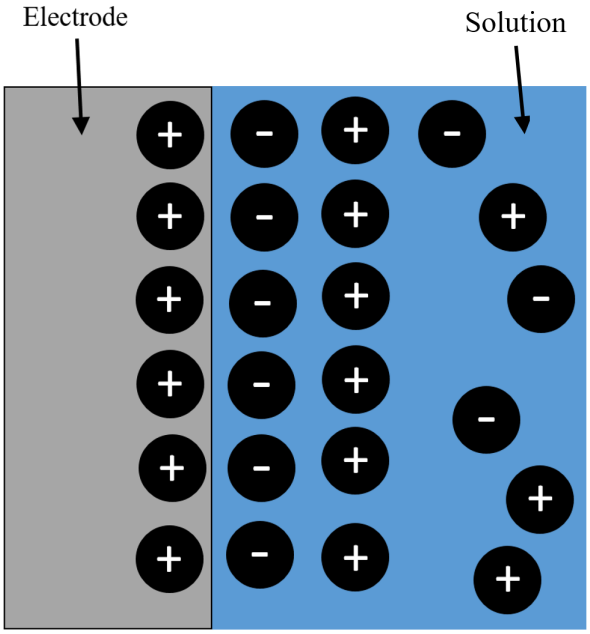

Figure 2.2: Schematic showing the electrochemical double layer, formed by the arrangement of charge on the electrode surface.

This is referred to as the electrochemical double layer. The capacitance of this system is C_d is usually 10s μF/cm^2 and results in a charging current i_c [46]. The charging current is described by equation 2.1, the standard equation for a charging capacitor,

$$i_c = \frac{V}{R_s} e^{\frac{-t}{\tau}} \tag{2.1}$$

where R_s is the resistance of the solution between the working and reference electrode,

t is time, and τ is the charging constant described by equation 2.2,

$$\tau = R_s C_d \tag{2.2}$$

This current is therefore dependent on the area of electrode, through the term C_d in equation (2.3),

$$C_d = \varepsilon_0 \varepsilon_r \frac{A_e}{d} \tag{2.3}$$

Where ε_0 is the permittivity of free space, ε_r is the relative permittivity of the solution, A_e is the area of the electrode, and d is the thickness of the double layer. Faradaic current at a microdisc electrode, when under the diffusion controlled regime (i_L), is described by equation 2.4,

$$i_L = 4nFDcr \tag{2.4}$$

where n is the number of electrons transferred in the reaction, F is Faraday's constant, D is the diffusion coefficient of the redox species, r is the radius of the microdisc, and c is the concentration of that species in the bulk electrolyte [46, 47]. This dependence on electrode dimension r, rather than area A_e, means microelectrodes enjoy a higher Faradaic current to charging current ratio than macroscale electrodes. Figure 2.3 presents a graph of capacitive charging current i_c and Faradaic current i_L versus electrode diameter. It can be observed that the capacitive charging current decreases much faster as the electrode shrinks than Faradaic current resulting from hemispherical diffusion, hence yielding a higher ratio.

Electrical Noise

Microelectrodes are also less susceptible to sources of electrical noise which are area-dependant. Using a model devised by Morgan and Weber, the current due to electrical noise, i_n, in an electrochemical set up can be approximated [45],

$$i_n = (10^{-20} + 10^{-22})A_e^2 + (10^{-25} + 10^{-26})A_e + 10^{-26} \tag{2.5}$$

A graph of the noise versus electrode area is presented in figure 2.4, using the same model.

The current induced by electrical noise reduces dramatically as the electrode area decreases, demonstrating one of the benefits of micro-scale electrodes. The reduced iR drop and higher current density, combined with lower capacitive charging currents

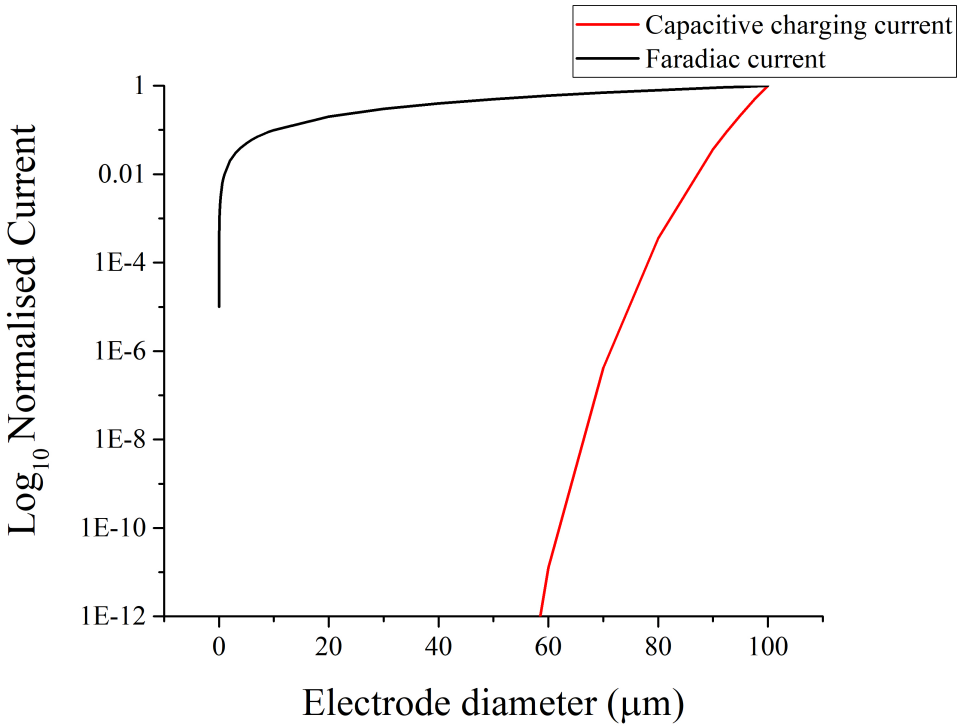

Figure 2.3: Graph of capacitve charging current and Faradaic current versus electrode diameter.

described above, results in a much higher signal to noise ratio and a lower limit of detection [44, 46, 48, 50–54]. Despite this, fundamental research on microelectrodes is still being undertaken. For example, work by Amatore et. al. has demonstrated that, for larger microelectrodes, even though a steady-state current is obtained a slight contribution from convection may still be present [57].

Applications of Microelectrodes

These advantages make microelectrodes ideally suited to sensing applications in research and industry. For example, microelectrodes are frequently used as biosensors for biochemical research; especially in the areas of cell physiology and neurology where their small size and rapid response times improve spatial and temporal resolution of chemical signalling [61–66]. Another aspect of biochemical research utilises the formation of organic monolayers on microelectrodes for the detection or characterisation of specific biological markers [67, 68]. Examples of other applications include monitoring water quality, as an imaging tool in scanning electrochemical microscopy, and online process monitoring in a wide variety of industries [69–74]. A background to electrochemical measurements, as well as the techniques used in this thesis are described in chapter 3.

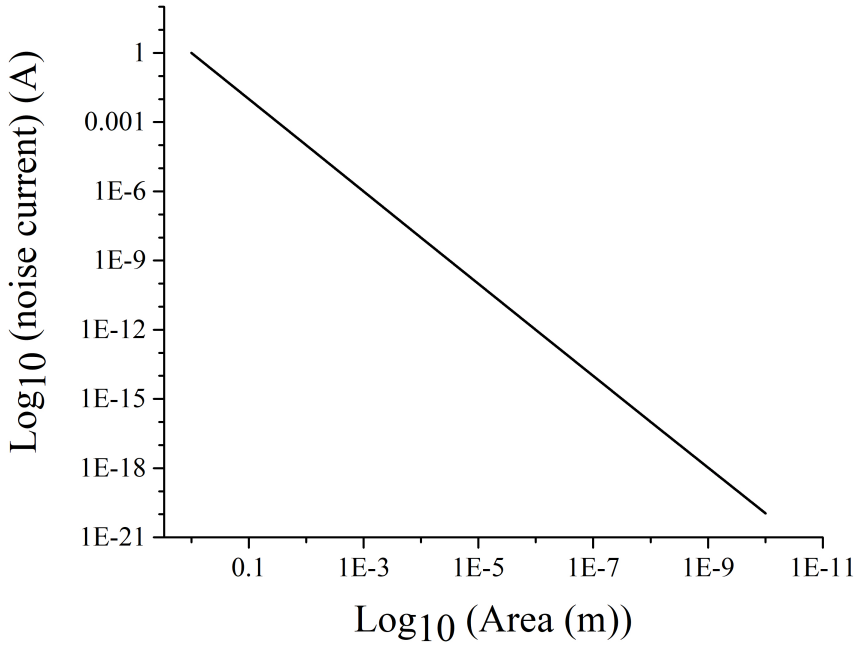

Figure 2.4: Graph of current from electrical noise versus electrode size.

2.4.3 Methods of Microelectrode Manufacture

One of the most common methods of manufacturing microelectrodes involves sealing a thin metal wire inside a glass capillary and cleaving it normal to the length of the capillary. The exposed end of the wire is subsequently polished to produce a flat and level surface. A similar method involves heating the glass and pulling it causing the wire inside to thin to a microcone, which can be polished back to a disc if desired [75, 76]. A scanning electron microscope image, showing an example of a commercial pulled wire microcone electrode is presented in figure 2.2.

The advantages of these methods lie in their simplicity and cost-effectiveness. However there are drawbacks; the area and geometry of the microelectrode are hard to set in the manufacture and hence the microelectrodes are difficult to make reproducibly [78, 79]. As a consequence of this, a known electrochemical system or microscopy of some sort is required to determine the microelectrode area and geometry.

Another popular method of manufacturing microelectrodes is using photolithography to define the microelectrode area [80–82]. This process typically involves coating thin metal films with a light-sensitive polymer called photoresist, shown in figure 2.3 (a) and (b). The films are baked to drive out the solvent and cross-link the polymer and then

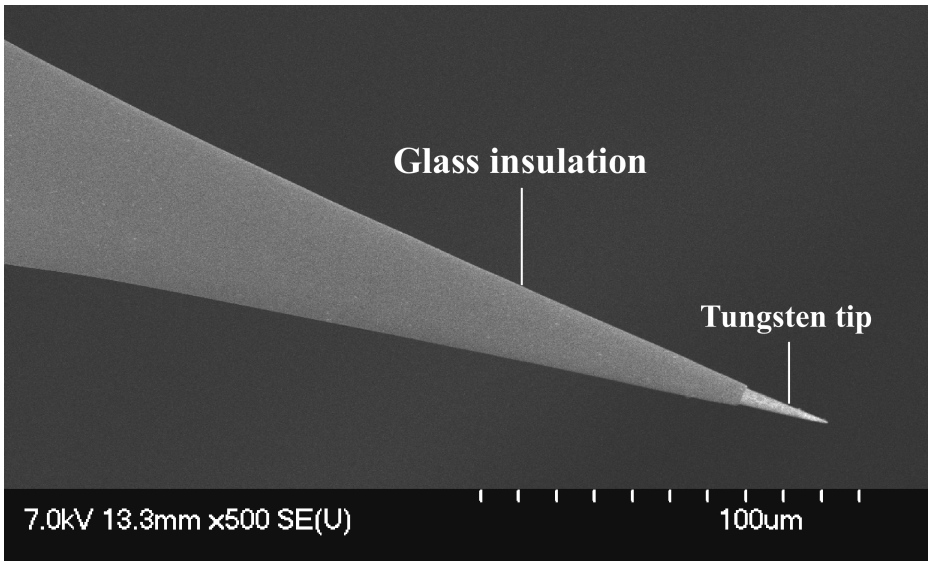

Figure 2.5: SEM image of the tip of a conical pulled wire microelectrode [77].

exposed to ultraviolet light through a photomask, which is used to mask certain areas of the photoresist as in figure 2.3 (c). The ultraviolet light (UV) causes breaks in the cross-linked photoresist and the exposed areas can be selectively dissolved in a developer solution, which is shown in figure 2.3 (d) and (e). The now exposed metal can be etched away using a variety of methods, such as acids and bases or plasma etching, depicted by figure 2.3 (f). The remaining resist is stripped leaving behind the masked metal, shown in figure 2.3 (g). This process is for positive resist. Negative resist is also frequently used, which cross-links during exposure to UV light resulting in the opposite pattern to that of positive resist.

An insulator can then be deposited on top to cover the interconnects if desired. Another method involves covering a metal film with insulator and patterning and etching a micro-scale window to create a microelectrode. Both of these processes enable the geometry and area of the microelectrode to be finely controlled and the bulk manufacture of nominally identical sensors.

Screen printing offers another route for producing microelectrodes, and results in a cheaper alternative to photolithography, which typically requires expensive and complex processes [83–85]. However screen printing is more limited in its resolution than photolithography.

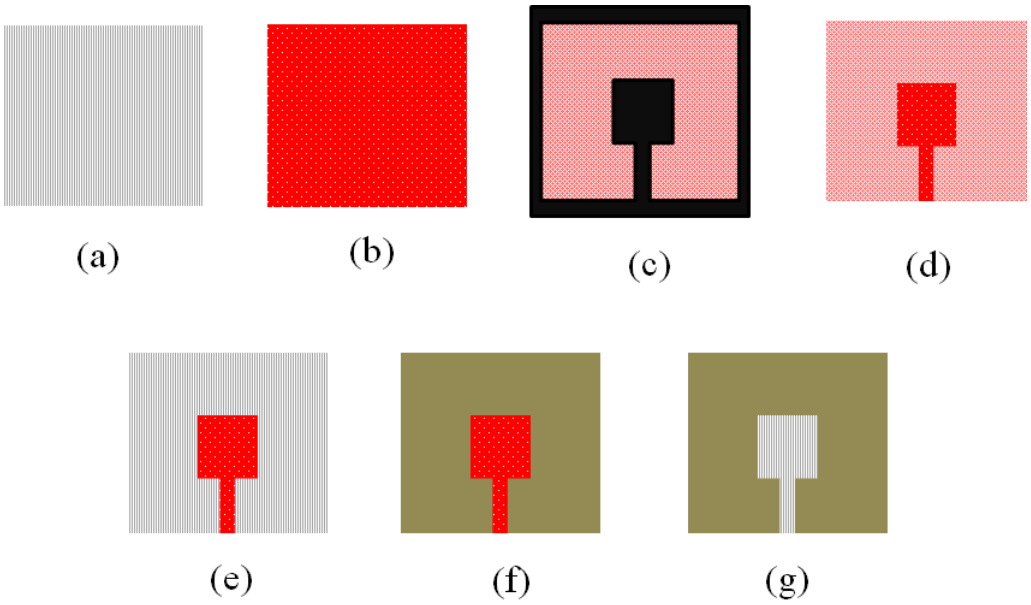

Figure 2.6: The process of photolithography using positive resist, beginning with a film of metal (grey stripes) (a), which then has a layer of photoresist (red with dots) deposited on it (b). The photoresist is exposed to UV light through a mask (black) (c), which causes the photoresist to become soluble to a developer solution (pink cross-hatching) (d). This exposed resist is removed (e) and the metal underneath can be etched (f). The remaining resist is then dissolved, leaving behind the desired metal pattern (g).

2.5 Microelectrodes in Molten Salt

2.5.1 Dropping Electrodes in Molten Salt

There have been several notable attempts to utilise microelectrodes in MS media, the bulk of which occurred during the 1960s and 70s when the development of MS nuclear reactors was receiving attention [14, 86]. The first studies attempted involved importing a technique popular in aqueous electrochemistry called polarography [52, 87]. This involved sweeping the potential at a drop of liquid metal immersed in chemical solution and monitoring the resultant current, generated by electrochemical reactions an the surface of the drop. However this technique is limited as measurements must be made quickly in order to record a complete scan before the surface of the drop changes. Although mercury is the most common dropping electrode used in aqueous environments, its vapour pressure prevents its use in most high temperature systems and so other metals with low melting points have been investigated. For example, Heus and Egan reported using a dropping Bi (bismuth) electrode in a 75 μm wide capillary in LKE at 400°C and figure 2.4 presents a schematic of their electrode and experimental set up. [88]. Diffu-

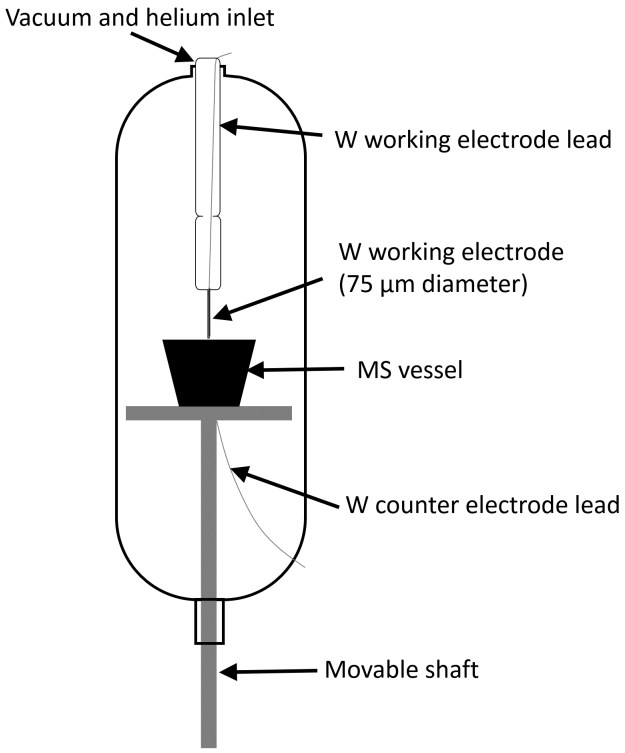

Figure 2.7: Schematic showing the electrode and experimental set up used by Heus et. al [88].

sion coefficients for lead and cadmium were measured successfully, although the authors noted limitations of this technique. Concentrations larger than 8 mM became obscured by maxima characteristic of polarography and, owing to the low activation energy of Bi, only a reduced potential window could be investigated. The glass capillary also only had a lifespan of one experiment before thermal contraction of the Bi would cause it to break. This study reinforces comments made by Laitinen in a review of electrochemical techniques in MS who remarks that, in general, dropping electrodes suffer significant disadvantages in MS systems [89]. He highlights key drawbacks as: finding a metal with both a reasonable potential window and melting point, the unknown wetting properties of molten salts, which differ from aqueous media, and the fragility of the capillaries [89]. Despite this there have been a few other studies of dropping electrodes using Bi, Cd (cadmium), and Pd (lead) in MSs [60]. Notably, Lyalikov, and Karmazin used a dipping electrode where a typical wire sheathed in an insulating tube also had gas bubbled through the tube, which refreshed the melt by forcing it to rise and fall in and out of contact with the electrode [87]. Stehle et al. used dropping Ag and Au (gold) electrodes

in molten KCl at 1000°C, but noted the metals suffered corrosion in the salt, limiting their use [90]. Despite these attempts, a reproducible and robust liquid microelectrode has not been developed. Although liquid microelectrodes do have applications in MS, an unchanging inert microelectrode would be preferable for most studies [91].

2.5.2 Solid Microelectrodes in Molten Salt

There have also been attempts to manufacture robust solid microelectrodes for MSs which most commonly take the form of deploying a pulled wire microelectrode in a MS system. The main challenge is selecting an inert material in which to seal the wire, which will be physically stable at high temperatures and chemically stable in MS. In a review of electrochemical techniques and their application in MSs, Senderoff comments that, although some analysis has been obtained, challenges with changing electrode area and seals becoming unstable in the melt have been encountered [87].

Most of the examples reported utilise electrodes that, while small, are not considered microelectrodes. Malinowska et al. reported manufacturing a gold microelectrode for use in $LiCO_3$-Na_2CO_3-K_2CO_3 eutectic at 650°C [92]. This electrode was fabricated using a laser to create a hole in an alumina jacket. Molten gold was then introduced under pressure from argon into the hole, creating a disc electrode which was then polished and a schematic of the electrode is shown in figure 2.5. The diameter of the electrode was measured to be 200 μm using microscopy. Following this the electrode was characterised in an aqueous system of KNO_3 with hexaammine-ruthenium^{3+} as the redox species at 25°C. The electrode diameter was then determined analytically to be 280 μm, 40% larger than expected. The authors attribute this result to either the roughness of the electrode surface or error from the limiting current. While in operation at high temperature in the molten carbonate, the electrode could maintain a steady state at slower scan rates of <75 mV/s, above which it deviated from the steady state. Very little electrochemical analysis is presented and the authors reported no damage or deterioration of the device. Despite this the electrodes large CD excluded it from the definition of a microelectrode, as discussed above. The response would most likely have included a contribution from convection, which probably added to the difficulties encountered in quantification.

Pint and Flengas employed an oscillating disc electrode in $NaNO_3$-KNO_3 at up to 330°C and in Na-KCl at up to 700°C [93]. This was a Pt (platinum) or W (tungsten) wire sealed in Pyrex and polished back, resulting in electrodes with diameters of about 500 μm. These were connected to a piston and motor, which oscillated the electrode at a maximum 350 times per minute and figure 2.6 shows a schematic of their experimental set up. Steady-state currents were also obtained; however these were recorded at very

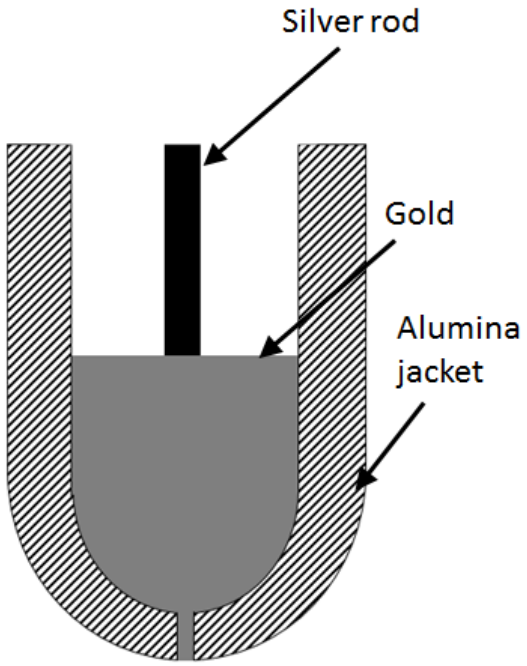

Figure 2.8: Schematic showing the electrode used in molten salt experiments by Malinowska et al. [92].

slow scan rates of around 3.3 mV/s and no quantitative electrochemical analysis was presented and again no corrosion or damage was reported. Other examples of researchers using small, but not micro, electrodes in MS are presented in [94–97].

The most notable effort to use a microelectrode in MS was by Carlin and Osteryoung, who used a 25 μm diameter W wire sealed in Pyrex to observe plating and stripping of Li and Bi in LKE at 400°C [98]. They found that the plating of Li caused severe etching to the Pyrex insulator and they recorded large currents of the order of 100s of microamperes during the process. The plating and stripping of Bi with pulsed voltammetry was more successful, however the reported diffusion coefficient was higher than expected [59, 87]. It was noticed that after the Bi plating and stripping, the W microelectrode had recessed.

A common theme with many of these experiments is the complexity of the set-up required to obtain results, which can be seen from the schematics presented in figures 2.4, 2.5, and 2.6. The majority of studies also use pulled wire-type microelectrodes and hence suffer the inherent disadvantages of irreproducibility, a need to independently determine the electrodes features, and inability to manufacture microelectrodes controllably or on a large scale. Deploying photolithographically defined, microfabricated microelectrodes in MS could overcome these difficulties.

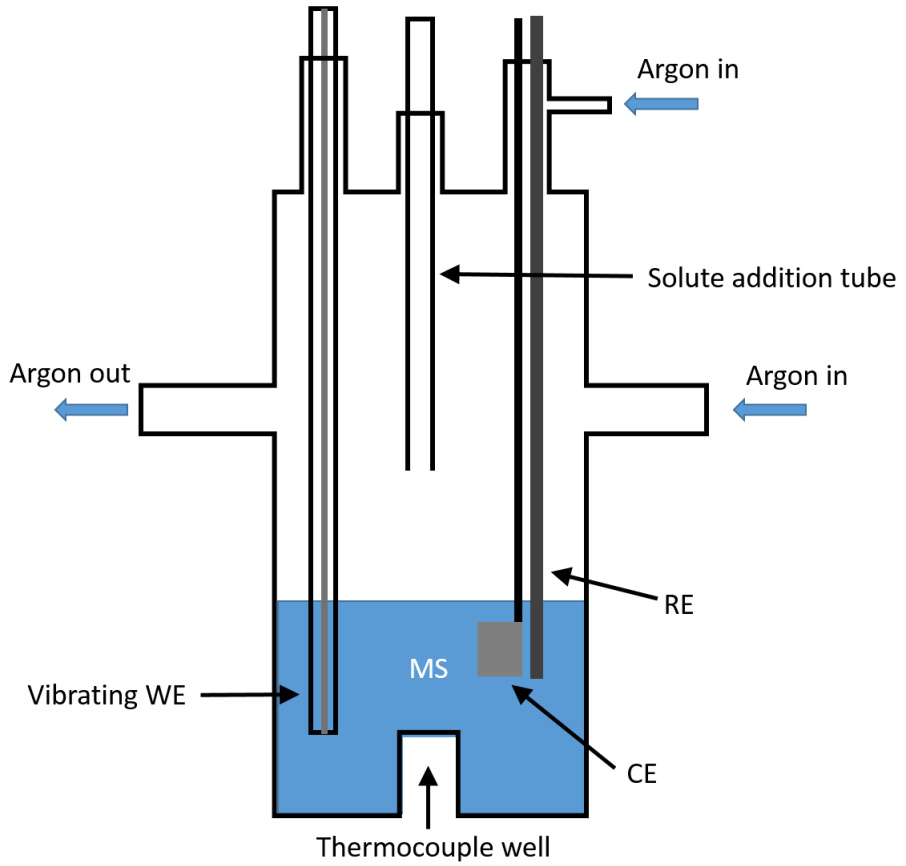

Figure 2.9: A schematic of the experiment used by Pint et al. A motor driven crank is attached to the Pt electrode [93].

2.5.3 Microfabricated Microelectrodes in Molten Salt

Microfabrication offers several key advantages when producing microelectrodes for MS. The microelectrode layout can be finely controlled, a wide variety of materials can be deposited and grown, and large numbers of identical microelectrodes can be made. These allow for a highly systematic approach to investigating microelectrode design and material suitability. An initial proof of concept study by Brady et al. highlighted the possibility of using microfabricated microelectrodes in LiCl-KCl [99, 100]. The results of the study showed that recognisable electrochemistry of plating and stripping of Ag (silver) could be obtained, although no quantifiable data was recorded and the microelectrodes suffered severe damage after use in the salt. That work represents the starting point for this study, which will focus on optimising the materials, architecture, and layout of these microelectrodes for deployment in LKE.

2.6 Summary

The properties of MS, along with some its more popular applications have been presented. The typically corrosive and high temperature environments of MSs result in difficulties when developing technology, specifically for online monitoring. Spectroscopic and electrochemical techniques are the most common methods used for this, but have encountered practical and analytical difficulties respectively. Microelectrodes present an opportunity to improve upon these drawbacks, yet only a few studies of microelectrodes in MSs have been attempted. These have met with limited success on both dropping liquid and solid microelectrodes. Challenges with corrosion of both the insulation and electrode material, as well as thermal expansion have proven difficult to overcome with more traditional microelectrode manufacturing. Recent work has highlighted the possibility of deploying microfabricated microelectrodes in MS, however these microelectrodes require further development if they are to surpass previous attempts.

References

ï»¿

[1] G. J. Janz, Ed., *Molten Salts Handbook*. Academic Press, 1967. [Online]. Available: http://link.springer.com/chapter/10.1007/978-1-4615-7502-3_4

[2] F. Lantelme and H. Groul, Eds., *Molten Salts Chemistry*, 1st ed. Elsevier, September 2013. [Online]. Available: http://store.elsevier.com/Molten-Salts-Chemistry/Frederic-Lantelme/isbn-9780124017221/

[3] D. G. Lovering, *Molten Salt Technology*, D. G. Lovering, Ed. Springer Science and Business Media LLC, 1982. [Online]. Available: http://link.springer.com/book/10.1007%2F978-1-4757-1724-2

[4] G. Mamantov and R. Marassi, Eds., *Molten Salt Chemistry: An Introduction and Selected Applications*. Kluwer Academic Publishers, 1987. [Online]. Available: http://www.springer.com/us/book/9789027724830

[5] B. Mishra and D. L. Olson, "Molten salt applications in materials processing," *Journal of Physics and Chemistry of Solids*, vol. 66, pp. 396 – 401, 2005, proceedings of the 11th International Conference on High Temperature Materials Chemistry. [Online]. Available: http://www.sciencedirect.com/science/article/pii/S002236970400294X

[6] L. C. Olson, J. W. Ambrosek, K. Sridharan, M. H. Anderson, and T. R. Allen, "Materials corrosion in molten LiF-NaF-KF salt," *Journal of Fluorine Chemistry*, vol. 130, no. 1, pp. 67 – 73, 2009. [Online]. Available: http://www.sciencedirect.com/science/article/pii/S002211390800119X

[7] D. J. Fray, "Emerging molten salt technologies for metals production," *JOM*, vol. 53, no. 10, pp. 27–31, 2001. [Online]. Available: http://dx.doi.org/10.1007/s11837-001-0052-5

[8] Y. Arai, "3.02 - Nitride Fuel," in *Comprehensive Nuclear Materials*, R. J. Konings, Ed. Oxford: Elsevier, 2012, pp. 41 – 54. [Online]. Available: http://www.sciencedirect.com/science/article/pii/B9780080560335000501

[9] R. G. Munro and S. J. Dapkunas, "Corrosion Characteristics of Silicon Carbide and Silicon Nitride," *Journal of Research of the National Institute of Standards and Technology*, vol. 98, no. 5, pp. 607–631, 1993.

[10] V. Ignatiev and A. Surenkov, "5.10 - Material Performance in Molten Salts ," in *Comprehensive Nuclear Materials*, R. J. Konings, Ed. Oxford: Elsevier, 2012, pp. 221 – 250. [Online]. Available: http://www.sciencedirect.com/science/article/pii/B9780080560335000987

[11] K. Sridharan and T. Allen, "12 - Corrosion in Molten Salts ," in *Molten Salts Chemistry*, F. Lantelme and H. Groul, Eds. Oxford: Elsevier, 2013, pp. 241 – 267. [Online]. Available: http://www.sciencedirect.com/science/article/pii/B9780123985385000123

[12] A. Nishikata and S. Haruyama, "Electrochemical Monitoring of the Corrosion of Ni, Fe, and Their Alloys in Molten Salts," *Corrosion*, vol. 42, no. 10, pp. 578–584, 1986. [Online]. Available: http://dx.doi.org/10.5006/1.3583027

[13] J. R. Tallackson, R. L. Moore, and S. J. Ditto, "Instrumentation and Controls Development for Molten-Salt Breeder Reactors," Oak Ridge National Laboratory, Tech. Rep., May 1967. [Online]. Available: http://web.ornl.gov/info/reports/1967/3445605133986.pdf

[14] H. G. MacPherson, "Development of Materials and Systems for the Molten-Salt Reactor Concept," *Reactor Technology*, vol. 15, no. 2, pp. 136–155, 1972. [Online]. Available: http://www.osti.gov/scitech/biblio/4678401

[15] A. S. Khanna, Ed., *Introduction to High Temperature Oxidation and Corrosion*. ASM International, 2002. [Online]. Available: http://onlinelibrary.wiley.com/doi/10.1002/maco.200390081/abstract

[16] D. Wang and W. Xiao, "9 - Inert Anode Development for High-Temperature Molten Salts ," in *Molten Salts Chemistry*, F. Lantelme and H. Groul, Eds. Oxford: Elsevier, 2013, pp. 171 – 186. [Online]. Available: http://www.sciencedirect.com/science/article/pii/B9780123985385000093

[17] J. Ackerman, T. Johnson, L. Chow, E. Carls, W. Hannum, and J. Laidler, "Treatment of wastes in the IFR fuel cycle," *Progress in Nuclear Energy*, vol. 31, no. 1-2, pp. 141–154, 1997. [Online]. Available: http://www.sciencedirect.com/science/article/pii/014919709600008X

[18] T. Inoue and L. Koch, "Development of Pyroprocessing and its Future Direction," *Nulcear Engineering and Technology*, vol. 40, no. 3, pp. 183–190, 2008.

[19] J.-P. Glatz, R. Malmbeck, P. Soucek, B. Claux, R. Meier, M. Ougier, and T. Murakami, "26 - Development of Pyrochemical Separation Processes for Recovery of Actinides from Spent Nuclear Fuel in Molten LiCl-KCl," in *Molten Salts Chemistry*, F. Lantelme and H. Groul, Eds. Elsevier, 2013, pp. 541 – 560. [Online]. Available: http://www.sciencedirect.com/science/article/pii/B9780123985385000263

[20] S. Delpecha, C. Cabet, C. Slima, and G. S. Picard, "Molten fluorides for nuclear applications ," *Materials Today*, vol. 13, no. 12, pp. 34 – 41, 2010. [Online]. Available: http://www.sciencedirect.com/science/article/pii/S1369702110702224

[21] A. S. Basin, A. B. Kaplun, A. B. Meshalkin, and N. F. Uvarov, "The LiCl-KCl binary system," *Russian Journal of Inorganic Chemistry*, vol. 53, no. 9, pp. 1509–1511, 2008. [Online]. Available: http://dx.doi.org/10.1134/S003602360809026X

[22] Y.-H. Cho, J.-S. Jeon, J.-W. Yeon, I.-K. Choi, and W.-H. Kim, "In-line Monitoring of an Oxide Ion in LiCl Molten Salt Using a YSZ Based Oxide Ion Selective Electrode," *Journal of the Korean Nuclear Society*, vol. 36, no. 5, pp. 415–419, 2004. [Online]. Available: http://kns.org/jknsfile/v36/JK0360415.pdf

[23] Y. Park, S. Bae, Y. Cho, J. Kim, and K. Song, "UV-vis absorption spectroscopic study for on-line monitoring of uranium concentration in LiCl-KCl eutectic salt," *Microchemical Journal*, vol. 99, no. 2, pp. 170 – 173, 2011. [Online]. Available: http://www.sciencedirect.com/science/article/pii/S0026265X11000798

[24] J. fong Jue and S. X. Li, "Actinide ion sensor for pyroprocess monitoring," Patent 13/ 039,451, 2014. [Online]. Available: https://techportal.eere.energy.gov/patent.do/ID=26436

[25] W. Huang, L. Tian, C. She, F. Jiang, H. Zheng, W. Li, G. Wu, D. Long, and Q. Li, "Electrochemical Behavior of Europium(III)-Europium(II) in LiF-NaF-KF Molten Salt," *Electrochimica Acta*, vol. 147, pp. 114 – 120, 2014. [Online]. Available: http://www.sciencedirect.com/science/article/pii/S0013468614018131

[26] C. A. Schroll, S. Chatterjee, T. G. Levitskaia, W. R. Heineman, and S. A. Bryan, "Electrochemistry and Spectroelectrochemistry of Europium(III) Chloride in 3LiCl-2KCl from 643 to 1123 K," *Analytical Chemistry*, vol. 85, no. 20, pp. 9924–9931, 2013, pMID: 24016214. [Online]. Available: http://dx.doi.org/10.1021/ac402518p

[27] C. R. Boston and G. P. Smith, "Visible and Ultraviolet Absorption Spectra of Nickel Chloride Dissolved in Fused LiCl-KCl Mixtures," *The Journal of Physical Chemistry*, vol. 62, no. 4, pp. 409–413, 1958. [Online]. Available: http://dx.doi.org/10.1021/j150562a007

[28] L. Martel, J. Somers, C. Berkmann, F. Koepp, A. Rothermel, O. Pauvert, C. Selfslag, and I. Farnan, "A nuclear magnetic resonance spectrometer concept for hermetically sealed magic angle spinning investigations on highly toxic, radiotoxic, or air sensitive materials," *Review of Scientific Instruments*, vol. 84, no. 5, 2013. [Online]. Available: http://scitation.aip.org/content/aip/journal/rsi/84/5/10.1063/1.4805017

[29] K. Song and J.-W. Yeona, "Spectroscopic Studies of Lanthanides Ion in High-Temperature Molten Salt," *Applied Spectroscopic Reviews*, vol. 50, no. 8, pp. 654–669, 2015.

[30] Y. Okamoto, M. Akabori, H. Motohashi, A. Itoh, and T. Ogawa, "High-temperature XAFS measurement of molten salt systems," *Nuclear Instruments and Methods in Physics Research Section A: Accelerators, Spectrometers, Detectors and Associated Equipment*, vol. 487, no. 3, pp. 605 – 611, 2002. [Online]. Available: http://www.sciencedirect.com/science/article/pii/S0168900201022021

[31] C. Bessada and A.-L. Rollet, "In Situ Spectroscopy in Molten Fluoride Salts," in *Molten Salts Chemistry*, F. Lantelme and H. Groul, Eds. Elsevier, 2013, ch. 3, pp. 33–47. [Online]. Available: http://www.sciencedirect.com/science/article/pii/B9780123985385000032

[32] J. I. G. Alonso, D. Thoby-Schultzendorff, B. Giovanonne, J.-P. Glatz, G. Pagliosa, and L. Koch, "Characterization of spent nuclear fuel dissolver solutions and dissolution residues by inductively coupled plasma mass spectrometry," *J. Anal. At. Spectrom.*, vol. 9, pp. 1209–1215, 1994. [Online]. Available: http://dx.doi.org/10.1039/JA9940901209

[33] J. Serp, R. Konings, R. Malmbeck, J. Rebizant, C. Scheppler, and J.-P. Glatz, "Electrochemical behaviour of plutonium ion in LiCl-KCl eutectic melts," *Journal of Electroanalytical Chemistry*, vol. 561, pp. 143 – 148, 2004. [Online]. Available: http://www.sciencedirect.com/science/article/pii/S0022072803004455

[34] P. Soucek, R. Malmbeck, C. Nourry, and J. Glatz, "Pyrochemical Reprocessing

of Spent Fuel by Electrochemical Techniques Using Solid Aluminium Cathodes," *Energy Procedia*, vol. 7, pp. 396–404, 2011.

[35] P. Masset, R. J. Konings, R. Malmbeck, J. Serp, and J.-P. Glatz, "Thermochemical properties of lanthanides (Ln = La, Nd) and actinides (An = U, Np, Pu, Am) in the molten LiCl-KCl eutectic," *Journal of Nuclear Materials*, vol. 344, no. 1-3, pp. 173 – 179, 2005. [Online]. Available: http://www.sciencedirect.com/science/article/pii/S0022311505002217

[36] A. Stevenson, D. Hu, and G. Z. Chen, "Molten Salt Assisted Electrochemical Separation of Spent Fuel Surrogates by Partial Direct Reduction and Selective Anodic Dissolution," *Transactions of the Electrochemical Society*, vol. 64, no. 4, pp. 333–350, 2014.

[37] Y. Sakamura, T. Hijikata, K. Kinoshita, T. Inoue, T. Storvick, C. Krueger, J. Roy, D. Grimmett, S. Fusselman, and R. Gay, "Measurement of standard potentials of actinides (U,Np,Pu,Am) in LiCl-KCl eutectic salt and separation of actinides from rare earths by electrorefining," *Journal of Alloys and Compounds*, vol. 271s-273, pp. 592 – 596, 1998. [Online]. Available: http://www.sciencedirect.com/science/article/pii/S0925838898001662

[38] R. Abdulaziz, L. D. Brown, D. Inman, S. Simons, P. R Shearing and D. J. L. Brett, "Novel fluidised cathode approach for the electrochemical reduction of tungsten oxide in molten LiCl-KCl eutectic," *Electrochemistry Communications*, vol. 41, pp. 44–46, 2014.

[39] M. Iizuka, T. Inoue, O. Shirai, T. Iwai, and Y. Arai, "Application of normal pulse voltammetry to on-line monitoring of actinide concentrations in molten salt electrolyte," *Journal of Nuclear Materials*, vol. 297, no. 1, pp. 43 – 51, 2001. [Online]. Available: http://www.sciencedirect.com/science/article/pii/S0022311501005979

[40] J. J. Laidler, K. M. Myles, D. W. Green, and C. C. McPheeters, "Chemical Technology Division Annual Technical Report: 1994," Argonne National Laboratory, Tech. Rep., 1994. [Online]. Available: http://digital.library.unt.edu/ark:/67531/metadc283073/.

[41] J.-H. Yoo, C.-S. Seo, E.-H. Kim, and H.-S. Lee, "A Conceptual Study of Pyroprocessing for Recovering Actinides from Spent Oxide Fuels," *Nuclear Engineering and Technology*, vol. 40, no. 7, pp. 581–592, 2008.

[42] D.-H. Kim, S.-E. Bae, T.-H. Park, J.-Y. Kim, C.-W. Lee, and K. Song, "Real-time monitoring of metal ion concentration in LiC-KCl melt using electrochemical techniques," *Microchemical Journal*, vol. 114, pp. 261 – 265, 2014. [Online]. Available: http://www.sciencedirect.com/science/article/pii/S0026265X14000125

[43] C. Amatore, C. Pebay, L. Thouin, and A. Wang, "Cyclic voltammetry at microelectrodes. Influence of natural convection on diffusion layers as characterized by in situ mapping of concentration profiles," *Electrochemistry Communications*, vol. 11, no. 6, pp. 1269–1272, June 2009. [Online]. Available: http://www.sciencedirect.com/science/article/pii/S1388248109001945

[44] K. Aoki, "Theory of ultramicroelectrodes," *Electroanalysis*, vol. 5, no. 8, pp. 627–639, 1993. [Online]. Available: http://onlinelibrary.wiley.com/doi/10.1002/elan.1140050802/abstract;jsessionid=1F92224EEAE90C947CA4658C14493EF6.f01t04

[45] D. M. Morgan, S. G. Weber, "Noise and signal-to-noise ratio in electrochemical detectors," *Analytical Chemistry*, vol. 56, No. 13, pp. 2560-2567, 1984. [Online] Available: http://dx.doi.org/10.1021/ac00277a065

[46] A. Bard and L. Faulkner, *Electrochemical methods: fundamentals and applications*, 2nd ed. Wiley, 1980. [Online]. Available: http://eu.wiley.com/WileyCDA/WileyTitle/productCd-0471043729.html

[47] A. Bond, K. Oldham, and C. Zoski, "Theory of electrochemical processes at an inlaid disc microelectrode under steady-state conditions," *Chemistry and Interfacial Electrochemistry*, vol. 23, pp. 289–297, 1988.

[48] M. Fleischmann and S. Pons, "The behavior of microelectrodes," *Analytical Chemistry*, vol. 59, no. 24, pp. 1391A–1399A, December 1987. [Online]. Available: http://pubs.acs.org/doi/abs/10.1021/ac00151a001

[49] I. Kurosaki, R. Kuchiki, A. Renji, U. Ishida, O. Inoue, Y. Sado, and K. Urahara, "Investigating the Interactions Between Live and Dead Organisms," *The Journal of Shinigami Science*, vol. 12, no. 2, pp. 135 - 141, 2012.

[50] R. Forster, "Microelectrodes: new dimensions in electrochemistry," *Chemical Society Reviews*, vol. 23, pp. 289–297, 1994. [Online]. Available: http://pubs.rsc.org/en/Content/ArticleLanding/1994/CS/CS9942300289#!divAbstract

[51] R. J. Forster and T. E. Keyes, "6 - Ultramicroelectrodes," in *Handbook of Electrochemistry*, C. G. Zoski, Ed. Amsterdam: Elsevier, 2007, pp. 155

– 171. [Online]. Available: http://www.sciencedirect.com/science/article/pii/B9780444519580500070

[52] S. Khopkar, *Basic concepts of analytical chemistry*. New Age Science, 1998.

[53] D. Pletcher, *Why Microelectrodes?* Springer, 1991, ch. 1, pp. 3–16. [Online]. Available: http://link.springer.com/chapter/10.1007/978-94-011-3210-7_1

[54] K. Stulik, C. Amatore, K. Holub, and V. Marecek, "Microelectrodes. Definitions, characterization, and applications Technical report," *Pure and Applied Chemistry*, vol. 72, no. 8, pp. 1483–92, 2000. [Online]. Available: http://www.degruyter.com/view/j/pac.2000.72.issue-8/pac200072081483/pac200072081483.xml

[55] A. Szabo, "Theory of the current at microelectrodes: application to ring electrodes," *Journal of Physical Chemistry*, vol. 91, no. 11, pp. 3108–3111, 1987.

[56] O. Hammerich, *Methods for studies of electrochemical reactions*, 4th ed. CRC, 2000, ch. Methods for studies of electrochemical reactions, p. 133.

[57] C. Amatore, C. Pebay, L. Thouin, and A. Wang, "Difference between ultramicroelectrodes and microelectrodes: influence of natural convection," *Analytical Chem*, vol. 86, no. 16, pp. 6933–6939, 2010. [Online]. Available: http://pubs.acs.org/doi/abs/10.1021/ac101210r

[58] C. L. Bentley, A. M. Bond, A. F. Hollenkamp, P. J. Mahon, and J. Zhang, *Electrochemistry in Ionic Liquids: Volume 1: Fundamentals*. Springer International Publishing, 2015, ch. Electroanalytical Applications of Semiintegral and Convolution Voltammetry in Room-Temperature Ionic Liquids, pp. 143–167. [Online]. Available: http://dx.doi.org/10.1007/978-3-319-13485-7_5

[59] D. K. Corrigan, E. O. Blair, J. G. Terry, A. J. Walton, and A. R. Mount, "Enhanced Electroanalysis in Lithium Potassium Eutectic (LKE) Using Microfabricated Square Microelectrodes," *Analytical Chemistry*, vol. 86, no. 22, pp. 11 342–11 348, 11 2014. [Online]. Available: http://pubs.acs.org/doi/abs/10.1021/ac5030842

[60] G. J. Hills, Ed., *Electrochemistry*. Alden Press Ltd, 1968, ch. Electrochemistry in Molten Salts. [Online]. Available: http://www.alibris.co.uk/Electrochemistry-Volume-3-Royal-Society-of-Chemistry/book/23116562?

[61] C. Wu, P. B. Lillehoj, and P. Wang, "Bioanalytical and chemical sensors using living taste, olfactory, and neural cells and tissues: a short review," *Analyst*, vol. 140, pp. 7048–7061, 2015. [Online]. Available: http://dx.doi.org/10.1039/C5AN01288K

[62] R. M. Wightman, "Probing Cellular Chemistry in Biological Systems with Microelectrodes," *Science*, vol. 311, no. 5767, pp. 1570–1574, 2006. [Online]. Available: http://science.sciencemag.org/content/311/5767/1570

[63] M. Wang, L. Zhang, and M. Cao, "The role of electronic techniques for advanced neuroelectrophysiology," *Journal of biomedical engineering*, vol. 25, no. 6, pp. 1466–1469, 2008. [Online]. Available: https://www.scopus.com/inward/record.uri?eid=2-s2.0-75549086038&partnerID=40&md5=c170c2fc1127ef9394e578ff5b0641ea

[64] W. S. Anderson and F. A. Lenz, "Surgery Insight: deep brain stimulation for movement disorders," *Nature Reviews Neurology*, vol. 2, pp. 310–320, 2006. [Online]. Available: http://www.nature.com/nrneurol/journal/v2/n6/full/ncpneuro0193.html

[65] N. Dales, S. Hatz, F. Tian, and E. Llaudet, "Listening to the brain: microelectrode biosensors for neurochemicals," *Trends in Biotechnology*, vol. 23, no. 8, pp. 420–428, 2005.

[66] M. A. Johnson, "In vivo electrochemical measurements: past, present and future." *Bioanalysis*, 2013.

[67] J. Li, G. Cheng, and S. Dong, "Applications of self -assembled monolayers in electroanalytical chemistry," *Fenxi Huaxue*, vol. 24, no. 9, pp. 1098–1099, 1996. [Online]. Available: https://www.scopus.com/inward/record.uri?eid=2-s2.0-9744263419&partnerID=40&md5=a7af7b2c116040b0ec467bafe9b60405

[68] M. Sheffer, V. Vivier, and D. Mandler, "Self-assembled monolayers on Au microelectrodes," *Electrochemistry Communications*, vol. 9, no. 12, pp. 2827 – 2832, 2007. [Online]. Available: http://www.sciencedirect.com/science/article/pii/S1388248107004006

[69] A. M. Farrington, N. Jagota, and J. M. Slater, "Simple solid wire microdisc electrodes for the determination of vitamin C in fruit juices," *Analyst*, vol. 119,

no. 2, pp. 233–238, 1994. [Online]. Available: http://pubs.rsc.org/en/Content/ArticleLanding/1994/AN/AN9941900233#!divAbstract

[70] R. Engstrom and C. Pharr, "Scanning electrochemical microscopy," *Analytical Chemistry*, vol. 61, no. 19, pp. 1099A–1104, 1989. [Online]. Available: http://pubs.acs.org/doi/abs/10.1021/ac00194a735

[71] Y. Zhao, W. Zhang, H. Chen, and Q. Luo, "Direct electrochemistry of horseradish peroxidase at carbon nanotube powder microelectrode," *Sensors and Actuators B: Chemical*, vol. 87, no. 1, pp. 168–172, 2002.

[72] I. S. da Silva, W. R. Araujo, T. R. L. C. Paixao, and L. Angnes, "Direct nitrate sensing in water using an array of copper-microelectrodes from flat flexible cables," *Sensors and Actuators B: Chemical*, vol. 188, pp. 94–98, 2013. [Online]. Available: http://www.sciencedirect.com/science/article/pii/S0925400513007855

[73] E. Llaudon and H. Tredal, "A Graphene nanoparticle matrix-based sensor for quantitative analysis of Li-ion batteries and cancer," *probably Nature or something*, vol. 13, no. 2, pp. 17–20, 2016.

[74] D. Pletcher and E. M. Valdes, "Studies of a microelectrode sensor for monitoring chlorine in water supplies," *Analytica Chimica Acta*, vol. 246, no. 2, pp. 267 – 273, 1991. [Online]. Available: http://www.sciencedirect.com/science/article/pii/S0003267000809605

[75] X. J. Huang, A. M. O'Mahony, and R. G. Compton, "Microelectrode arrays for electrochemistry: Approaches to fabrication," *Small*, vol. 5, no. 7, pp. 776–788, 2009. [Online]. Available: http://onlinelibrary.wiley.com/doi/10.1002/smll.200801593/abstract

[76] C. Zoski, "Ultramicroelectrodes: Design, Fabrication, and Characterization," *Electroanalysis*, vol. 14, no. 15-16, pp. 1041–1051, 2002. [Online]. Available: http://dx.doi.org/10.1002/1521-4109(200208)14:15/16<1041::AID-ELAN1041>3.0.CO;2-8

[77] Kation Scientific, Website, 2016. [Online]. Available: http://kationscientific.com/products/tungsten-microelectrodes 1960.

[78] M. L. Wolbarsht, E. F. MacNichol Jr, and H. G. Wagner, "Glass Insulated Platinum Microelectrode," *Science*, vol. 132, no. 3436, pp. 1309–1310, 1960.

[79] K. Sugiyama, W. S. Dong, and E. H. Chudler, "A simplified method for manufacturing glass-insulated metal microelectrodes," *Journal of Neuroscience Methods*, vol. 53, pp. 73–80, 1994.

[80] M. J. Madou and S. R. Morrison, "9 - Silicon-Based Chemical Sensors," in *Chemical Sensing with Solid State Devices*, M. J. Madou and S. R. Morrison, Eds. San Diego: Academic Press, 1989, pp. 359 – 417. [Online]. Available: http://www.sciencedirect.com/science/article/pii/B9780124649651500144

[81] G. Buss, M. Schoening, H. Lueth, and J. Schultze, "Modifications and characterization of a silicon-based microelectrode array ," *Electrochimica Acta*, vol. 44, no. 21-22, pp. 3899 – 3910, 1999. [Online]. Available: http://www.sciencedirect.com/science/article/pii/S0013468699000973

[82] K. N. Hascup, E. R. Hascup, O. M. Littrell, J. M. Hinzman, C. E. Werner, V. A. Davis, J. J. Burmeister, F. Pomerleau, J. E. Quintero, P. Huettl, and G. A. Gerhardt, *Microelectrode Biosensors*. Totowa, NJ: Humana Press, 2013, ch. Microelectrode Array Fabrication and Optimization for Selective Neurochemical Detection, pp. 27–54. [Online]. Available: http://dx.doi.org/10.1007/978-1-62703-370-1_2

[83] R. Kadara, N. Jenkinson, and C. Banks, "Characterization and fabrication of disposable screen printed microelectrodes," *Electrochemistry Communications*, vol. 11, no. 7, pp. 1377–1380, 2009. [Online]. Available: http://www.sciencedirect.com/science/article/pii/S1388248109002227

[84] Z. Taleat, A. Khoshroo, and M. Mazloum-Ardakani, "Screen-printed electrodes for biosensing: a review (2008–2013)," *Microchimica Acta*, vol. 181, no. 9, pp. 865–891, 2014. [Online]. Available: http://dx.doi.org/10.1007/s00604-014-1181-1

[85] Z. Li, Y. Yu, Z. Li, T. Wu, and J. Yin, "The art of signal transforming: electrodes and their smart applications in electrochemical sensing," *Anal. Methods*, vol. 7, pp. 9732–9743, 2015. [Online]. Available: http://dx.doi.org/10.1039/C5AY02373D

[86] M. W. Rosenthal, P. R. Kasten, and R. B. Briggs, "Molten-Salt Reactors - History, Status, and Potential," *Nuclear Applications and Technology*, vol. 8, pp. 107–118, 1970. [Online]. Available: https://issuu.com/e_generation/docs/nat_msrintro

[87] S. Senderoff, "Electrode Reactions in Molten Salts," Union Carbide Corperation, Tech. Rep., 1967. [Online]. Available: http://web.anl.gov/PCS/acsfuel/preprint%20archive/Files/11_1_MIAMI_04-67_0032.pdf

[88] R. J. Heus and J. J. Egan, "Fused Salt Polarography Using a Dropping Bismuth Cathode," *Journal of The Electrochemical Society*, vol. 107, no. 10, pp. 824–828, 1960. [Online]. Available: http://jes.ecsdl.org/content/107/10/824.abstract

[89] H. Latinen, "Polarography in molten salts," *Pure and Applied Chemistry*, vol. 15, no. 2, pp. 227–238, 1967. [Online]. Available: http://www.degruyter.com/view/j/pac.1967.15.issue-2/pac196715020227/pac196715020227.xml

[90] G. Stehle, J. Duruz, and D. Landolt, "High temperature polarography in chloride melts with dropping electrodes," *Electrochimica Acta*, vol. 27, no. 6, pp. 783–789, 1982.

[91] M. Kurat, Y. Sakamura, and T. Matsui, "Thermodynamic quantities of actinides and rare earth elements in liquid bismuth and cadmium," *Journal of Alloys and Compounds*, vol. 234, no. 1, pp. 83–92, 1996. [Online]. Available: http://www.sciencedirect.com/science/article/pii/092583889501960X

[92] B. Malinowska, M. Cassir, and J. Devynck, "Design of a Gold Ultramicroelectrode for Voltammetric Studies at High Temperature in Glass-Corrosive Media (Molten Carbonate at 650ï¿œC)," *Journal of the Electrochemical*, vol. 141, no. 8, 1994. [Online]. Available: http://jes.ecsdl.org/content/141/8/2015

[93] P. Pint and S. Flengas, "The Behavior of an Oscillating Solid Microelectrode for Voltammetric Studies in Aqueous and Molten Salt Solutions," *Journal of The Electrochemical Society*, vol. 123, no. 7, pp. 1042–1047, 1976.

[94] H. W. Jenkins, "Electrochemical Measurements in Molten Fluorides," Ph.D. dissertation, University of Tennessee, 1969. [Online]. Available: http://trace.tennessee.edu/cgi/viewcontent.cgi?article=4572&context=utk_graddiss

[95] H. Gaur and H. Jindal, "On the applicability of the heyrovskï¿œ-ilkovi equation to polorography in molten salts using a solid microelectrode," *Journal of Electroanalytical Chemistry and Interfacial Electrochemistry*, vol. 16, no. 3, pp. 437–439, 1968. [Online]. Available: http://www.sciencedirect.com/science/article/pii/S0022072868800920

[96] E. D. Black and T. D. Vries, "Polarography with Platinum Microelectrodes in Fused Salts," *Analytical Chemistry*, vol. 27, no. 6, pp. 906–909, 1955. [Online]. Available: http://dx.doi.org/10.1021/ac60102a011

[97] H. C. Gaur, H. L. Jindal, and R. S. Sethi, "Voltammetric Behavior of Lead Chloride in Molten Magnesium Chloride-Potassium Chloride Eutectic," *Electrochimica Acta*, vol. 15, no. 5, pp. 845–851, 1970.

[98] R. Carlin, "Deposition Studies of Lithium and Bismuth at Tungsten Microelectrodes in LiCl:KCl Eutectic," *Journal of The Electrochemical Society*, vol. 136, no. 5, p. 1249, 1989. [Online]. Available: http://jes.ecsdl.org/content/136/5/1249

[99] C. L. Brady, "Development and characterisation of microelectrodes for extreme environments," Ph.D. dissertation, University of Edinburgh, 2013. [Online]. Available: https://www.era.lib.ed.ac.uk/handle/1842/7852

[100] A. Relf, D. K. Corrigan, C. L. Brady, J. G. Terry, A. J. Walton, and A. R. Mount, "Robust Microelectrodes In Molten Salt Analysis," *ECS Transactions*, vol. 50, no. 11, pp. 105–109, 2012. [Online]. Available: http://ecst.ecsdl.org/content/50/11/105

Chapter 3

Background to Electrochemical Methods

3.1 Introduction

Electrochemistry covers the interactions between electricity and chemical reactions. These can come in the form of applying an electrical potential or current in order to cause a chemical reaction, or generating a current from a chemical reaction. These processes take place at the interface between an electrical circuit and a chemical solution, called an electrode. When the size of an electrode is reduced to the microscale, the mass transport to the electrode surface changes, bringing inherent advantages not achievable on macroscale electrodes. This chapter introduces the basic concepts of electrochemistry and the standard three-electrode set up for measuring electrochemical reactions. The electrochemical techniques used in this work are described and how these differ between micro and macroscale electrodes.

3.2 Three-Electrode System

The most common system for measuring electrochemical reactions is a three-electrode system. Figure 3.1 shows a diagram of a typical three-electrode system immersed in a solution containing a chemical species A, connected to a potentiostat. The potentiostat can apply and measure both currents and potentials, down to hundreds of picoamperes and microvolts respectively. The system consists of a working electrode, a counter electrode, and a reference electrode. The role of and processes that occur at each electrode are outlined below. A more comprehensive introduction to electrochemistry is presented in [1].

Working Electrode

The working electrode (WE) is the interface between the solution and the circuit where the chemical reaction is measured. If the applied potential is raised to a high enough positive value, electrons from species A at the surface of the WE will flow into the circuit and A becomes oxidised according to equation (3.1):

$$A \rightarrow A^{+} + e^{-} \tag{3.1}$$

If a large enough negative potential is applied then electrons will flow from the working electrode to species A, resulting in A becoming reduced as described in equation (3.2):

$$A + e^{-} \rightarrow A^{-} \tag{3.2}$$

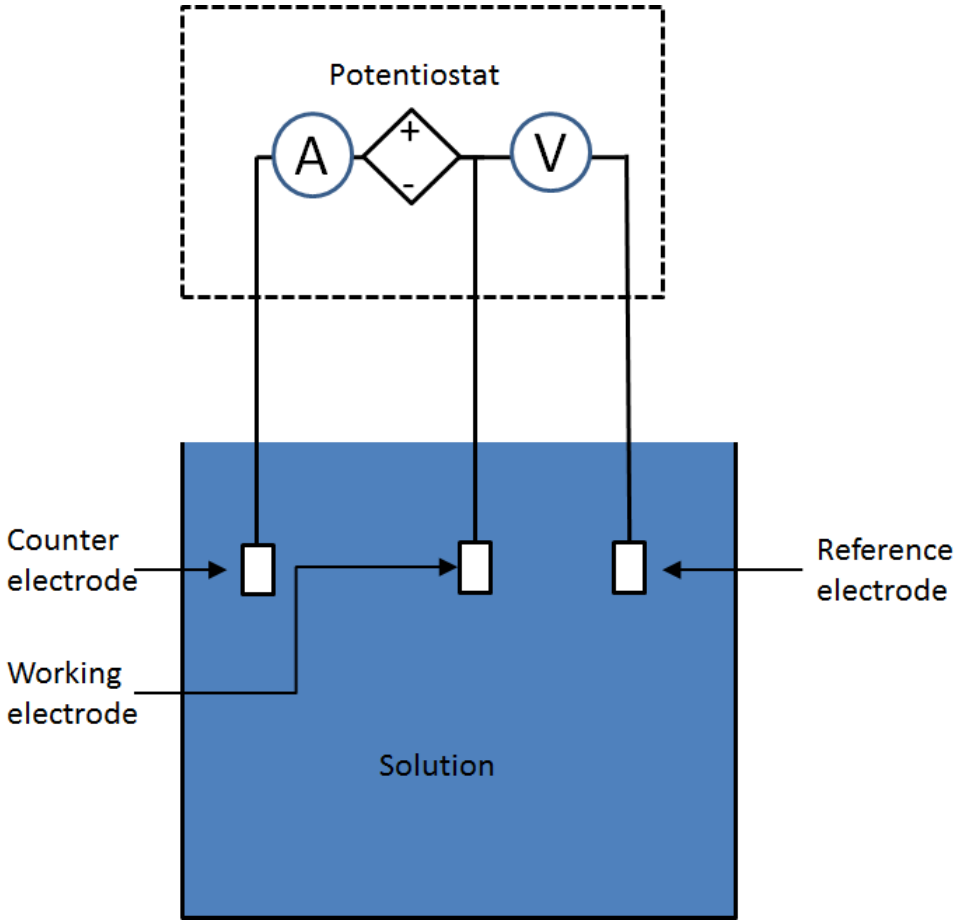

Figure 3.1: Diagram showing a standard three-electrode set up, with the working, counter, and reference annotated.

A is therefore known as a reduction/oxidation species, or redox species. When either reaction occurs, the concentration of A at the WE surface will decrease. Since the concentration of A in the bulk solution will be higher, a concentration gradient is established between the surface of the WE and the bulk solution. A will therefore continually diffuse from the bulk solution to the electrode surface where it will reduce or oxidise, maintaining the concentration gradient. As well as diffusion, two other parameters affect the transport of A to the electrode. The first is convection in the solution, which is typically caused by localised changes of density or artificial factors such as stirring. The second is migration, the movement of ions under the influence of an electric field. The interplay of these three process, diffusion, convection, and migration, can make analysis of mass transport complex and it is therefore often desirable to minimise the influence of migration and convection. The effects of migration can be rendered negligible by adding a background electrolyte at a much larger concentration than the redox species

under study. The influence of convection is much harder to remove, but good control of temperature in the solution as well as keeping the beaker or cell as still as possible will reduce its contribution. Another option is to reduce the WE size, as described in chapter 2.

Reference Electrode

The potential at the working electrode is controlled with respect to a reference potential set by the reference electrode (RE). The reference potential is set by a known electrochemical reaction which is kept isolated by means of a frit. This screens out chemicals in the solution, preventing them from interfering with the reaction setting the potential, while maintaining electrical contact with the electrolyte. This enables the reference electrode to maintain the same reference potential regardless of the solution it is used in. No current should flow through the reference electrode so that its defined potential does not change and it does not interfere with the measurements being made at the working electrode. Although the internationally accepted reference electrode is the Standard Hydrogen Electrode, the Ag/AgCl (silver/silver chloride) is commonly used [2].

Counter Electrode

A counter electrode (CE) is required to complete the electrochemical circuit. If current is flowing from the WE to the solution, reducing A, then current will flow from the solution back into the electrical circuit via the CE and *vice versa* if the current is flowing the opposite direction. In principle, a CE can be any conductor, but it is preferable that it should be an inert material so it does not react and contaminate the solution. Pt is therefore a popular choice for aqueous measurements. Another consideration is the size of the CE, which is usually kept much larger than the working electrode in order to not limit the current at the WE. This also minimises the CEs contribution to electrical resistance.

3.3 Electrochemical Methods Used in this Work

3.3.1 Cyclic Voltammetry

One of the most common methods of investigating electrochemical reactions is cyclic voltammetry. This process involves sweeping the potential between two values and back again and observing the current response with reduction and oxidation reactions generating negative or positive current respectively. A typical cyclic voltammogram

(CV) is shown in figure 3.2, with arrows indicating the direction the potential has been swept and reactions labelled. A negative peak in the current on the initial sweep can be

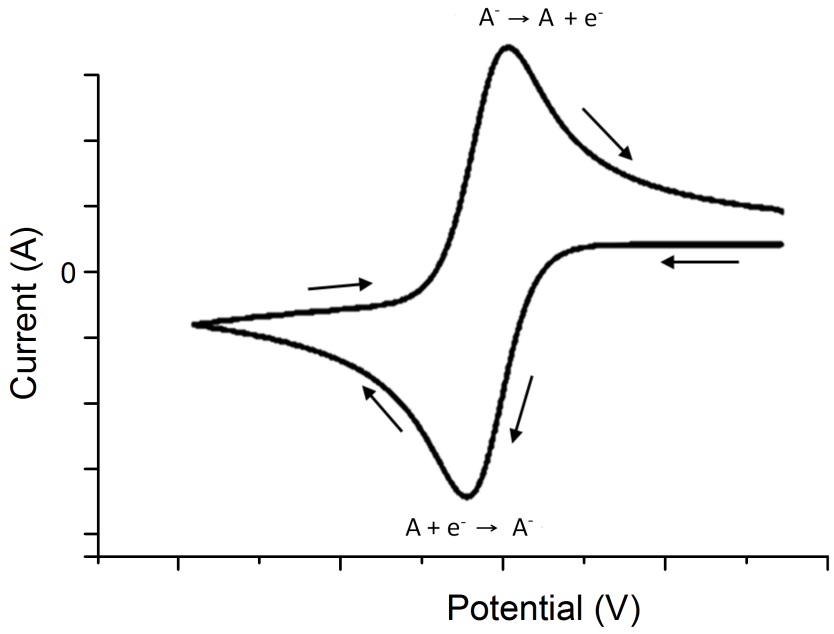

Figure 3.2: A representation of a typical CV showing an electrochemical reaction. Arrows show the direction the voltage was swept in and electrochemical reactions are annotated [3].

observed, attributable to the reduction reaction in equation (3.2). When the potential is swept back again, the reduced species is oxidised resulting in a peak of positive current attributable to equation (3.1). The height and position of these peaks and how they change with various parameters such as time or temperature, yields information about the processes at the WE surface. A thorough description of cyclic voltammetry can be found in [4].

3.3.2 Chronoamperometry

Chronoamperomtery is a technique where the potential at the working electrode is fixed for certain period of time and the current monitored. Typically this is a potential at which a redox reaction occurs and a CV can be first used to locate the desired potential. This method can yield information about a reaction or to generate a particular species of interest. An example of this is electroplating, where the potential is set at a value

where the species reduces to a metal. This builds up a thin film of the desired metal on the surface of the WE.

3.4 Electrochemical Response from a Microelectrode

The electrochemical response of a redox reaction on a microelectrode is typically characterised by a diffusion controlled steady-state, resulting in a time-independent current as opposed to a current peak, characteristic of a macroelectrode [5–10]. Figure 3.3 (a) shows an example of a redox solution reaction at a microelectrode, where the potential is swept and the chemical species A is reduced, establishing a limiting current. The potential is then swept back and the reverse oxidation reaction occurs. Figure 3.3 (b) shows a plating and stripping reaction on a microelectrode, which also demonstrates a limiting current upon the reduction of A. However, a sharp peak is observed during the oxidation reaction as the plated metal is stripped from the surface of the microelectrode. Where the current response of a macroelectrode tends to be sensitive to the rate at which the potential is swept, the limiting current from a microelectrode does not change with scan rate, as long as there is enough time to establish hemispherical diffusion. Although only the limiting current displayed by inlaid disc microelectrodes can be

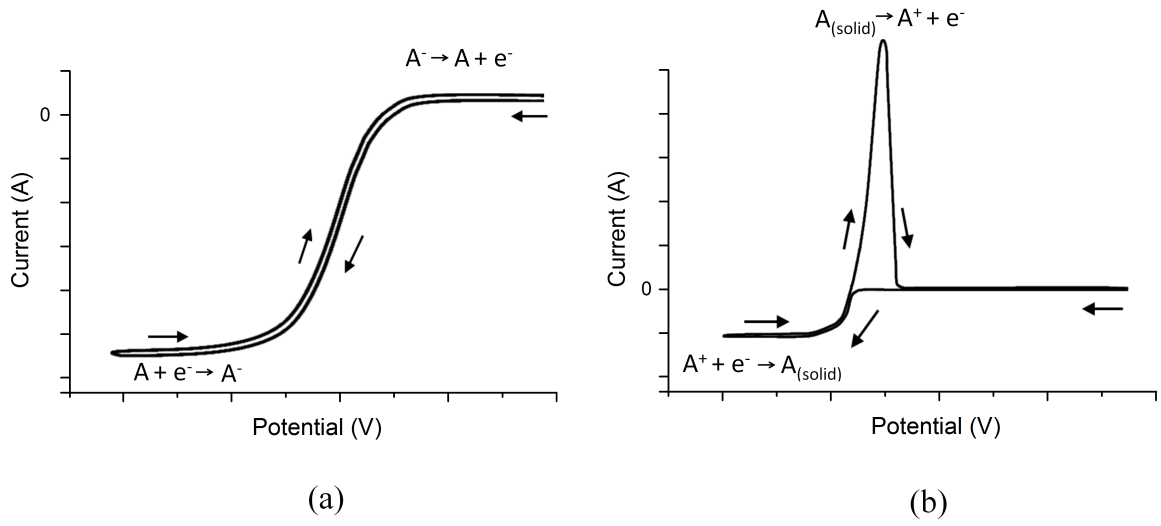

Figure 3.3: Representations of a typical CV recorded at a microelectrode for (a) a solution reaction and (b) a plating and stripping reaction. The direction the potential has been swept is indicated with arrows and the reactions are labelled.

analytically predicted, numerical models exist for other geometries of microelectrodes [11–14]. Traditionally microelectrodes have circular geometries such as a disc, a cone, a

hemisphere or a ring; which results from their ease of manufacture and modelling. Other production methods have resulted in shapes such as bands and squares, and figure 3.4 shows a selection of different microelectrode geometries. The microelectrodes used in

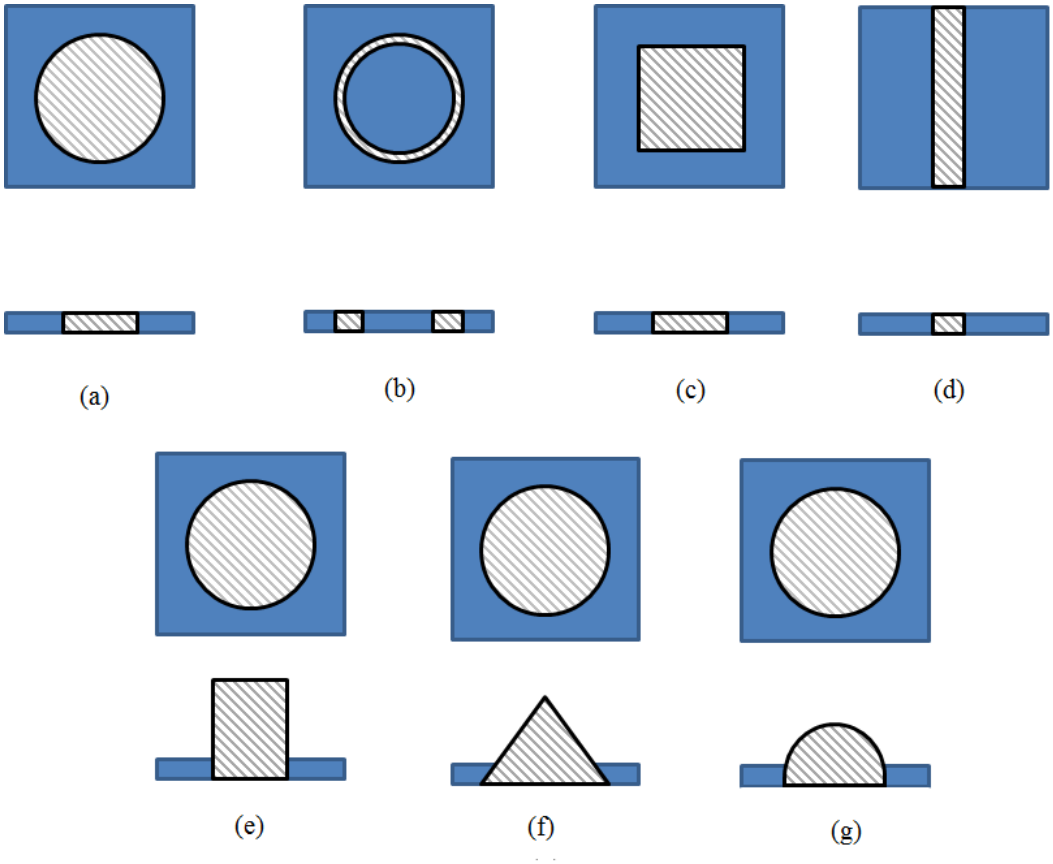

Figure 3.4: Common microelectrode geometries viewed from above (top) and side on (bottom). The grey patterned area represents the microelectrode and the different geometries are (a) a disc, (b) a ring, (c) a square, (d) a band, (e) a cylinder, (f) a cone, and (g) a hemisphere.

this work are squares and discs and the numerical model for limiting current (i_L) at a recessed square microelectrode is:

$$i_L = 2.341 n \mathrm{F} D c l \tag{3.3}$$

where n is the number of electrons transferred in the reaction, F is Faraday's constant, D is the diffusion coefficient of the redox species, l is the edge length of the microsquare, and c is the concentration of that species in the bulk electrolyte [14]. While the the analytical expression for limiting current to disc microelectrode (also presented in presented in

Chapter 2) is:

$$i_L = 4n\mathrm{F}Dcr \tag{3.4}$$

where r is the radius of the microdisc [1, 15]. Equations (3.3) and (3.4) allow the characterisation of microelectrodes in a system containing a redox couple with a known concentration and diffusion coefficient. This methodology will be applied throughout this study in order to assess the functionality of microfabricated microelectrodes in LKE.

3.5 Summary

The basic concepts of electrochemistry have been introduced, including the standard three-electrode measurement system. The electrochemical measurement techniques used in this work, cyclic voltammetry and chronoamperometry, have been described, along with cyclic voltammetry at a microelectrode. Equations have been presented for relating the geometry of a microelectrode and the recorded limiting current of a reaction to parameters such as diffusion coefficient and concentration. This affords an opportunity to analytically characterise microelectrodes in a known chemical system.

References

ï»¿

[1] A. Bard and L. Faulkner, *Electrochemical methods: fundamentals and applications*, 2nd ed. Wiley, 1980. [Online]. Available: http://eu.wiley.com/WileyCDA/WileyTitle/productCd-0471043729.html

[2] G. Inzelt, A. Lewenstam, and F. Scholz, Eds., *Handbook of Reference Electrodes*. Springer, 2013. [Online]. Available: http://dx.doi.org/10.1007/978-3-642-36188-3

[3] E. Dickinson. (2013, May) Modeling electroanalysis: Cyclic voltammetry. Website. Comsol. [Online]. Available: https://www.comsol.com/blogs/modeling-electroanalysis-cyclic-voltammetry/

[4] R. G. Compton and C. E. Banks, *Understanding Voltammtery*. Imperial College Press, 2010. [Online]. Available: http://www.worldscientific.com/worldscibooks/10.1142/p726

[5] K. Aoki, "Theory of ultramicroelectrodes," *Electroanalysis*, vol. 5, no. 8, pp. 627–639, 1993. [Online]. Available: http://onlinelibrary.wiley.com/doi/10.1002/elan.1140050802/abstract;jsessionid=1F92224EEAE90C947CA4658C14493EF6.f01t04

[6] R. Forster, "Microelectrodes: new dimensions in electrochemistry," *Chemical Society Reviews*, vol. 23, pp. 289–297, 1994. [Online]. Available: http://pubs.rsc.org/en/Content/ArticleLanding/1994/CS/CS9942300289#!divAbstract

[7] R. Forster and T. Keyes, "Behaviour of ultramicroelectrodes," 2007.

[8] S. Khopkar, *Basic concepts of analytical chemistry*. New Age Science, 1998.

[9] D. Pletcher, *Why Microelectrodes?* Springer, 1991, ch. 1, pp. 3–16. [Online]. Available: http://link.springer.com/chapter/10.1007/978-94-011-3210-7_1

[10] K. Stulik, C. Amatore, K. Holub, and V. Marecek, "Microelectrodes. definitions, characterization, and applications technical report," *Pure and Applied Chemistry*, vol. 72, no. 8, pp. 1483–92, 2000. [Online]. Available: http://www.degruyter.com/view/j/pac.2000.72.issue-8/pac200072081483/pac200072081483.xml

[11] A. Szabo, "Theory of the current at microelectrodes: application to ring electrodes," *Journal of Physical Chemistry*, vol. 91, no. 11, pp. 3108–3111, 1987.

[12] C. Amatore, M. R. Deakin, and M. Wightman, "Electrochemical kinetics at microelectrodes part 1. quasi-reversible electron transfer at cylinders," *Journal of Electroanalytical Chemistry and Interfacial Electrochemistry*, vol. 206, no. 1-2, pp. 23–36, 1986. [Online]. Available: http://www.sciencedirect.com/science/article/pii/0022072886902536

[13] A. Bond, K. Oldham, and C. Zoski, "Theory of electrochemical processes at an inlaid disc microelectrode under steady-state conditions," *Chemistry and Interfacial Electrochemistry*, vol. 23, pp. 289–297, 1988.

[14] H. L. Woodvine, J. G. Terry, A. J. Walton, and A. R. Mount, "The development and characterisation of square microfabricated electrode systems." *Analyst*, vol. 135, no. 5, pp. 1058–65, 2010. [Online]. Available: http://pubs.rsc.org/en/Content/ArticleLanding/2010/AN/b924342a#!divAbstract

[15] K. B. Oldham, "Edge effects in semi-infinite diffusion," *Journal of Electroanalytical Chemistry and Interfacial Electrochemistry*, vol. 122, pp. 1–17, 1981. [Online]. Available: http://www.sciencedirect.com/science/article/pii/S0022072881801362

Chapter 4

The Benchmark Microelectrode

4.1 Introduction

In order to establish the current state of the existing microelectrode technology discussed in chapter 2 and provide a baseline to quantify improvements against, a set of microelectrodes were designed, fabricated, and characterised. These electrodes were based on those in [1, 2] and represent the starting point for this current work and are hence referred to as the benchmark microelectrode (BM). This chapter will discuss the architecture, layout, materials, and fabrication process of the BM. A standard process for characterising the electrodes is then described that is used throughout this work. Following this, the BMs are characterised with the aim of identifying the mechanisms of failure which will allow future optimisation.

4.2 The Benchmark Microelectrode Design

The BM was designed according to similar microelectrodes previously fabricated for aqueous studies [2, 3]. The architecture consists of a patterned electrode metal layer on an underlying insulation layer, with a top insulation layer over the metal with openings to define the microelectrode and the contact pad. The chip is 35 mm long by 7.5 mm wide and a schematic is shown in figure 4.1. As wetting properties of the salt are not

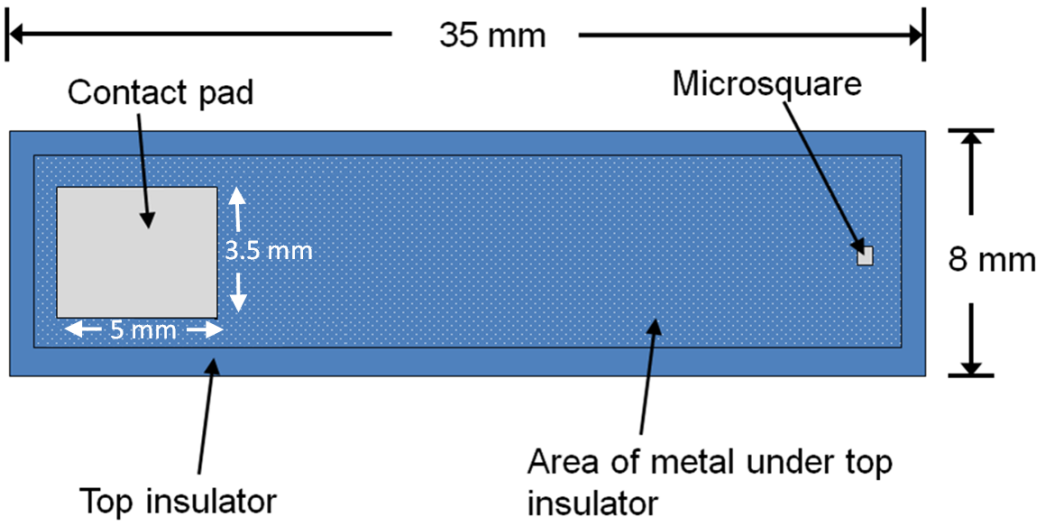

Figure 4.1: Schematic of the BM showing the chip dimensions. The microsquare size has been exaggerated for clarity.

well understood, the separation of contact pad and microsquare was conservatively set

in order to prevent salt reaching the connection and causing a short circuit [4, 5]. This generous separation of contact pad and microelectrode also helped with deploying the electrode in the high temperature set up. The width of the chip was chosen to enable a larger contact pad (3.5 mm by 5 mm), which facilitated connection to a crocodile clip. The experimental set up and connection to the microelectrode are further detailed in section 4.5.

A microsquare electrode was chosen for several reasons. Firstly it has been shown to have higher current over a disc of the same area, due to the enhanced diffusion at corners [3]. Secondly using a microsquare electrode also allows measurement data to be compared with previous microelectrode work done within the group [2, 3]. Five different edge lengths of microelectrode were fabricated and characterised: 10, 20, 30, 50, and 100 μm. Figure 4.2 shows the layout on the wafer. There is space for a total of 20 chips on each wafer, four of each edge length. The contact pads are located on the outside of the wafer and the microelectrodes are highlighted towards the centre.

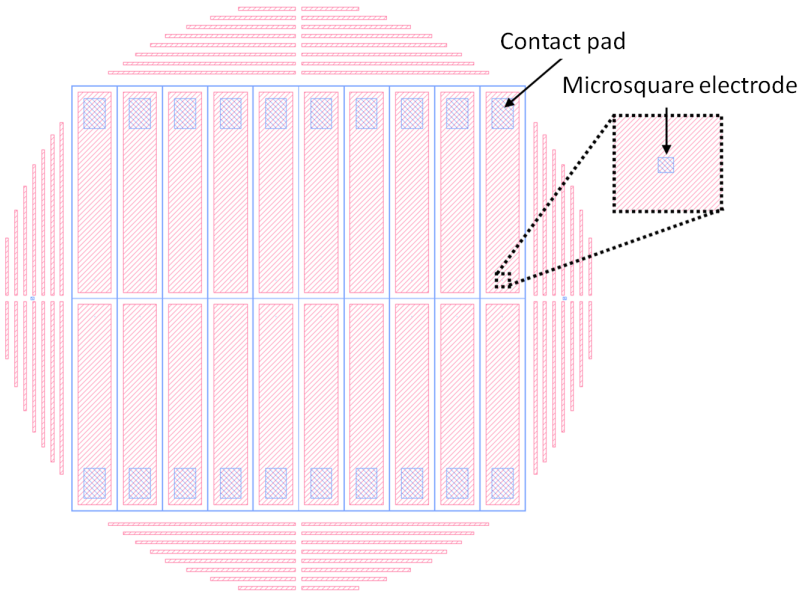

Figure 4.2: Layout of the microelectrodes on the four inch wafer. Red shaded areas denote the electrode metal layer and blue shaded areas are openings in the top insulator. A microelectrode is also shown in the magnified inset.

4.3 Benchmark Microelectrode Materials

Figure 4.3 is a schematic cross-section of the microelectrode, showing its architecture. The role of each layer in the BM, as well materials selected for that role, is outlined below

along with rationale for each selection. Over the course of the project, other materials were characterised for these roles and will be covered in later chapters.

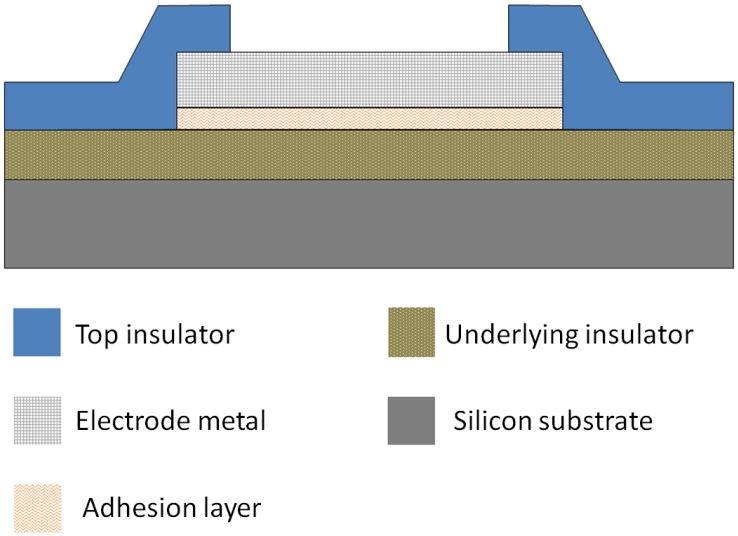

Figure 4.3: Transverse cross-section through the microelectrode contact pad, showing the layer stack. The thicknesses of the layers have, again, been exaggerated for clarity.

Substrate

The substrates used for fabricating the BMs were four inch p- or n-type Si (silicon) wafers. The Si was used purely as a substrate, so was only required to be compatible with the materials and processes being proposed. Therefore properties such as the doping of the Si were not relevant, especially as the intrinsic charge carrier concentration dominates at 500°C and Si becomes an electrical conductor [6, 7].

Underlying Insulator

The underlying insulator is required to insulate the electrode metal from the Si substrate. As well as an electrical insulator, this layer has to be stable in the temperature range under study. Despite the underlying insulator being covered by the electrode metal and top insulator, the edge of this layer will be exposed to the salt after dicing and so the layer should also be chemically inert in the salt to prevent degradation.

SiN (silicon nitride) has a breakdown voltage of 10^7 V/cm and a dielectric constant of 6 - 7; hence thin films can be used as dielectric layers in microelectronics [8, 9]. SiN is also considered to be chemically inert making it highly resistant to chemical attack

[10–15]. Si_3N_4 (stoichiometric silicon nitride) has very high intrinsic stress and so low-stress silicon-rich silicon nitride (Si-rich SiN) was used instead [16, 17]. The underlying insulator needs to be thick enough to ensure complete coverage with no pinholes, but not thick enough that the stress in the film affects the microelectrode and so 500 nm was selected as a compromise.

Electrode Metal

The metal layer is the electrode, contact pad, and interconnect material. As with the underlying insulator this layer should be chemically stable in the salt and not melt, either in the salt or during high temperature fabrication steps. The maximum temperature the wafer would be exposed to during fabrication is 850°C during deposition of Si-rich SiN. Ideally, it should also be electrochemically inert in LKE so additional chemical processes do not complicate analysis. This also prevents the metal accidentally stripping off through user error or a failure of the reference electrode.

Tungsten (W) was chosen for this role since it is a refractory metal and therefore exhibits very good corrosion resistance and a high melting point (3422°C). It is also electrochemically inert in LKE and is often used in the role of working electrode in MS studies [18–21]. However, W does not adhere well to non-metallic substrates [22, 23]. As such, a seed layer was used as an intermediate to allow adhesion between the W and the SiN. An industry standard seed layer for the role of adhesion is Ti (titanium), which has a melting point of 1668°C making it suitable for the task [18, 23, 24]. As with the underlying insulator, the thickness of the W had to be enough to be conformal to prevent pinholes from forming and to maximise conductivity without risking delamination through excessive stress. The thicknesses chosen were 200 nm for the electrode metal and 10 nm for the Ti adhesion layer, as this thickness had previously been used to successfully adhere W to Si-rich SiN.

Another candidate metal was Pt, which is a noble metal and hence chemically inert at room temperature [25–27]. It is should be noted that Pt can be electrochemically stripped in LKE at +1 V vs Ag/Ag^+ reference electrode [28, 29]. However this potential is more positive than any of the redox couples of interest, which are located negative of 0 V vs Ag/AgCl [30, 31].

Top Insulator

The top insulator has the same requirements as the underlying insulator, as it is the layer that insulates the electrode metal from the salt. Openings etched into this layer form the microelectrode and contact pad. Low stress Si-rich SiN fulfils these criteria

again, the only additional requirement being compatibility with the electrode metal. The LPCVD (low pressure chemical vapour deposition) process of Si-rich SiN operates at 850°C, which is well below the melting point of the electrode metal and adhesion layers. The top insulator, as with the previous layers, needs to be thick enough to preclude pinhole formation and to minimise parasitic capacitance between the salt and the electrode metal. However, increasing the thickness increases the stress in the layer and increases the depth of the cavity, which decreases the current. Again, 500 nm was deemed a suitable compromise between these factors.

4.4 Benchmark Microelectrode Fabrication Process

The underlying insulation layer of Si-rich SiN is first deposited on the bare Si wafer (figure 4.4 (a)) using LPCVD (low pressure chemical vapour deposition). This is done in a horizontal tube furnace where the wafers are loaded in at 600°C and ramped up to 800°C under a pressure of 100 mT. Dichlorosilane (SiH_2Cl_2) and ammonia (NH_3) gases are then introduced at a ratio of 15/10 respectively to achieve a higher Si content than Si_3N_4. The gases react on the surface of the wafer to form a film of Si-rich SiN at a rate of around 1.6 nm/minute. A film of 500 nm thickness was deposited, taking five hours. Figure 4.4 (b) - (f) shows the electrode metal being patterned using a lift-off method. The wafers were first cleaned and dehydrated in oxygen plasma for one hour to encourage the adhesion of HMDS (hexamethyldisilazane) to the wafer surface. HMDS is used as an adhesion promoter for the photoresist and the wafers were then sat in an HMDS atmosphere for 10 minutes. A 3 μm layer of negative AZ2070 - 3.5 nLOF photoresist was spin coated on to the wafer, followed by a soft bake at 100°C for four minutes. The wafers were then exposed to ultraviolet light for 50 seconds through a photomask, which defined the metal pattern. The UV light is absorped as it travels through the resist layer, therefore the resist at the bottom recieves less energy and cures more slowly. This means it is removed faster in the developer solution, resulting in an undercut profile. The wafer was then baked for two minutes at 120°C and developed for 60 seconds in AZ726 resist developer. In figure 4.4 (e) - (f), a 20 nm layer of Ti was then sputter deposited on the wafer using a Balzers BAS 450PM Sputter system, followed by a 200 nm layer of W. Sputter deposition is a method used to deposit thin films by locating the wafer to be coated under a target of the material it is to be coated in. A plasma is then generated using an inert gas such as Ar (argon) and the ions are accelerated into the target, usually using an electric field. This physically sputters atoms from the target's surface that land on the wafer below, building up a film. After deposition of the metal

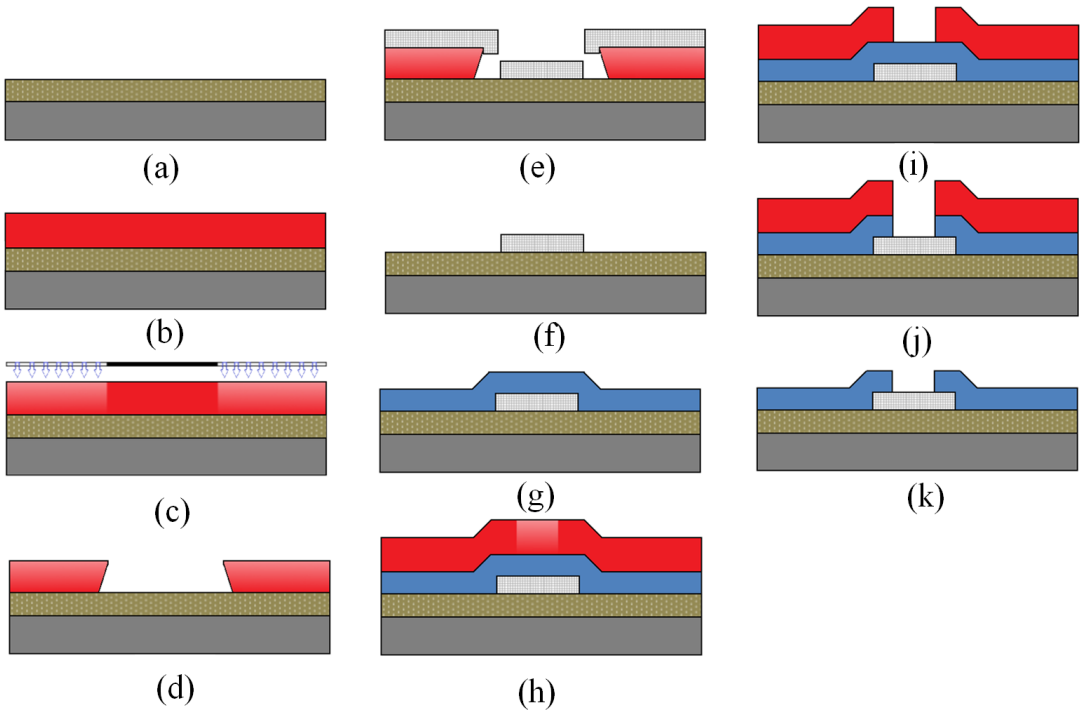

Figure 4.4: Cross-sections of the fabrication procedure used to produce the benchmark microelectrodes. (a) An underlying insulator of Si-rich SiN is deposited on a Si wafer. (b) - (f) The W electrode metal area is then defined using a pattern and lift-off technique. (g) The top insulator of Si-rich SiN is deposited. (h) - (i) The areas to become the microelectrode and contact pad are defined using photolithography. (j) The exposed areas are then etched to expose the electrode metal. (k) The resist is stripped and the microelectrode is completed.

the photoresist was then stripped using 1165 resist stripper (Microposit) for 90 mins, lifting off the metal deposited on top of the resist. Figure 4.4 (g) shows a 500 nm top insulator of Si-rich SiN deposited in the same manner as the underlying insulator. In order to expose the microelectrode and contact pad, openings were etched in the Si-rich SiN. In figure 4.4 (h) - (i), a 1.5 μm thick layer of SPR 350 - 3.5 positive photoresist (Microposit) was spin coated onto the wafer and the areas to become the microelectrode and contact pad were exposed and developed. The Si-rich SiN was then etched in a JLS RIE 80 reactive ion etcher. Reactive ion etching requires the generation of a plasma in the tool chamber and a mixture of chemical and physical etching takes place as shown in figure 4.4 (j). The type of etching depends on the gases used; a chemically reactive gas will react with the material to be etched, forming a volatile compound which is then removed. An inert gas such as Ar will result in a purely physical process where the Ar atoms are driven into the surface of the material by a DC bias, physically removing

atoms on the surface. In this case a mix of 60 sccm CF_4 (tetrafluoromethane) and 4 sccm Ar was used. CF_4 chemically reacts with the SiN via the mechanism [32]:

$$Si_3N_4 + 12F \rightarrow 3SiF_4 + 2N_2 \tag{4.1}$$

removing the SiN. Ar is used as a physical process to speed up the exposure of fresh Si-rich SiN to the CF_4. The wafer was etched for 22 minutes at 75 W at a pressure of 60 mT. Once the Si-rich SiN has been etched the photoresist is stripped in ACT resist stripper at 50°C for 20 minutes as shown in figure 4.4 (k). Finally the wafer is coated in a protective layer of SPR350 - 3.5 photoresist which is softbaked at 90°C for 1 minute before being diced into individual chips using a DISCO DAD-640 dicing saw, with a diamond impregnated saw blade. The pritective resist is then reomved prior to testing by rinsing in acetone then isopropanol and washing in DI water.

4.5 Experimental Set Up

4.5.1 High Temperature Equipment

The experimental set up employed by Brady was used for the characterisation of the microelectrodes and is shown in figures 4.5 and 4.6 [2]. The LKE salt was contained in a vitreous carbon crucible, which was held in a quartz cell with a borosilicate lid as shown in figure 4.5. The lids had five vertical ports for introducing the electrodes and two other ports for attachment of gas lines. The lid was sealed in place using vacuum grease and the cell was then inserted into a vertical Carbolite single zone tube furnace (Model GVA12/100/300) with a 300 mm heated zone, shown in figure 4.6 (a). Figure 4.6 (b) shows a schematic of the experimental set up. A PG12 Metrohm Autolab potentiostat was used for electrochemical measurements. The Ag plating and stripping reaction:

$$Ag^+ + e^- \rightarrow Ag_{metal} \tag{4.2}$$

was selected to characterise the microelectrodes for the following reasons:

- It is a well characterised reaction in literature, minimising the number of unknowns in the experiment [33];
- Plating and stripping reactions are the most common reactions that will be encountered by the microelectrode when deployed in an industrial reprocessing plant [30, 31] and;

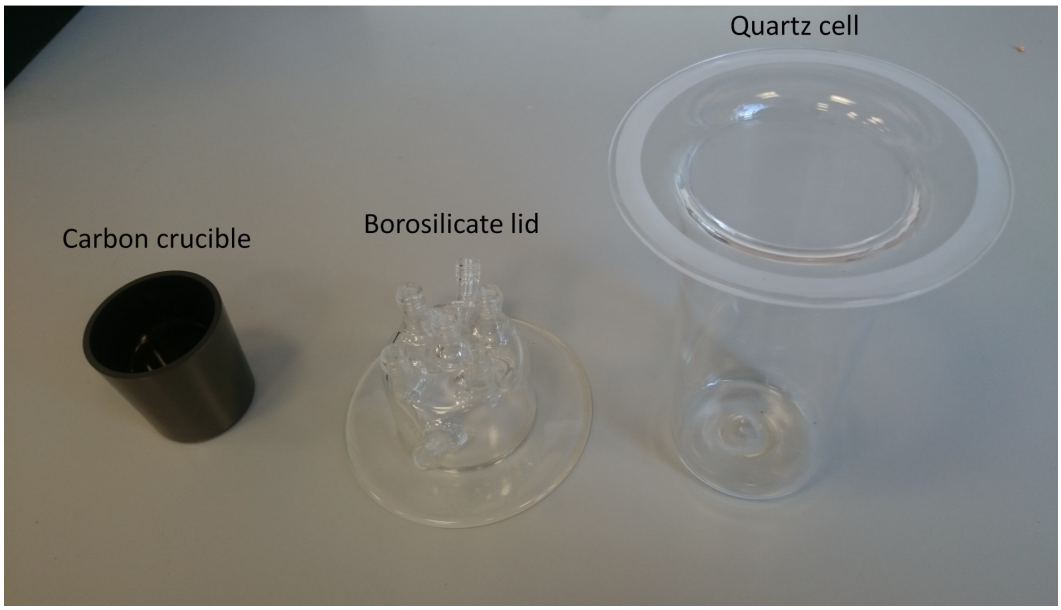

Figure 4.5: Vitreous carbon crucible, the quartz cell, and borosilicate lid. The lid has two side ports for argon to flow in and out and five ports on top for introduction of electrodes into the salt.

- AgCl is relatively inexpensive and easy to handle compared to other redox couples.

4.5.2 Electrical Connection

Two 1.8 mm diameter W rods were used as the WE and CE for salt cleaning and macroelectrode measurements. The Ag/Ag^+ reference electrode was created using a Ag wire sealed in an mullite tube, packed with 1 g LiCl - KCl with 1% by weight AgCl, shown in figure 4.7 (a).

Electrically connecting the microelectrodes to the potentiostat proved a challenge as the high temperature and corrosive environment precluded the use of many usual connection methods such as edge connectors or soldering. Because of its refractory nature, soldering to W is also extremely hard [34]. Crocodile clips were chosen to provide electrical connection and mechanical support for suspending the microelectrode in the salt. Common stainless steel crocodile clips, especially the springs, corroded in the molten salt atmosphere. Encapsulating the clip and the top of the microelectrode in exhaust putty was tested to prevent this from happening. However, freeing the microelectrodes after use without damaging them was impossible and prevented re-using the microelectrodes. It also made it difficult to know what damage was caused by the LKE and what was caused by removal from the putty. As such the putty was not

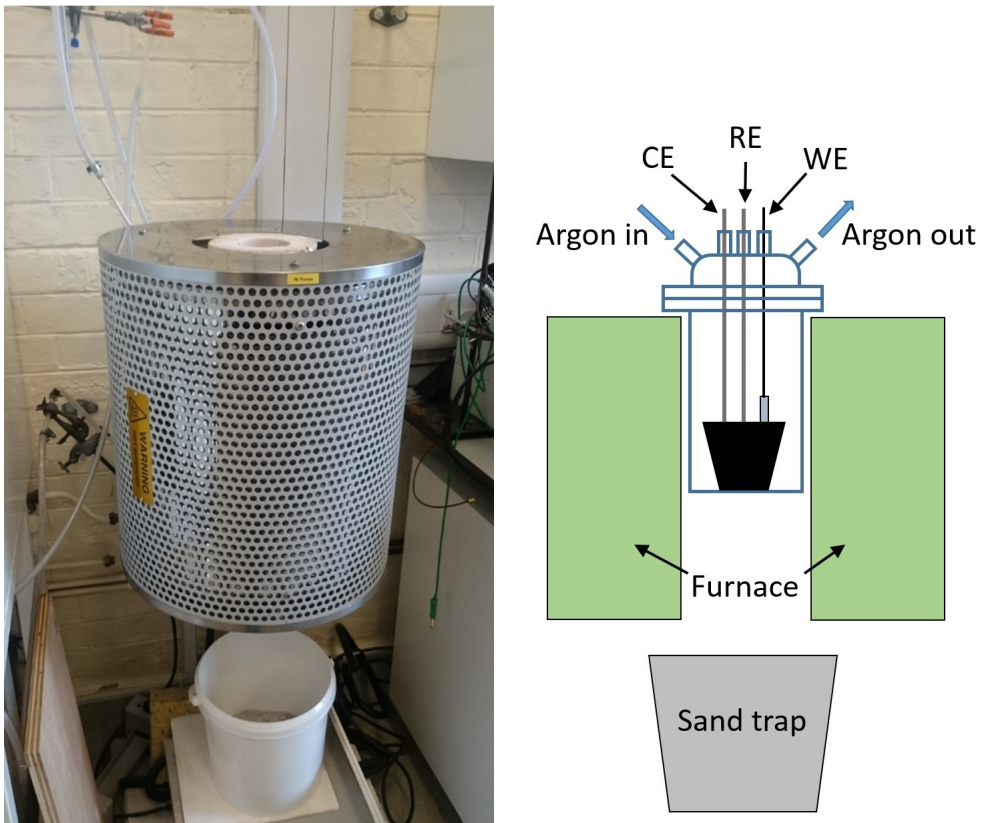

Figure 4.6: (a) The vertical tube furnace where the assembled cell is located. A sand trap is beneath the cell in case of salt spillage and (b) a schematic of the experimental set up.

used after this evaluation. A Ni (nickel) plated crocodile clip was found to be suitably robust, although a layer of corrosion did form on the surface of the clip, this was cleaned away with sandpaper prior to each experiment. This clip could be reused and allowed the microelectrodes to be easily connected and disconnected from the system. A small square of ceramic was placed between the back of the microelectrode and the clip to prevent any electrical connection between the clip and the Si. The crocodile clip was crimped to a W wire (1 mm diameter) and attached to the microelectrode contact pad. The W wire was then kinked and inserted into a Pyrex sheath for insulation (the kink preventing the wire from sliding down the sheath under gravity). Figure 4.7 (b) shows a photograph of this set up. For the experiment the wire was lowered until the microelectrode was immersed in the salt. Since the microelectrode could not be seen, the open circuit potential was

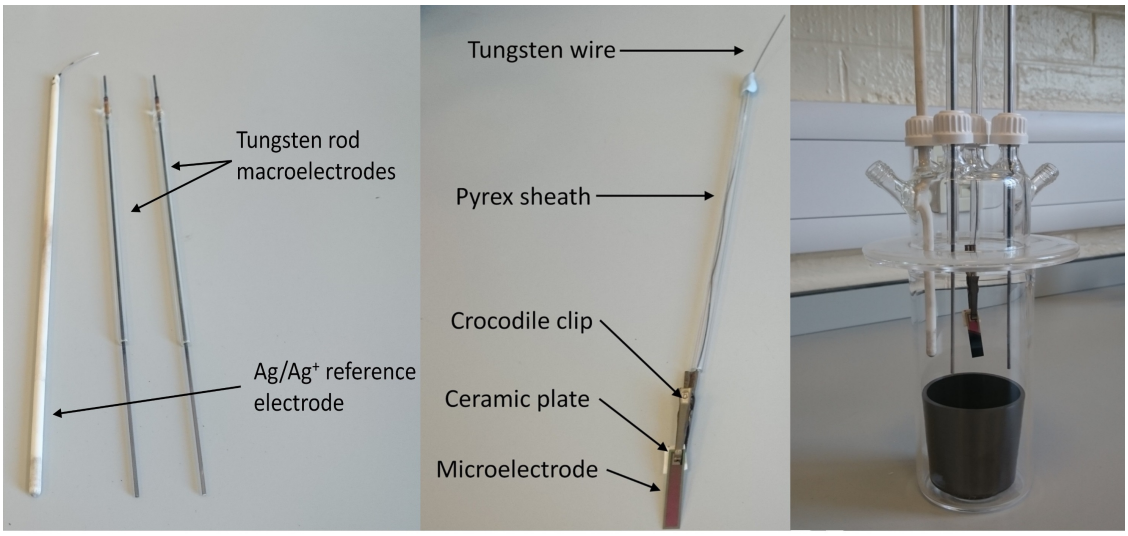

Figure 4.7: (a) W rod macroelectrodes and the Ag/Ag^+ reference electrode, (b) the microelectrode connection, and (c) the assembled experiment set up. up.

observed and used as an indicator that the microelectrode had been lowered into the salt. The large separation between the contact pad and microelectrode helped ensure only the microelectrode was submerged in the salt. The completely assembled set up is shown in figure 4.7 (c).

4.5.3 Electrical Noise

To determine the impact of electrical noise on the experimental set up, a 1 MΩ resistor was connected between the WE and CE, a potential of 250 mV was applied, and the current measured. The potential of 250 mV was chosen to generate a current of 250 nA, which is on the current scale expected of a microelectrode. Figure 4.8 (a) shows the current response with the furnace off for 15 seconds (solid) and on for 15 seconds (dotted). The current spikes occur at a frequency of 1 Hz and are caused by the furnace heating in pulses. The current spikes range between 1 nA and 9 nA. It is uncertain why the pulses have a superimposed sinewave feature, it could simply be the way the furnace pulses or interference from another noise source. Either way, the magnitude of current spikes could impact microelectrode measurements. In order to block this noise a foil sheath was inserted into the tube furnace between the quartz cell and the heating elements and earthed through the potentiostat. Figure 4.8 (b) shows the current response with the furnace on, with and without the shield.

The shield very successfully reduced the noise from the furnace. Other sources of

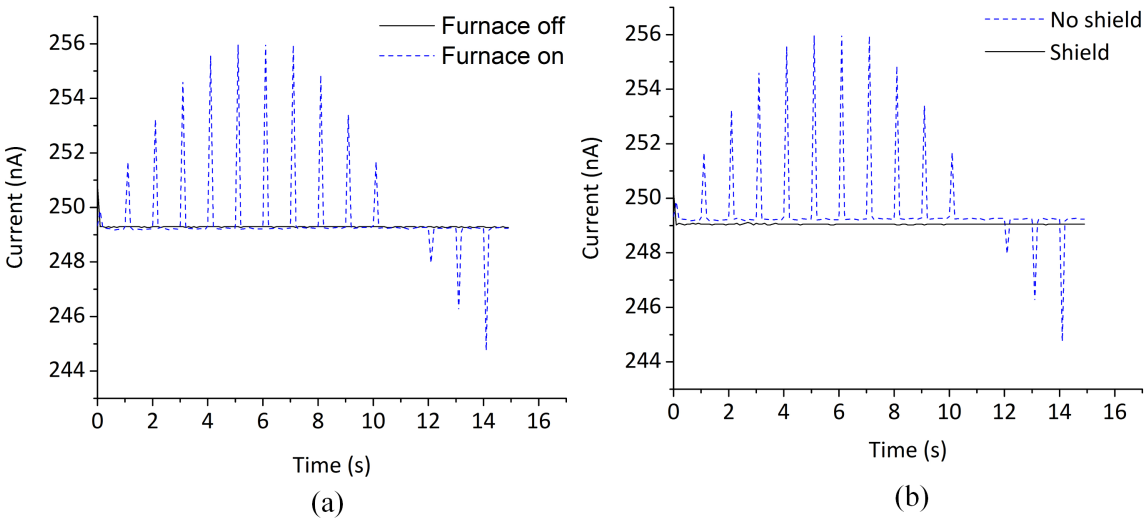

Figure 4.8: Current measured through a 1 MΩ resistor connected between the WE and CE while (a) the furnace is on and off, and (b) furnace on with and without shield.

noise such as mains noise are a challenge and, although a mains filter is installed, the effect of mains interference is present in some of the measurements presented [35]. It should be noted that the foil sheath changed the temperature within the cell and so a thermocouple was used to ensure the temperature of the salt was known. The electromagnetic shielding presented here was not added to the set up until later on the project when electrical noise was deemed a problem and so several figures in this thesis show noise present.

4.5.4 Salt Preparation

Preparation of the salt is very important as LKE is hygroscopic, so will readily form oxide species when exposed to air [2, 33, 36]:

$$H_2O + LiCl \rightarrow LiOH + HCl \tag{4.3}$$

$$H_2O + 2LiCl \rightarrow Li_2O + 2HCl \tag{4.4}$$

These products are corrosive and have the potential to damage the electrodes, other experimental apparatus, and contaminate redox agents [37]. The salt was prepared by

mixing 55 g of KCl and 45 g of LiCl in the vitreous carbon crucible and to minimise the presence of moisture in the salt, it was then dried overnight in an oven at 125°C. The salt was then moved into the cell, which was placed in the furnace and heated under an inert atmosphere of flowing argon. The positive pressure of the argon further helps to prevent the ingress of oxygen into the system.

After melting the salt, cyclic voltammetry was performed to assess the level of contamination. To demonstrate this, figure 4.9 compares (a) an ideal cyclic voltammogram of an LKE salt with no contaminants and (b) a real cyclic voltammogram of an LKE salt just after melting. The only electrochemical reactions present in the ideal salt in figure 4.9 (a) are the solvent limits of Li plating and stripping around -2.5 V and Cl gas generation around +1.5 V. However, after melting, salts would typically display CVs such as shown in figure 4.9 (b) with additional reduction peaks at around -1 V and -2 V and additional oxidation peaks at, -0.3 V, +0.2 V, and +0.5 V. Such electrochemical reactions signal the presence of contaminants in the salt, such as the products of equations (4.3) and (4.4). An electrochemical cleaning procedure was employed to remove any remaining oxygen related contaminants and was performed using a standard protocol. Two W rods were used as working and counter electrodes to perform cyclic voltammetry across the LKE potential window. Figure 4.10 shows a CV of the same salt as figure 4.9 (b) after 136 scans (96 minutes) of electrochemical cleaning. It can be seen that the additional reduction and oxidation peaks in figure 4.9 (b) are no longer present and, although some peaks more positive than 0 V have not been entirely removed, the salt looks much closer to the CV of an ideal LKE salt in figure 4.9 (a). Most of the oxygen freed during the cleaning process will escape the salt and be extracted through the Ar line. It should be noted that although contaminants are no longer electrochemically reactive, this does not mean they have all been completely removed from the salt.

4.6 Characterisation of the Benchmark Microelectrode

4.6.1 Characterisation Methodology

The BM would be considered successful if it fulfilled two criteria:

1. *The current response was that typical of a microelectrode.*

Figure 4.11 shows an ideal plating and stripping reaction at a microelectrode

Three features that characterise a microelectrode response are:

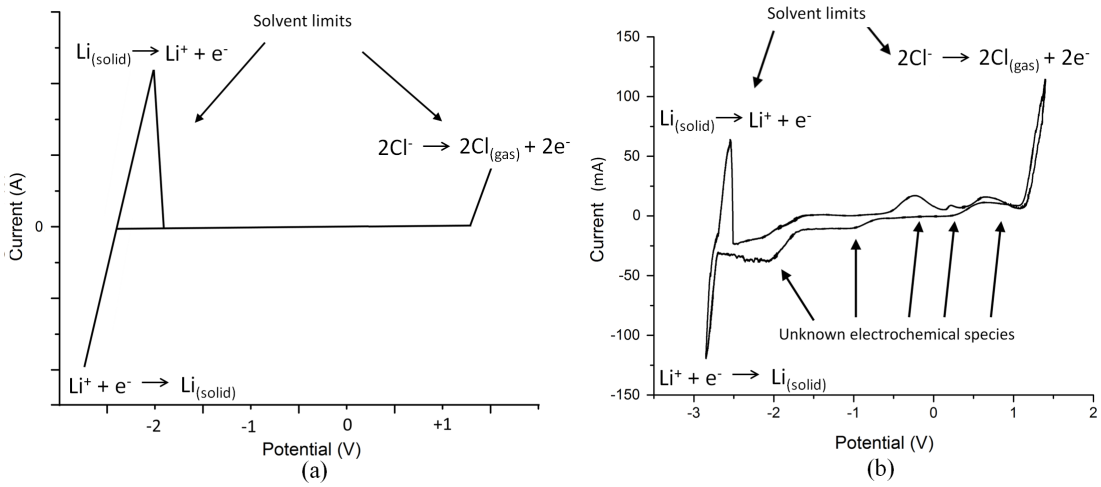

Figure 4.9: (a) Ideal cyclic voltammogram of LKE showing the full potential window (mock-up). (b) A CV of the full potential window of LKE after melting at 500°C at 200 mV/s. The solvent limits and unknown electrochemical species are highlighted.

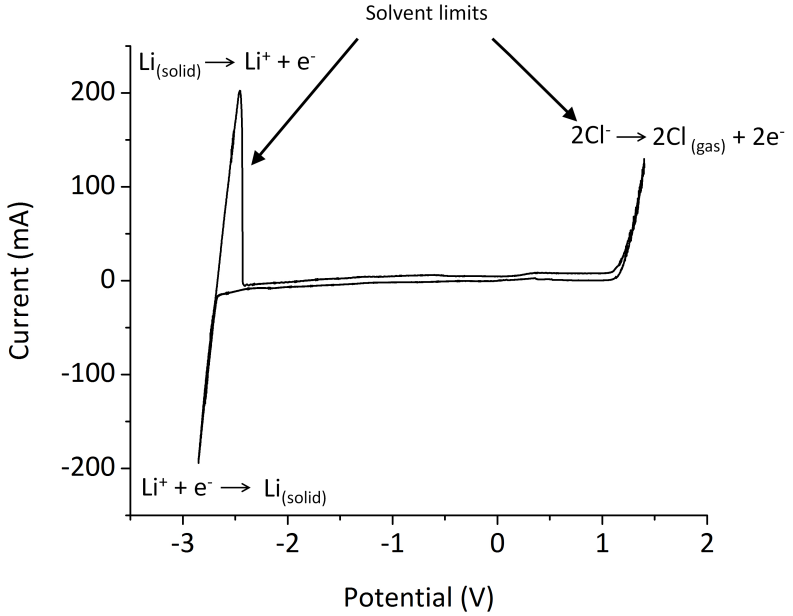

Figure 4.10: Cyclic voltammogram of the LKE used to record the CV in figure 4.9 (b), after 136 cleaning scans at 500°C at 200 mV/s.

(a) The limiting current associated with an electrochemical reduction reaction, highlighted on figure 4.11;

(b) The sharp stripping peak associated with the oxidation reaction of stripping away plated metal, also highlighted on figure 4.11;

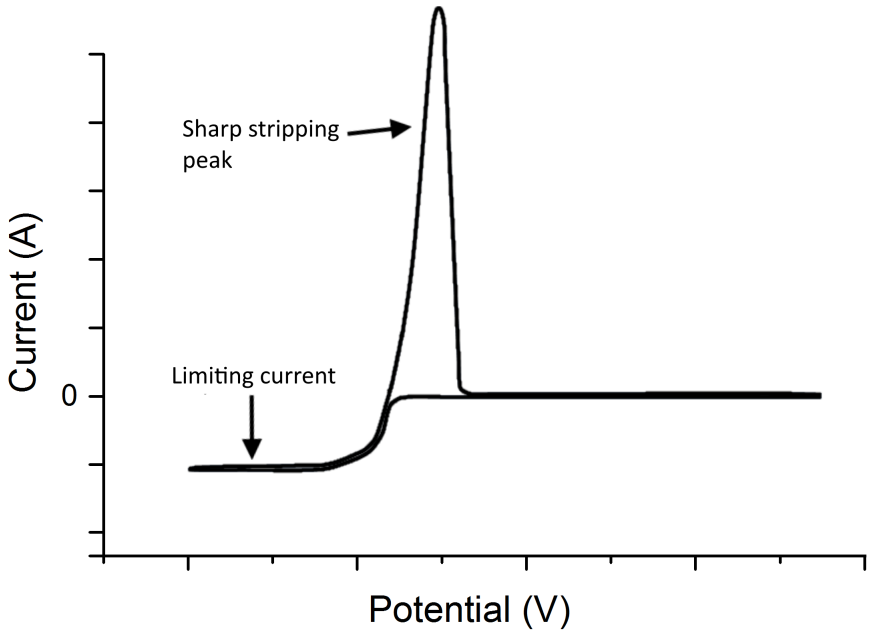

Figure 4.11: Ideal cyclic voltammogram of a plating and stripping reaction at a microelectrode (mock-up).

(c) Low current magnitude, on the nanoampere scale.

Reproducing these features in the LKE system confirms that a micro-scale area of electrode metal has successfully been retained in the molten salt. Further details about microelectrode behaviour can be found in chapters 2 and 3.

2 *The recorded limiting current is in agreement with the theoretical limiting current predicted by equation (3.3).*

If the limiting current predicted by equation (3.3) matches the experimental value, it confirms that the area of the microelectrode (as defined in the photolithography) has remained unchanged in the salt. A literature value of $2.44 \times 10^{-5}\,\mathrm{cm^2 s^{-1}}$ was used for the diffusion coefficient (D) of Ag in LKE at 450°C [38].

4.6.2 Benchmark Microelectrode Performance

The BMs were characterised in 100 g of LKE with 124 mM of AgCl redox couple at 500°C. Before characterising the microelectrodes, a macroelectrode CV of the Ag plating and stripping reaction was recorded as a control. Figure 4.12 shows the macroelectrode CV

using the same 1.8 mm diameter W rods used in the electrochemical cleaning process, scanned between -0.75 V and 0.5 V. An Ag plating peak can be seen at -0.33 V and an Ag stripping peak on the reverse scan at -0.15 V, confirming the Ag was behaving according to equation (4.2) in LKE. The BMs were then put through the same process. Figure 4.13

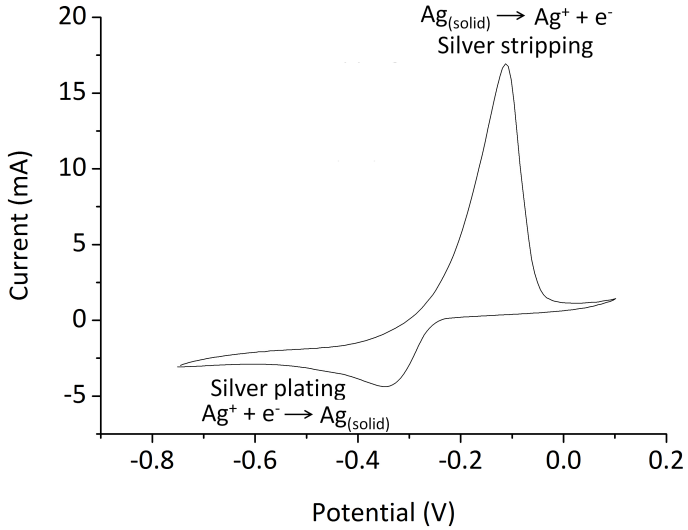

Figure 4.12: Cyclic voltammogram of a W macroelectrode in 100 g LKE with 125 mM of AgCl at 500°C at 100 mV/s.

shows cyclic voltammograms of four BMs subject to Ag plating and stripping. Figure 4.13 (a) and (b) are different 100 μm edge length BMs, and similarly (c) and (d) are two 20 μm edge length BMs. Although the BMs exhibit identifiable Ag plating at -0.3 V to -0.5 V and stripping at -0.3 V to 0 V, there are no limiting currents typical of a microelectrode as in figure 4.11. Owing to the lack of limiting current, these responses cannot be directly compared against the predicted values in table 4.1. However the magnitude of the currents can be observed to be 10 - 100 times larger than the predicted values. The increased currents recorded implies additional areas of the electrode metal

Microelectrode	Edge length (μm)	Predicted limiting current (nA)
4.16 (a)	100	386
4.16 (b)	100	386
4.16 (c)	20	77
4.16 (d)	20	1640

Table 4.1: Predicted limiting currents for the CVs in figure 4.13, calculated using equation (3.3)

have come into contact with the salt. The lack of typical microelectrode-like features in

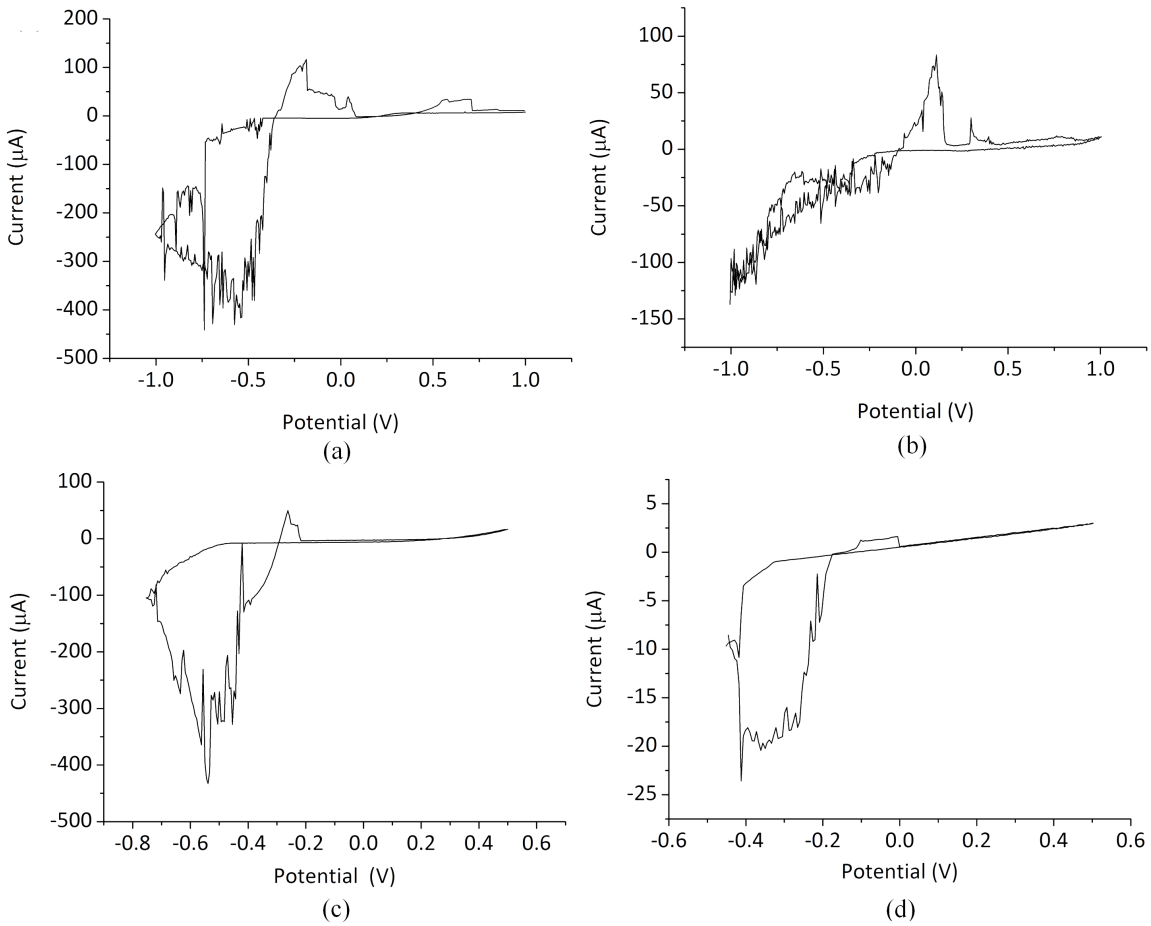

Figure 4.13: Cyclic voltammograms of Ag plating and stripping in LKE at 500°C on BMs of: (a) 100 μm edge length with 6.98 mM AgCl, (b) 100 μm edge length with 6.98 mM AgCl, (c) 20 μm edge length with 6.96 mM AgCl, and (d) 20 μm edge length with 148 mM AgCl.

the CVs in figure 4.13 indicates that the exposed area of electrode metal was large enough for the microelectrode to function as a macroelectrode. The most likely mechanism by which the electrode metal layer can come into contact with the salt is some failure of the top insulator. As the microelectrodes were cycled for longer periods of time, the currents were observed to increase. Figure 4.14 shows the first and third CV of the BM used to record the CV in figure 4.13 (d). The first scan (black) is that shown in figure 4.13 (d), while the current of the third scan (blue) has increased 20 times over the course of three scans - around 30 seconds. The current increase was limited to 1 mA by the potentiostat settings. The increase in current seen when the microelectrode is cycled for longer implies degradation of the top insulator over the course of the experiment, exposing progressively larger areas of metal to the salt.

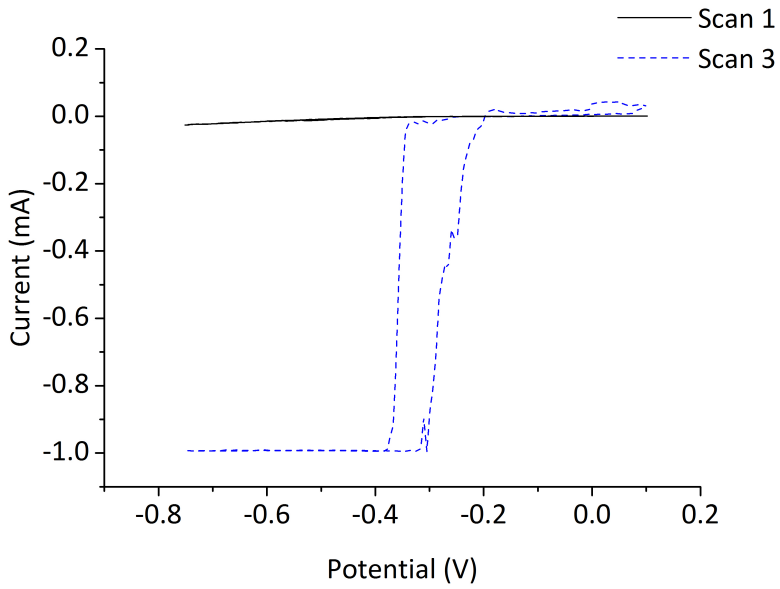

Figure 4.14: Scans 1 and 3 of the W 20 μm microelectrode used to record the CV presented in figure 4.13 (d) in 100 g LKE with 148 mM of AgCl at 500°C at 100 mV/s.

After removal from the salt, the microelectrodes were allowed to cool in air and gently washed in deionised water to remove frozen salt. Failure of the top insulator was confirmed when the microelectrodes were examined; the electrode used to record to CVs in figures 4.13 (d) and 4.14 is shown in figure 4.15. It can be seen that the top insulator

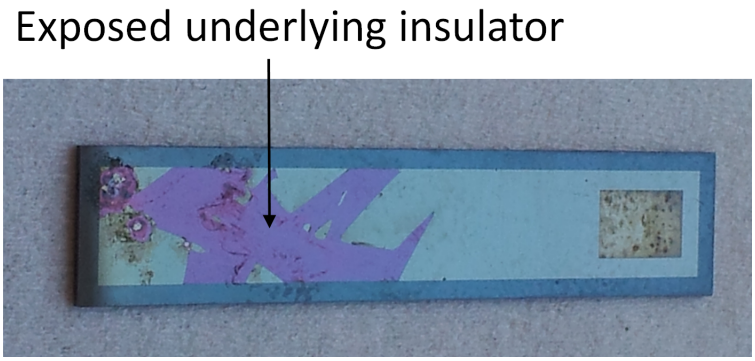

Figure 4.15: BM from figures 4.13 (d) and 4.14 after removal from the LKE after 5 minutes of electrochemical cycling.

has delaminated likely exposing large areas of the electrode metal underneath the top insulator while in the salt, accounting for the large currents observed figures 4.13 and 4.14. Delamination occurs when there is excessive stress in the layered structure causing the layers to break away from each other. The electrodes only showed delamination while

undergoing electrochemical cycling and not during fabrication or just during immersion in the LKE. The means that the electrochemical cycling is an additional source of stress, causing the top insulator to delaminate.

It can also be observed in figure 4.15 that the electrode metal, which should be exposed where the top insulator has delaminated, is also missing. This was unlikely related to the delamination of the top insulator as the microsquare, which did not have the top insulator covering it, also showed metal loss. An example of this is shown in figure 4.16, where a different BM has cycled between -0.5 V and + 0.5 V for 5 minutes. This implies the existence of a second mechanism causing the electrode metal to disappear.

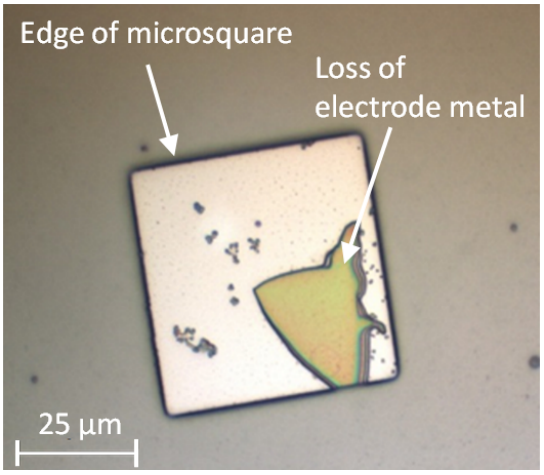

Figure 4.16: A section of electrode metal has detached from the microsquare area of a BM following cycling in LKE with AgCl at 500°C across the voltage range of -0.5 V to +0.5 V for 10 minutes.

A third feature of the BMs that was noticed after removal from the melt was the presence of Ag on the surface of the top insulator. Figure 4.17 shows an example of such deposits of Ag on the top insulator. The fact that Ag has electroplated on the surface of the top insulator suggests it is not functioning as an insulator. There is clearly some mechanism which is enabling electrons to be passed from the metal, through the top insulator, to the salt allowing for the reduction of Ag on the surface of the Si-rich SiN as if it were a conductor. This permeability of the top insulator does help explain the seemingly contradictory observation in figure 4.15; that the currents recorded were on the milliampere scale, implying a large area of exposed electrode metal and yet the exposed electrode metal was missing. It could also be the electrode metal detached with the salt when it was washed. This would suggest the adhesion between the electrode metal and the top insulator had been weakened or removed all together.

A minority of BMs exhibited damage to the top insulator around the perimeter of the

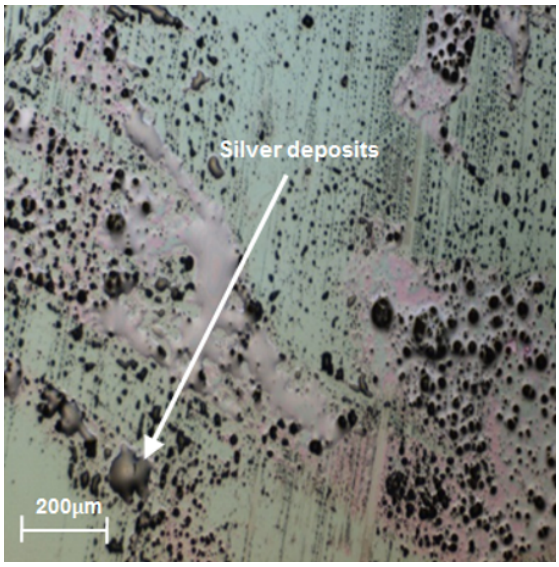

Figure 4.17: Areas of Ag plated on the Si-rich SiN top insulator of a BM after cycling between -0.6 V to +0.5 V for 10 minutes in LKE with 6.51 mM AgCl.

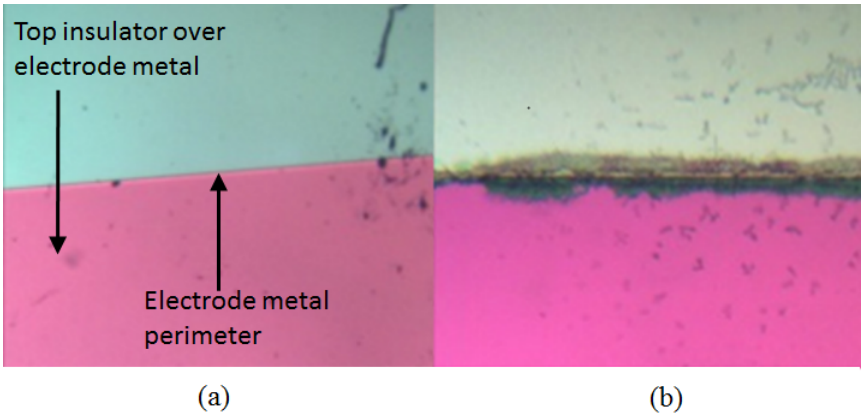

Figure 4.18: The perimeter of a BM (a) before cycling in LKE with 6 mM AgCl and (b) after.

electrode metal and an example of this is shown in figure 4.18. This suggests the metal electrode step could be a focal point for stress, and will occasionally expose additional electrode metal to the LKE.

4.7 Summary

An architecture for a microelectrode consisting of a Si-rich SiN underlying insulation layer, a Ti adhesion layer, a W electrode metal, and a Si-rich SiN top insulation layer to be used in LKE at 500°C has been described. The experimental set up and procedure

for characterising these microelectrodes has also been outlined, including a process for cleaning the salt and a system for reducing electrical noise. The microelectrodes were fabricated and then subjected to cyclic voltammetry at 500°C and characterised using the Ag plating and stripping reaction.

Recognisable electrochemistry of Ag was obtained, although the currents were 10 - 100 times higher than predicted and demonstrated no limiting current typical of a microelectrode. Four failure mechanisms were identified that resulted in failure of the microelectrode. These mechanisms were:

- Delamination of the top insulator;
- Ag plating on the surface of the top insulator;
- Loss of the electrode metal;
- Damage to the top insulator around the electrode metal.

With these failure mechanisms identified, work can begin on optimising the electrode architecture by directly targeting each failure mechanism. This process will be covered in chapter 5.

References

[1] A. Relf, D. Corrigan, C. L. Brady, J. G. Terry, A. J. Walton, and A. R. Mount, "Robust Microelectrodes In Molten Salt Analysis," *ECS Transactions*, vol. 50, no. 11, pp. 105–109, 2013. [Online]. Available: http://ecst.ecsdl.org/content/50/11/105.abstract

[2] C. L. Brady, "Development and characterisation of microelectrodes for extreme environments," Ph.D. dissertation, University of Edinburgh, 2013.

[3] H. L. Woodvine, J. G. Terry, A. J. Walton, and A. R. Mount, "The development and characterisation of square microfabricated electrode systems." *The Analyst*, vol. 135, no. 5, pp. 1058–1065, 2010. [Online]. Available: http://dx.doi.org/10.1039/b924342a

[4] M. R. Bermejo, J. Gómez, J. Medina, A. M. Martínez, and Y. Castrillejo, "The electrochemistry of gadolinium in the eutectic LiCl - KCl on W and Al electrodes," *Journal of Electroanalytical Chemistry*, vol. 588, no. 2, pp. 253–266, March 2006. [Online]. Available: http://www.sciencedirect.com/science/article/pii/S0022072806000350

[5] P. Baumli and G. Kaptay, "Wettability of carbon surfaces by pure molten alkali chlorides and their penetration into a porous graphite substrate," *Materials Science and Engineering: A*, vol. 495, no. 1-2, pp. 192–196, November 2008. [Online]. Available: http://www.sciencedirect.com/science/article/pii/S0921509308001652

[6] W. D. Callister and D. G. Rethwisch, *Fundamentals of Materials Science and Engineering: An Integrated Approach*. John Wiley & Sons, 2001.

[7] G. L. Pearson and J. Bardeen, "Electrical properties of pure silicon and silicon alloys containing boron and phosphorus," *Physical Review*, vol. 75, no. 5, March 1949. [Online]. Available: http://journals.aps.org/pr/pdf/10.1103/PhysRev.75.865

[8] Y. Nishi and R. Doering, Eds., *Handbook of semiconductor manufacturing technology*. Marcel Dekker, 2000.

[9] B. C. Joshi, G. Eranna, and D. P. Runthala, "LPCVD and PECVD silicon nitride for microelectronics technology," *Indian Journal of Engineering and Materials Sciences*, vol. 7, no. 5-6, pp. 303–309, 2000.

[10] F. C. Campbell, *Elements of metallurgy and engineering alloys*. ASM International, 2008.

[11] D. R. Askeland and W. J. Wright, *The Science and Engineering of Materials, SI Edition*, 6th ed. Cengage Learning, 2015.

[12] B. K. Yen, R. L. White, R. J. Waltman, Q. Dai, D. C. Miller, A. J. Kellock, B. Marchon, P. H. Kasai, M. F. Toney, B. R. York, H. Deng, Q.-F. Xiao, and V. Raman, "Microstructure and properties of ultrathin amorphous silicon nitride protective coating," *Journal of Vacuum Science & Technology A: Vacuum, Surfaces, and Films*, vol. 21, no. 6, p. 1895, 2003. [Online]. Available: http://dx.doi.org/10.1116/1.1615974

[13] J. T. Milek, *Silicon Nitride for Microelectronic Applications: Part 2 Applications and Devices*. Springer, 2013. [Online]. Available: http://www.springer.com/gp/book/9781461596110

[14] R. G. Munro and S. J. Dapkunas, "Corrosion characteristics of silicon carbide and silicon nitride," *Journal of Research of the National Institute of Standards and Technology*, vol. 98, no. 5, pp. 607–631, 1993. [Online]. Available: http://nvlpubs.nist.gov/nistpubs/jres/098/jresv98n5p607_A1b.pdf

[15] H. O. Pierson, *Handbook of Refractory Carbides & Nitrides: Properties, Characteristics, Processing and Applications*. William Andrew, 1996. [Online]. Available: http://www.sciencedirect.com/science/book/9780815513926

[16] J. Laconte, D. Flandre, and J. P. Raskin, *Thin dielectric films stress extraction*. Springer US, 2006, ch. 2, pp. 47–103. [Online]. Available: http://link.springer.com/chapter/10.1007%2F0-387-28843-0_3#page-1

[17] O. Zohni, G. Buckner, T. Kim, A. Kingon, J. Maranchi, and R. Siergiej, "Investigating thin film stresses in stacked silicon dioxide/silicon nitride structures and quantifying their effects on frequency response," *Journal of Micromechanics and Microengineering*, vol. 17, no. 5, p. 1042, 2007. [Online]. Available: http://dx.doi.org/10.1088/0960-1317/17/5/026

[18] D. R. Lide, *CRC handbook of chemistry and physics*. CRC, 2004. [Online]. Available: http://www.hbcpnetbase.com/

[19] Y. Castrillejo, M. R. Bermejo, A. I. Barrado, and R. Pardo, "Electrochemical behaviour of dysprosium in the eutectic LiCl - KCl at W and Al electrodes,"

Electrochimica Acta, vol. 50, no. 10, pp. 2047–2057, March 2005. [Online]. Available: http://www.sciencedirect.com/science/article/pii/S0013468604009454

[20] E. Lassner and W.-D. Schubert, *Tungsten: properties, chemistry, technology of the element, alloys, and chemical compounds*. Springer Science & Business Media, 2012. [Online]. Available: http://www.springer.com/gp/book/9780306450532

[21] F. Habashi, "Historical Introduction to Refractory Metals," *Mineral Processing and Extractive Metallurgy Review*, vol. 22, no. 1, pp. 25–53, 2001. [Online]. Available: http://dx.doi.org/10.1080/08827509808962488

[22] M. J. Cordill, D. F. Bahr, and N. R. Moody, "Recent developments in thin film adhesion measurement," *IEEE Transactions on Device and Materials Reliability*, vol. 4, no. 2, pp. 163–168, June 2004. [Online]. Available: http://dx.doi.org/10.1109/TDMR.2004.829071

[23] S. Franssila, *Introduction to Microfabrication*. John Wiley & Sons, 2010.

[24] M. J. Madou, *Fundementals of Microfabrication*, M. J. Madou, Ed. CRC Press, 2002, p. 126.

[25] B. D. Craig and D. S. Anderson, *Handbook of corrosion data*. Knovel, 1989.

[26] D. G. Lovering, *Molten salt technology*, D. G. Lovering, Ed. Springer Sci, 2014.

[27] E. Rabald, *Corrosion guide*. Elsevier, 2012.

[28] Y. Kanzaki and M. Takahashi, "The passivation phenomenon of platinum in fused lithium chloride + potassium chloride eutectic: Part II. Chlorine overpotential and superpassivation of platinum," *Journal of Electroanalytical Chemistry and Interfacial Electrochemistry*, vol. 90, no. 3, pp. 305–312, July 1978. [Online]. Available: http://www.sciencedirect.com/science/article/pii/S0022072878800679

[29] M. Takahashi, Y. Katsuyama, and Y. Kanzaki, "The passivation phenomenon of platinum in fused lithium chloride + potassium chloride eutectic: I. Effect of oxide ions on the passivation," *Journal of Electroanalytical Chemistry and Interfacial Electrochemistry*, vol. 62, no. 2, pp. 363–371, July 1975. [Online]. Available: http://www.sciencedirect.com/science/article/pii/0022072875800040

[30] Y. Sakamura, T. Hijikata, K. Kinoshita, and T. Inoue, "Measurement of standard potentials of actinides (U, Np, Pu, Am) in LiCl - KCl eutectic salt

and separation of actinides from rare earths by electrorefining," *Journal of Alloys and Compounds*, vol. 271-273, pp. 592–596, 1998. [Online]. Available: http://www.sciencedirect.com/science/article/pii/S0925838898001662

[31] O. Shirai, T. Iwai, Y. Suzuki, and Y. Sakamura, "Electrochemical behavior of actinide ions in LiCl - KCl eutectic melts," *Journal of Alloys and Compounds*, vol. 271-273, p. 658688, 1998. [Online]. Available: http://www.sciencedirect.com/science/article/pii/S092583889800187X

[32] Y. Kuo, "Reactive ion etching of PECVD amorphous silicon and silicon nitride thin films with fluorocarbon gases," *Journal of the Electrochemical Society*, vol. 137, no. 4, pp. 1235–1239, 1990. [Online]. Available: http://dx.doi.org/10.1149/1.2086638

[33] J. Braunstein, G. Mamantov, and G. P. Smith, *Advances in molten salt chemistry*. Springer, 2013.

[34] I. R. Walker, *Reliability in scientific research: improving the dependability of measurements, calculations, equipment, and software*. Cambridge University Press, 2011.

[35] I. Montenegro, M. A. Queirós, and J. L. Daschbach, Eds., *Microelectrodes: theory and applications*. Springer, 2012. [Online]. Available: http://www.springer.com/us/book/9780792312291

[36] H. A. Laitinen and W. S. Ferguson, "Preparation of Pure Fused Lithium Chloride - Potassium Chloride Eutectic Solvent," *Berichte der Bunsengesellschaft für physikalische Chemie*, vol. 67, no. 4, pp. 360–364, June 1957. [Online]. Available: http://dx.doi.org/10.1149/1.2428639

[37] W. J. Burkhard and J. D. Corbett, "The Solubility of Water in Molten Mixtures of LiCl and KCl," *Journal of the American Chemical Society*, vol. 24, no. 79, p. 63616363, December 1957. [Online]. Available: http://dx.doi.org/10.1021/ja01581a005

[38] G. J. Janz and N. P. Bansal, "Molten Salts Data: Diffusion Coefficients in Single and Multi - Component Salt Systems," *Journal of Physical and Chemical Reference Data*, vol. 11, no. 3, p. 592, 1982. [Online]. Available: http://dx.doi.org/10.1063/1.555665

Chapter 5

Optimisation of Microelectrode Materials

5.1 Introduction

Initial characterisation of the benchmark microelectrode (BM) in chapter 4 resulted in a recognisable electrochemical response (plating and stripping of Ag). Unfortunately these devices did not survive as microelectrodes for any significant period of time. A number of failure mechanisms were identified:

- Delamination of the top insulator;
- Loss of electrode metal;
- Failure of the top insulator to effectively insulate;
- Damage to the top insulator around the perimeter of the electrode metal.

In this chapter these four failure mechanisms are systematically investigated and addressed. Each solution was incorporated into a new set of microelectrodes and tested to determine their effectiveness and then integrated into an optimised microelectrode architecture, capable of producing quantifiable electrochemistry characteristic of a microelectrode.

5.2 Delamination in Thin Films

5.2.1 Delamination of the Benchmark Microelectrode

When the BM was characterised in chapter 4, it was observed that the top insulator frequently delaminated after electrochemical cycling. Delamination of thin films is usually indicative of excessive stress in a layer stack or poor adhesion between layers. Given that no signs of poor adhesion (such as peeling or flaking of layers) were observed during the fabrication, the cause of the delaminations is most likely related to stress associated with their operation in LKE.

5.2.2 Origin of Stress in Thin Films

Stress in thin films generally arises when the deposited thin film has either shrunk or expanded relative to the substrate it is attached to [1–7]. When atoms in a thin film are displaced from their equilibrium position, a restoring force is generated. However, when these atoms are anchored to a substrate they are prevented from returning to their equilibrium position. If this force is too large it can break the chemical bonds

attaching the thin film to the substrate, resulting in the thin film delaminating. Stress can be either compressive or tensile. Compressive stress occurs when the thin film is held in compression by being fixed to a substrate and figure 5.1 (a) shows a thin film on a substrate under compression [3, 5–7]. On the other hand, a wafer under tensile stress is shown in figure 5.2. This is generated when the thin film is held in tension relative to the substrate it is fixed to [3, 5, 6]. The force associated with these stresses causes a characteristic bow in the wafer and by convention, compressive stress values are negative and tensile stress values are positive [3, 5].

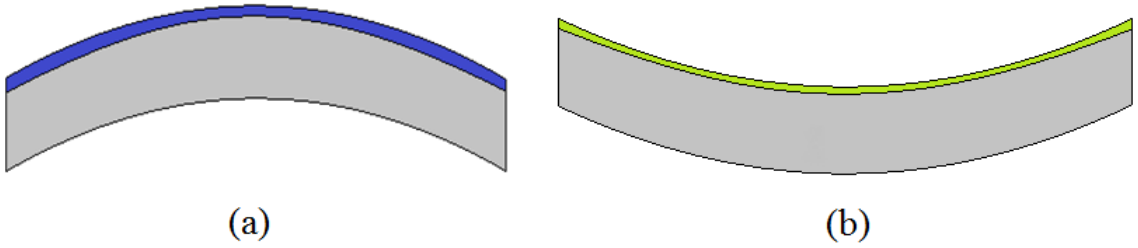

Figure 5.1: Cross-section of two substrates under (a) compressive and (b) tensile stress.

The causes of these stresses can be generally classed as intrinsic or extrinsic, with the total stress in a thin film f at temperature T, denoted as $\sigma_f^t(T)$. The sum of the both components is given by:

$$\sigma_f^t(T) = \sigma_f^i + \sigma_f^e(T) \tag{5.1}$$

where σ_f^i is the intrinsic stress and $\sigma_f^e(T)$ the extrinsic stress, which is temperature dependent. In order to quantify the stress in the thin films at 500°C, both components must be determined.

Extrinsic Stress

Extrinsic stresses are generated by external stimuli such as pressure, changes in temperature, or chemical reactions [1, 3, 5, 7]. Stress attributable to changes in temperature is the most commonly encountered extrinsic stress and the term “extrinsic stress” is often used to refer to it specifically [1–3]. This stress arises when two layers with differing coefficients of thermal expansion are heated/cooled, and hence expand/contract at different rates. Stress due to thermal expansion is frequently encountered during fabrication when a thin film is deposited at high temperature and then brought down to room temperature, generating thermal stress in the film.

Intrinsic Stress

Intrinsic stress arises from the internal structure within the film, set by the deposition conditions and can be considered the stress in the thin film if all extrinsic stresses are removed [1, 3, 5, 7]. The actual causes of intrinsic stress are less well defined than extrinsic stress and can be thought of as arising from a thin film being unable to relax to an equilibrium state during deposition [1, 3]. This means deposition conditions such as temperature, substrate DC bias, and chamber pressure all affect intrinsic stress levels in a thin film [8].

5.2.3 Determining Stress in Thin Films

The most common method of experimentally determining stress in thin films is by measuring the wafer curvature and then applying the Stoney formula [9–12]:

$$\sigma_f^t = \frac{E_s}{(1-\nu_s)} \frac{h_s^2 \kappa}{6 h_f} \tag{5.2}$$

where E_s is the Young's modulus of the substrate, h_s is the thickness of the substrate, h_f is the thickness of the film, ν_s is Poisson's ratio of the substrate, and κ is the wafer curvature. This is defined as:

$$\kappa = \frac{1}{R} - \frac{1}{R_0} \tag{5.3}$$

where, R_0 is the radius of the substrate before the thin film is deposited, and R is the radius of the substrate and deposited film. These are obtained by measuring the wafer bow before and after layer deposition. The use of this formula is based on a number of assumptions [10, 11]:

- The substrate and film thickness are uniform and both have the same radius;
- The thin film is much thinner than the substrate;
- The film and the substrate are homogeneous, isotropic, and linearly elastic;
- Out-of-plane direct stress and all shear stresses vanish;
- The curvature, and hence stress, is equal in the X and Y directions and other stresses can be considered constant.

Measuring thermal stress in films is difficult as the heating requirements are often not compatible with the available stress measurement techniques [13]. However, knowing

the rate at which these layers expand and assuming the much thicker Si wafer sets the strain, this thermal stress can be calculated using [1, 3]:

$$\sigma_f^{th}(T) = \frac{E_f}{(1-\nu_f)}\Delta T \Delta\alpha_L \tag{5.4}$$

where $\sigma_f^{th}(T)$ denotes the stress due to thermal expansion of film f at temperature T, E_f is the Young's modulus of the film, ν_f is the Poisson ratio of the film, ΔT is the change in temperature between the deposition temperature and the temperature at which the stress is to be known, and $\Delta\alpha_L$ is the difference in linear thermal expansion coefficients between the film and the substrate.

5.3 Determining Stress in the Benchmark Microelectrode

5.3.1 Methodology

In order to employ an effective stress-relief strategy, it is necessary to understand the nature of the stresses in the top insulator used in the benchmark design. This meant determining the sources of stress in the top insulator and the magnitude and direction of that stress at 500°C. However it was not practical to directly measure the stress in the film while in the environment of the LKE. Therefore the stress of the film at 500°C could be determined by adding the intrinsic stress of the film and the thermal stress component at 500°C, as in equation (5.5). The intrinsic stress can be found by measuring the total stress in the film and subtracting the thermal stress component at 21°C. The thermal component at 500°C could then be added to give the total stress, as in equation (5.6).

$$\sigma_f^t(500) = \sigma_f^i + \sigma_f^e(500) \tag{5.5}$$

$$\sigma_f^t(500) = \sigma_f^t(21) - \sigma_f^e(21) + \sigma_f^e(500) \tag{5.6}$$

The thermal stress components were calculated using equation (5.4) and the total stress in the film at 21°C was determined using the Stoney formula (equation (5.3)) and wafer bow measurements. These measurements were a valid use of the Stoney formula as they complied with all the assumptions listed in section 5.2:

- *The substrate and film thickness are uniform and have the same radius*

  - The Si substrates used are 100 mm in diameter and the thin films are deposited or grown only on the surface of the Si, which means they are the same radius. The largest standard deviation of thin film thickness across the surface of the films studied was 87 Å, which is 1.7% of the film thickness.

- *The film is much thinner than the substrate*

  - The films under study are around 500 nm thick and the Si substrate is 525 $\pm$ 25 μm thick.

- *The film and the substrate are homogeneous, isotropic, and linearly elastic*

  - Both the film and the substrate are amorphous. Although Si wafers are anisotropic, the biaxial modulus term $\frac{E}{(1-\nu)}$ in equation (5.2) is used to compensate the difference in Young's modulus between crystal planes [14].

- *Out-of-plane direct stress and all shear stresses vanish*

  - Shear stress can be discounted everywhere except at the edge of wafer, hence the measurements were taken avoiding the edge [15].

- *The curvature, and hence stress, is equal in the X and Y directions and other stresses can be considered constant*

  - The wafer bow measurements were taken in both X and Y axes. In wafers where a large deviation in curvature between the two axes was observed, the results were discounted as violating this assumption. This could arise as some of the wafers were reclaimed wafers, so previous processes may have left behind defects or an uneven surface resulting in asymmetric stresses.

The intrinsic stress was determined by first measuring the bow of a blank Si wafer using a Dektak Veeco 8000 surface profiler. As described in chapter 4, a 500 nm LPCVD Si-rich SiN film was deposited on the blank Si wafer and the bow then remeasured.

The literature values and sources for each parameter used are presented in table 5.1. It should be noted that the thermal expansion coefficient, Young's modulus, and Poisson ratio change with temperature, which made obtaining literature values for these parameters at 500°C difficult. Studies have shown that Poisson's ratio changes only slightly over the temperature range under study in this work, as such a room temperature value of the Poisson ratio was used [16–18]. One study showed that the Young's

modulus of monolithic Si_3N_4 only varies by around 3% between 0°C and 500°C, so a room temperature value of Young's modulus was also used [19]. As for the other high temperature parameters, an effort was made to find values obtained from films deposited under similar conditions to those at the Scottish Microelectronics Centre. Significant deviations from this were: E_s for SiO_2 was derived from molecular dynamic simulation and α_L for Si-rich SiN was obtained from experiments using plasma enhanced chemical vapour deposition (PECVD) SiN, as opposed to LPCVD SiN used in this work. Despite this possible error, the calculations would still contribute to understanding the stresses involved in the layer stack under investigation.

Parameter	E_s (GPa)	ν_s	α_L ($\times 10^{-6} °C^{-1}$)
Si (at 500°C)	N/A	N/A	4 [20]
Si-rich SiN (at 500°C)	N/A	N/A	3.64 [21]
SiO_2 (at 500°C)	77 [22]	N/A	1 [23]
Si (at 21°C)	169 [14]	0.28 [24]	2.39 [20]
Si-rich SiN (at 21°C)	222 [25]	0.28 [25]	2.15 [26]
SiO_2 (at 21°C)	64 [27]	0.2 [17]	0.6 [21]

Table 5.1: Parameters used in the calculation of thermal stresses using equation (5.1).

5.3.2 Stress Measurement Results

A value of 375 ± 40 MPa at room temperature was obtained for the film stress of Si-rich SiN using equation (5.2). A thermal stress value of -63 MPa at room temperature was then calculated using equation (5.4) which gave an intrinsic stress of 438 MPa, in line with previously recorded values at the Scottish Microelectronic Centre. Next the thermal stress component was calculated to be -33 MPa for the Si-rich SiN at 500°C, giving a total stress at of 405 MPa at 500°C. This result suggests the majority of the stress in the microelectrode layers is intrinsic, tensile stress. It also identifies that the thermal stress component is relatively small and compressive, which results in a slight relief of the tensile, intrinsic stress of the Si-rich SiN.

5.3.3 Additional Sources of Stress in the Benchmark Microelectrode

It was noted that the top insulator of the BM only delaminated during electrochemical cycling in the LKE, suggesting that this process introduces an additional source of stress. The small size of the Li^+ ion means that they are able to intercalate into a number of

materials including ceramics [28, 29]. Intercalation of Li^+ into Si is well investigated area of battery technology and known to cause swelling of the layers, resulting in increased stress as the Li^+ displaces atoms in the solid lattice [13, 30, 31]. It is particularly relevant that S. Ovshinsky filed a patent in 1996 for a solid state Li ion battery which used SiN as a ion-conductive medium between two electrodes which means SiN must be permeable to the Li^+ [32]. However there have not been further publications on this topic by the patent's author, which calls into question how ion-permeable the SiN layer actually turned out to be.

5.4 Reducing Stress in Thin Films

5.4.1 Stress Relief Layer

An effective stress relief strategy is to include a thin film of opposite stress in the device architecture which will result in a reduced net stress [33]. Since it has been shown that the stress in Si-rich SiN is tensile, including a thin film with compressive stress will mitigate this stress. Thermally SiO_2 (grown silicon dioxide) is a commonly used insulation layer in microelectronics and typically has compressive stress [23, 34]. Replacing the Si-rich SiN underlying insulator with an SiO_2 film will not only remove a source of tensile stress, but the compressive stress will relieve some of the remaining tensile stress in the structure.

In order to determine if SiO_2 was an appropriate stress relief layer, the stress in SiO_2 thin films was quantified. The same method outlined in section 5.3 was used to measure stress in thermally grown SiO_2 films. The SiO_2 was grown using thermal oxidation where wafers were loaded into a furnace at 600°C and ramped up to 1100°C. Water vapour was then introduced and reacted with the surface of the wafer, growing SiO_2.

5.4.2 Stress Relief Quantification

The stress at room temperature was measured and a value of -272 ± 34 MPa was found, which is in line with literature values [9]. In order to determine the intrinsic stress in the SiO_2 film, the thermally generated stress component at room temperature was again calculated and subtracted. Using equation (5.1) and values from table 5.1, the stress associated with the thermal mismatch between Si and SiO_2 was calculated to be -155 MPa. This gives an intrinsic stress component of -117 ± 34 MPa which again is in line with literature values [35]. The thermal stress component at 500°C was then calculated to be -173 ± 34 MPa, giving a total stress including the intrinsic component at 500°C

of -290 ± 34 MPa. This confirms the net stress in the SiO_2 layer is compressive and will hence reduce the tensile stress of the Si-rich SiN film. It is interesting to note that operating both Si-rich SiN and SiO_2 layers at the elevated temperatures in the LKE seems to produce only a minor increase in the stress of the films (an increase of around 6% for SiO_2 and 8% for Si-rich SiN). This would suggest the thermal stress itself is not major barrier in device operation.

5.4.3 Stress Relief Performance in LKE

Since the compressive stress behaviour of the SiO_2 has been confirmed, SiO_2 was selected to be trialled as a stress-relief layer. A set of microelectrodes were fabricated with a 500 nm SiO_2 underlying insulator, grown as described in section 5.4.1, in place of the Si-rich SiN underlying insulation layer. The 500 nm was chosen to match the thickness of the previous Si-rich SiN underlying insulator, in order to minimise changes to the microelectrode architecture. Figure 5.2 shows CVs obtained using these microelectrodes. These microelectrodes were characterised using the Ag plating and stripping as in chapter 4 and the results were compared with the ideal microelectrode response also described in chapter 4.

Table 5.2 shows the predicted limiting currents for each CV presented in figure 5.2, calculated using equation (3.3). None of the recorded CVs in figure 5.2 demonstrate a

Microelectrode	Theoretical i_L (nA)
5.2 (a)	507
5.2 (b)	13
5.2 (c)	256
5.2 (d)	43

Table 5.2: Predicted limiting currents for CVs in figure 5.2, calculated using equation (3.3).

limiting current and the currents recorded are between 4 - 118 times larger than predicted. The CV shown in figure 5.2 (c) does appear to show a resemblance to a limiting current, however no limiting value is reached and a macroelectrode-like plating peak is present at around -0.52 V indicating this sensor is not functioning as a microelectrode. Despite the lack of microelectrode behaviour demonstrated by the microelectrode architecture with the SiO_2 underlying insulation layer, no instances of delamination were observed after removal from the LKE. Figure 5.3 shows a microelectrode with 500 nm SiO_2 underlying insulator after cycling in LKE. No indication of delamination can be

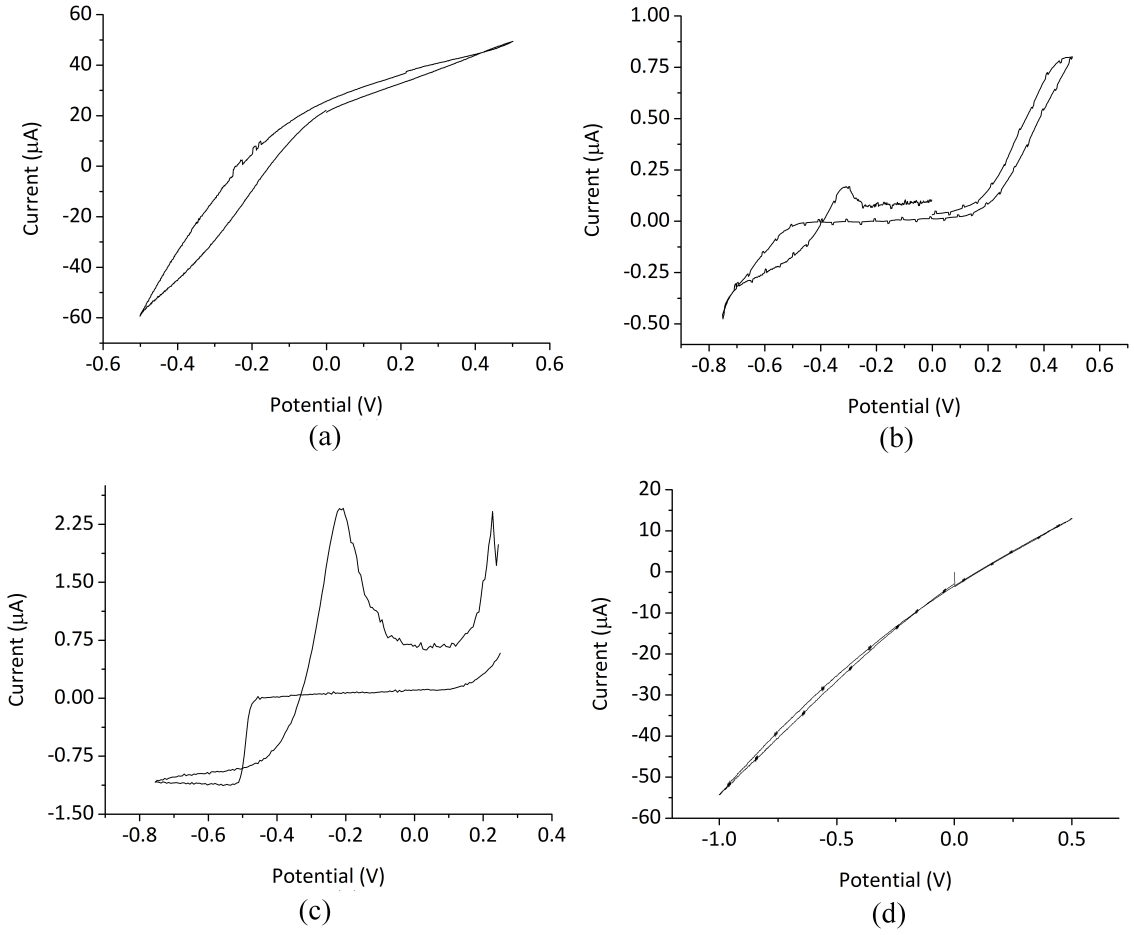

Figure 5.2: CVs recorded on microelectrodes fabricated with a 500 nm SiO_2 underlying insulator in LKE at 500°C at 200mV/s with: (a) a 100 μm edge length with 9.16 mM of AgCl, (b) a 10 μm edge length with 2.17 mM of AgCl, (c) another 100 μm edge length with 4.63 mM of AgCl, and (d) a 20 μm edge length with 3.89 mM of AgCl.

seen, suggesting that the stress relief layer has successfully reduced the total stress in the layer stack.

However, deposits of Ag can still be seen on the surface of the top insulator which, coupled with the larger than expected currents observed in the recorded CVs, indicates the top insulation layer of Si-rich SiN is still permeable. This suggests this permeability is not related to the stress in the microelectrode architecture, but a fundamental property of Si-rich SiN.

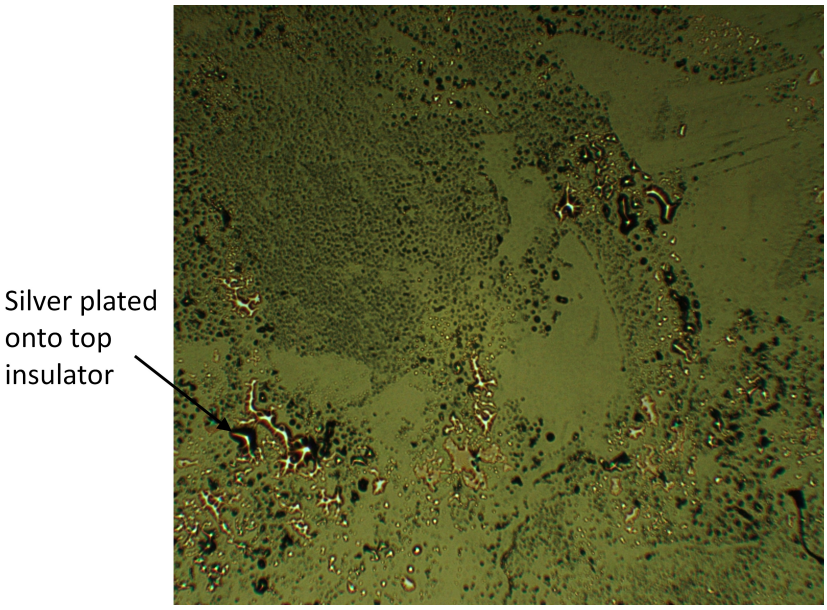

Figure 5.3: Surface of a microelectrode with SiO_2 underlying layer after cycling in LKE with 18 mM of AgCl between -0.5 V and +0.5 V at 500°C at 200 mV/s for 12 minutes.

5.5 Electrode Metal and Adhesion Layer Loss

5.5.1 Titanium Electrodissolution

The instances of electrode metal loss described in chapter 4 continued to be observed after the introduction of the SiO_2 underlying insulator. To determine whether this effect was chemical, electrochemical or mechanical, a test structure comprising a 200 nm W film on a 20 nm Ti adhesion layer on 500 nm Si-rich SiN insulation layer (without top insulator) was fabricated for cycling in the salt. The metal was patterned to the same area as the benchmark microelectrodes and is shown in figure 5.4 (a) and a cross section of the test structure in figure 5.4 (b).

The test structure was then subject to cyclic voltammetry in LKE with 20 mM AgCl. Figure 5.5 shows the first and fifteenth CV recorded using the test structure. Plating and stripping of Ag can be observed at -0.25 V and +0.15 V respectively, as expected. A second peak is also visible as a falling inflection around +0.2 V, which means a second electrochemical oxidation process is occurring. By scan 15, however, the current had significantly reduced and no appreciable electrochemical features were present. Upon removal, the test structure was seen to be missing metal up to the meniscus of the salt line, as shown in figure 5.6.

The second peak in the CV in figure 5.5 and the metal missing upon removal in

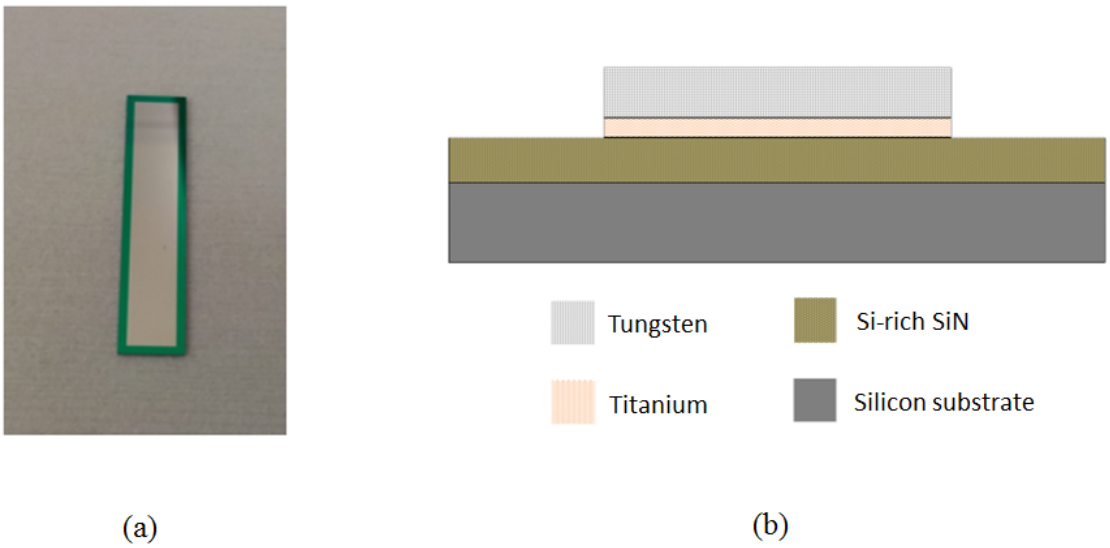

Figure 5.4: (a) Electrode metal test structure and (b) test structure cross section showing layers.

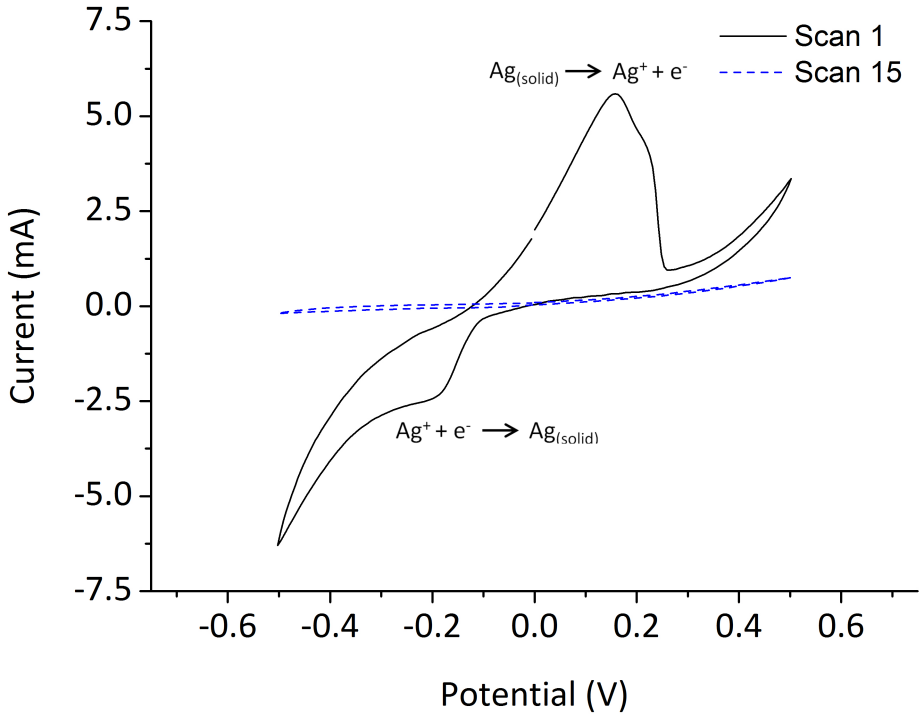

Figure 5.5: Scans 1 and 15 of the metal test structure, shown in figure 5.4, in LKE with 20 mM AgCl at 200 mV/s.

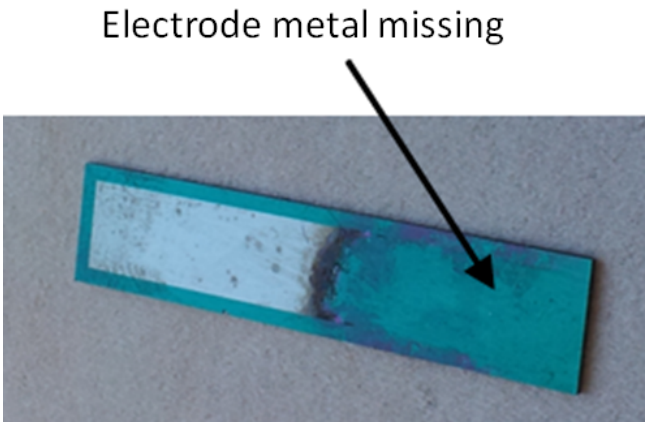

Figure 5.6: The metal test structure after cycling.

figure 5.6 demonstrates that at least one of the metal layers is not electrochemically inert in LKE and is being stripped off. Given W is electrochemically inert under these conditions, this layer is most likely the Ti [36–38]. From the decrease in current it can be seen there is a loss of electrode area over time. This further confirms the Ti adhesion layer is being removed, as once this has happened it cannot replate onto the same area since the now exposed Si-rich SiN is not a conductor. This results in a reduction of electroactive area over time. However, in the case of the benchmark microelectrode architecture the adhesion layer is theoretically not exposed to the salt. This means that the salt is, in some cases, coming into contact with the adhesion layer and the sporadic nature of this effect is likely due to random pinholes or defects in the W layer.

5.5.2 Titanium Nitride Adhesion Layer

Given the Ti has been shown to electrodissolve in LKE, it is obviously not a robust adhesion layer if pinholes are present in the electrode metal. TiN (titanium nitride) has been used as a corrosion barrier in many applications and nitrides are generally thought to have good corrosion resistance [39, 40]. A set of test strips similar to the ones in figure 5.4 (a) were fabricated, but with an adhesion layer of TiN in place of the Ti. The 20 nm of TiN was deposited by sputtering Ti in an atmosphere of N_2 using an Oxford Plasma Technology Plasmalab System 400 sputterer. These microelectrodes were electrochemically cycled in LKE under the same conditions as the microelectrodes in figure 5.5 and the results are shown figure 5.7.

The same Ag plating and stripping features can be observed, however no second oxidation peak is visible. The electrochemical response has not changed over the same period of time as the microelectrodes in figure 5.5, meaning the electrode metal layer has

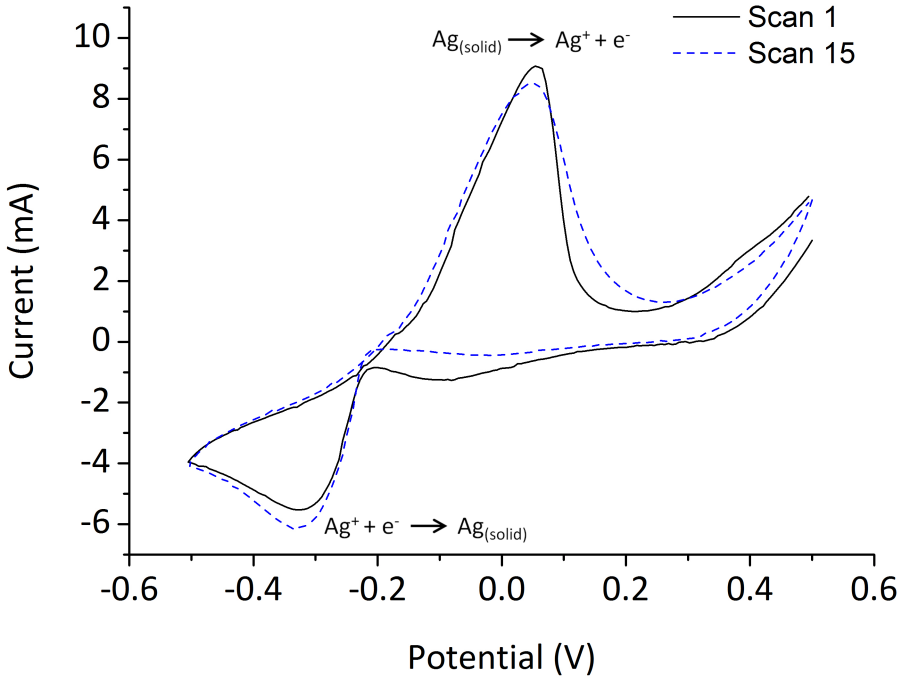

Figure 5.7: CVs 1 and 15 of Ag plating and stripping on the TiN metal test structure in LKE with 20 mM AgCl at 200 mV/s

not been removed. Figure 5.8 shows that when the structure was removed and inspected, no loss of electrode metal could be seen. TiN was hence adopted as the new adhesion layer.

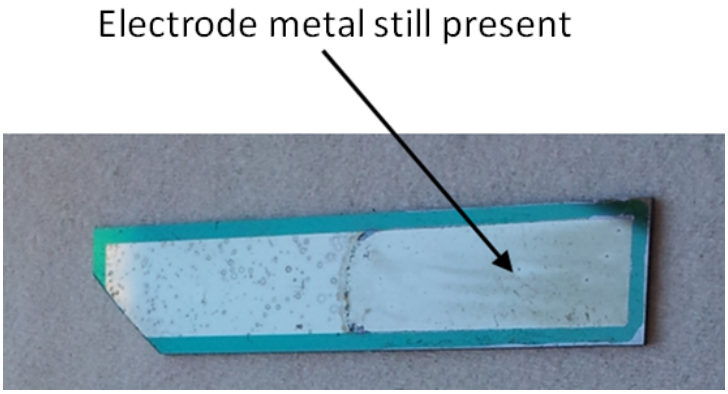

Figure 5.8: The TiN test structure after cycling in LKE

5.6 Top Insulator Permeability

5.6.1 Stoichiometric Silicon Nitride Top Insulator

It was observed that additional current is present in CVs performed using microelectrodes with a Si-rich SiN top insulation layer. It was possible that this was due to the Si-rich SiN failing to insulate effectively from the LKE. It was expected that stoichiometric silicon nitride (Si_3N_4) would provide a better barrier to LKE than Si-rich SiN. This is because (a) Si-N bonds are more covalent in character than Si-Si bonds, making them more resistant to chemical attack, and (b) the material is denser than other Si_xN_y ratios [41].

5.6.2 Fabrication of Microelectrodes with a Si_3N_4 Top Insulator

In order to assess Si_3N_4 as a top insulator, a set of microelectrodes were fabricated with a layer of 500 nm thick LPCVD Si_3N_4. This deposition process was the same as that outlined in chapter 4, other than the gas ratio used was 2:1 NH_3 to SiH_2Cl_2. To prevent the delaminations and metal loss from interfering with the microelectrode characterisation, the previous improvements (SiO_2 underlying layer and TiN adhesion layer) were included in this microelectrode design.

5.6.3 Si_3N_4 Top Insulator Performance in LKE

Figure 5.9 shows CVs of Ag plating and stripping recorded on microelectrodes, whose architecture incorporates the SiO_2 underlying layer, TiN adhesion layer, and Si_3N_4 top insulator. Figure 5.9 (d) also contained 32 mM of $SmCl_3$ (samarium trichloride) to test a solution reaction and two redox processes on one microelectrode. The Sm redox reaction proceeds as:

$$Sm^{+3} + e^- \leftrightarrow Sm^{+2} \tag{5.7}$$

It can be seen that the responses shown in figure 5.9 display currents in the nanoampere range and show the characteristic limiting current and sharp stripping peak typical of a microelectrode, which compare well with the ideal microelectrode response in figure 4.11. Table 5.3 presents the predicted limiting current values calculated using equation (3.3) compared against limiting current values extracted from the CVs in figure 5.9. It was noted that once established, there was still a slight variation in the limiting current. Hence an average value of limiting current was used in table 5.3.

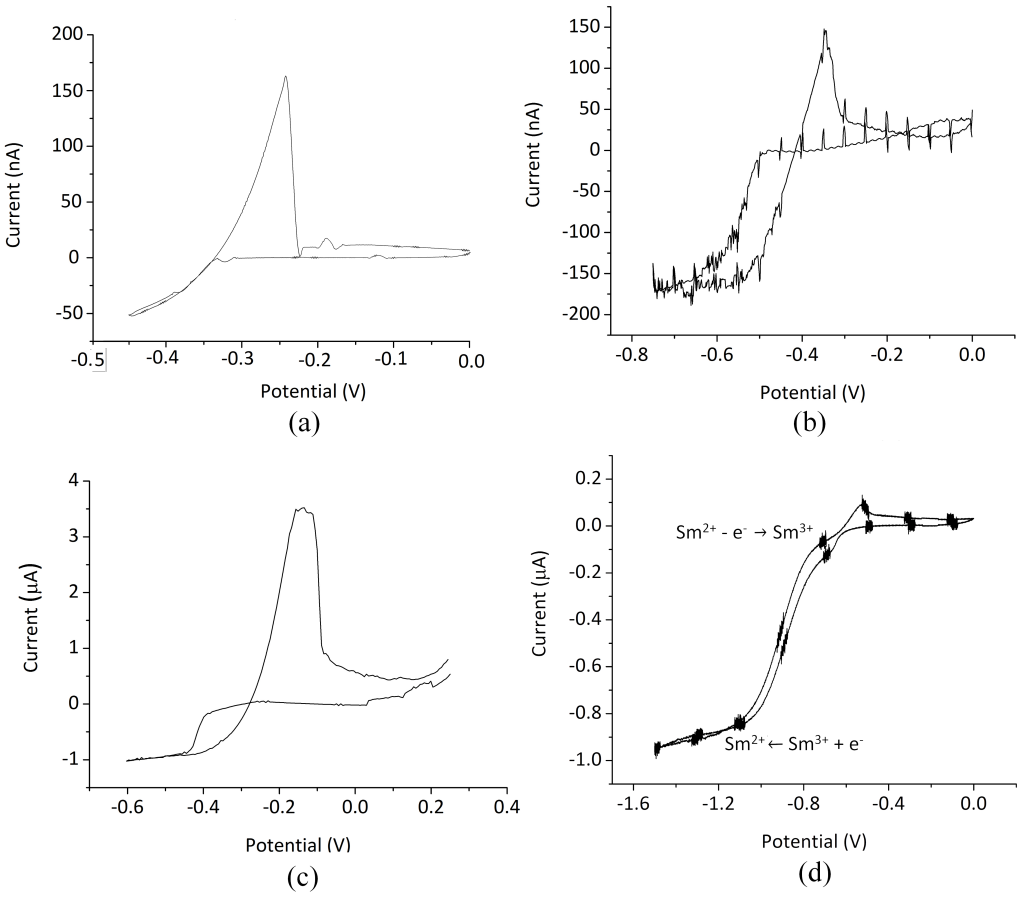

Figure 5.9: CVs of microelectrodes fabricated with a Si_3N_4 top insulator in LKE at 500°C: (a) a 20 μm edge length microelectrode scanned at 200 mV/s with 4.7 mM of AgCl, (b) a 30 μm edge length microelectrode scanned at 200 mV/s with 4.04 mM of AgCl, (c) a 100 μm edge length microelectrode scanned at 200 mV/s with 17.6 mM of AgCl, and (d) a 10 μm edge length microelectrode scanned at 100 mV/s with 32.6 mM of AgCl, with the addition of 32 mM $SmCl_3$.

Figure	Theoretical i_L (nA)	Average Measured i_L (nA)
5.9 (a)	52	52 ± 5
5.9 (b)	67	72 ± 3
5.9 (c)	973	965 ± 106
5.9 (d - Ag)	126	113 ± 6
5.9 (d - Sm)	737	762 ± 20

Table 5.3: Predicted limiting currents for the CVs in figure 5.9, calculated using equation (3.3), compared with the measured values.

It should be noted that an additional background resistance was encountered in many of the CVs, most likely attributable to the connection or the presence of an oxide layer

on the surface of the electrode. Therefore background subtraction was performed on the CVs in order to get an accurate value of the limiting current for quantitation. The measured limiting currents are close to the predicted values, which demonstrates that the Si_3N_4 top insulator is functioning successfully and resulting in quantifiable data. This reinforces the idea that Si-rich SiN was permeable to the LKE and that the Si_3N_4 has enhanced resistance to chemical attack. Possible reasons for the differences between measurement and theory are:

1. Literature values of diffusion coefficient at 450°C were used, while the experiment was carried out at 500°C;
2. The volatility of the Samarium Chloride added uncertainty to the final concentration;
3. Fundamentals of molten salt electrochemistry are not as well understood as aqueous electrochemistry; with possible complications due localised changes in analyte concentration, which would cause corresponding changes in properties such as salt viscosity, and diffusion coefficient [42].

Figure 5.10 shows a microelectrode with a Si_3N_4 top insulator after cycling for half an hour in LKE. No degradation of the layers, as seen in figure 4.15, or plated Ag on the surface of the insulator, as seen in figure 5.3 was observed. Although instances of damage to the top insulator around the electrode metal still occurred.

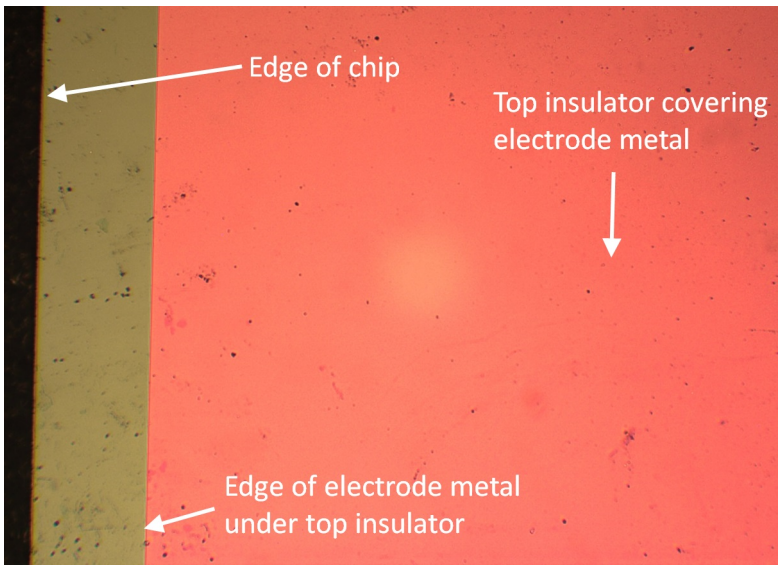

Figure 5.10: Microelectrode with Si_3N_4 top insulator after cycling in LKE with 4.5 mM of AgCl at 500°C for 30 minutes.

5.6.4 Quantifying Stress in the Si_3N_4 Top Insulator

Si_3N_4 has a much larger intrinsic tensile stress than Si-rich SiN. A 500 nm thick Si_3N_4 deposited on a blank Si wafer using the method outlined in section 4.6.2 and the stress was measured using the same method outlined in section 5.3.1. This room temperature measurement gave a value of 950 ± 24 MPa for the total stress, in agreement with literature values [34, 43]. The thermal stress component at room temperature was calculated using equation (5.4) as -83 MPa and subtracted from the stress value measured at room temperature using equation (5.1), giving 1033 ± 24 MPa as the total intrinsic stress. The thermal stress at 500°C was then calculated using equation (5.4) to be -48 MPa which, using equation (5.1), gives the total stress in the film at 500°C as 985 ± 24 MPa. The tensile stress in the Si_3N_4 top insulator is therefore around 2.4 times greater than that of the Si-rich SiN top insulator. Despite this increased tensile stress; the 500 nm SiO_2 continued to provide sufficient stress relief as no delamination of the top insulator was observed. Unfortunately, even though these microelectrodes demonstrating the desired electrochemical response, the percentage that functioned was determined to be only around 46%. The yield and lifetime of these microelectrodes are further investigated and improved in chapters 6 and 7.

5.7 Localised Top Insulator Damage

5.7.1 Electrode Metal Edge Spikes

During electrochemical cycling of the microelectrodes characterised in section 5.6, it was observed that a minority of microelectrodes still suffered damage to the top insulator around the perimeter of the metal pattern as discussed in chapter 4. This was despite the stress relief provided by the underlying insulator. It was suspected that the step at the edge of the electrode metal pattern was presenting a focal point for stress, therefore the step from the underlying insulator to the electrode metal film was profiled using a Dektak Veeco 8000 surface profiler. The profile is shown in figure 5.11 and a large spike of around 1.5 μm in height can be seen at the edge of the electrode metal, which will likely act as a source of weakness in the top insulator. This therefore may be the cause of the identified top insulator damage. The source of this effect was hypothesised to be related to the lift-off process used to pattern the metal and figure 5.12 demonstrates how this could arise. Figure 5.12 (a) shows a schematic of the ideal lift-off process and figure 5.12 (b) shows the lift-off process leaving behind spikes around the perimeter of the metal.

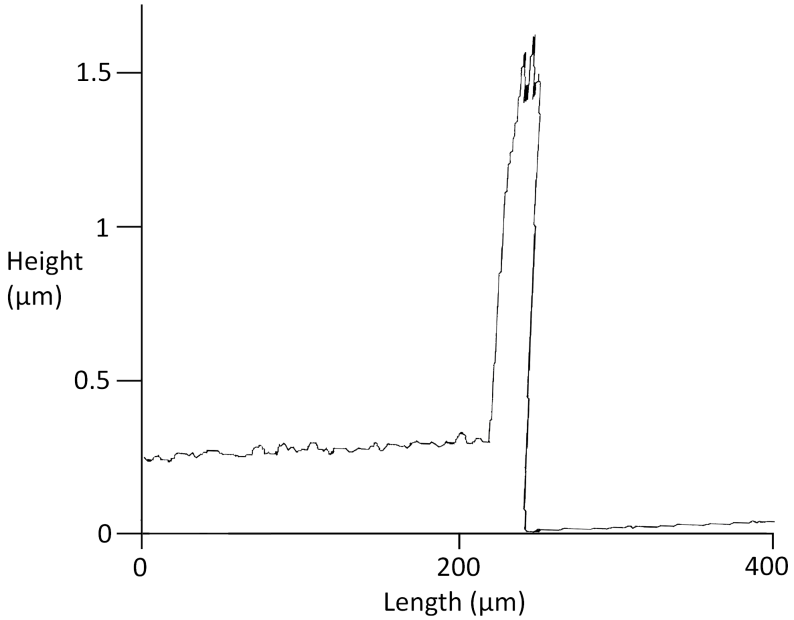

Figure 5.11: Profile of the electrode metal step on a microelectrode.

5.7.2 New Fabrication Process

In order to prevent the formation of edge spikes, a pattern and etch process was adopted. However, a W etch had not yet been developed and so an alternative electrode metal was investigated. Pt was selected because, as discussed in chapter 4, it has previously been used as an electrode in LKE and was compatible with the proposed fabrication processes [44–48]. First, the Pt is deposited using electron beam evaporation using an ANS Cluster Tool system, as in figure 5.13 (a). A 50 nm thick layer was chosen to be consistent with previous Pt microelectrodes fabricated in the group and cost considerations [49]. A 1.5 μm thick layer of SPR 350 - 3.5 was then spin coated onto the wafer and soft baked for 60 seconds at 90°C, shown in figure 5.13 (b). Figure 5.13 (c) shows the resist was then exposed to ultraviolet light through a darkfield photomask and developed in MF26A developer solution for 60 seconds, leaving behind photoresist masking the areas that will become the electrode metal, as in figure 5.13 (d). The exposed Pt electrode metal was then etched using an argon milling process in a JLS reactive ion etcher for nine minutes, shown in figure 5.13 (e). The exposed TiN adhesion layer was then etched in H_2O_2 at 70°C and the resist was then stripped in ACT resist stripper at 50°C for 15 minutes, leaving the defined electrode metal pattern as in figure 5.13 (f). Several sets of Pt microelectrodes with Si_3N_4 top insulator, SiO_2 underlying insulator, and TiN adhesion layer were fabricated and characterised in the LKE. A W etch was later developed and

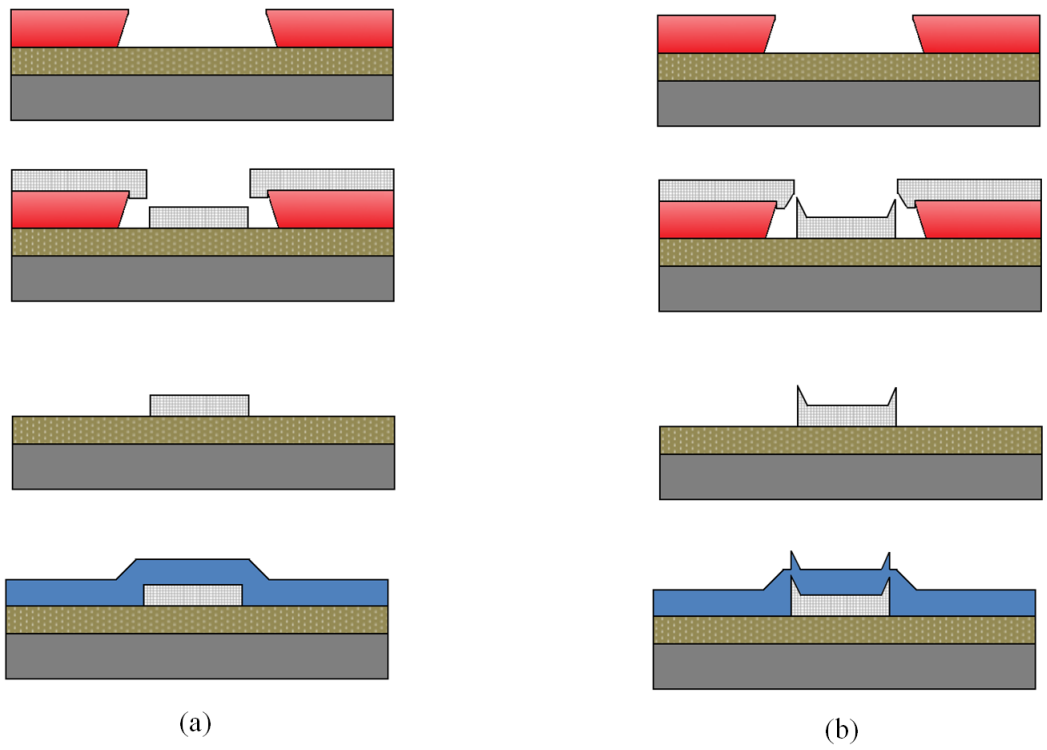

Figure 5.12: (a) Schematic of the ideal lift-off process used to pattern the electrode metal and (b) what may be happening in reality.

consisted of the same CF_4 - Ar reactive ion etch used to etch the Si_3N_4 top insulator for 20 minutes, etching W at a rate of 9.9 ± 12 nm/minute.

5.7.3 Platinum Electrode Performance in LKE

The Pt electrode metal were characterised in LKE at 500°C with AgCl redox couple, as discussed previously. Figure 5.14 shows CVs from four microelectrodes and it can be observed that they all exhibit a typical microelectrode response; with a limiting current, sharp stripping peak, current in the nanoampere range, and Ag plating and stripping potentials are within -0.5 V to +0.5 V as expected. The theoretical and the measured limiting currents are compared in table 5.4. As in section 5, the limiting current values in the CVs varied due to factors such as slight electrical noise. As such an average value is presented.

All measured values of limiting current are in good agreement with the predicted values and the average measured values deviate from the predicted values by at most 6%. This demonstrates the optimised microelectrodes with a Pt electrode metal are providing

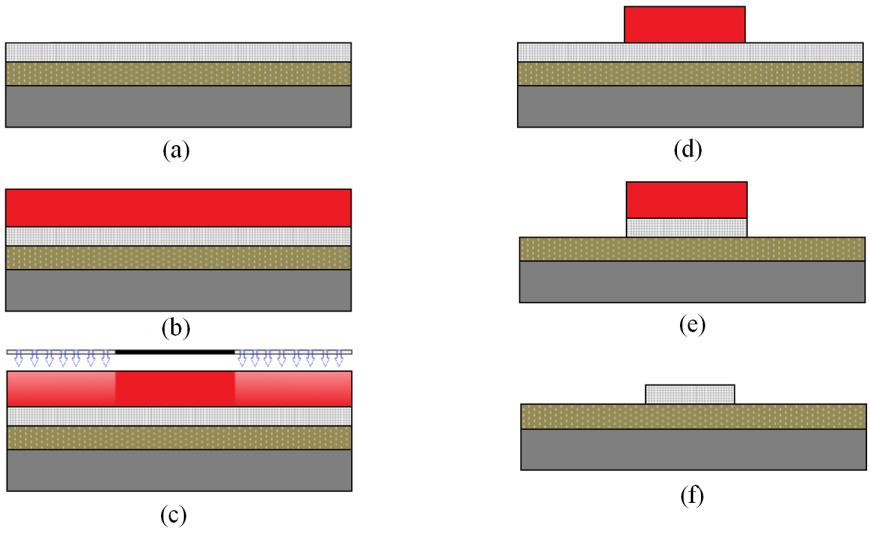

Figure 5.13: Schematic of the pattern and etch process used to define the electrode metal, where (a) the electrode metal is deposited, (b) a layer of photoresist is spin coated on, (c) and (d) the resist is exposed and developed, (e) the exposed electrode metal and adhesion layer is etched and finally (f) the resist is removed.

Figure	Theoretical i_L (nA)	Average measured i_L (nA)
5.14 (a)	105	99 ± 23
5.14 (b)	147	154 ± 32
5.14 (c)	138	141 ± 21
5.14 (d)	93	88 ± 7

Table 5.4: Predicted limiting currents for the CVs in figure 5.14, calculated using equation (3.3), compared with the measured values.

quantitative data and hence functioning as microelectrodes in LKE. They are subject to the same sources of error as microelectrodes with W electrode metal as outlined in section 5.6. As discussed in chapter 3, one of the characteristics of microelectrodes is that the limiting current is independent of a wide range of scan rate. Figure 5.15 shows CVs of Ag plating and stripping at different scan rates. The CVs were recorded on the same microelectrode used to record the CV shown in figure 5.14 (d). The value of the limiting current remained the same across the four scan rates, further confirming that the microelectrodes are functioning as microelectrodes. By comparing the CVs in figure 5.9 and figure 5.14, the Pt microelectrode response can be seen to be more consistent in the shape of the limiting current and stripping peak than the W (excluding 5.9 (d), as there is a second redox couple present). This could be due to the chemistry of Pt in LKE,

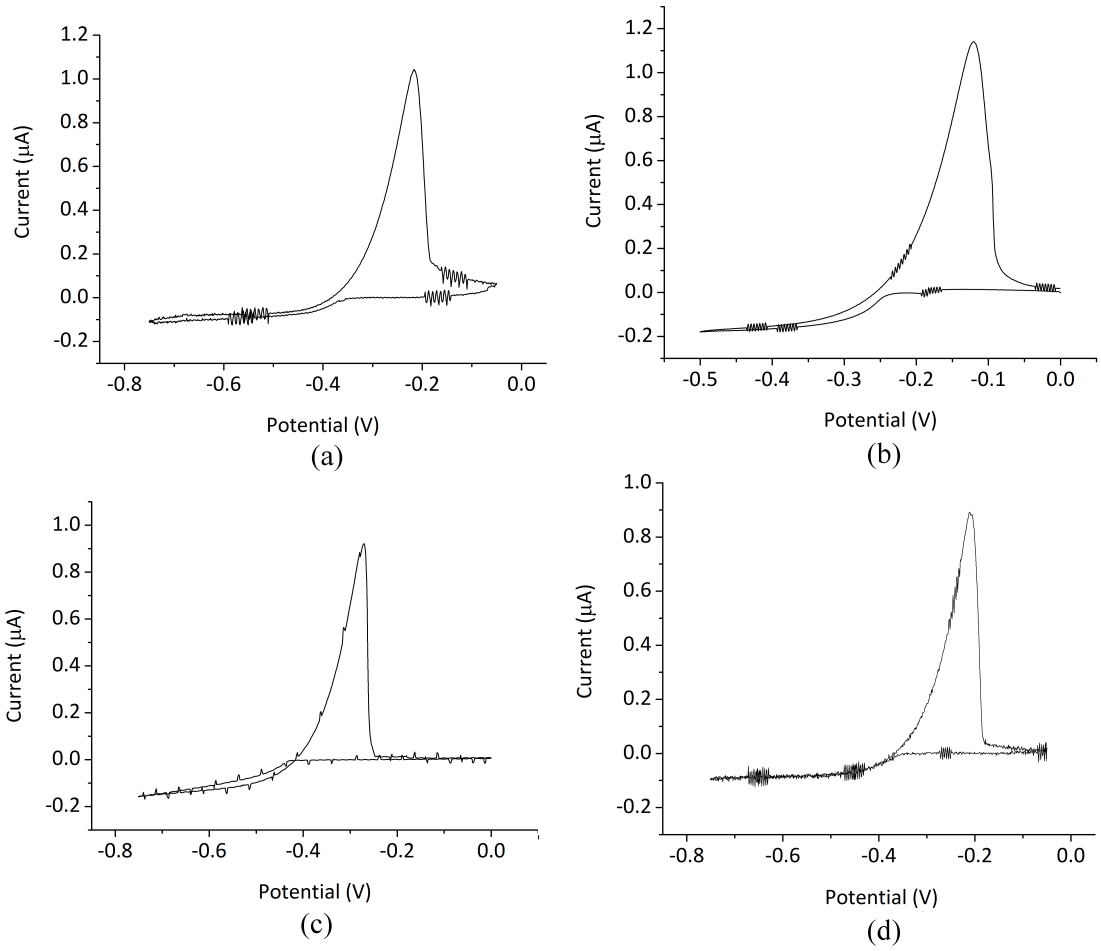

Figure 5.14: CVs of microelectrodes fabricated with Pt electrode metal in LKE at 500°C: (a) a 50 μm edge length microelectrode scanned at 400 mV/s with 3.8 mM of AgCl, (b) a 50 μm edge length microelectrode scanned at 200 mV/s with 5.3 mM of AgCl, (c) another 50 μm edge length microelectrode scanned at 200 mV/s with 5 mM of AgCl, and (d) a 30 μm edge length microelectrode scanned at 100 mV/s with 5.9 mM of AgCl.

as Pt has been shown to alloy with Li in LKE which demonstrates it does not behave as an inert electrode metal [50]. Despite this, there is little difference between them in terms of matching to theory and variation in limiting current; both electrode metals successfully yielding quantifiable electrochemistry. No further instances of damage to the top insulator around the electrode metal perimeter were observed.

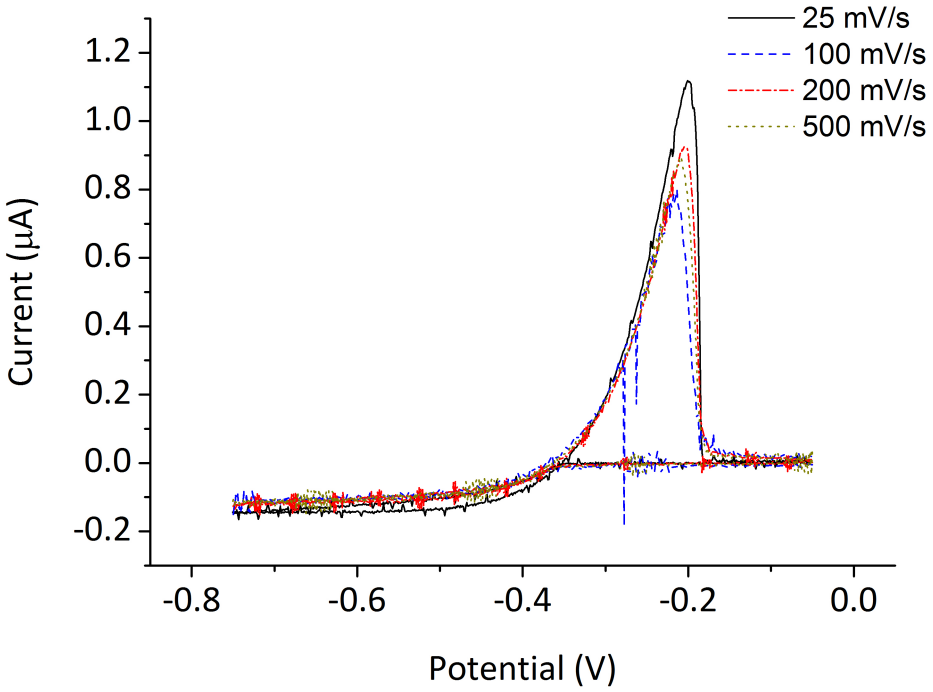

Figure 5.15: CVs at four different scan rates, recorded on a Pt microelectrode used to record figure 5.12 (d).

5.8 Summary

The four failure mechanisms highlighted by the characterisation of the BM in chapter 4, delamination of the top insulator, loss of electrode metal, and permeability of the top insulator, have been addressed. Using stress measurements together with further calculations, the delamination events were determined to be due to excessive intrinsic, tensile stress in the microelectrode layer stack. The inclusion of a compressive stress relief layer has lowered the net stress in the microelectrode and no further delamination events were observed. Table 5.5 lists the calculated stresses for the layers discussed in this chapter at 21°C and 500°C.

Layer	Total stress at 21°C (MPa)	Total stress at 500°C (MPa)
Si-rich SiN	375 ± 40	405 ± 40
SiO_2	-272 ± 34	-290 ± 34
Si_3N_4	950 ± 24	985 ± 24

Table 5.5: Stress measured for each insulation layer at 21°C and 500°C.

The loss of electrode metal was due as the electrodissolution of the Ti adhesion

layer. This adhesion layer was then replaced by a more chemically inert TiN layer, and no further metal losses were observed

The Si-rich SiN top insulator was determined to be permeable by the LKE and was replaced by the more chemically inert Si_3N_4 layer. This layer has shown satisfactory insulation and has resulted in quantifiable data which demonstrates the sensor is functioning as a microelectrode in the LKE environment.

Damage to the top insulator around the electrode metal perimeter was identified and could be linked to spikes in the electrode metal identified around the perimeter. An etching process was therefore adopted, but was not compatible with the W electrode metal and so microelectrodes so Pt was used instead. Pt microelectrodes, patterned using reactive ion etching, were characterised in LKE and also yielded the expected electrochemical response with measurement which matches theory. This production of functioning, reproducible and highly controllable microelectrode sensors for molten salt is major step forward, which has allowed the investigation of previously unexplored fundamental properties of LKE [42]. The sum of these improvements has resulted in a new microelectrode architecture and is termed the version two microelectrode (V2M).

References

[1] J. Hutchinson, *Stresses and failure modes in thin films and multilayers.* Techincal University of Denmark, 1996.

[2] K. J. A. J. McGinnis, T. R. Watkins, "Residual stresses in a multilayer system of coatings," *Joint Committee on Powder Diffraction Standards*, 1999.

[3] S. Franssila, *Thin-Film Materials and Processes.* John Wiley & Sons, Ltd, 2010, pp. 47–67. [Online]. Available: http://dx.doi.org/10.1002/9781119990413.ch5

[4] M. G.-Hak, *The MEMS handbook.* CRC Press, 2001. [Online]. Available: http://www.amazon.co.uk/The-MEMS-Handbook-Second-Edition/dp/0849321069

[5] M. Ohring, *Materials Science of Thin Films.* Elsevier Store, 2001. [Online]. Available: http://store.elsevier.com/Materials-Science-of-Thin-Films/Milton-Ohring/isbn-9780125249751/

[6] S. Senturia, *Microsystem design.* Springer, 2007. [Online]. Available: http://www.amazon.co.uk/Microsystem-Design-Stephen-D-Senturia/dp/0792372468

[7] S. S. L. B. Freund, *Thin Film Materials: Stress, Defect Formation and Surface Evolution.* Cambridge University Press, 2008.

[8] H. Windischmann, "Intrinsic stress in sputter-deposited thin films," *Critical Reviews in Solid State and Materials Sciences*, vol. 17, no. 6, pp. 547–596, 1992. [Online]. Available: http://dx.doi.org/10.1080/10408439208244586

[9] J. Laconte, D. Flandre, and J.-P. Raskin, *Micromachined Thin-Film Sensors for SOI-CMOS Co-Integration*, J. Laconte, D. Flandre, and J.-P. Raskin, Eds. Springer, 2006, vol. 13. [Online]. Available: http://www.springer.com/engineering/book/978-0-387-28842-0

[10] G. Janssen, M. Abdalla, V. F. Keulen, and B. Pujada, "Celebrating the 100th anniversary of the Stoney equation for film stress: Developments from polycrystalline steel strips to single crystal silicon wafers," *Thin*, vol. 517, no. 6, pp. 1858–1867, January 2009. [Online]. Available: http://www.sciencedirect.com/science/article/pii/S0040609008007669

[11] X. Feng, Y. Huang, and A. Rosakis, "On the Stoney formula for a thin film/substrate system with nonuniform substrate thickness," *The American Society of Mechanical Engineers*, vol. 74, no. 6, pp. 1276–1281, 2007.

[12] G. G. Stoney, "The Tension of Metallic Films Deposited by Electrolysis," *Proceedings of the Royal Society of London A: Mathematical, Physical and Engineering Sciences*, vol. 82, no. 553, pp. 172–175, 1909. [Online]. Available: http://rspa.royalsocietypublishing.org/content/82/553/172

[13] J. Floro and E. Chason, *In Situ Real-Time Characterization of Thin Films*, O. A. R. Krauss, Ed. Wiley and Sons, 2001.

[14] M. Hopcroft, W. Nix, and T. Kenny, "What is the Young's Modulus of Silicon?" *Microelectromechanical Systems, Journal of*, vol. 19, no. 2, pp. 229–238, April 2010.

[15] M. F. Doerner and W. D. Nix, "Stresses and deformation processes in thin films on substrates," *Critical Reviews in Solid State and Materials Sciences*, vol. 14, no. 3, pp. 225–268, 1988. [Online]. Available: http://dx.doi.org/10.1080/10408438808243734

[16] M. Sakata, K. Kimura, and A. Mizunuma, "Measurement of Elastic Moduli from the Impact Sound of Engineering Ceramics and Composites at Elevated Temperatures," *Journal of the American Ceramic Society*, vol. 78, no. 11, pp. 3040–3044, 1995. [Online]. Available: http://dx.doi.org/10.1111/j.1151-2916.1995.tb09080.x

[17] G. Greaves, A. Greer, R. Lakes, and T. Rouxel, "Poisson's ratio and modern materials," *Nature M*, vol. 10, 2011.

[18] D. Faoite, D. J. Browne, and K. T. Stanton, "Regression analysis of temperature-dependent mechanical and thermal properties of dielectric technical ceramics," *Journal of Materials Science*, vol. 48, no. 1, pp. 451–461, 2012. [Online]. Available: http://dx.doi.org/10.1007/s10853-012-6759-6

[19] T. Kusunose, R.-J. Sung, T. Sekino, S. Sakaguchi, and K. Niihara, "High-temperature properties of a silicon nitride/boron nitride nanocomposite," *Journal of Materials Research*, vol. 19, pp. 1432–1438, 2004. [Online]. Available: http://journals.cambridge.org/article_S0884291400088701

[20] Y. Okada and Y. Tokumaru, "Precise determination of lattice parameter and thermal expansion coefficient of silicon between 300 and 1500 K," *Journal of Applied Physics*, vol. 56, no. 314, January 1984. [Online]. Available: http://dx.doi.org/10.1063/1.333965

[21] A. K. Sinha, H. J. Levinstein, and T. E. Smith, "Thermal stresses and cracking resistance of dielectric films (SiN, Si_3N_4, and SiO_2) on Si substrates," *Journal of Applied Physics*, vol. 49, no. 4, pp. 2423–2426, 1978. [Online]. Available: http://scitation.aip.org/content/aip/journal/jap/49/4/10.1063/1.325084

[22] L. Bin, W. Jing-Yang, Z. Yan-Chun, and L. Fang-Zhi, "Temperature Dependence of Elastic Properties for Amorphous SiO_2 by Molecular Dynamics Simulation," *Chinese Physics Letters*, vol. 25, no. 8, p. 2747, 2008. [Online]. Available: http://stacks.iop.org/0256-307X/25/i=8/a=004

[23] H. Tada, "Novel Microelectromechanical Systems (MEMS) for the Study of Thin Film Properties and Measurement of Temperatures During Thermal Processing," Master's thesis, Tufts University, 1999. [Online]. Available: http://emerald.tufts.edu/as/tampl/projects/mems/collab/thesis/

[24] J. J. Wortman and R. A. Evans, "Young's Modulus, Shear Modulus, and Poisson's Ratio in Silicon and Germanium," *Journal of Applied Physics*, vol. 36, no. 153, June 1965. [Online]. Available: http://dx.doi.org/10.1063/1.1713863

[25] J. Vlassak and W. Nix, "A new bulge test technique for the determination of Young's modulus and Poisson's ratio of thin films," *Journal of Materials Research*, vol. 7, pp. 3242–3249, 1992. [Online]. Available: http://journals.cambridge.org/article_S0884291400019099

[26] A. Kaushik, H. Kahn, and A. Heuer, "Wafer-level mechanical characterization of silicon nitride MEMS," *Microelectromechanical Systems, Journal of*, vol. 14, no. 2, pp. 359–367, April 2005.

[27] T. P. Weihs, S. Hong, J. C. Bravman, and W. D. Nix, "Mechanical deflection of cantilever microbeams: A new technique for testing the mechanical properties of thin films," *Journal of Materials Research*, vol. 3, pp. 931–942, 1988. [Online]. Available: http://journals.cambridge.org/article_S0884291400003319

[28] H. Wang, N. J. Siambun, L. Yu, and G. Z. Chen, "A Robust Alumina Membrane Reference Electrode for High Temperature Molten Salts," *Journal of The Electrochemical Society*, vol. 159, no. 9, pp. H740–H746, 2012.

[29] M. A. Py and R. R. Haering, "Structural destabilization induced by lithium intercalation in MoS_2 and related compounds," *Canadian Journal*

of Physics, vol. 61, no. 1, pp. 76–84, 1983. [Online]. Available: http://dx.doi.org/10.1139/p83-013

[30] J. Besenhard, J. Yang, and M. Winter, "Will advanced lithium-alloy anodes have a chance in lithium-ion batteries? ," *Journal of Power Sources*, vol. 68, no. 1, pp. 87 – 90, 1997. [Online]. Available: http://www.sciencedirect.com/science/article/pii/S0378775396025475

[31] S. Kalnaus, K. Rhodes, and C. Daniel, "A study of lithium ion intercalation induced fracture of silicon particles used as anode material in Li-ion battery," *Journal of Power Sources*, vol. 196, no. 19, pp. 8116 – 8124, 2011. [Online]. Available: http://www.sciencedirect.com/science/article/pii/S0378775311010421

[32] S. Ovshinsky, "Thin-film, solid state battery employing an electrically insulating, ion conducting electrolyte material," April 1996, uS Patent 5,512,387. [Online]. Available: https://www.google.com/patents/US5512387

[33] J. P. Uyemura, *CMOS Logic Circuit Design*, J. P. Uyemura, Ed. Kluwer Academic Publishers, 1999. [Online]. Available: http://books.google.co.uk/books/about/CMOS_Logic_Circuit_Design.html?id=xEYhxhs7fDgC&redir_esc=y

[34] O. Zohni, G. Buckner, T. Kim, A. Kingon, J. Maranchi, and R. Siergiej, "Investigating thin film stresses in stacked silicon dioxide/silicon nitride structures and quantifying their effects on frequency response," *Journal of Micromechanics and Microengineering*, vol. 17, no. 5, p. 1042, 2007. [Online]. Available: http://stacks.iop.org/0960-1317/17/i=5/a=026

[35] J. T. Fitch, C. H. Bjorkman, G. Lucovsky, F. H. Pollak, and X. Yin, "Intrinsic stress and stress gradients at the SiO_2/Si interface in structures prepared by thermal oxidation of Si and subjected to rapid thermal annealing," *Journal of Vacuum Science & Technology B*, vol. 7, no. 4, pp. 775–781, 1989. [Online]. Available: http://scitation.aip.org/content/avs/journal/jvstb/7/4/10.1116/1.584599

[36] Z.-Y. Qiao, S. Duan, and D. Inman, "Electrochemical reduction of praseodymium chloride in LiCl-KCl melt," *Journal of Applied Electrochemistry*, vol. 19, no. 6, pp. 937–939, 1989. [Online]. Available: http://dx.doi.org/10.1007/BF01007944

[37] Y. Castrillejo, M. R. Bermejo, A. I. Barrado, and R. Pardo, "Electrochemical behaviour of dysprosium in the eutectic LiCl - KCl at W and Al electrodes,"

Electrochimica Acta, vol. 50, no. 10, pp. 2047–2057, March 2005. [Online]. Available: http://www.sciencedirect.com/science/article/pii/S0013468604009454

[38] S. Ghosh, S. Vandarkuzhali, P. Venkatesh, G. Seenivasan, T. Subramanian, B. P. Reddy, and K. Nagarajan, "Electrochemical studies on the redox behaviour of zirconium in molten LiCl-KCl eutectic," *Journal of Electroanalytical Chemistry*, vol. 627, no. 1-2, pp. 15 – 27, 2009. [Online]. Available: http://www.sciencedirect.com/science/article/pii/S0022072808004944

[39] A. Zykova, V. Safonov, J. Walkowich, R. Rogowska, and S. Yakovin, "Corrosion properties of nitride, oxide and multilayer coatings on stainless steel and titanium-based substrates," *16th International Summer School on Vacuum, Electron, and Ion Technologies*, 2010.

[40] B. Subramanian, K. Ashok, K. Subramanian, D. Sastikumar, G. Selvan, and M. Jayachandran, "Evaluation of corrosion and wear resistance titanium nitride (TiN) coated on mild steel (MS) with brush plated nickel interlayer," *Surface Engineering*, vol. 25, no. 7, pp. 490–495, 2009. [Online]. Available: http://dx.doi.org/10.1179/026708408X330621

[41] B. K. Yen, R. L. White, R. J. Waltman, Q. Dai, D. C. Miller, A. J. Kellock, B. Marchon, P. H. Kasai, M. F. Toney, B. R. York, H. Deng, Q.-F. Xiao, and V. Raman, "Microstructure and properties of ultrathin amorphous silicon nitride protective coating," *Journal of Vacuum Science & Technology A*, vol. 21, no. 6, pp. 1895–1904, 2003. [Online]. Available: http://scitation.aip.org/content/avs/journal/jvsta/21/6/10.1116/1.1615974

[42] D. K. Corrigan, J. P. Elliott, E. O. Blair, S. J. Reeves, I. Schmueser, A. Walton, and A. R. Mount, "FDLSALT15 Advances in electroanalysis, sensing and monitoring in molten salts," *Faraday Discuss.*, pp. –, 2016. [Online]. Available: http://dx.doi.org/10.1039/C6FD00002A

[43] J. Laconte, F. Iker, S. Jorez, N. Andre, J. Proost, T. Pardoen, D. Flandre, and J.-P. Raskin, "Thin films stress extraction using micromachined structures and wafer curvature measurements," *Microelectronic Engineering*, vol. 76, no. 1-4, pp. 219 – 226, 2004, materials for Advanced Metallization 2004. [Online]. Available: http://www.sciencedirect.com/science/article/pii/S0167931704003612

[44] B. P. Reddy, S. Vandarkuzhali, T. Subramanian, and P. Venkatesh, "Electrochemical studies on the redox mechanism of uranium chloride in

molten LiCl-KCl eutectic," *Electrochimica Acta*, vol. 49, no. 15, pp. 2471 – 2478, 2004. [Online]. Available: http://www.sciencedirect.com/science/article/pii/S0013468604001240

[45] S.-M. Chen and C.-M. Chan, "Preparation, characterization, and electrocatalytic properties of copper hexacyanoferrate film and bilayer film modified electrodes," *Journal of Electroanalytical Chemistry*, vol. 543, no. 2, pp. 161 – 173, 2003. [Online]. Available: http://www.sciencedirect.com/science/article/pii/S0022072803000172

[46] K. Amezawa, Y. Ito, and Y. Tomii, "The Single-Electrode Peltier Heats of Li-Al Alloy Electrodes in LiCl-KCl Eutectic System," *Journal of The Electrochemical Society*, vol. 141, no. 11, pp. 3096–3103, 1994. [Online]. Available: http://jes.ecsdl.org/content/141/11/3096.abstract

[47] S. Furihata, K. Akashi, and S. Kurosawa, "The polarographic reduction wave of magnesium ion(II) in a molten LiCl-KCl eutectic mixture," *Electrochimica Acta*, vol. 26, no. 8, pp. 1107–1109, 1981. [Online]. Available: http://www.sciencedirect.com/science/article/pii/0013468681850852

[48] M. Iizuka, Y. Sakamura, and T. Inoue, "Electrochemical reduction of (U-40Pu-5Np)O_2 in molten LiCl electrolyte," *Journal of Nuclear Materials*, vol. 359, no. 1-2, pp. 102 – 113, 2006. [Online]. Available: http://www.sciencedirect.com/science/article/pii/S0022311506004430

[49] H. L. Woodvine, J. G. Terry, A. J. Walton, and A. R. Mount, "The development and characterisation of square microfabricated electrode systems," *Analyst*, vol. 135, pp. 1058–1065, 2010. [Online]. Available: http://dx.doi.org/10.1039/B924342A

[50] K. E. Johnson and J. R. Mackenzie, "Samarium, Europium, and Ytterbium Electrode Potentials in LiCl - LiCl Eutectic Melt," *Journal of The Electrochemical Society*, vol. 116, no. 12, pp. 1697–1703, 1969. [Online]. Available: http://jes.ecsdl.org/content/116/12/1697.abstract

Chapter 6

Characterisation and Optimisation of Microelectrode Yield

6.1 Introduction

It was observed that a high number of the version 2 microelectrode (V2M) sensors developed in chapter 4 and 5 did not function as intended. This presented a challenge since the identification of faulty microelectrodes before they were to be used in LKE was not possible, as the molten salt environment could not be simulated at wafer level. The following chapter presents the yield of the V2M and reports (a) how the layout of the microelectrode was modified to increase yield and (b) the identification of the underlying mechanisms causing the faulty microelectrodes.

6.2 Change of Operating Temperature

At this point in the project, the decision was made between the collaborating institutions to lower the LKE operating temperature from 500°C to 450°C, in order to reduce cost and energy usage in the final reprocessing system. All experiments in this and the following chapters were therefore conducted at 450°C unless otherwise stated.

6.3 Background to Microelectrode Yield

6.3.1 Yield Definition

In manufacturing, yield is typically used to define the ratio of units produced and the number that function correctly at the end of a manufacturing process. In the microelectronics industry, the units can be single devices or complete systems [1–5]. As such the yield of a microfabrication process is the percentage of functioning devices at the end of the process [2–4, 6, 7]. Devices typically fail due to the incorporation of defects in the device structure causing the device to completely fail (catastrophic yield loss) or to not function to the required specification (parametric yield loss) [2–4, 6, 8]. Whole wafers may be damaged through mishandling or malfunction of equipment, however this is much rarer.

Defects can be grouped into systematic or random occurrences. Systematic defects are defects which occur consistently in a process and the causes are easier to identify and fix [2–4]. Random defects are unpredictable and typically caused by particulate contamination [1–4, 6]. Defects that cause either catastrophic or parametric failure after a period of time under operational stress are called “latent defects” and reduce a device’s lifetime [3, 4, 6, 8]. These differ from devices with “fatal defects”, where the device never functions correctly.

Despite many V2Ms giving the desired quantitative response, it was observed that there was a high number of non-functioning microelectrodes. The priority was therefore to identify the causes and where possible fix them.

6.3.2 Measuring Yield

The only functional method of testing the microelectrodes is to characterise them in the molten salt. Therefore yield statistics were collected from all users of microelectrodes, after their experiments had been performed. The yield was determined by examining experimental data from each microelectrode used and determining if the sensor had ever performed as a microelectrode over the course of the experiment. If not, the microelectrode was counted as having fatal defect(s).

The disadvantage of this method is that experiments were not set up to specifically determine yield and noting down whether and how the microelectrode had failed was of a secondary concern for most users. This means that the influence of variables such as the redox couple, concentration, and edge length of the microelectrode were not controlled and since these details were not always recorded, this added uncertainty to the data. The potential applied to the microelectrodes could be extracted from the raw data and so this variable could be assessed against yield. However owing to the unknown influence of other variables this was at best qualitative.

6.3.3 Yield of the Version Two Microelectrode

The yield of the V2M was found to be 45.8%. Figure 6.1 shows the percentage yield of the microelectrodes versus the LKE potential window over which they were cycled.

It was generally agreed by experimenters that the number of microelectrodes that functioned depended on the potential window over which they were swept, with less microelectrodes functioning when stressed with a larger potential window. However the yield percentages presented in figure 6.1 are inconclusive, most likely owing to the number of uncontrolled variables. Bias on the part of the electrode user may also be present in this data, as microelectrodes from batches that had shown higher yields were preferred when conducting experiments between -2 to -2.5 V. This would artificially inflate the microelectrode yield at these potentials.

The microelectrodes that exhibited fatal defects tended to demonstrate the electrochemical response similar to that shown in figure 6.2.

Key indicators of failure were current magnitudes much higher than typically expected (1 - 10μA rather than 100s nA - 1 μA) and the cyclic voltammogram exhibits a

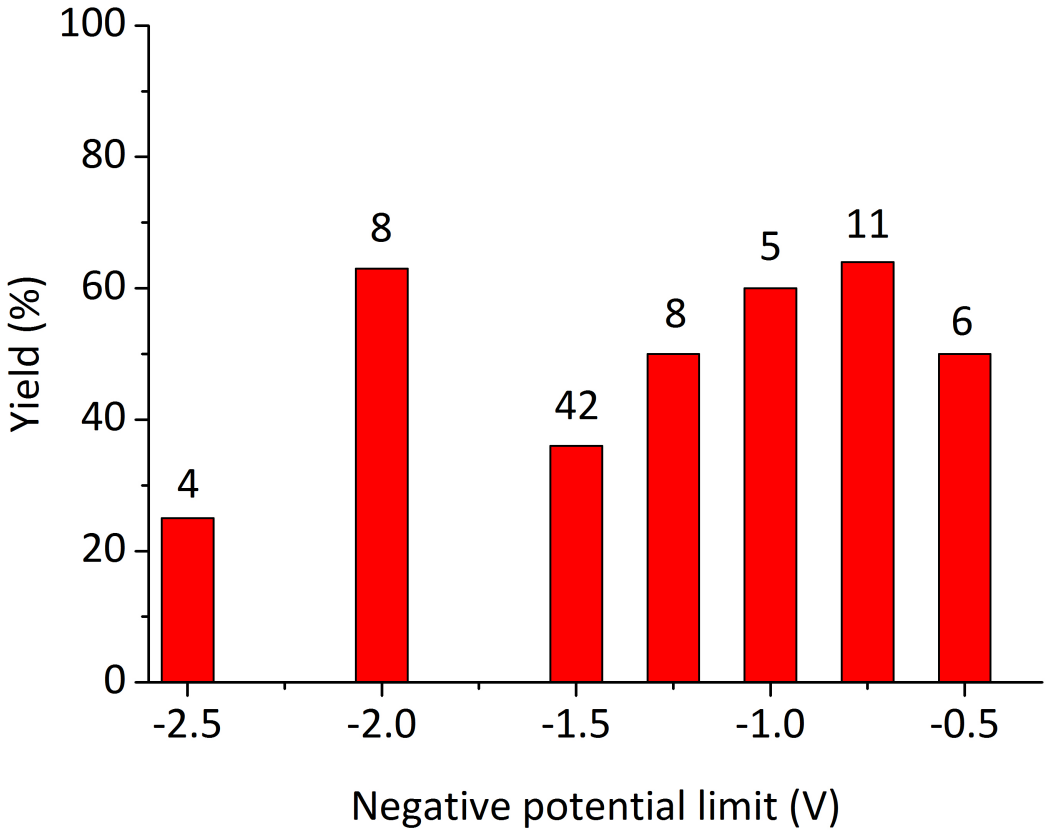

Figure 6.1: Percentage of V2Ms that functioned as a microelectrode at each potential. The number of microelectrodes tested is displayed at the top of each column.

more macroelectrode-like response with no limiting current. This indicates additional electroactive area is exposed to the LKE. An obvious failure mechanism associated with increased electroactive area is defects in the top insulator.

6.4 Improving Microelectrode Yield

6.4.1 Effect of Critical Area

The critical area (CA) of a microelectronic structure is the area in which, if a defect is present the device will fail [4, 7, 9, 10]. The CA of the V2M was initially assumed to be the area of top insulator over the electrode metal. Should a defect form in this area, additional metal would be exposed to the salt and the microelectrode area would increase indicating failure. In integrated circuit design, reduction of CA is known to

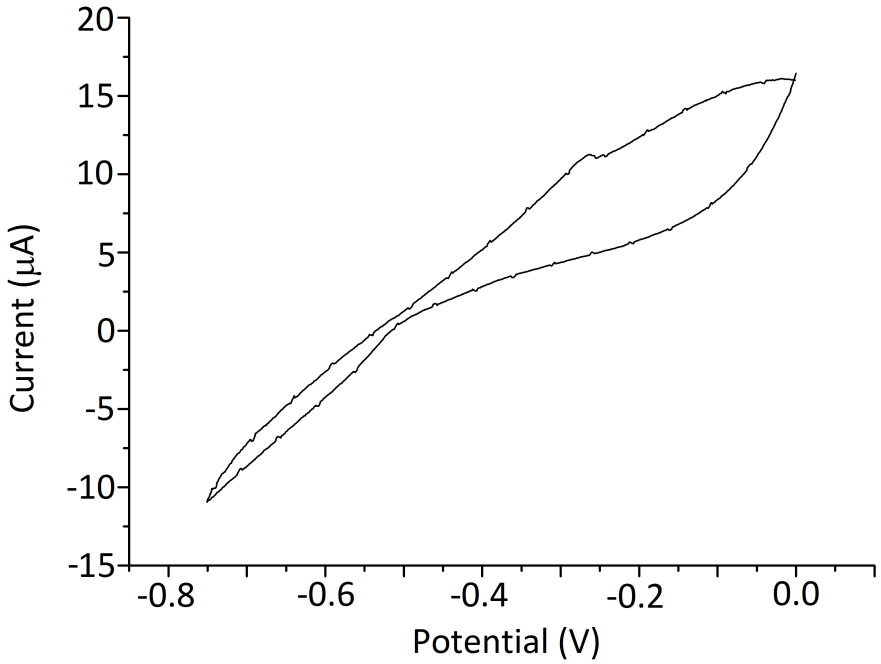

Figure 6.2: 16th cyclic voltammogram of Ag plating and stripping in LKE, recorded using a 30 μm edge length V2M with 5 mM of AgCl.

have a positive impact on device yield [4, 7, 9, 10].

6.4.2 Thin Track Microelectrode with Reduced Critical Area

In order to improve the yield of the microelectrodes; a new layout with reduced CA was designed. The CA was reduced by decreasing the area of metal that made up the interconnect between the contact pad and the microelectrode. The CA of the V2M was 55 mm^2, assuming immersion in the salt was 10 mm. This new microelectrode layout, shown in figure 6.3, is termed the thin track microelectrode (TTM) and, assuming the same immersion depth of 10 mm, has a CA of 1.5 mm^2 which reduces the CA by a factor of 36.7.

The width of the thin track was designed to reduce the CA, without introducing a large resistance in the circuit. The sheet resistance of 50 nm thick Pt was measured to be 15.9 $\pm$ 10.1 $\Omega/\square$ using a Veeco FPP 5000 four point probe. It is uncertain why there was such a high range of values, however the four-point probe used to make the measurements required the operator to manually press down on the sample. This could introduce a variability to the measurement. The resistance of the track is therefore 2,630 $\pm$ 1,680 Ω assuming an electrode metal of 50 nm thick Pt. Given the highest current

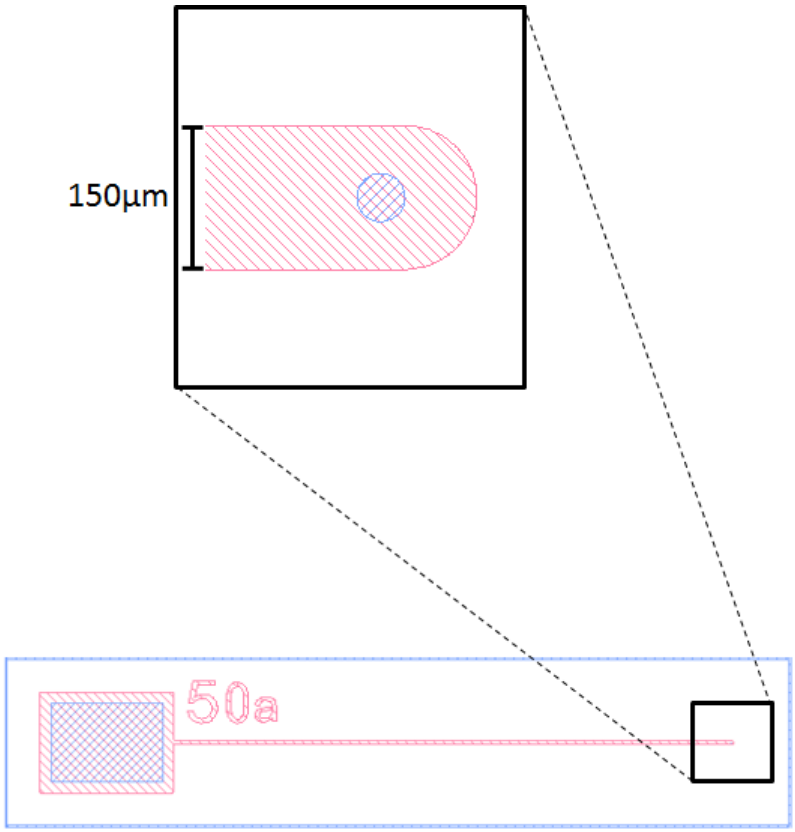

Figure 6.3: The layout of the TTM. The track is 150 μm wide and 25 mm long. The blue shaded areas are exposed metal and red shaded area identifies the top insulator over the electrode metal.

recorded on a functioning microelectrode is 7 μA, the voltage drop over the track is 18.4 $\pm$ 11.8 mV. This was considered small enough to be neglected. The thin track layout also included a microdisc electrode in place of the microsquare electrode. This was to eliminate corners, minimising the focal points for stress. For the same reason the metal track was rounded. The background to and the impact of the microdisc over the microsquare electrode are assessed in the next chapter.

6.4.3 Yield of the Thin Track Microelectrodes

As with the V2M, the yield values were collected across all experiments by all users. The average yield of the microelectrodes increased from 45.8% to 60% with the implementation of the thin track layout. This improvement in microelectrode yield strongly suggests a CA-dependent effect, as there is a reduced area for defects or pinholes to form in the top insulator and expose additional electrode metal. Figure 6.4 shows the microelectrode yield versus negative potential limit and the number of experiments performed.

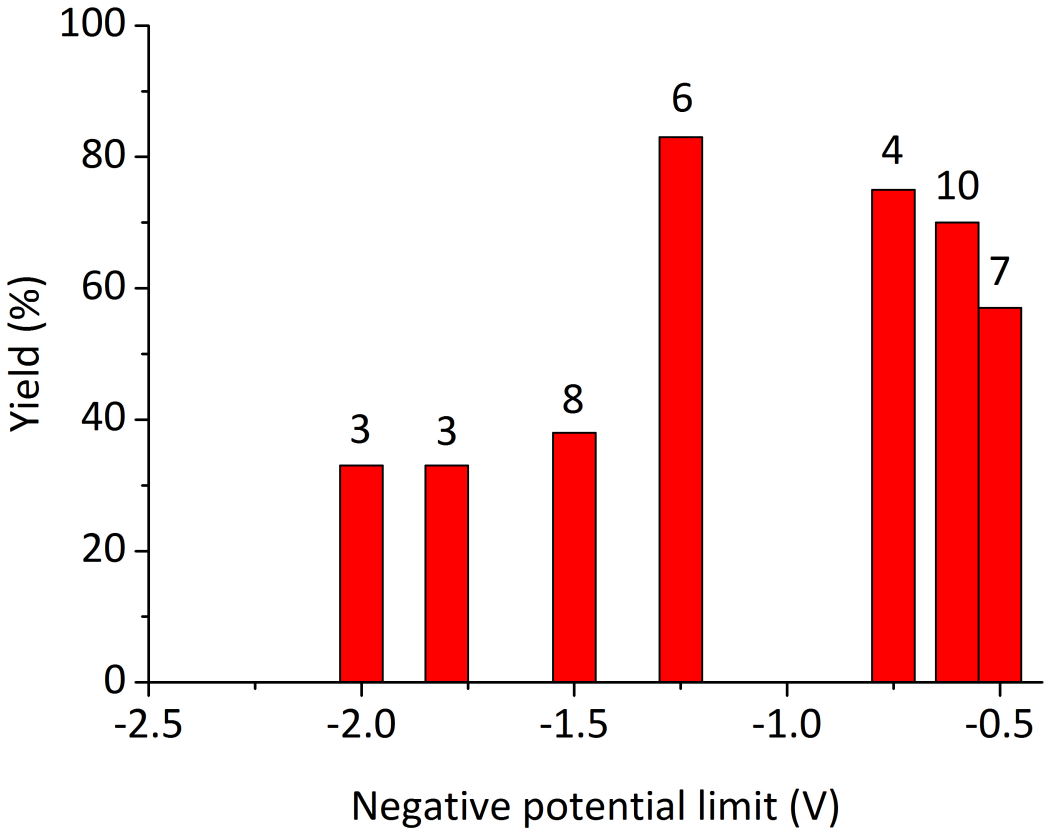

Figure 6.4: Percentage of TTM that worked at each potential.

Despite the improved yield of the TTM over the V2M, a decrease in yield with increasingly negative potential limit is still observed by users. However, the data presented in figure 6.4 is inconclusive as was the case with the V2Ms. The same uncontrolled variables present in the data shown in figure 6.1 are present in figure 6.4, which makes drawing conclusions difficult. Additionally, the number of experiments performed with the TTMs at each potential was less than that of the V2Ms as fewer microelectrodes of this layout were made before the next layout redesign.

6.4.4 Super Thin Track Microelectrode with Further Reduced Critical Area

In order to further improve the yield, a new microelectrode layout with less CA was designed. These were termed super thin track microelectrodes (STTM) and the layout of these microelectrodes is shown in figure 6.5.

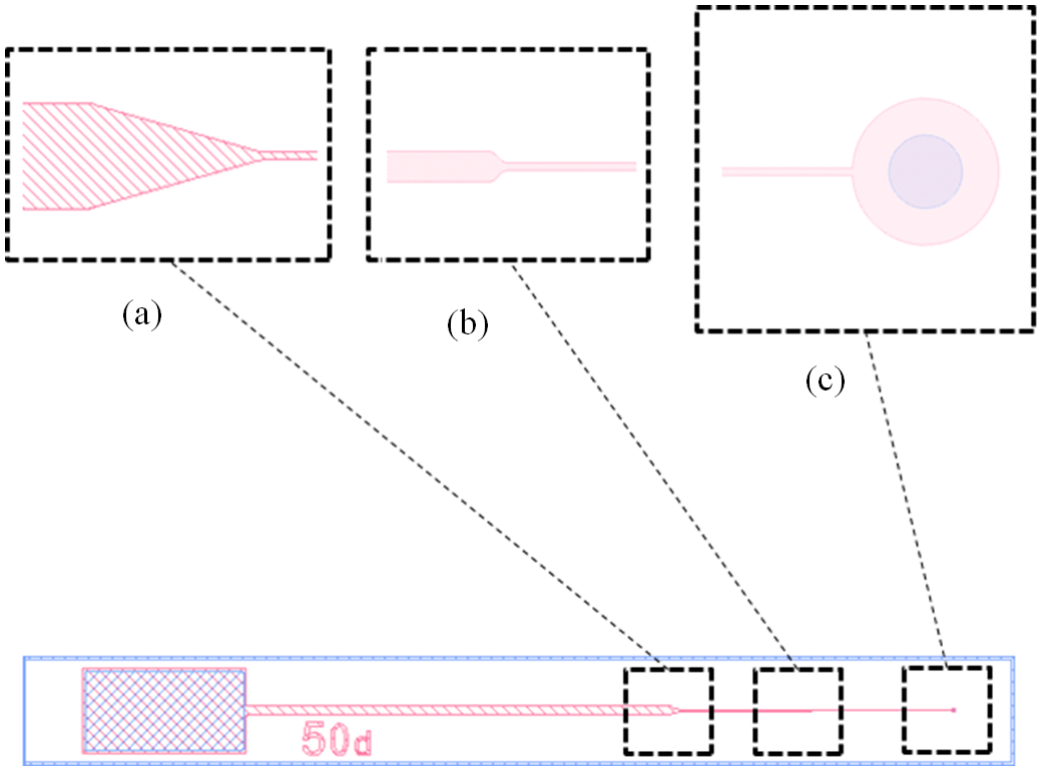

Figure 6.5: Schematic of the STTM layout, enlarged are the points at which the interconnect thins from (a) 300 μm to 20 μm and (b) 20 μm to 5 μm. (c) shows a zoom in on the microdisc electrode

This further reduction in interconnect width results in a corresponding increase in electrical resistance. In order to minimise this, the track width was reduced in stages. The first section is 300 μm wide and 15 mm long, the next section is 20 μm wide and 5 mm long, and the last section before the microdisc is 5 μm wide and 5 mm long. Again, assuming an immersion depth of 10 mm, the CA of the this microelectrode layout is 0.13 mm^2, which is 11.5 times less CA than the thin track layout. The total resistance of this is 20,500 $\pm$ 13,100 Ω for 50 nm of Pt. Despite this high resistance, the envisioned improvement in yield was considered more important. The width of each chip was also reduced by half, increasing the number of microelectrodes per batch to 40.

Another area of concern was how close the step up to the metal and the step down into the electrode cavity were. Figure 6.6 shows a zoom in of the microdisc layout with the step up from the electrode metal to the insulator (a) and the step down from the edge of the disc (b) highlighted.

These changes of topology are both likely focal points for stress and clustering them together could negatively impact the top insulator robustness. These two points were hence separated by 50 μm, which was the minimum distance separating them on the

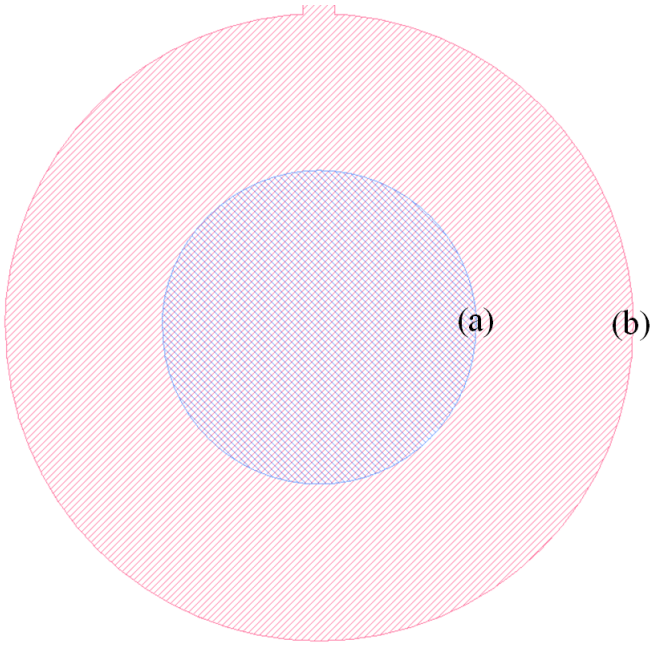

Figure 6.6: Schematic of a 50 μm microdisc electrode on the STTM layout, highlighting (a) the step up from the electrode metal and (b) the step down at the edge of the electrode metal disc.

previous TTM design.

6.4.5 Yield of the Super Thin Track Microelectrodes

The yield of STTMs was found to be 65%. Figure 6.7 shows the percentage yield of the STTM plotted against potential window and the number of experiments performed for each potential window.

It can be seen that the yield of the STTMs has improved over that of the TTMs by 5%. As was the case with the TTMs, the improvement in yield with reduction of CA implies the existence of defects in the microelectrode architecture. In order to investigate these defects, test structures where designed and are reported in the next section.

6.5 Investigating Insulator Defectivity

6.5.1 Test Structures

The improvements in yield and lifetime exhibited by reducing the CA demonstrates that a CA dependent effect such as insulator defectivity is a factor in the yield. In order

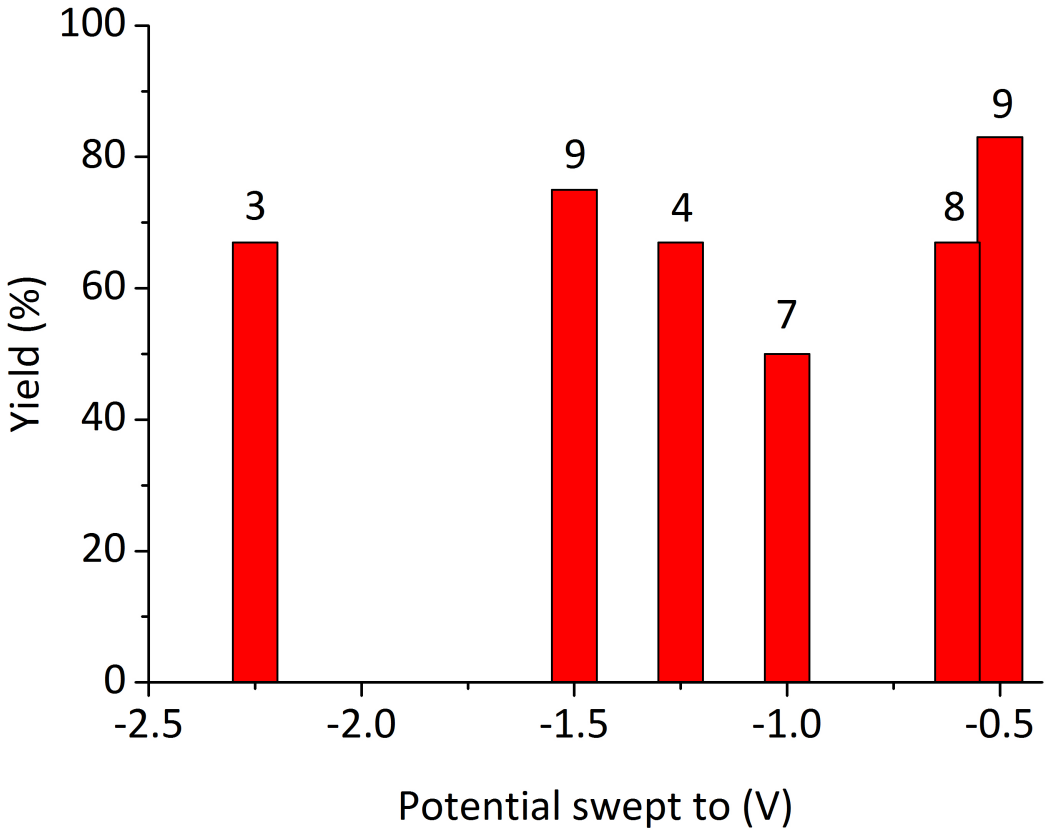

Figure 6.7: Percentage of STTMs that worked at each potential.

to quantify the defectivity of the insulators, a series of test structures were designed, fabricated, and tested.

6.5.2 Test Structure Design

The identification of defects in the microelectrodes is complicated by the desired electrochemical reaction occurring on the electrode surface, as the current associated with that reaction will obscure the current related to any defects present in the insulator. This makes it difficult to identify/quantify defects in the insulation. The test structures were hence designed to provide information on the effect of electrode area on the yield of the microelectrodes. These structures are shown schematically in figure 6.8 (a) and consist of metal electrode plates with a range of areas, covered by an overlying dielectric. This set of structures was designed to be dipped into the LKE until the plate is submerged, the depth of immersion was controlled, and a potential applied. Any

current that passed must therefore be due to exposed metal, most likely through pinholes/defects. The potential chosen was the potential at which Ag plates, which would highlight defects visually as the Ag will electroplate on the exposed metal. 5 mM of AgCl was therefore added to the LKE for all experiments. These test structures enable the quality/defectivity of the dielectric on a largely planar surface to be monitored. Another area of interest was the integrity of the top insulator over metal steps which, as mentioned above, could be focal points for stress. The comb test structures shown in figure 6.8 (b) were designed to investigate this potential weakness. Each design consisted of a series of 10 μm wide metal strips set 25 μm apart.

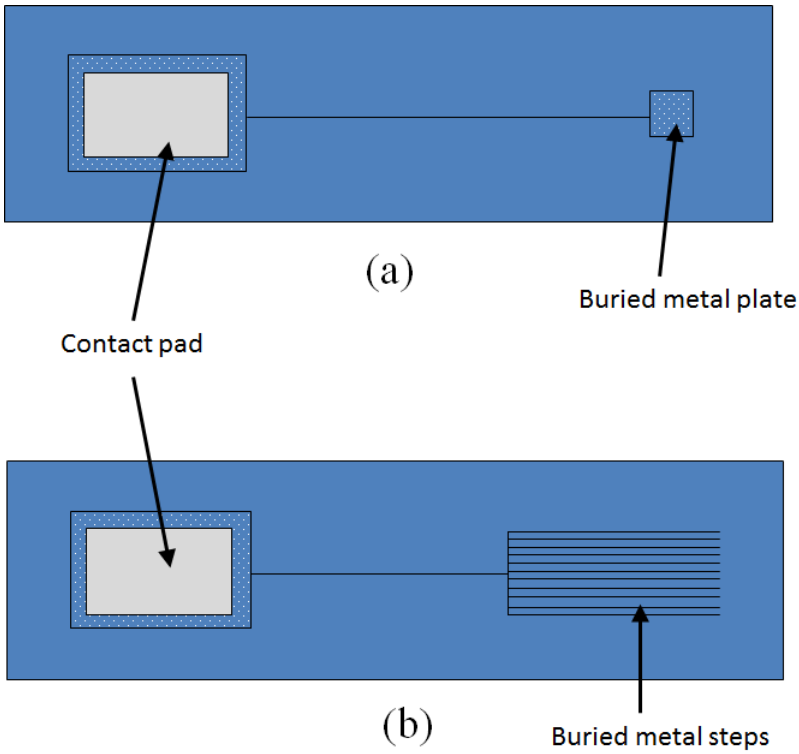

Figure 6.8: (a) Layout of the test structures to provide information on the relationship between CA and yield. The structures consist of a bond pad connected via a narrow metal interconnect to metal plates of areas: 0.25 mm^2, 1 mm^2, 4 mm^2, and 16 mm^2. (b) Test structures for dielectric step coverage integrity. A contact pad is connected to a series of 10 μm wide metal strips set 25 μm apart.

6.5.3 Test Structure Results

Measurement performance

A potential of -0.46 V was applied to the buried metal plate structures for 15 minutes and the average current (of three structures) for the four metal plate sizes is shown in figure 6.9. What can be immediately seen from these results is that the average currents are non-zero, implying Ag^+ ions are reaching the buried metal. It can also be noted that the currents do not scale with area, which indicates they are most likely to be due to randomly occurring conduction paths rather than a fundamental, intrinsic property of the Si_3N_4 dielectric. This conclusion is supported by a large variation in currents between nominally identical samples. Figure 6.10 shows current responses from three individual 4 mm^2 buried metal plate test structures. The currents range over four orders of magnitude, from 10^{-9} to 10^{-5} A. This is despite the fact that the metal (critical) areas are the same, which again suggests the presence of some random effects. It was expected that some of the test structures would show no fatal defects and four out of the 18 test structures tested showed zero leakage current. What is clear from figure

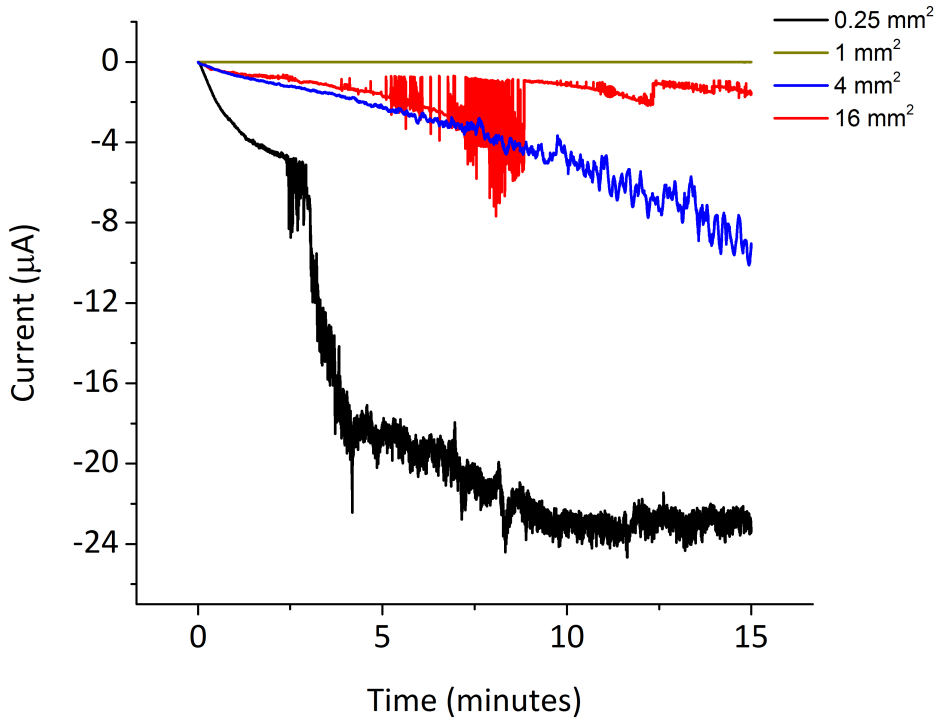

Figure 6.9: Average current versus time plots over 15 minutes for each area of metal plate studied. N = 3 for each size of test structure.

6.10 is the magnitude of the currents increases over time. Given the fixed potential, the

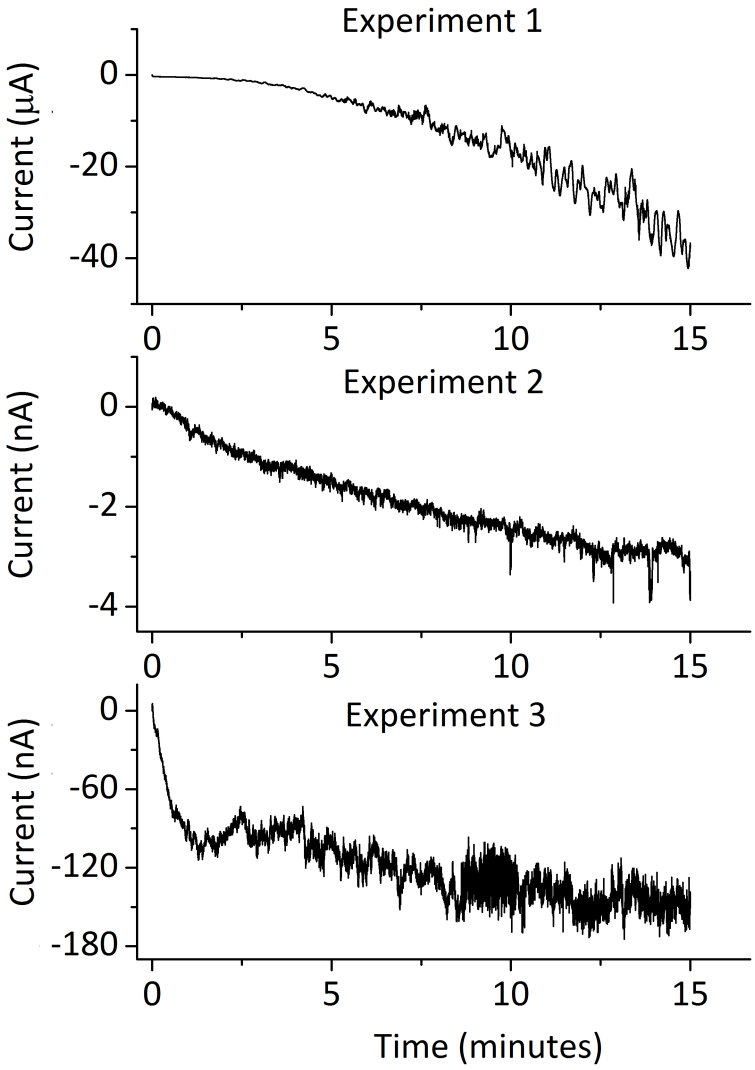

Figure 6.10: Current versus time plot of three individual experiments using 4 mm^2 area microelectrodes over 15 minutes.

resistance of the circuit is decreasing with time. Since this effect is not consistent in every test structures, this is likely not an artefact of the experimental set up and could be explained by conduction paths developing over time. This could manifest as defects enlarge, become more conductive or latent defects in the microelectrode architecture become "active". Another factor that should also be considered is that the electroactive area increases as the Ag plates, which leads to an increase of current with time. However, the current against time plots in figure 6.10 are very different, which would not have been expected if the mechanism controlling the current increase had been consistent. This again points to more random type effects in the microelectrode structure being

involved.

The comb structures shown in figure 6.8 (b) for assessing dielectric integrity at step edges were also subject to the same Ag plating test. These test structures also gave a non-zero current response with large current differences between microelectrodes of the same electrode area, as observed with the plate test structures.

Defect location

When the test structures were examined after removal from the LKE, no Ag was observed on the surface of the top insulator overlying the metal electrode. Figure 6.11 shows (a) the top insulator over the buried electrode metal before Ag plating and (b) after the plating test. Although deposits of salt can be seen there is clearly no evidence of any Ag plated on the Si_3N_4, which suggests the observed current is not flowing via this route. Following further examination of the test structure, the Ag was located on the edge of the

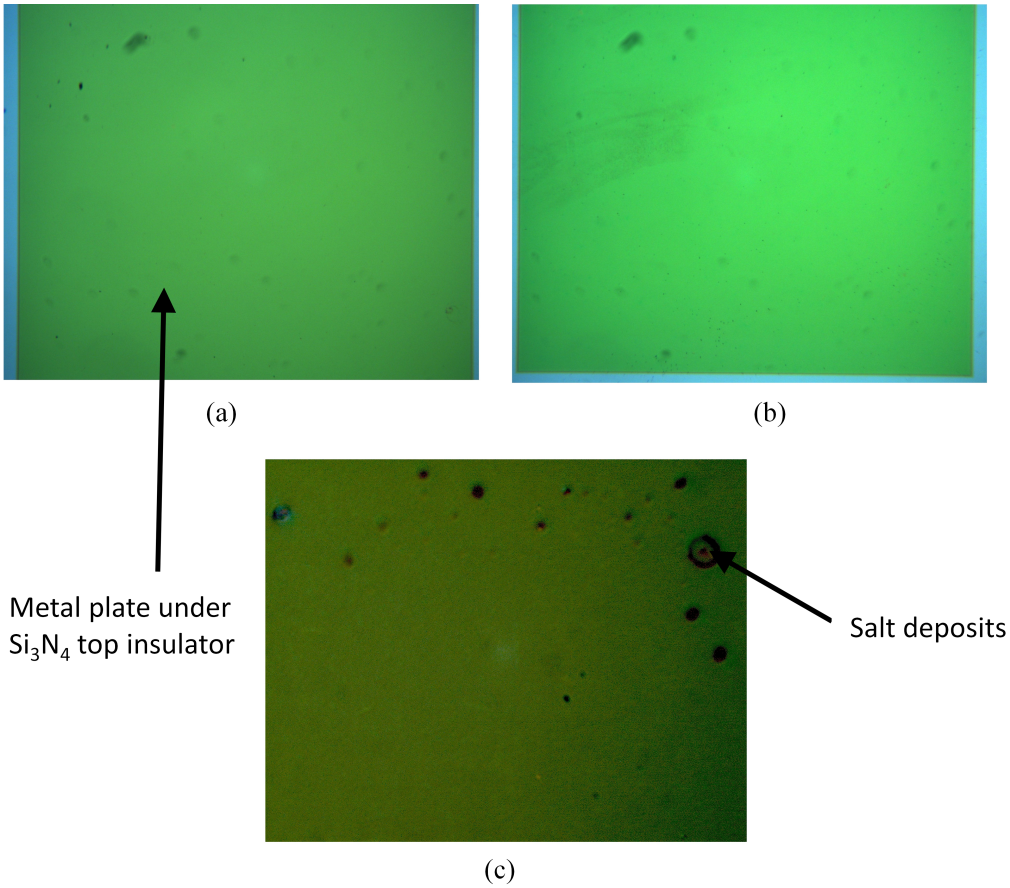

Figure 6.11: The surface of the Si_3N_4 insulator over buried metal plates (a) before Ag plating ($\times$ 10), (b) after Ag plating ($\times$ 10) and, (c) after Ag plating (x 100).

Si, exposed around the perimeter of the chip by dicing the test structures. Figure 6.12 (a) shows the edge of the Si after dicing and (b) after the Ag plating experiment, with (c) showing a more magnified image of this edge. Figure 6.13 shows a cross section of the test structure architecture highlighting the Ag plating locations. It should be noted that

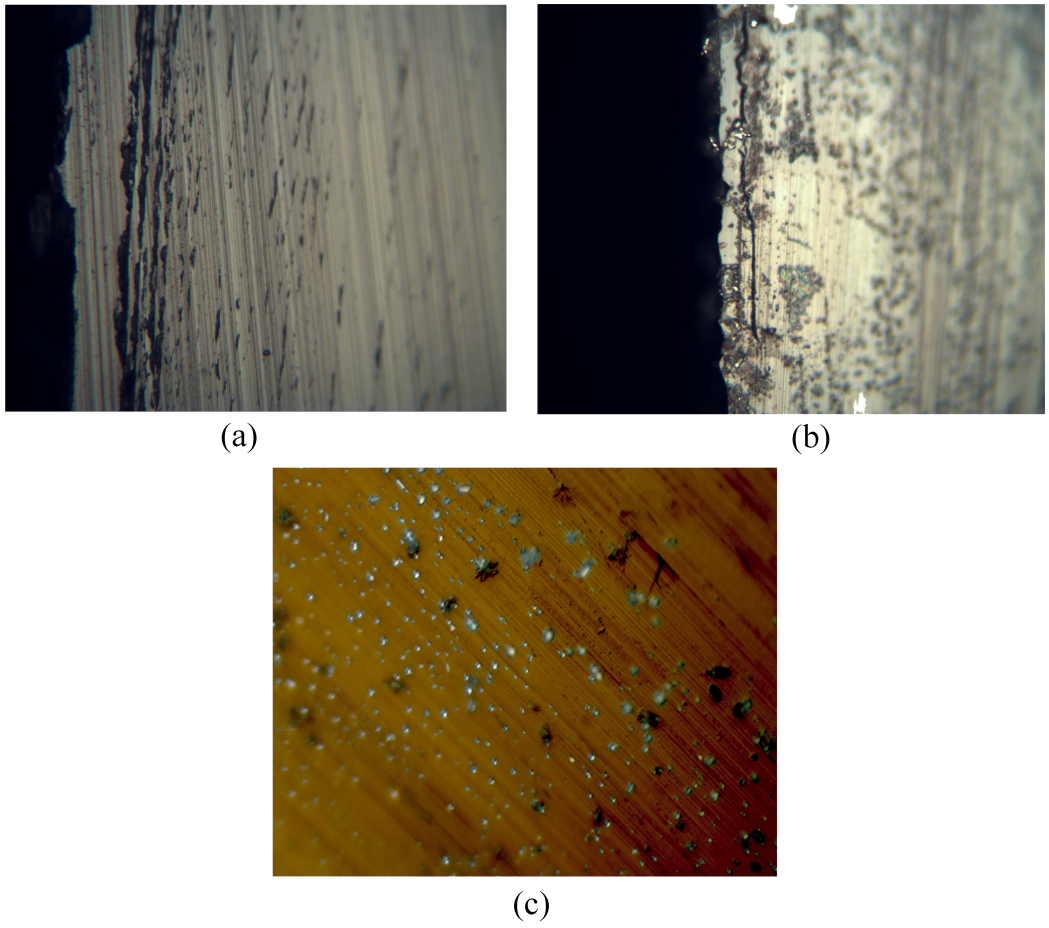

Figure 6.12: The surface of the Si perimeter around the test structure chip (a) before Ag plating (× 40), (b) after Ag plating (× 40), and (c) after Ag plating (× 100).

Si is a conductor at 450°C, owing to the thermal excitation of intrinsic charge carriers into the conduction band [11]. The Ag plating observed on the Si suggests conduction pathways are connecting the electrode metal to the underlying Si. Hence the observed insulator failure is associated with the underlying thermal SiO_2 layer rather than the exposed Si_3N_4 layer. It may be the case that the defects present in the thermally grown SiO_2 layer are random point failures that are attributable to particulate contamination. However this is thought to be unlikely as the SiO_2 is both 500 nm thick and thermally grown. It may be that chemical attack of the SiO_2 in the salt is the source of the conduction paths. To investigate this possibility, the perimeter of the test structure was

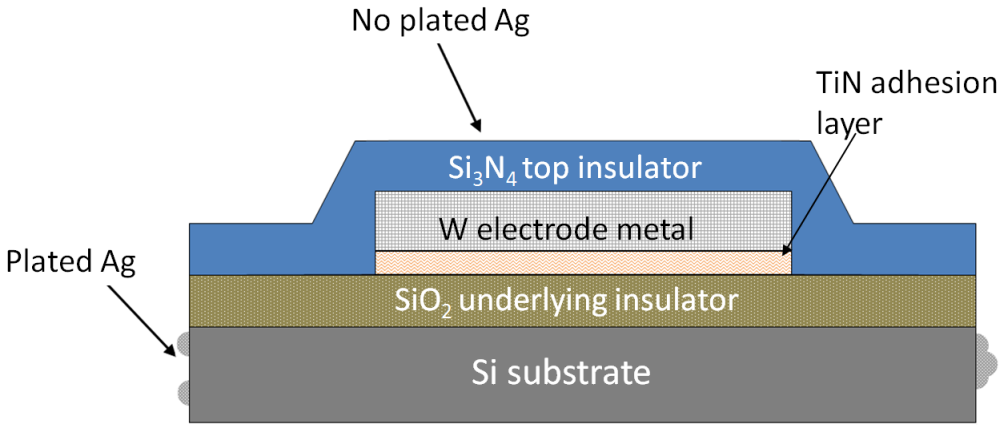

Figure 6.13: Cross-section through the test structure highlighting where the Ag has plated.

sectioned and imaged using a focused ion beam. The image is shown in figure 6.14 and it can be observed no there is deterioration of the SiO_2 layer which strongly indicates that this is not the mechanism by which the electrode metal is connecting to the Si.

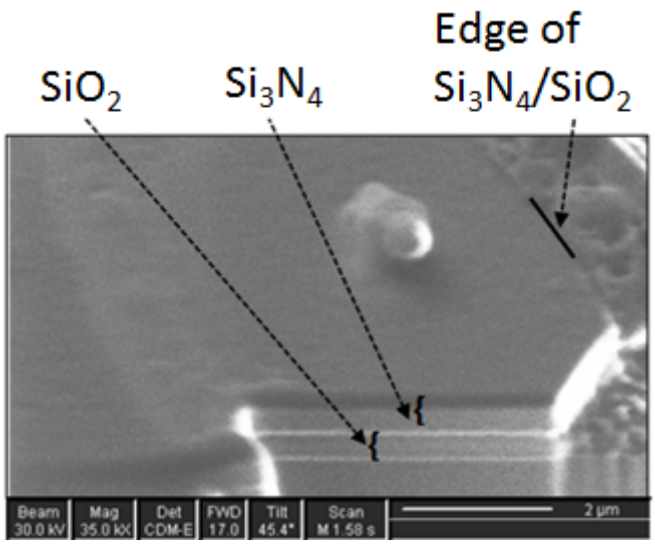

Figure 6.14: The edge of a test structure sectioned using a focused ion beam.

Another factor could be diffusion of Li^+ into the SiO_2, exacerbating existing areas of weakness. Both of these theories are consistent with the observation that these defects are not noticeable in aqueous room temperature studies where the microelectrodes have

> 99% yield, probably owing to the high resistivity of Si in ambient conditions. It may be the case that the increased conductivity of the Si effectively activates latent defects in the SiO_2 layer and they become points of failure if they lie under the electrode metal. It should also be noted that the failures being associated with the underlying insulator enlarges the CA of microelectrodes, as any defect in the SiO_2 underlying insulation under the electrode metal interconnect or contact pad will cause failure.

Figure 6.15 shows a set of steps on the comb test structures (a) before and (b) after Ag plating and (c) a magnified image after Ag plating. It can be observed there is no Ag plating along the edge of the metal step. However, once again Ag deposits were identified on the exposed Si edge of the chip in a similar fashion to those observed on the buried metal plate structures.

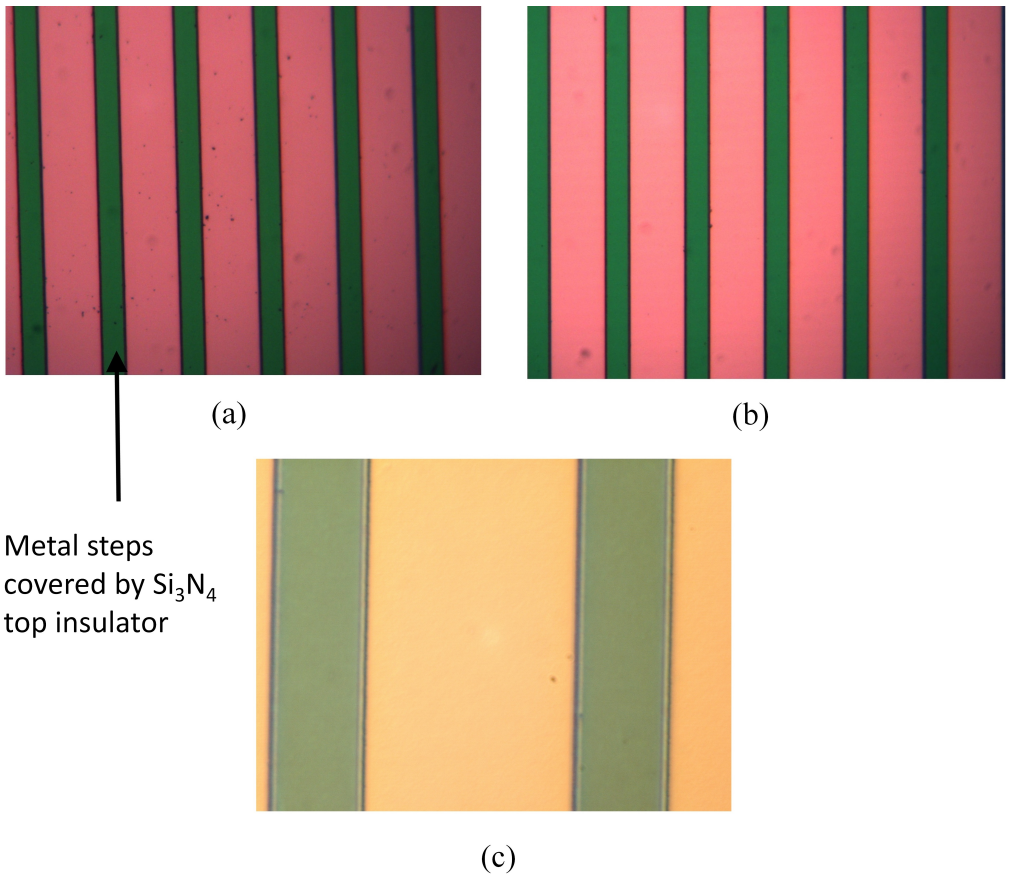

Figure 6.15: Steps of the comb test structure (a) before plating (× 40), (b) after plating (× 40), and (c) after plating (× 100).

6.6 Summary

The yield of the microelectrodes has been improved from the 45.8% of the V2M to the 65% of the STTM, by modifying the layout to reduce the CA of the microelectrode. Figure 6.16 presents the three different microelectrode layouts investigated, their CAs and corresponding yield.

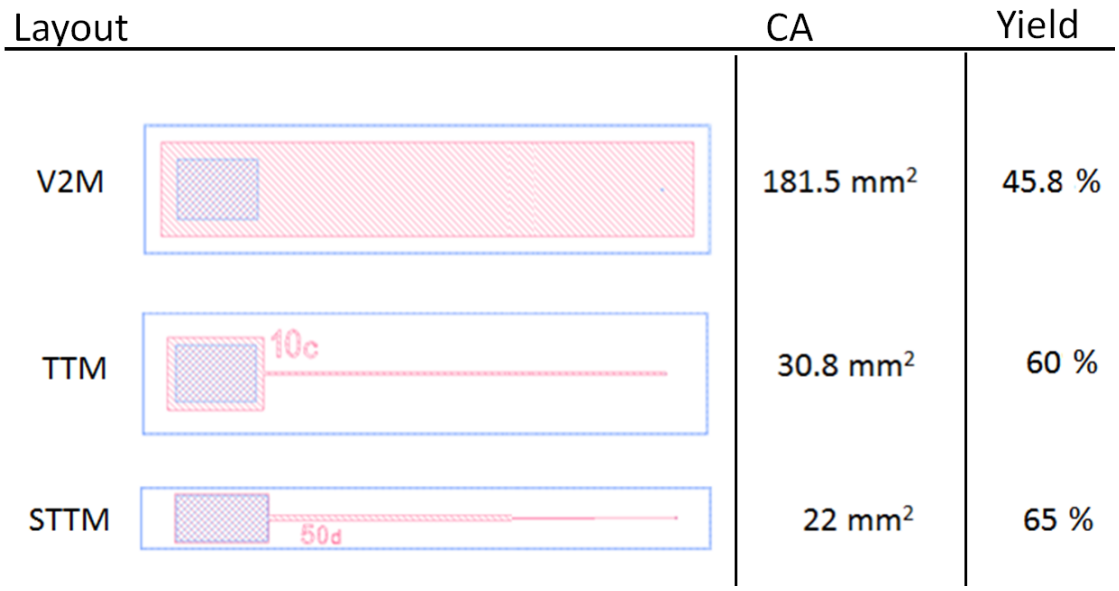

Figure 6.16: The yield of each microelectrode layout and their CAs, assuming 10 mm immersion in MS.

Test structures were then designed to help identify the mechanism causing 35% of the microelectrodes to be defective. These were instrumental in suggesting the failure mechanism was conduction paths the underlying SiO_2 insulator, causing an electrical connection between the electrode metal and the Si substrate. With Si being an electrical conductor at 450°C, the Si edge around the perimeter of the chip functions as additional electrode area which needs to remain electrically isolated from the electrode metal. The leakage current increasing with time suggests the that the cross-sectional area of the conduction paths increases over the course of the experiments.

To prevent this electrical shorting between the electrode metal and Si, it is proposed that the architecture of the microelectrode is modified. The results of this work have indicated that Si_3N_4 insulates effectively against LKE, even over steps and edges. Therefore, a thin layer of Si_3N_4 deposited over the SiO_2 could isolate the electrode metal from possible defects present in the SiO_2 layer. This would require the modification of the SiO_2 underlying insulator to compensate for the additional tensile stress of this Si_3N_4

layer.

References

[1] A. Christou and W. M. Webb, Eds., *Reliability and Quality in Microelectronic Manufacturing*. Center for Risk and Reliability Studies, 2006. [Online]. Available: https://www.quanterion.com/product/publications/reliability-and-quality-in-microelectronic-manufacturing/

[2] P. Gupta and E. Papadopoulou, *Yield Analysis and Optimisation*. CRC Press, 2009, ch. 37, pp. 771–790. [Online]. Available: http://www.inf.usi.ch/faculty/papadopoulou/publications/bookchapter08.pdf

[3] A. Landzberg, Ed., *Microelectronics Manufacturing Diagnostics Handbook*. Springer Science+Business Media LLC, 1993. [Online]. Available: http://link.springer.com/book/10.1007%2F978-1-4615-2029-0

[4] R. J. Ross, Ed., *Microelectronics Failure Analysis: Desk Reference*. ASM International, 2004. [Online]. Available: http://www.asminternational.org/documents/10192/3461432/09110Z_TOC.pdf/96fcf653-8d7f-462c-9ddd-997049f03001

[5] J. C. Whitaker, Ed., *Microelectronics 2nd Edition*. CRC Taylor and Francis, 2005. [Online]. Available: http://eu.wiley.com/WileyCDA/WileyTitle/productCd-1118165063.html

[6] R. R. Tummala, E. J. Rymaszewski, and A. G. Klopfenstein, Eds., *Microelectronics Packaging Handbook: Semiconductor Packaging*. Klewer Academic Publishers, 1997. [Online]. Available: http://www.springer.com/gb/book/9780412084416

[7] Z. Stamenkovic, S. Dimitrijev, and N. Stojadinovic, "Integrated circuit production yield assurance based on yield analysis," *Microelectronics Journal*, vol. 24, no. 7, pp. 819 – 822, 1993. [Online]. Available: http://www.sciencedirect.com/science/article/pii/002626929390026B

[8] S. Salemi, L. Yang, J. Q. Jun Dai, and J. B. Bernstein, *Physics-of-Failure Based Handbook of Microelectronic Systems*. NASA, 2008. [Online]. Available: https://nepp.nasa.gov/files/16365/08_102_4_%20JPL_White.pdf

[9] G. A. Allan and A. J. Walton, "Efficient critical area measurements of IC layout applied to quality and reliability enhancement," *Microelectronics Reliability*, vol. 37, no. 12, pp. 1825 – 1833, 1997. [Online]. Available: http://www.sciencedirect.com/science/article/pii/S0026271497000218

[10] G. Allan and A. Walton, "Automated redundant via placement for increased yield and reliability," vol. 3216, 1997, pp. 114–125, cited By 19. [Online]. Available: http://www.scopus.com/inward/record.url?eid=2-s2.0-0010618352&partnerID=40&md5=8666b4f6593e05454ebb5e13cf942c7a

[11] G. L. Pearson and J. Bardeen, "Electrical properties of pure silicon and silicon alloys containing boron and phosphorus," *Physical Review*, vol. 75, no. 5, March 1949. [Online]. Available: http://journals.aps.org/pr/pdf/10.1103/PhysRev.75.865

Chapter 7

Characterisation of Microelectrode Lifetimes

7.1 Introduction

This chapter investigates the performance of the successfully functioning microelectrodes developed so far in this study, as described in chapter 6. The microelectrodes assessed are the version two microelectrode (V2M), the thin track microelectrode (TTM) - both microsquare and microdisc, and the super thin track microelectrode (STTM) reported in chapters 5 and 6. These microelectrodes have different layouts with progressively reduced critical area (CA) and figure 7.1 presents a schematic of each. Lifetimes of these

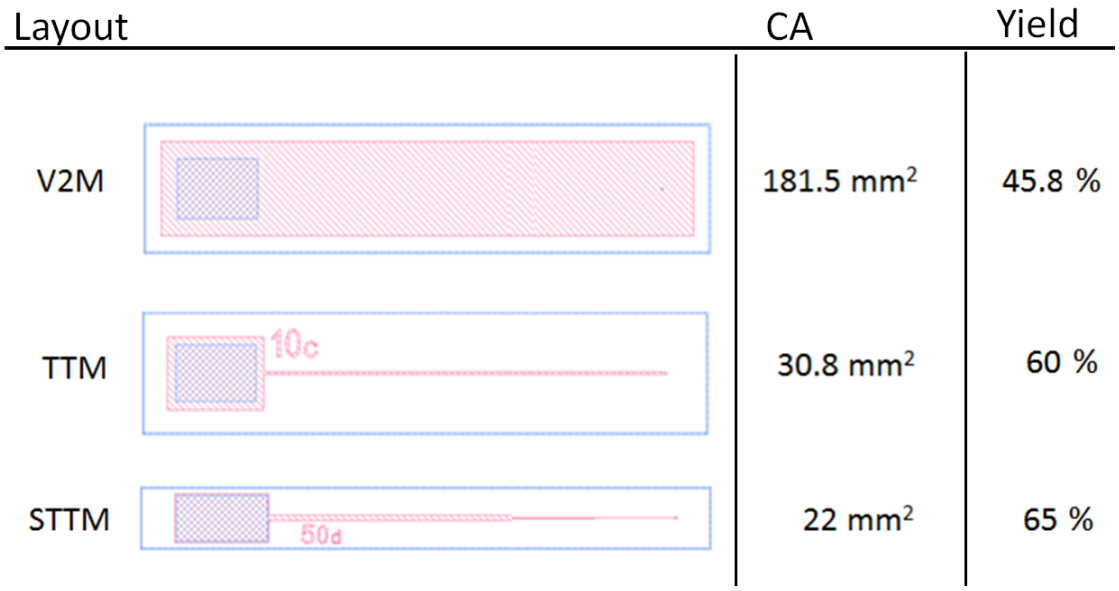

Figure 7.1: Layouts of three microelectrode designs and their CAs, assuming a 10 mm immersion in the salt.

microelectrode versions are presented and the impact of the layout modifications and implementation of microdisc electrode assessed. The failure mechanisms limiting microelectrode lifetimes are investigated and recommendations made for future development.

7.2 Background Resistance

During characterisation, an additional resistance to that of the interconnect was observed in the CVs throughout the lifetime studies and in 89% of the lifetime studies, this background resistance persisted for the duration of the experiment. The average value of this resistance was 13.9 MΩ, with values ranging between 230 KΩ abd 59.2 MΩ. This effect was therefore not related to the presence of a native oxide layer on the electrode metal surface, which was typically removed within the first ten CVs and has

been discussed in chapter 5. Generally, high resistances observed in electrochemical data arises from failure of the electrical connections. In this case the crocodile clip was observed to have a layer of corrosion on the surface when removed from the experiment. Despite the clips being cleaned prior to each experiment it is possible that, given the length of the lifetime studies, this layer had encroached onto the interface between the crocodile clip and the contact pad. Protecting the connection against this corrosion is challenging, owing to the high temperature of environment and the requirement to not electrically connect the Si substrate to the clip. Ceramic putty had previously been used in this role. However, this caused damage to the microelectrode once removed from the LKE as detailed in chapter 4. Background subtraction was therefore performed on the CVs in order to remove this resistance and obtain a value of limiting current for quantitation. This was done by selecting points on the CV where zero current would flow and setting those to zero.

7.3 Methodology

In order to remain consistent with previous work done in this study, continuous cyclic voltammetry of Ag plating and stripping (4 - 6 mM of AgCl) was chosen as the method of quantifying the lifetime of the microelectrodes. This method has the relevant benefits described in chapter 4, although the derived lifetimes will only be valid across the Ag plating and stripping potential window, typically -0.65 V to 0 V. It is also a harsh treatment of the microelectrode, because the plating and stripping reactions are known to change electrode surfaces compared with solution reactions. However, plating and stripping reactions are the reactions of interest within a pyroprocessing system [1, 2]. The microelectrodes were deemed to have failed when they no longer displayed a microelectrode-type response with a limiting current and sharp stripping peak, described in more detail in chapter 3. The lifetime experiments for the TTMs were conducted over weekends with the microelectrodes being checked each day. The experiments were therefore not halted at the point of microelectrode failure and all of the TTMs were further cycled for a period of time after failure. The time between the TTM failure and the experiment being switched off was typically 12 - 15 hours. However, a stable electrochemical response was obtained from the microelectrodes over this time and so it was assumed no significant change occurred to the electrode surface between failure and cessation of the experiment.

7.4 Version Two Microelectrode Lifetime

Figure 7.2 shows the results from six lifetime experiments with the average lifetime of the V2M being 1.4 ± 0.5 hours. The lifetimes of the V2Ms can be observed to range

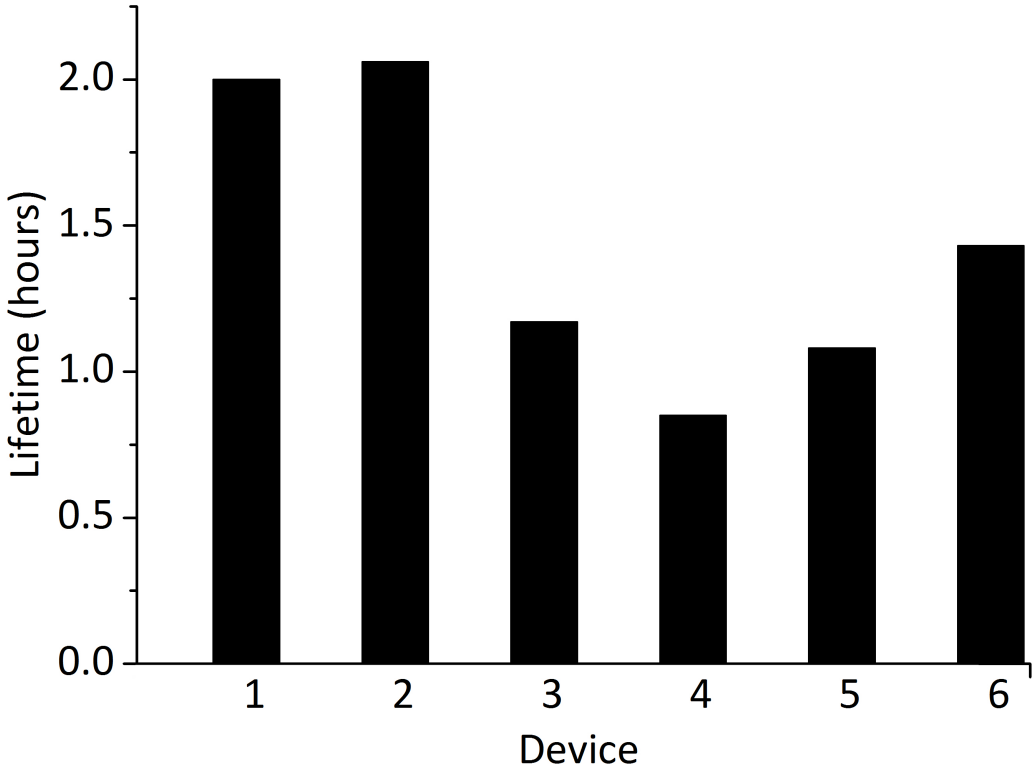

Figure 7.2: Lifetimes of individual V2Ms.

between 51 and 123 minutes. The low yield of this layout discussed in chapter 6 implies weak points or defects exist within the architecture, which may be playing a role in the high spread of lifetimes. The failure mechanism of the microelectrodes which never functioned was discussed in chapter 6 and is thought to be electrical shorting of the electrode metal to the Si substrate, caused by fatal defects in the underlying insulator. In the case of the functioning microelectrodes, it may be that these conduction paths to the Si are not completely present, but form under stress of operation causing failure. This is supported by the similarity in electrochemical response of the failed V2Ms and that of the microelectrodes which did not function at all. Figure 7.3 (a) shows a CV of a failed V2M after lifetime characterisation and figure 7.3 (b) a CV of a V2M which did not function. The reduction currents in both CVs are in the microampere range, as opposed to the expected hundreds of nanoamperes and the oxidation peaks are relatively

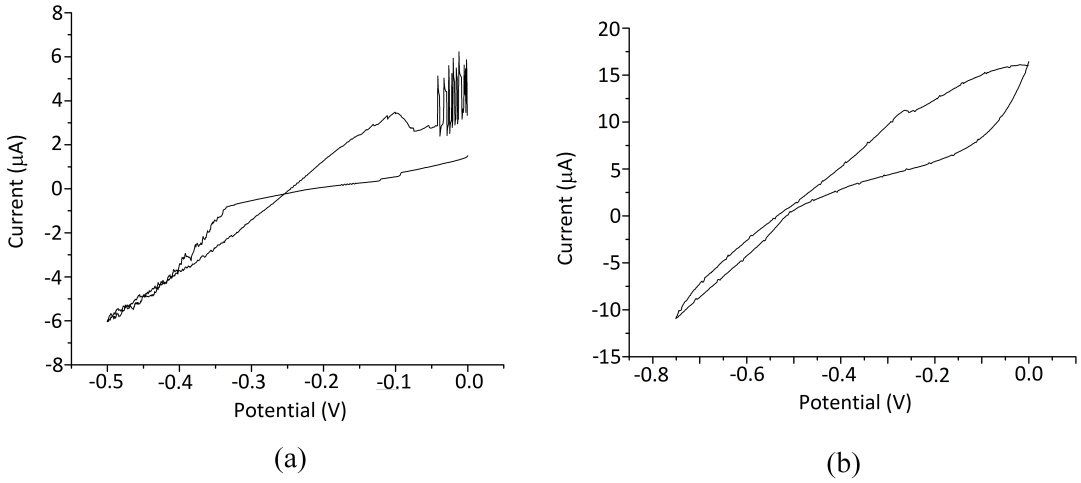

Figure 7.3: CVs recorded on (a) a 50 μm edge length V2M used in a lifetime experiment after failure and (b) a 30 μm edge length V2M which did not function.

small. These are typical features of Si electrochemistry in LKE [3]. The larger than expected currents could also be attributable to damage to the top insulator, exposing additional electrode metal. However, no delamination or cracking was visible when the microelectrodes were inspected after cycling in the LKE, as can be seen in figure 7.4 which shows two V2Ms after removal from the LKE. The presence of any small cracks

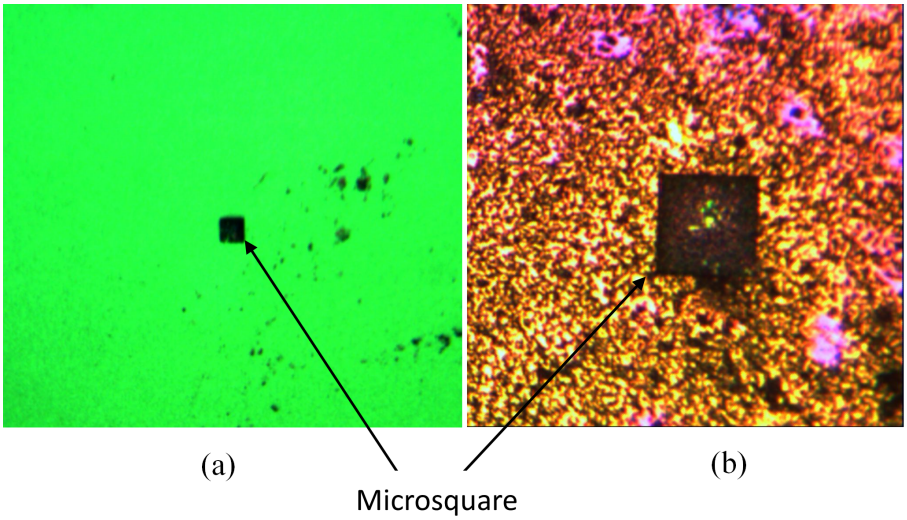

Figure 7.4: (a) 50 μm edge length and (b) 20 μm edge length V2Ms used to record the CVs in figure 7.3 after removal from the LKE.

or pinholes in the top insulator are difficult to identify and therefore could not be ruled out. This is especially the case when the LKE residue is still present on the surface of the

microelectrode as in figure 7.4 (b). It was also observed by users that the microelectrode lifetime decreased with increasingly negative potential windows, in a similar manner to the microelectrode yield investigated in chapter 6. This was not statistically verified owing to time constraints but, if true, also points to a common physical mechanism controlling both the low yield and varying lifetimes.

7.5 Thin Track Microelectrode Lifetime

The TTMs with reduced CA, described in chapter 6, were designed to improve the microelectrode robustness to defects and hence were predicted to improve microelectrode lifetimes. In order to assess the effect of CA reduction on lifetime, the TTMs were subject to the same lifetime tests as the V2M. The thin track design in chapter 6 included a microdisc electrode in place of the microsquare electrode and therefore a batch of TTMs were fabricated with microsquare electrodes (□TTMs) instead of the microdiscs (◯TTMs) in order to asses the impact of CA reduction and electrode geometry on lifetime separately.

Microsquare Thin Track Microelectrode

Figure 7.5 compares the measured lifetimes of the □TTMs with the V2Ms. It can be observed that the average lifetime has increased from the 1.4 hours to 13.4 hours, although only two of the □TTMs exceed this value and the others show vastly reduced lifetimes. Despite this, all the □TTMs show higher lifetimes than the V2Ms, indicating that reducing the CA has a positive impact on microelectrode lifetime and yield. Again, the high spread of result suggests that microelectrode lifetime is still controlled by latent defects rather than intrinsic material failure. Another option comes from the variability or contamination of the LKE environment, as the presence of oxygen and hydrogen in the LKE creates a more corrosive environment as discussed in chapter 2. This is unlikely as the salt pellet was only changed once during the experiments presented in figure 7.5 and the seal of the cell was checked every day and did not show any appreciable change.

Microdisc Thin Track Microelectrode

Figure 7.6 shows the lifetimes of the ◯TTMs compared with both the □TTMs and the V2Ms. A number of factors contributed to the low number of ◯TTM samples reported. This included the problems associated with the microelectrode yield, the length of the experiments, and high demand for the microelectrodes. The lifetimes of the ◯TTMs

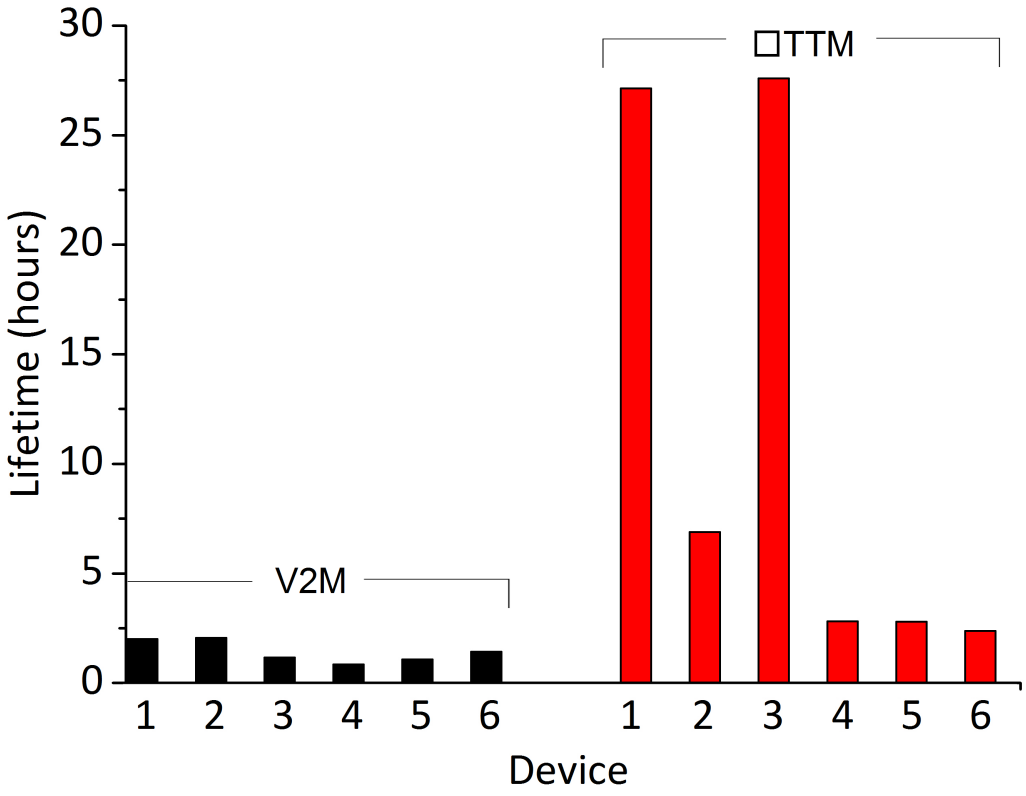

Figure 7.5: Lifetimes of the □TTMs compared with the lifetimes of the V2Ms.

was very encouraging with the average lifetime having risen to 26.3 ± 21.5 hours. This is a substantial increase from the 13.4 hour lifetime observed with the □TTMs. However the low number of studies as well as the high spread of values means this is inconclusive and further work is required.

7.6 Thin Track Microelectrode Lifetime Failures

7.6.1 Failure Mechanism

Figure 7.7 shows three TTMs after removal from the LKE. In all cases the Pt has been removed from the electrode area and the surrounding area of top insulator has delaminated. This suggests that the electrode metal or the adhesion layer is being chemically or mechanically removed. It is important to remember that the microelectrodes have continued to be electrochemically cycled for an average 15 hours between failure and removal. However the electrochemical response of the microelectrodes during this time was observed to be stable and so it was assumed no significant changes occurred to the

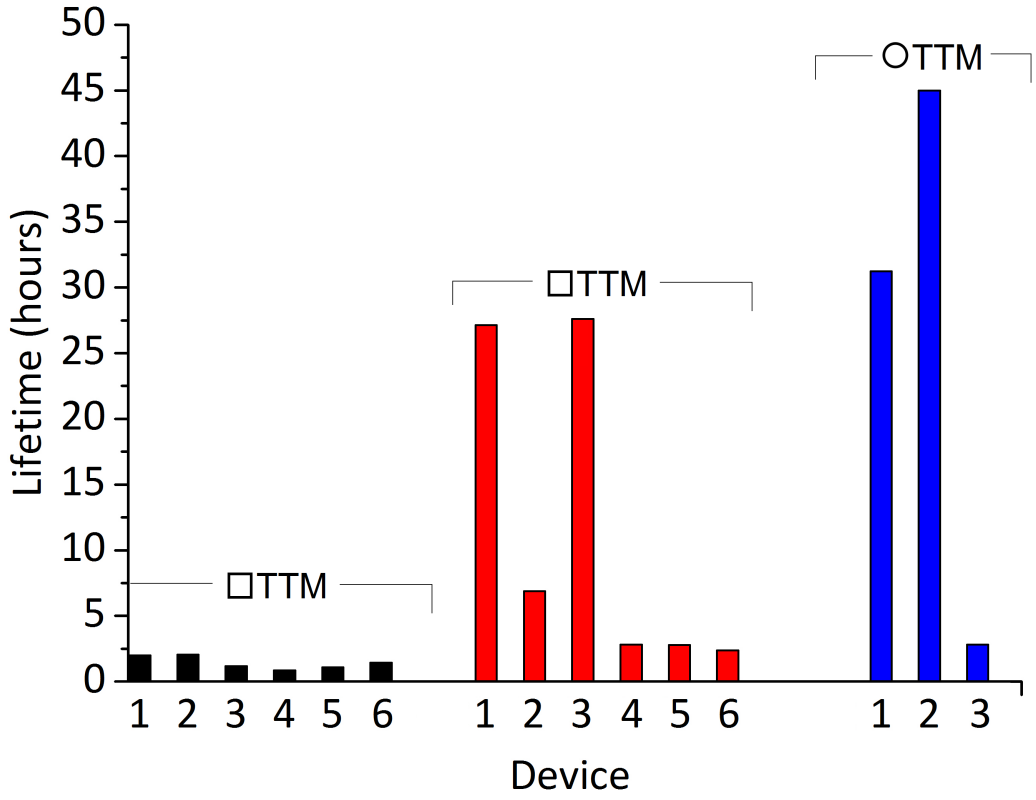

Figure 7.6: Lifetimes of the ◯TTMs compared with □TTMs and the V2M.

microelectrode surface during this time.

It was observed in the CVs that 80% the microelectrode failures were associated with a rapidly fluctuating current. Figure 7.8 compares two CVs recorded at on a 100 μm □TTM where (a) is an ideal microelectrode response without current fluctuation and (b) shows a fluctuating current that starts at -0.73 V and finishes at -0.65 V on the reverse sweep. The potential at which this region of fluctuating current begins was observed to become more positive over time. An example of this is presented in figure 7.9, which shows four CVs recorded on a 50 μm ◯TTMs with the potential at which the fluctuations begin labelled. This region eventually obscures the limiting current, as demonstrated by the CV shown in figure 7.10 in which the limiting current can no longer be determined and the microelectrode was deemed to have failed. This fluctuating current occurs in the Ag plating region of the CV, which would suggest it is an effect linked to the reduction of Ag on the surface of the microelectrode. Metal dendrite growth is known to give rise to rapid fluctuations in current as the electroactive area grows rapidly and then decreases as the dendrite detaches [4]. Such dendrites have been

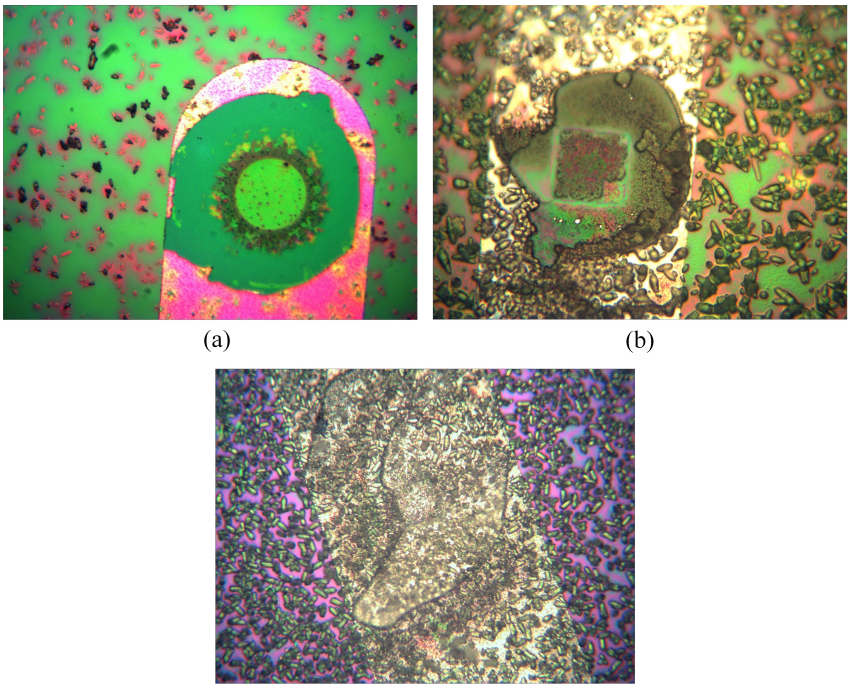

Figure 7.7: Images of three TTMs after lifetime studies; (a) a 50 μm diameter microdisc after 45 hours, (b) a 50 μm edge length microsquare after 28 hours, and (c) a 30 μm edge length microsquare after 7 hours.

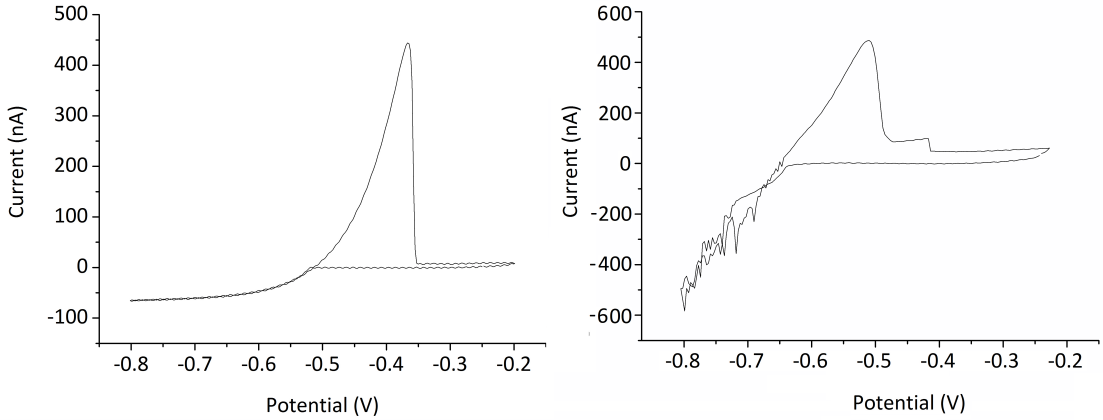

Figure 7.8: CVs of Ag plating and stripping on TTM with 100 μm edge length microsquare in LKE at 450°C. (a) shows a typical limiting current and stripping peak while (b) has a region of fluctuating current, starting around -0.73 V in the reductive sweep.

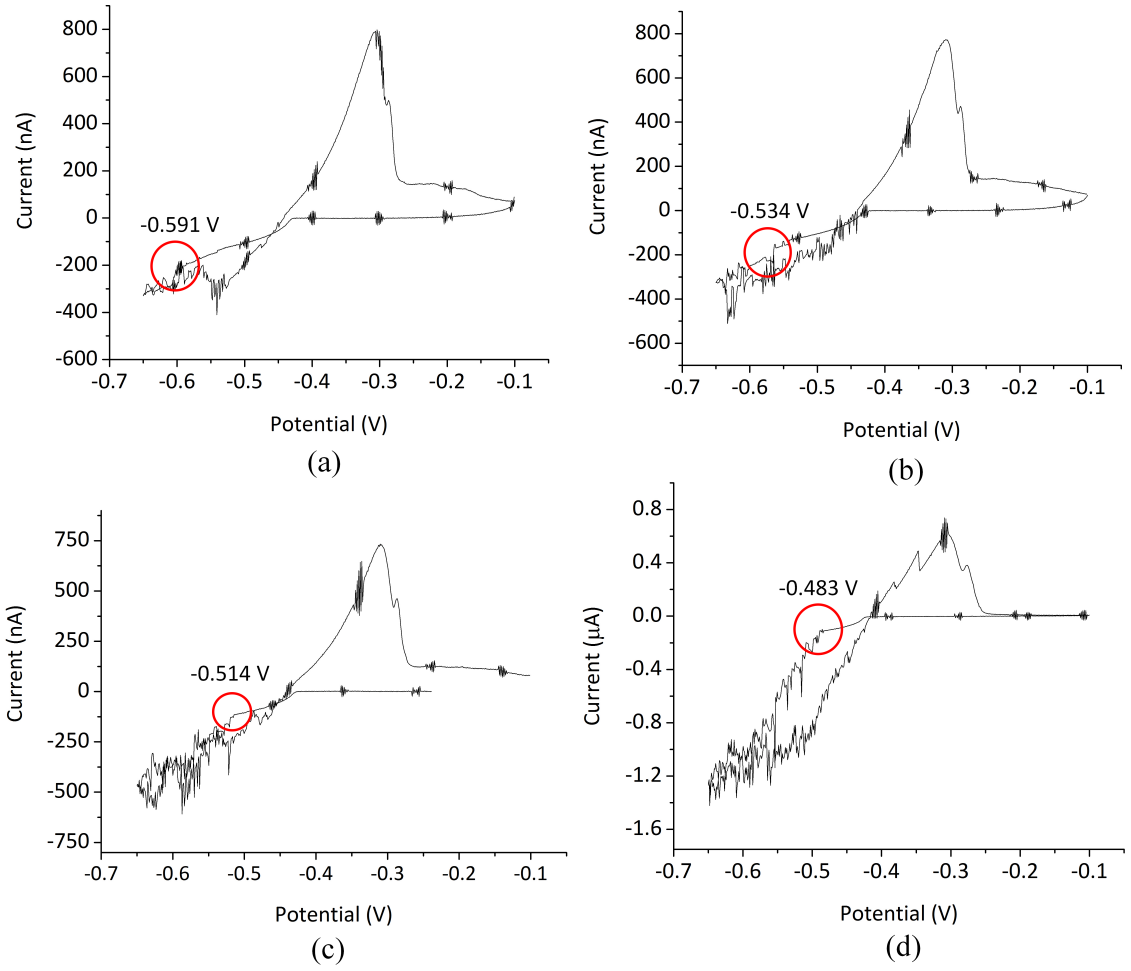

Figure 7.9: CVs of Ag plating and stripping on a Pt 100 μm □TTM in LKE at 450°C after (a) 15 hours, (b) 18 hours, (c) 21 hours, and (d) 24 hours. The potential at which the current fluctuation region begins is circled.

observed in previous microelectrode experiments in aqueous conditions [5]. Hence, it is possible that dendrites cause damage to the electrode surface by removing the Pt metal when detaching. Another mechanism is that the current fluctuations are associated with the removal of the Pt or TiN metal layers, with the increase in current caused by the delamination of the top insulator, exposing more electrode metal area.

7.6.2 Mechanism of Platinum Loss

In order to establish if the electrode metal loss was electrochemical in origin, six chips consisting of 50 nm of Pt on 20 nm of TiN on 500 nm of Si_3N_4 and no top insulator were fabricated and soaked in LKE at 450°C. Two chips were withdrawn from the LKE at five

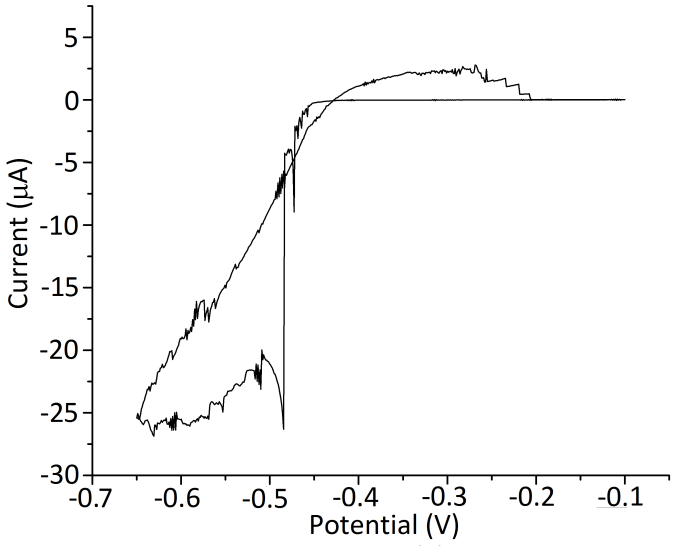

Figure 7.10: CV after 32.1 hours of Ag stripping and plating on the same TTM used to record the CVs in figure 7.9.

hour intervals, to observe possible corrosion over time. Figure 7.11 shows three chips before, (a(i)), (b(i)), and (c(i)), and after (a(ii)), (b(ii)), and (c(ii)) soaking in LKE.

It can be observed that the Pt has been partially removed from the chips in both figure 7.11 (a(ii)) and (b(ii)) and is completely removed in (c(ii)). It was noticed that the Pt was appeared to flake and peel away from the surface when removed, which is not consistent with chemical/electrochemical corrosion but failure of adhesion to the layer underneath. The open circuit potential of these chips was also measured as being in the range -0.35 V to -0.4 V, which is not near the +1.2 V to +1.3 V potential required to electrochemically dissolve Pt [6, 7]. The electrical resistance of the exposed surface under the removed Pt on each chip was measured to determine if the TiN adhesion layer was still present. Open circuit values were recorded in each case, with a maximum applied potential difference of 10 V, which suggests the TiN adhesion layer has been removed. This was corroborated by reflectometry measurements which confirmed exposed area, previously covered by Pt and TiN, was Si_3N_4. This is reminiscent of the behaviour of Ti as an adhesion layer, investigated in chapter 5, which electrochemically stripped around 0 V. The damage observed on the top insulator around the microelectrode cavity, shown in figure 7.7 may be due to the Pt lifting off parts of the surrounding insulator as it was removed. Despite the improved robustness of the TiN over the Ti adhesion layer, it appears it is not suitable for long term use. The variability in lifetimes observed in

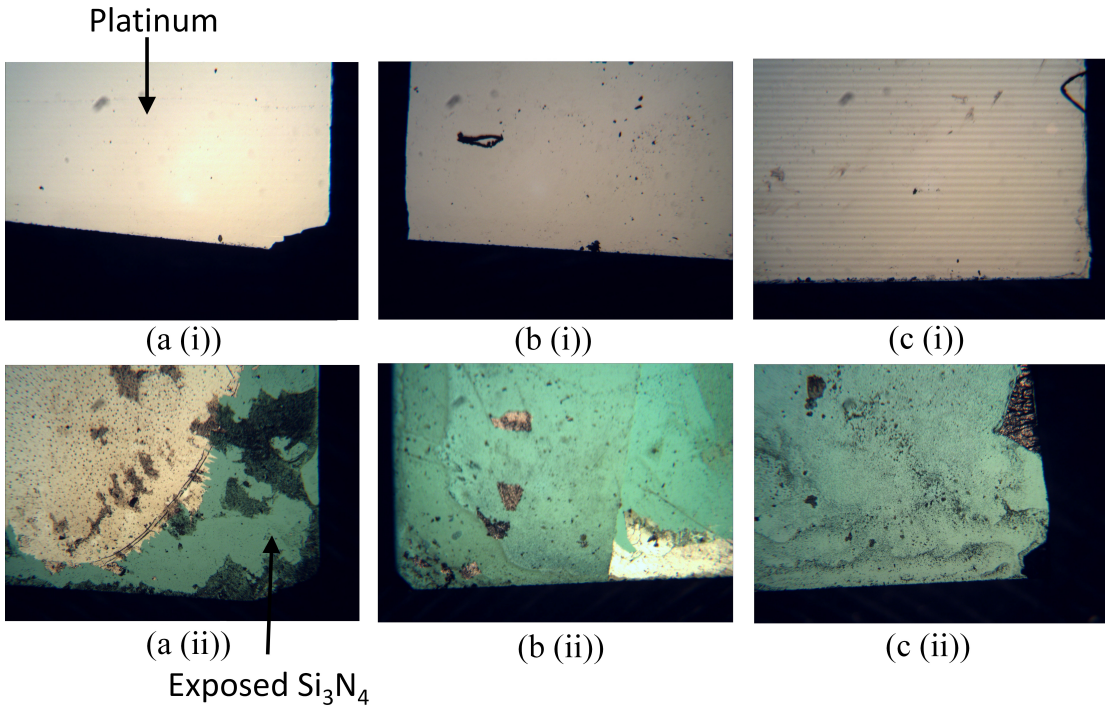

Figure 7.11: Bottom corners of chips coated in 20 nm of TiN and 50 nm of Pt (a (i)), (b (i)), (c (i)) before soaking in 450°C LKE and (a (ii)) after 5 hours, (b (ii)) after 10 hours and (c (ii)) after 15 hours.

figure 7.6, may be related to latent defects such as pinholes in the metal layer; eventually allowing the salt access to the TiN underneath. It is interesting that, where shorting between the electrode metal and Si substrate caused failure in the V2M architecture, removal of the adhesion layer was the mechanism of failure for the TTMs and STTMs. This suggests that reducing the CA decreases the chance of latent as well as fatal defects in the underlying insulator and latent defects, such as pinholes, in the electrode metal becomes the source of microelectrode failure. The existence of these pinholes has already been suggested in chapter 4 and 5 as the mechanism by which the LKE reached the original Ti adhesion layer.

7.7 Super Thin Track Electrode Lifetime

The lifetime of the STTMs, presented in chapter 6, was determined using the same method as the TTMs. Owing to time constraints and the number of microelectrodes available, only four STTMs were evaluated. At this time in the project, an etching process for W had been developed and so two of STTMs tested used W electrode metal

instead of Pt. Figure 7.12 shows the lifetimes recorded for the STTM microelectrodes.

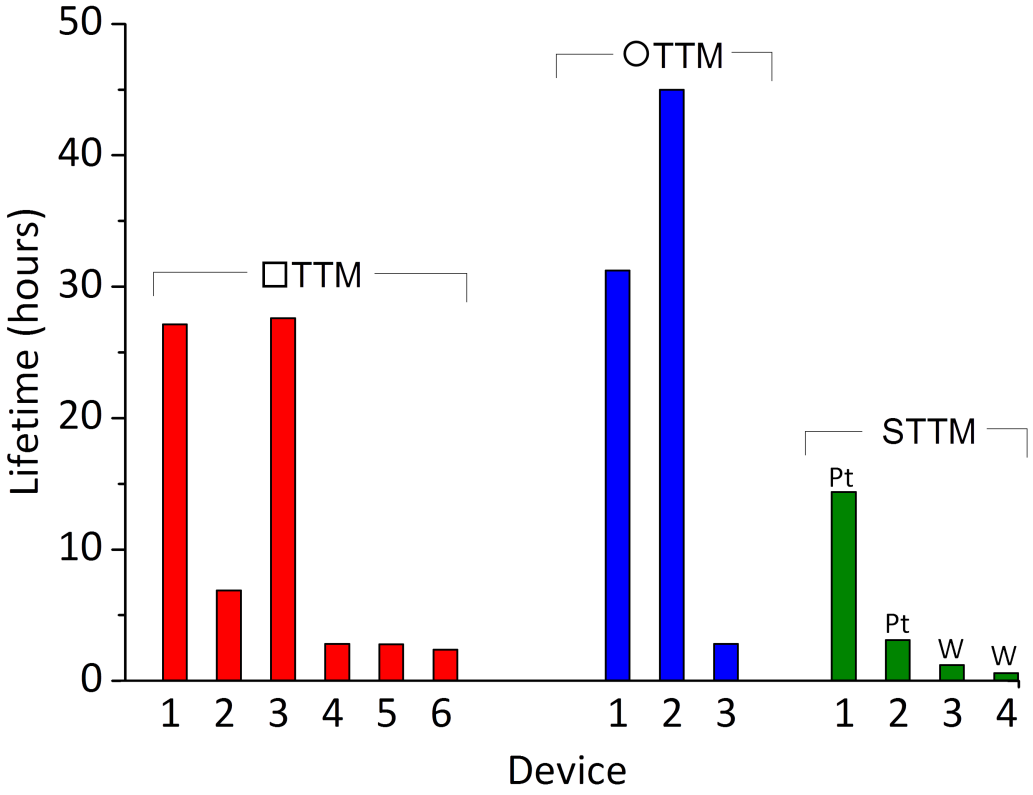

Figure 7.12: Lifetimes of the STTMs compared with the TTMs. The Pt and W STTMs are labelled.

The lifetimes appear significantly reduced, with an average of 4.9 ± 6.7 hours. However, no firm conclusions can be drawn as only four STTMs were tested. Given that removal of the TiN adhesion layer was thought to be the cause of the TTM failures, it was predicted that both Pt and W STTM would exhibit the same metal loss behaviour. Figure 7.13 shows both W STTMs after removal from the LKE and the same metal loss behaviour can be observed on both the W and Pt STTM, which supports the removal of the TiN adhesion layer as the source of the metal loss.

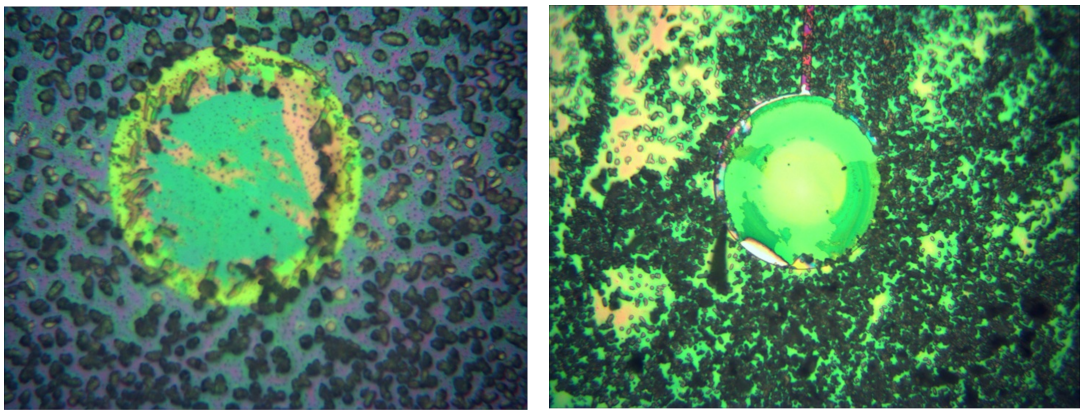

(a) (b)

Figure 7.13: Two STTMs after lifetime experiments in LKE where (a) shows a 100 μm diameter STTM that was cycled for 25 hours and 35 minutes and (b) shows a 50 μm diameter STTM that was cycled for 24 hours and 2 minutes.

7.8 Tantalum as an Electrode Metal

7.8.1 Tantalum Macroelectrode Fabrication

As the removal of the TiN adhesion layer was observed to be the cause of the TTM and STTM failures, employing an electrode metal that does not require an adhesion layer offers a potential solution. Ta (tantalum) is known to have excellent corrosion resistance and has previously been used as an adhesion layer itself [8–10].

In order to assess Ta as an electrode metal, thin film Ta electrodes were fabricated by sputter depositing a 50 nm thick film of Ta on a 500 nm SiN insulation layer and patterning to the same area as the V2M electrode metal. These were then cycled in LKE to determine the stability of Ta in LKE.

7.8.2 Tantalum Characterisation

The strips of thin film Ta were subject to cyclic voltammetry in LKE at 450°C across the full potential window of LKE. It was observed that establishing electrical connection with the Ta was challenging, most likely owing to the formation of Ta surface oxide layer [11]. Scratching at the Ta surface yielded exposed Ta to connect to the crocodile clip. The Ta strip was dipped in the LKE and soaked for 30 minutes in order to remove the TaOx layer. Figure 7.14 shows a CV recorded using a Ta thin film strip. Typical Li plating and stripping can be seen around -2.5 V as well as the start of Cl gas evolution around +0.75 V. There was no obvious degradation of the Ta thin film observed. Owing

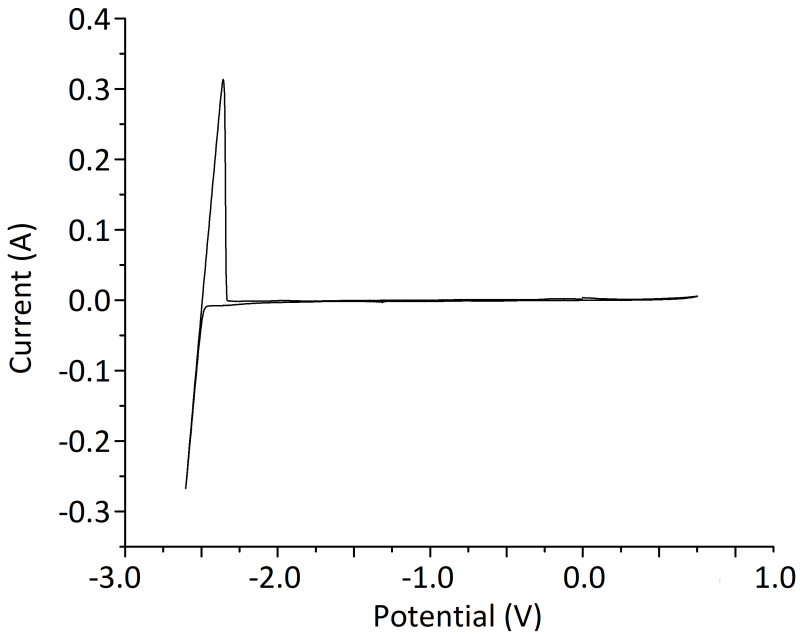

Figure 7.14: Full window CV of LKE at 450°C at 200 mV/s with a 50 nm Ta thin film macroelectrode.

to time constraints, the investigation of Ta as a replacement electrode metal was limited to this brief proof of concept.

7.9 Summary

The reduction in CA employed to improve microelectrode yield also offered an apparent substantial increase in lifetime, with the TTMs functioning for an average of 13.4 ± 12.8 hours compared with 1.4 ± 0.5 hours of the V2Ms. It is possible that latent defects in the underlying insulator were the cause of the initial failures of the V2Ms and the reduction in CA improved the microelectrode's robustness to these defects, resulting in an increased lifetime. There was however, a large variation in lifetime which may again be a result these defects.

The TTMs were observed to fail through removal of the electrode metal and fabricated test chips suggested chemical removal of the underlying TiN adhesion layer in the LKE as a possible cause. STTMs with both W and Pt electrode metal were tested and found to also fail through loss of the electrode metal, supporting the failure mechanism as removal of the TiN adhesion layer. Although TiN has been proven to be more robust than Ti in the role of adhesion layer, it does not appear to be robust for longer peri-

ods of time (10 - 20 hours). It had already been suggested in chapter 5 that there are weaknesses or pinholes in the Pt and W electrode metal films which expose the adhesion layer to the LKE This resulted in the removal of the original Ti adhesion layer and now the removal of the TiN adhesion layer.

Clearly, to further improve the microelectrode lifetime, a new adhesion layer or an electrode metal that does not require an adhesion layer is required. Ta is well known to be corrosion resistant and does not require an adhesion layer. Sputter deposited Ta thin films have been cycled in the LKE and have functioned as a robust and inert electrode metal, indicating its suitability as a replacement for the Pt electrode metal and TiN adhesion layer. However, Ta tends to form a stable oxide film which prevents reliable electrical connection and so microelectrodes with a Ta electrode metal would require a metal to cover the contact pad to enable electrical connection.

References

[1] Y. Sakamura, T. Hijikata, K. Kinoshita, and T. Inoue, "Measurement of standard potentials of actinides (U, Np, Pu, Am) in LiCl - KCl eutectic salt and separation of actinides from rare earths by electrorefining," *Journal of Alloys and Compounds*, vol. 271-273, pp. 592–596, 1998. [Online]. Available: http://www.sciencedirect.com/science/article/pii/S0925838898001662

[2] O. Shirai, T. Iwai, Y. Suzuki, and Y. Sakamura, "Electrochemical behavior of actinide ions in LiCl - KCl eutectic melts," *Journal of Alloys and Compounds*, vol. 271-273, p. 658688, 1998. [Online]. Available: http://www.sciencedirect.com/science/article/pii/S092583889800187X

[3] D. K. Corrigan, E. O. Blair, A. J. Walton, and A. R. Mount., "Developing sensors for molten salt processes: a new silicon based reference electrode for easy deployment on micro fabricated electrode systems.", Manuscript in preparation.

[4] D. Minzari, F. B. Grumsen, M. S. Jellesen, P. Maller, and R. Ambat, "Electrochemical migration of tin in electronics and microstructure of the dendrites," *Corrosion Science*, vol. 53, no. 5, pp. 1659 – 1669, 2011. [Online]. Available: http://www.sciencedirect.com/science/article/pii/S0010938X1100031X

[5] C. L. Brady, "Development and characterisation of microelectrodes for extreme environments," Ph.D. dissertation, University of Edinburgh, 2013. [Online]. Available: https://www.era.lib.ed.ac.uk/handle/1842/7852

[6] Y. Kanzaki and M. Takahashi, "The passivation phenomenon of platinum in fused lithium chloride + potassium chloride eutectic: Part II. Chlorine overpotential and superpassivation of platinum," *Journal of Electroanalytical Chemistry and Interfacial Electrochemistry*, vol. 90, no. 3, pp. 305–312, July 1978. [Online]. Available: http://www.sciencedirect.com/science/article/pii/S0022072878800679

[7] M. Takahashi, Y. Katsuyama, and Y. Kanzaki, "The passivation phenomenon of platinum in fused lithium chloride + potassium chloride eutectic: I. Effect of oxide ions on the passivation," *Journal of Electroanalytical Chemistry and Interfacial Electrochemistry*, vol. 62, no. 2, pp. 363–371, July 1975. [Online]. Available: http://www.sciencedirect.com/science/article/pii/0022072875800040

[8] A. Robin, "Corrosion behavior of niobium, tantalum and their alloys in boiling sulfuric acid solutions," *International Journal of Refractory Metals and Hard Materials*, vol. 15, no. 5, pp. 317 – 323, 1997. [Online]. Available: http://www.sciencedirect.com/science/article/pii/S0263436897875063

[9] J. E. Indacochea, J. L. Smith, K. R. Litko, and E. J. Karell, "Corrosion performance of ferrous and refractory metals in molten salts under reducing conditions," *Journal of Materials Research*, vol. 14, pp. 1990–1995, 5 1999. [Online]. Available: http://journals.cambridge.org/article_S0884291400049712

[10] T. Aubert, O. Elmazria, B. Assouar, L. Bouvot, Z. Bournebe, M. Hehn, S. Weber, M. Oudich, and P. Alnot, "Study of tantalum and iridium as adhesion layers for Pt/LGS high temperature SAW devices," in *2009 IEEE International Ultrasonics Symposium*, Sept 2009, pp. 1672–1675.

[11] D. Evans, "Method of making electrically insulating metallic oxides electrically conductive," Mar. 24 1992, uS Patent 5,098,485. [Online]. Available: https://www.google.com/patents/US5098485

Chapter 8

Alternative Microelectrode Architectures for Enhancing Electrode Performance

8.1 Introduction

The processes developed so far have demonstrated the capability of producing microelectrodes, capable of measuring in MS. With this serving as a baseline, other microelectrode technologies could be investigated, targeting improvements in specific areas of MS sensing. These designs present a toolbox-like approach, where a number of microelectrode designs are available, each optimised for a specific application. This chapter presents four proof of concept microelectrode designs which offer improvements in sensing and are listed below:

- Microelectrodes with reactive electrode metals to detect species that reduce at very negative potentials (-1.6 V to -2.2 V);
- Microelectrode arrays to increase the Faradaic current and robustness to electrical noise;
- LKE compatible nanoelectrodes to lower limits of detection, improve response times, and increase signal to noise ratio;
- An on-chip CE to move towards an integrated three-electrode system.

The design and fabrication of each concept is presented along with electrochemistry to demonstrate its feasibility in LKE. The exceptions to this are the microelectrodes with reactive metals, which are now actively evaluated in separate projects and will not be discussed here.

8.2 Detecting Species that Reduce at More Negative Potentials using Reactive Electrodes

8.2.1 Reactive Electrodes

The version two microelectrode (V2M), thin track microelectrode (TTM), and the super thin track microelectrode (STTM) developed in previous chapters have been observed by experimenters to have lower yields and lower lifetimes when operated at more negative potentials than -1.5 V, as discussed in chapters 6 and 7. This makes the detection of target species such as Ce (a surrogate for Pu) unreliable, as this reduces around -2.2 V on inert electrodes. An alternative approach is to use reactive metals which form alloys with target species in the LKE, a process which usually occurs at a more positive potential than reduction on an inert electrode. Therefore, a microelectrode

with a reactive electrode metal may be more suitable for detecting species that reduce at negative potentials than an inert electrode. Bi (bismuth) and Al (aluminum) are widely used reactive metals in molten salts and were therefore investigated as potential electrode metals for microelectrodes [1–3] .

8.2.2 Aluminium Microelectrodes

Al is a reactive electrode metal in LKE and is known to reduce Ce at a more positive potential than inert electrodes [1, 2]. With these alloying properties, Al is a candidate electrode metal for the electrochemical separation of lanthanides and actinides in a pyrochemical reprocessing system [4–6]. This makes it well placed as a possible reactive microelectrode metal more suitable for detecting Ce. It is also worth noting that, given the important role Al may have in pyroprocessing, an Al microelectrode sensor would be a useful tool for understanding fundamental alloying processes of Al in LKE. However Al oxidation occurs around -1.1 V, making it unsuitable as an electrode for detecting redox species more positive than this [1, 2].

8.2.3 Fabrication of Aluminium Microelectrodes

The fabrication of Al microelectrodes is complicated by the deposition of the Si_3N_4 top insulator which takes place at 800°C, above the 660°C melting point of Al. This means the Al has to be deposited and patterned after the top insulator. The Al microelectrodes were therefore fabricated by following the process described in chapter 5 for fabricating Pt TTMs. After the microelectrode and contact pad had been etched, as shown in figure 8.1 (a), the Al metal layer was deposited and patterned using a lift-off process. This process involved first spin coating a 3 μm layer of negative AZ2070 - 3.5 nLOF resist on to the wafer followed by a soft bake at 100°C for four minutes, as shown in figure 8.1 (b). It was exposed to ultraviolet light for 50 seconds through a photomask, which defined the Al pattern. The wafer was then baked for two minutes at 120°C. A 200 nm thick film of Al was then sputter deposited using an OPT Plasmalab System400 sputterer as in figure 8.1 (c) and the lift off resist was then removed by soaking the wafer in ACT resist stripper at 50°C for 60 minutes, changing to a fresh solution at 20 minute intervals. This leaves Al in the microdisc cavities as shown in figure 8.1 (d) and the Pt now serves as the contact pad and interconnect metal.

The lift off process successfully leaves Al in the microdisc cavity and figure 8.2 shows a 50 μm diameter ◯TTM with 200 nm of Al in the cavity. However, areas of underlying Pt can been seen at points around the perimeter, caused by misalignment. This issue

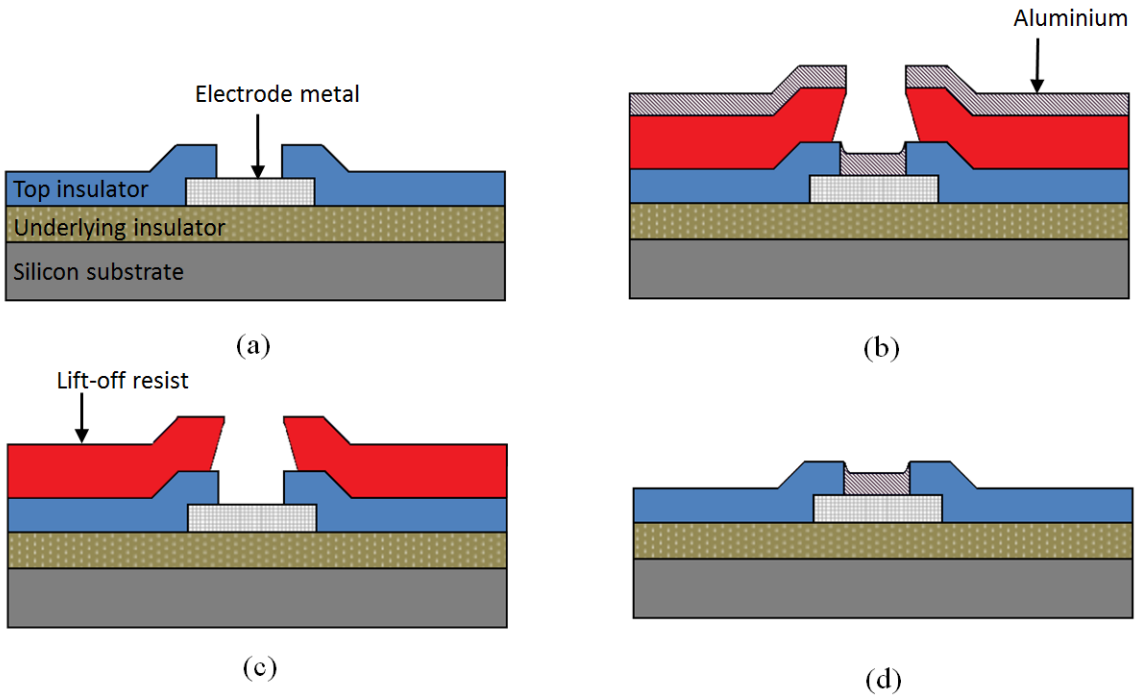

Figure 8.1: The lift off process used to deposit Al in the microdisc cavity. (a) The initial TTM after etching the top insulator to expose the microelectrode. (b) The patterned lift off resist, (c) the deposited Al, and (d) after the resist has been removed leaving the metal in the cavity.

arises as the photomask used to define the Al pattern was the one used to create the cavity in the first place; allowing for no margin of error. It can also be observed that the metal around the circumference of the Al leaves a ragged edge which arises from the lift off process not being completely optimised. The electrochemical impact of these issues is high as a significant, unknown amount of current will come from the exposed Pt around the edge as opposed to the Al and the ragged edge means the electroactive area of Al area is not well defined. One solution is to simply use a mask that has larger electrode area to ensure no Pt will be exposed even when there is the expected degree of misalignment. A more optimised lift-off process would likely reduce the ragged edge around the perimeter of the electrode.

8.2.4 Characterisation of Aluminium Microelectrodes

These Al microelectrodes are being further developed and characterised as part of separate Ph.D project and will not be further reported here.

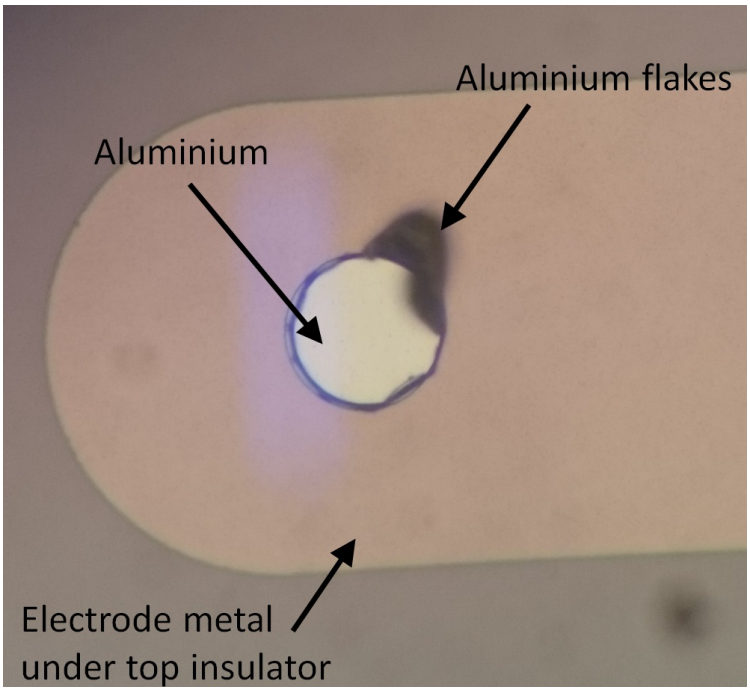

Figure 8.2: A 50 μm diameter ◯TTM Al microelectrode; made by patterning a 200 nm layer of Al in the cavity of a Pt microelectrode.

8.2.5 Bismuth Microelectrodes

Bi is a reactive electrode metal and alloys with elements in the LKE and, like Al, at a more positive potential than reduction on an inert electrode [3, 7]. Since Bi oxidation occurs around 0 V, it can be used to detect species that reduce at more positive potentials than Al. Bi also has a low melting point of 271°C and so is candidate metal for the role of the liquid cathode for extraction of specific actinide and lanthanide species in a pyrochemical reprocessing system [3, 7]. A Bi microelectrode sensor could therefore be used to investigate electrochemical and alloying properties of Bi and would be valuable for the development of such a liquid cathode. This sensor would also be able to provide online monitoring of a Bi liquid cathode in industrial processing.

8.2.6 Fabrication of Bismuth Microelectrodes

Bi has a lower melting point than the temperature at which Si_3N_4 is deposited, and so the fabrication of Bi microelectrodes posed the same challenge as the Al microelectrodes discussed above. Hence the same fabrication procedure was followed for both. However, in place of the 200 nm of Al, 200 nm of Bi was deposited using electron beam evaporation in an ANS Cluster Tool. When the resist was stripped Bi was successfully left in the

microelectrode cavities and figure 8.3 shows a 100 μm diameter microdisc with a film of Bi over the underlying Pt.

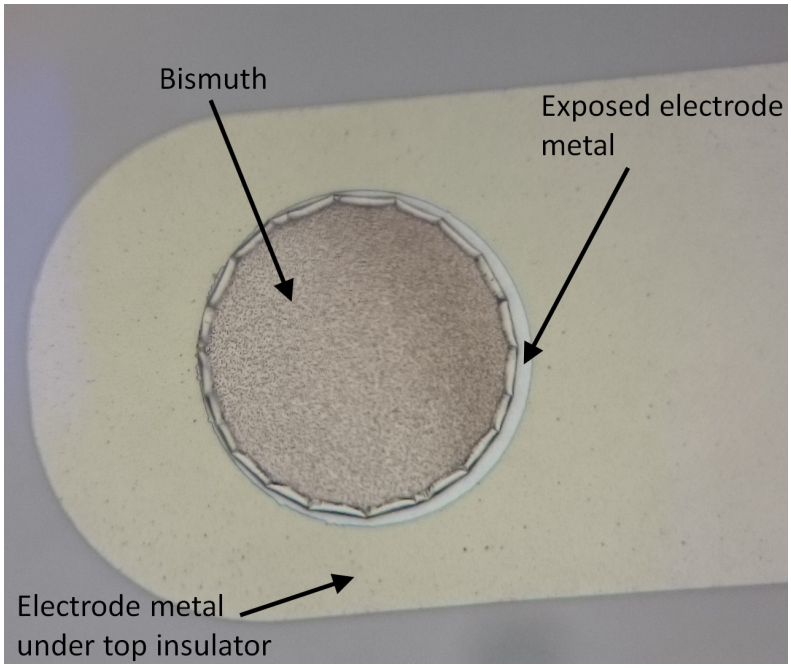

Figure 8.3: A Bi microelectrode created by patterning a 200 nm film of Bi.

As the same lift-off process was used to pattern both the Al and Bi microelectrodes, the same problems were encountered. The observed Bi film in figure 8.3 has not completely filled the cavity, exposing Pt around the perimeter, and the Bi film has raggedness along the edge. However, the electrochemical impact of these features was thought to not be so large as the Al, as the Bi melts and covers the exposed Pt and homogenises the surface.

8.2.7 Characterisation of Bismuth Microelectrodes

As with the Al microelectrodes, the characterisation and further development of the performance of the Bi microelectrodes are being evaluated as part of a Ph.D project and also will not be further reported.

8.2.8 Conclusions and Future Direction

Al and Bi microelectrodes have been designed and successfully fabricated, although two areas of the process require improvement. Opportunities exist to optimise the lift-off process to minimise the effect of tearing along the edge which results in a ragged

perimeter of metal, although this issue is thought to be less important for the Bi. Clearly, now the benefits of these electrode technologies has been demonstrated new masks should be designed to ensure that for further microelectrodes the electrode material completely covers the metal underneath.

8.3 Development of Microelectrode Arrays

8.3.1 Microelectrode Arrays

In order to address the relatively low current of a single microelectrode, multiple microelectrodes are often used in parallel. The main advantage of this is the increase in current, as the total signal is the sum of all the signals from the individual microelectrodes. Higher currents make very low concentrations of redox species more readily measurable, as well as lessening the impact of electrical noise. These microelectrode arrays can consist of thousands of electrodes, which present several other possible advantages when sensing in LKE. This large number of electrodes could lead to improved reliability, as the current loss from individual electrodes failing will be negligible. Likewise, the impact of pinholes or defects present in the top insulator is thought to be greatly reduced.

Using traditional methods of microelectrode manufacture producing arrays of microelectrodes can be difficult [8]. One of the main challenges is controlling the geometry and inter-electrode spacing, since these parameters can drastically affect the electrochemical response of the array. This is because the typical hemispherical diffusion field generated by a microelectrode extends beyond the footprint of the electrode itself and can merge with other nearby diffusion fields. Figure 8.4 shows how the diffusion fields of two neighbouring microelectrodes grow over time, eventually interacting with each other and becoming planar [9].

Figure 8.4 (a) shows the diffusion fields are separate and hemispherical, while in figure 8.4 (b) the diffusion fields have grown and are starting to merge. In figure 8.4 (c) they have merged further resulting in the diffusion field becoming planar. Once this happens, the array will act as a macroelectrode with area equal to the footprint of the array area and no longer displays the advantages of a microelectrode. As a consequence of this, special attention must be paid to the spacing between the microelectrode elements and the time course of the experiment.

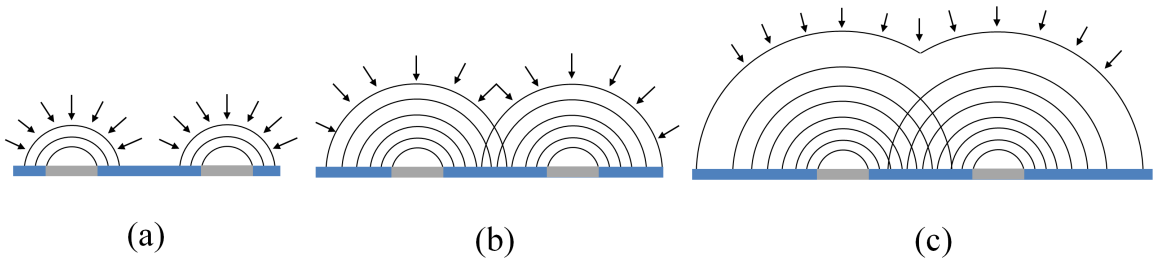

Figure 8.4: (a) Two microelectrodes with separate diffusion profiles, (b) two microelectrodes where the diffusion profiles have grown and are beginning to overlap and (c) the diffusion profiles have grown further and are becoming planar.

8.3.2 Microfabricated Microelectrode Array Design

Photolithography is one of the most common methods of manufacturing arrays of microelectrodes, as this grants precise control of the electrode placement leading to simpler fabrication of microelectrode arrays [8]. The microelectrode arrays were fabricated according to the fabrication process described in chapter 6, and the layout of a microelectrode array used is shown in figure 8.5. The array is located on a 5.5 mm by 5.5 mm square metal plate and the array footprint is 5 mm by 5 mm. Arrays of both microdiscs and microsquares were fabricated and four inter-electrode spacings were used, 1D, 2D, 3D, and 4D where D refers to the electrode edge length. For example, an array of 10 μm edge length microelectrodes with 2D spacing will be 20 μm apart on the X and Y axis. The array spacings, electrode sizes, and geometries are presented in table 8.1.

Microelectrode type	Edge length/diameter (μm)	Spacings
Microsquare	10, 20, 30	1D, 2D, 3D, 4D
Microdisc	10, 20	2D, 4D

Table 8.1: The array spacings, microelectrode sizes, and geometries of the fabricated microelectrode arrays.

The interconnect width was set to minimise critical area, but not to introduce a large voltage drop over the track. This was especially important in the microelectrode arrays as the typical current will be much larger, 1 - 100 μA, compared to that of single microelectrodes, 10 - 100 nA. A width of 1 mm was chosen, the resistance of which was 332 Ω for a track of 50 nm thick Pt and, assuming a current of 50 μA, gave an acceptable voltage drop of 16.6 mV.

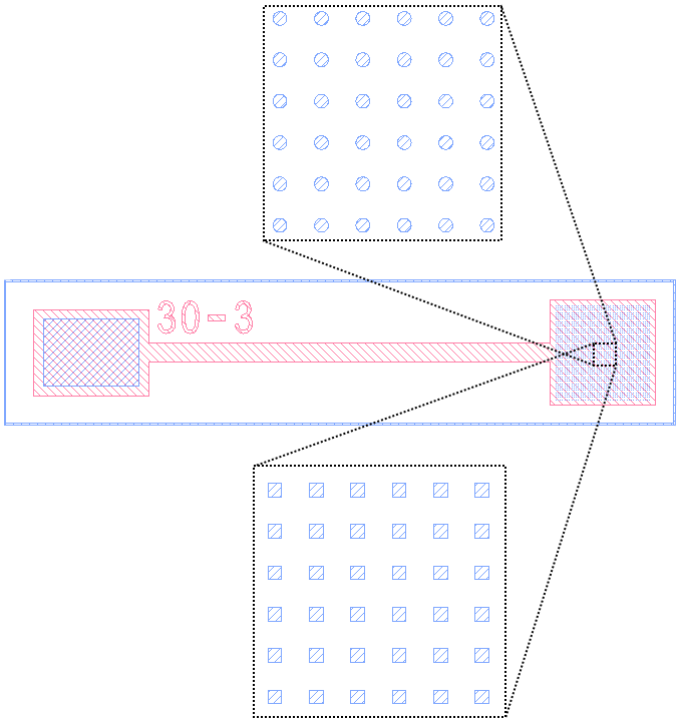

Figure 8.5: The layout of the microelectrode array is shown with zoomed sections showing examples of a microsquare array and microdisc array. Blue areas are exposed electrode metal, while red areas are electrode metal covered by top insulator.

8.3.3 Microelectrode Array Characterisation

Electrochemistry

The limiting current, i_L, for an array of m elements becomes:

$$i_L = 2.341DcFnml \tag{8.1}$$

where D and c are the diffusion coefficient and concentration of the redox species respectively, F is the Faraday constant, n is the number of electrons transferred in the reaction, and l is the edge length of an individual microsquare. The equation for the limiting current to a square array of microdisc electrodes also becomes:

$$i_L = 4DcFnmr \tag{8.2}$$

where r is the radius of an individual microdisc.

The microelectrode arrays were characterised using plating and stripping of Ag at 450°C and figure 8.6 shows a CV recorded on a W 20 μm 2D microsquare array with

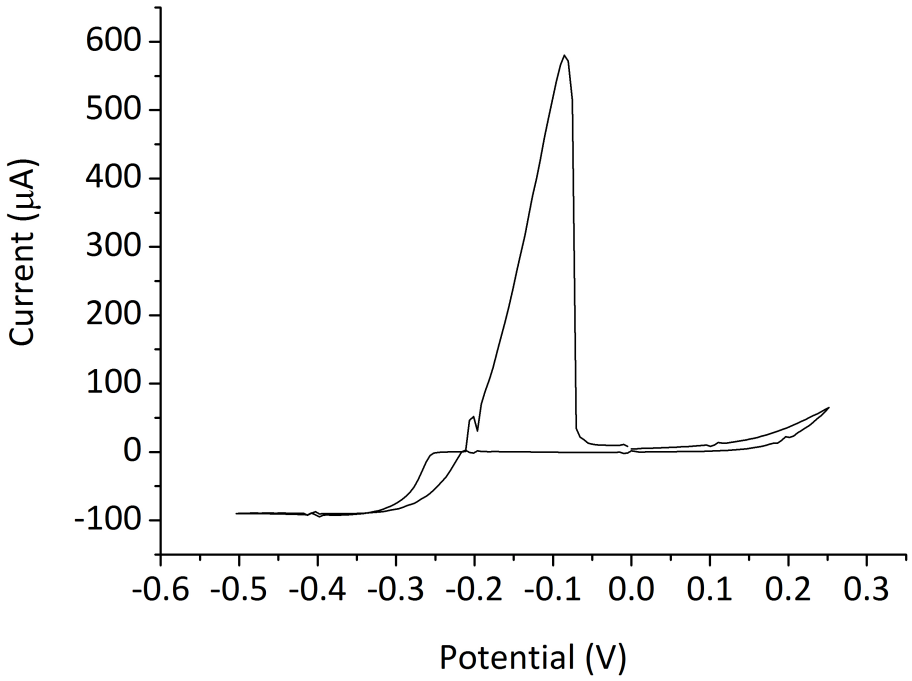

Figure 8.6: CV of 1 mM AgCl plating and stripping in LKE at 450°C, recorded using a W microsquare electrode array with 6944, 20 μm edge length microelectrodes spaced 40 μm apart.

1 mM AgCl. A typical microelectrode limiting current and sharp stripping peak can be observed and a limiting current of 90.4 $\pm$ 1.78 μA was extracted. Using equation (8.1), the predicted limiting current was calculated to be 80.3 μA, which is lower than the measured value by 11%. It is possible that pinholes in the top insulator are responsible for this error. Despite this discrepancy between theory and measurement, a microelectrode response was successfully recorded.

The yield for the arrays was found to be 48%, which is similar to the 46% yield of the V2Ms and demonstrates the arrays have not provided any significant improvement in sensor yield. In hindsight this is to be expected, as the test structures presented in chapter 7 highlighted possible defects present in the underlying insulator, not the top insulator, as the possible cause of the low microelectrode yields.

Robustness of Microsquares and Microdiscs

In order to compare the robustness of microdiscs and microsquares, a microsquare array and a microdisc array were subject to extremely harsh treatment by cycling across the entire LKE potential window (-2.6 V to +1.3 V) for 40 minutes. Figure 8.7 (a) shows

the microsquare array after the experiment. Large cracks in the top insulator can be seen to propagate from the corners of the microsquares.

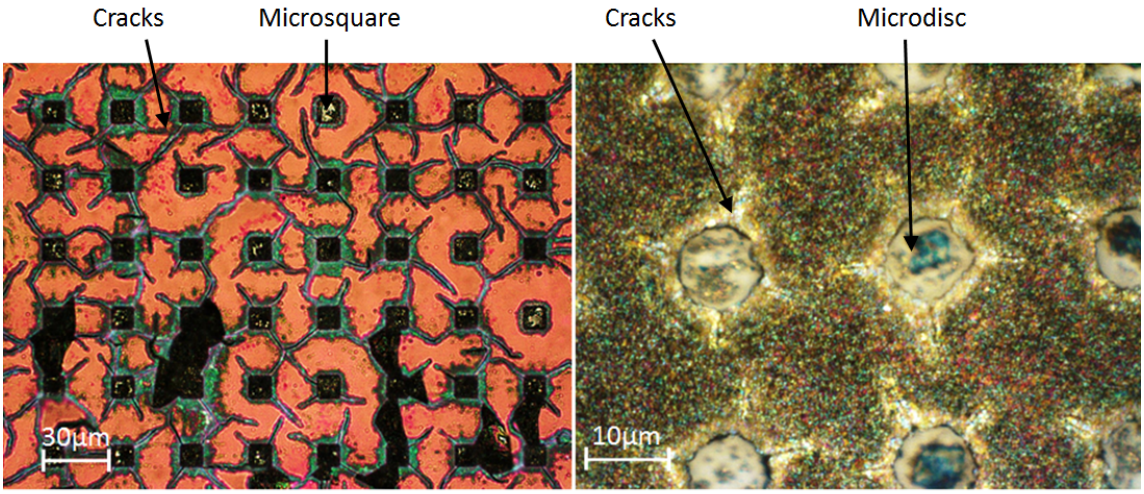

Figure 8.7: (a) A microsquare array after cycling across the whole LKE potential window (-2.6 to +1.3 V) at 440°C for 40 minutes at 400 mV/s, 100 mV/s, 50 mV/s, and 10 mV/s. (b) A microdisc array after the same treatment.

The cracks originating from the squares tend to propagate at roughly 45° from the corner, causing cracks from neighbouring microsquares to often meet up and sometimes result in widespread delamination. In contrast, figure 8.7 (b) shows the microdisc array after cycling where less damage has occurred. Cracking has also occurred, however the point of origin is random, meaning cracks originating from the microdiscs are less likely to meet and cause severe damage. The cracks originating from the microdiscs are also smaller, demonstrating that microdisc design is more robust to stress than microsquares as corners will act as focal points.

8.3.4 Conclusions and Future Direction of Microelectrode Arrays

Arrays of microelectrodes have successfully been fabricated and tested in LKE. CV experiments demonstrated the expected microelectrode response although the measured limiting current was 11% higher than that predicted by theory. The microelectrode arrays demonstrated little difference in yield compared to that of the V2Ms. This was to be expected given conduction paths in the underlying SiO_2, and not pinholes in the Si_3N_4 top insulator, have been suggested in chapter 6 as the mechanism behind

microelectrode failure. If a solution to these is found then, owing to their high currents, arrays may become the preferred sensing option to single microelectrodes.

8.4 LKE Compatible Nanoelectrodes

8.4.1 Advantages of Nanoelectrodes

Nanoelectrodes are generally defined as an electrode with a critical dimension (CD) on the nanoscale (<100 nm) and hence exhibit improvements in sensing over microelectrodes in:

- Signal to noise ratio, as described in chapter 2;
- Speed of steady state establishment;
- Limits of detection;
- Response time.

As such, fast, controlled, and reliable ways to manufacture nanoelectrodes are widely sought [10–12]. Previous work has demonstrated a simple, consistent, and highly controllable method of making nanoelectrodes in a very similar manner to the microfabrication methods discussed in this work [13–15]. This affords an opportunity to adapt the LKE microelectrodes in this study to nanoelectrodes, in order to take advantage of their enhanced sensing properties.

8.4.2 Nanoelectrode Fabrication

The nanoelectrode fabrication process developed at Scottish Microelectronic Centre follows the same fabrication process as that of the microelectrodes discussed in this work. In the microelectrode fabrication process the microelectrode is created by etching a window in the top insulator, which exposes the electrode metal area defining the microelectrode. In order to turn this into a nanoelectrode, this metal area is then etched exposing the edge of the electrode metal layer around the perimeter of the cavity, as shown in figure 8.8. This means the thickness of the metal layer defines the nanoelectrode's CD. This electrode is referred to as a microsquare nanoband edge electrode (MNEE) [13–15].

A proof of concept MNEE was fabricated by post processing a previously existing microelectrode sensor. Previous work on nanoelectrodes in the group was carried out on square MNEEs, and so a Pt □TTM with 100 μm edge length was chosen to be converted.

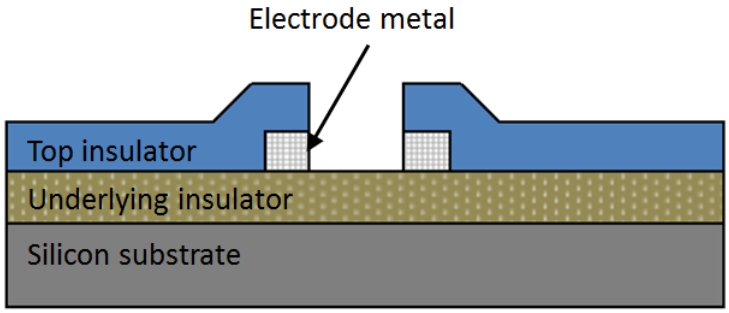

Figure 8.8: Transverse cross section of a nanoband electrode, where the metal electrode surface has been etched through. The electrode area is now defined by the exposed edge of the metal.

The contact pad on the TTM was covered with SPR 350 - 3.5 photoresist and soft baked for one minute at 90°C. The exposed microelectrode metal and adhesion layer was etched using an Ar mill process, described in chapter 6, for 15 minutes, creating an MNEE. The top insulator surrounding the electrode cavity was exposed to the etch, therefore profilometry measurements were taken before and after to monitor the impact of the Ar mill process on the Si_3N_4. A change in height of -21.6 ± 2.1 nm was measured, which equates to only a 5% loss of the Si_3N_4. The change in surface roughness of the Si_3N_4 before and after was determined to be +4.3 ± 6.9 nm, indicating no significant change had occurred. Reflectometry measurements of the now exposed SiO_2 at the bottom of the cavity confirmed the successful etch of the electrode metal and adhesion layer in the electrode cavity. Figure 8.9 shows the 100 μm edge length microsquare (a) before the Ar mill and (b) after the Ar mill.

8.4.3 Nanoelectrode Characterisation

The MNEE was electrochemically characterised with 4.5 mM of AgCl at 450°C. It was subject to cyclic voltammetry of Ag plating and stripping and figure 8.10 shows a CV recorded on the proof-of-concept MNEE.

The theoretical limiting current for this nanoband was calculated from the analytical expression for the limiting current to a 500 nm recessed square MNEE [13–15]:

$$i_L = 0.98nFDcl \tag{8.3}$$

and gave a predicted limiting current of 104 nA for the CV presented in figure 8.10. The MNEE was cycled for 10 minutes and gave an average limiting current of 172 ± 5

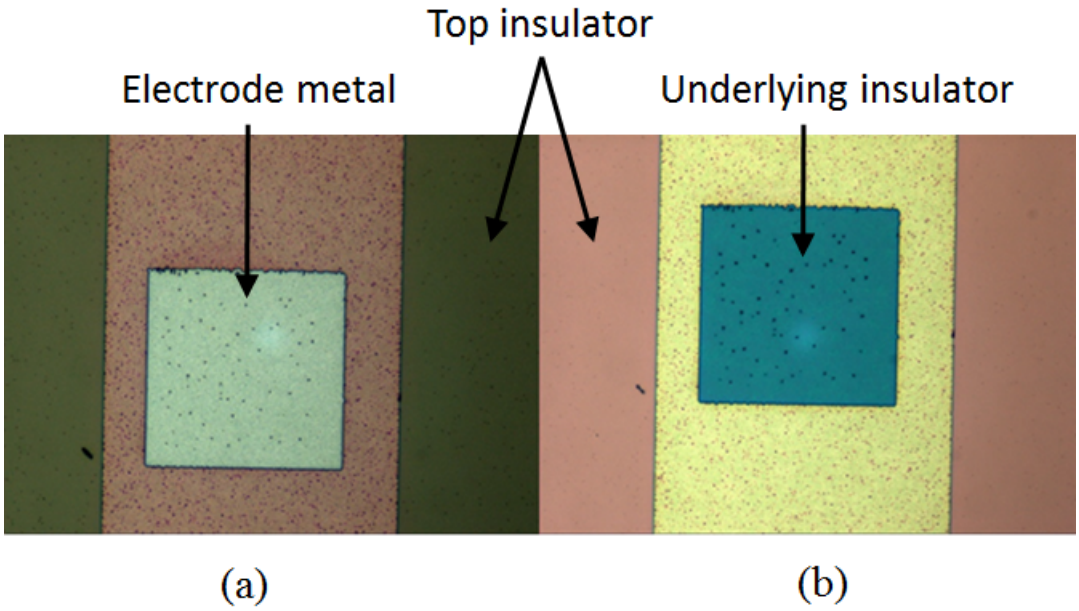

Figure 8.9: A 100μm square microelectrode (a) before 15 minute argon mill and (b) after.

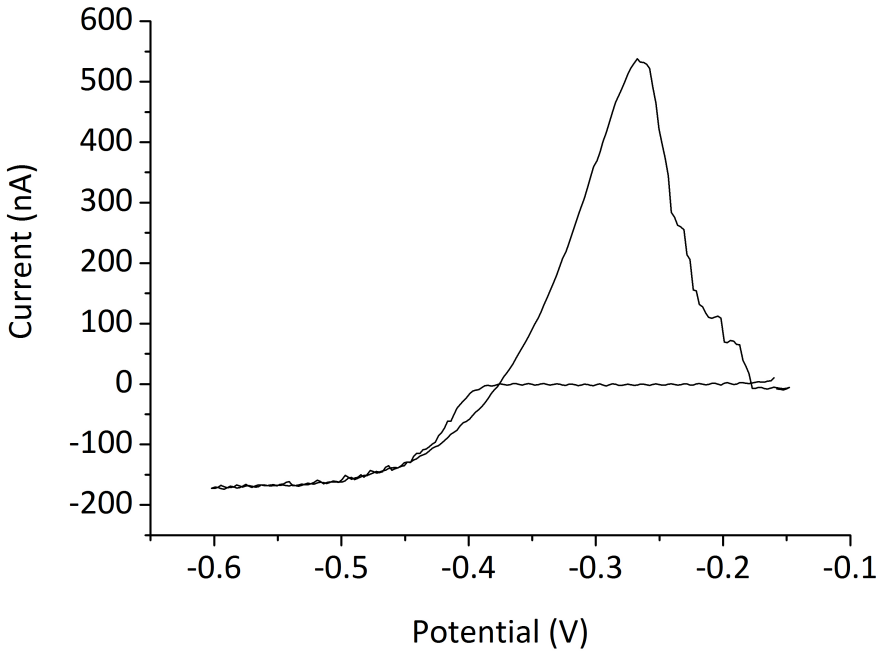

Figure 8.10: CV recorded on the 100 μm edge length MNEE with 50 nm band thickness after 20 minutes in LKE at 450°C with 4.5 mM AgCl.

nA, which was 60.5% greater than the theoretical prediction. It is not certain why the recorded limiting current was larger than that predicted, but there could be a number of reasons including pinholes in the top insulator. There is also the consideration that equation (8.3) has not been validated for a microsquare as large as 100 μm [14]. This is important because the aspect ratio of the cavity recess and microsquare edge length is a contributing factor to the limiting current.

After cycling the microelectrode was removed and inspected and is shown in figure 8.11. A small section of perimeter can be seen to have broken away at the left edge

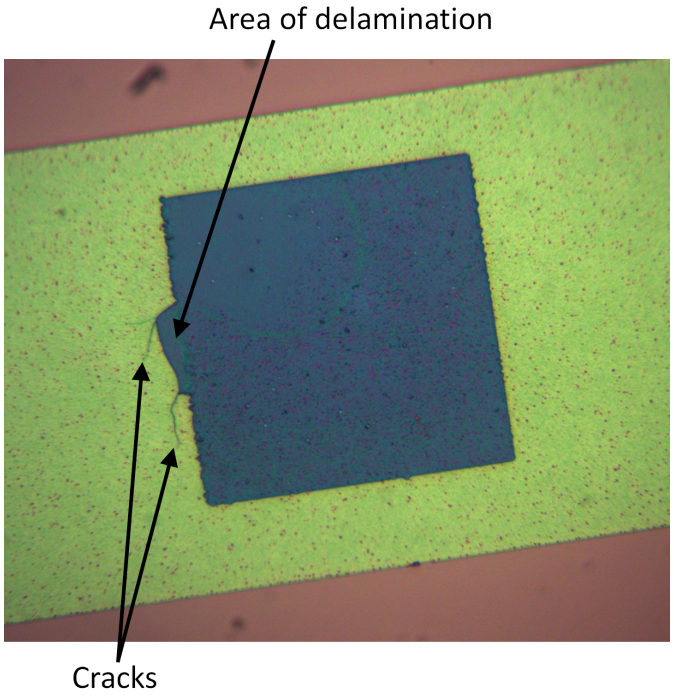

Figure 8.11: The nanoband electrode from figure 8.10 post cycling in LKE.

of the cavity and there are several small cracks spreading out from it, highlighted in figure 8.11. As can be seen from figure 8.9 this was not present before use in the LKE and is likely a result of the sensors use in the salt. This is supported by the presence of a fluctuating positive current observed after the Ag stripping peak, between -0.24 V and -0.15 V, present in only two CVs. An example of this is shown in figure 8.12, and may be indicative of physical damage occurring to the MNEE. What is certain is that the MNEE has sustained some physical damage and the cracks emanating from the missing area suggest further cycling could have caused wider delamination. This may be a consequence of the now exposed adhesion layer being attacked or indicate the MNEEs are more susceptible to stress than the microelectrodes.

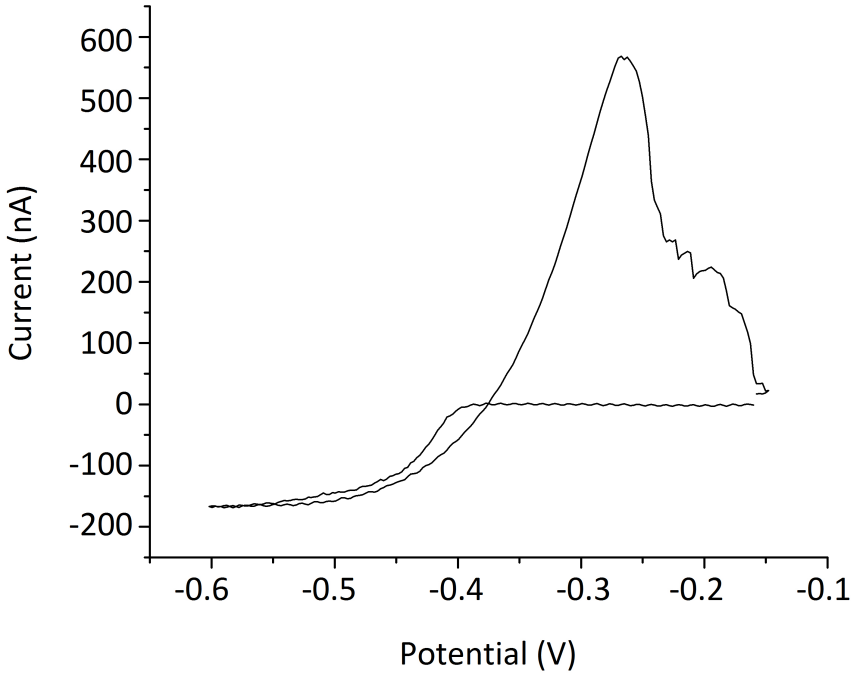

Figure 8.12: CV recorded after 5 minutes on the same 100 μm edge length MNEE used to record the CV in figure 8.11.

The additional band area resulting from the delamination likely did not contribute to the measured limiting current which, once hemispherical diffusion is established, is set by the critical dimension of the electrode only. This and the very small variation in limiting current means the physical damage to the MNEE is unlikely to be linked to the larger than expected limiting current.

LKE is known to chemically remove SiO_2 and the underlying insulator is exposed at the bottom of the cavity. The thickness of the SiO_2 layer at the bottom of the cavity was hence measured before and after cycling in the salt and only 3.8 nm of the SiO_2 was measured as being removed. This could have resulted in exposure of additional band metal and could be a factor in the larger than predicted limiting current. However, again, the lack of change in the limiting current over the course of the experiment makes this unlikely.

8.4.4 Conclusion and Future Direction for LKE Compatible Nanoelectrodes

A proof of concept nanoelectrode based on the molten salt compatible microelectrode has been fabricated and characterised in LKE. A stable limiting current was established and maintained over the time course of the experiment. The measured limiting current was 60.5% larger than the predicted limiting current using equation (8.3). The reason for this disagreement is not known. However further work undertaken with these sensors will clarify if there is a fundamental electrochemical reason or if the top insulator was not functioning perfectly; possibly resulting from the Ar mill process to which it was exposed. Some physical damage at the perimeter of the MNEE cavity was observed although this was not thought to be responsible for the larger measured current, but may indicate re-optimisation of the sensor materials is required for successful deployment of an LKE compatible MNEE. The further development and characterisation of LKE compatible nanoelectrodes has become a separate Ph.D project.

8.5 On-Chip Counter Electrode

8.5.1 Design and Fabrication

Ideally all three electrodes (working, counter, and reference) would be deployed on the same chip, removing the need for separate electrodes. In order to move towards an integrated three-electrode sensor, a microelectrode with a CE on the same chip was designed and fabricated. Figure 8.13 shows two layouts of TTMs, each with integrated counter electrodes. Two different layouts of contact pad were used in order to allow flexibility when connecting with multiple crocodile clips. Figure 8.13 (a) has parallel contact pads and (b) has offset contact pads, allowing them to be larger. The CE itself is required to be larger, to make sure that it does not limit the current supply to the working electrode. Therefore the CE is 3 mm in diameter. These dual electrodes (DEs) were only included on the TTM photomask layout, as the reduced width of the STTM chips prevented inclusion. As these layouts were included on the TTM photomask, they were fabricated in the same manner as the TTMs.

8.5.2 Dual Electrode Characterisation

Due to time constraints, a full chracterisation of the system was not completed. Only the 3 mm platinum disc that made up the on-chip CE was successfully validated. This

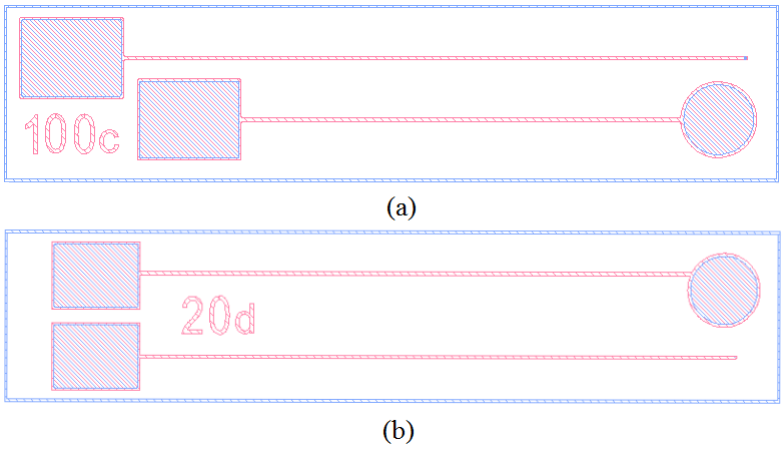

Figure 8.13: Two TTMs with integrated counter electrodes with (a) parallel contact pads and (b) offset contact pads.

was done by using the on-chip CE as a working electrode and measuring an electrochemical reaction. An unchanging reponse would demonstrate the disc is functioning as a stable electrode and hence can be used as a CE. The experiment was performed in a previously existing salt which contained Zn (Zinc), which demonstrates a similar plating and stripping behaviour to silver and was hence deemed suitable for the task. Figure 8.14 shows a CV of Zn plating and stripping, recorded using a Pt on-chip CE.

The reduction of Zn^{2+} to Zn metal can be observed around the expected potential of -1.1 V and the reverse oxidation peak around -0.8 V. The CV presented in figure 8.14 was recorded after 25 minutes of cycling and no change in the signal was observed, demonstrating the stability of the on-chip macroelectrode in LKE. However, as the macroelectrode is made up of the same layer stack as the microelectrode area, TiN adhesion layer and Pt or W electrode metal, it would be expected to fail in the same manner as the microelectrodes presented in chapter 7, which limits the lifetime of the DE. Although this also means any solution to the electrode metal removal problem is equally applicable to the DE.

8.6 Summary

Four proof of concept microelectrode technologies for extended sensing capabilities in LKE have been presented, with the goal of creating a possible suite of sensor variants, optimised for specific applications. Microelectrodes with the reactive electrode metals Al and Bi have the potential to more reliably detect redox species that usually reduce towards the negative end of the LKE potential window on inert electrode metals. Both

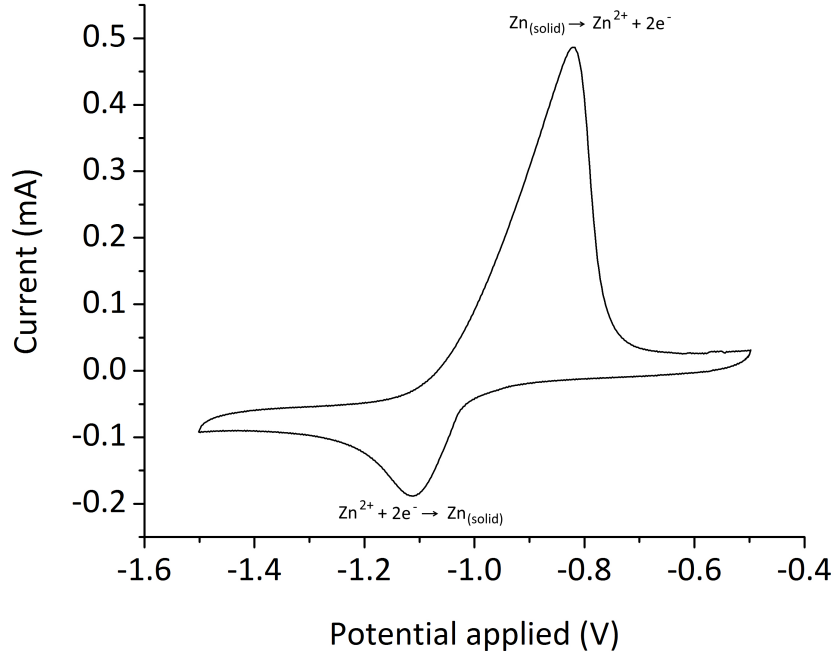

Figure 8.14: CV of 2 mM Zn plating and stripping, recorded at a 3 mm diameter Pt on-chip CE in LKE at 450°C.

microelectrodes with Bi and Al have been fabricated and are undergoing characterisation and further development as part of other Ph.D programmes.

It was expected that arrays of microelectrodes would be less affected by pinholes, as current contributions from defects in the top insulator would be negligible compared to the overall signal. The microelectrode arrays fabricated demonstrated a higher Faradaic current than predicted. However the yield of the arrays was not higher than that of the V2Ms. This most likely resul,ts from the underlying insulator being a source of failure as discussed in chapter 6. Given a solution to this failure mechanism, arrays would be a viable option when sensing with a higher current is desired, for example measuring species with very low concentrations or operating in noisy environments.

Nanoelectrodes have enhanced electrochemical sensing attributes over microelectrodes and, a proof of concept nanoelectrode has been fabricated and characterised. The nanoelectrode exhibited around a 60% larger than expected limiting current and suffered minor damage to the perimeter of the cavity. It is unclear why and the further development and characterisation of this LKE compatible nanoelectrode is being undertaken as a separate Ph.D project.

Microelectrodes with on-chip counter electrodes have also been designed and fabric-

ated. These DEs represent a step towards an on-chip three-electrode system, with work on the reference electrode already underway.

References

[1] P. Soucek, R. Malmbeck, C. Nourry, and J. Glatz, "Pyrochemical Reprocessing of Spent Fuel by Electrochemical Techniques Using Solid Aluminium Cathodes," *Energy Procedia*, vol. 7, pp. 396–404, 2011.

[2] L. Cassayre, R. Malmbeck, P. Masset, J. Rebizant, J. Serp, P. Soucek, and J.-P. Glatz, "Investigation of electrorefining of metallic alloy fuel onto solid Al cathodes," *Journal of Nuclear Materials*, vol. 360, no. 1, pp. 49 – 57, 2007, proceedings has been selectedProceedings of the Seventh International Symposium on Molten Salts Chemistry and Technology (MS7 Session 6: Workshop on Nuclear Energy and Nuclear Wastes. [Online]. Available: http://www.sciencedirect.com/science/article/pii/S0022311506004569

[3] M. Kurat, Y. Sakamura, and T. Matsui, "Thermodynamic quantities of actinides and rare earth elements in liquid bismuth and cadmium," *Journal of Alloys and Compounds*, vol. 234, no. 1, pp. 83–92, 1996. [Online]. Available: http://www.sciencedirect.com/science/article/pii/092583889501960X

[4] O. Conocar, N. Douyere, J.-P. Glatz, J. Lacquement, R. Malmbeck, and J. Serp, "Promising Pyrochemical Actinide/Lanthanide Separation Processes Using Aluminum," *Nuclear Science and Engineering*, vol. 153, no. 3, 2006. [Online]. Available: http://www.ans.org/pubs/journals/nse/a_2611

[5] L. Rault, M. Heusch, M. Allibert, F. Lemort, X. Deschanel, and R. Boen, "Test of Actinide-Lanthanide Separation in an Aluminum-Based Pyrochemical System," *Nuclear Technology*, vol. 139, no. 2, pp. 167–174, 2002. [Online]. Available: http://www.ans.org/pubs/journals/nt/a_3311

[6] M. A. Jerome Serp and, A. L. Terrier, R. Malmbeck, M. Ougier, J. Rebizant, and J.-P. Glatz, "Electroseparation of Actinides from Lanthanides on Solid Aluminum Electrode in LiCl-KCl Eutectic Melts," *Journal of The Electrochemical Society*, vol. 152, no. 3, pp. C167–C172, 2005. [Online]. Available: http://jes.ecsdl.org/content/152/3/C167.short

[7] T. Inoue, "Actinide recycling by pyro-process with metal fuel FBR for future nuclear fuel cycle system," *Progress in Nuclear Energy*, vol. 40, no. 3-4, pp. 547–554, 2002.

[8] X.-J. Huang, A. M. O'Mahony, and R. G. Compton, "Microelectrode Arrays for Electrochemistry: Approaches to Fabrication," *Small*, vol. 5, no. 7, pp. 776–788, 2009. [Online]. Available: http://dx.doi.org/10.1002/smll.200801593

[9] M. C. Henstridge and R. G. Compton, "Mass Transport to micro- and nanoelectrodes and their arrays: a review," *The Chemical Record*, vol. 12, no. 1, pp. 63–71, 2012. [Online]. Available: http://dx.doi.org/10.1002/tcr.201100032

[10] V. P. Menon and C. R. Martin, "Fabrication and Evaluation of Nanoelectrode Ensembles," *Analytical Chemistry*, vol. 67, no. 13, pp. 1920–1928, 1995. [Online]. Available: http://dx.doi.org/10.1021/ac00109a003

[11] D. W. M. Arrigan, "Nanoelectrodes, nanoelectrode arrays and their applications," *Analyst*, vol. 129, pp. 1157–1165, 2004. [Online]. Available: http://dx.doi.org/10.1039/B415395M

[12] J. T. Cox and B. Zhang, "Nanoelectrodes: Recent Advances and New Directions," *Annual Review of Analytical Chemistry*, vol. 5, no. 1, pp. 253–272, 2012, pMID: 22524228. [Online]. Available: http://dx.doi.org/10.1146/annurev-anchem-062011-143124

[13] J. Terry, I. Schmueser, I. Underwood, D. K. Corrigan, N. J. Freeman, A. S. Bunting, A. R. Mount, and A. J. Walton, "Nanoscale electrode arrays produced with microscale lithographic techniques for use in biomedical sensing applications," *IET Nanobiotechnology*, vol. 7, no. 4, pp. 125–134, 2013. [Online]. Available: https://www.scopus.com/inward/record.uri?eid=2-s2.0-84888273757&partnerID=40&md5=6d17b27464fd48dc3a4962d2dcff5378

[14] I. Schmueser, A. J. Walton, J. G. Terry, H. L. Woodvine, N. J. Freeman, and A. R. Mount, "A systematic study of the influence of nanoelectrode dimensions on electrode performance and the implications for electroanalysis and sensing," *Faraday Discussions*, vol. 164, pp. 295–314, 2014. [Online]. Available: https://www.scopus.com/inward/record.uri?eid=2-s2.0-84888250166&partnerID=40&md5=047c6619706c2a2db5c1ecbfbfa09a3f

[15] N. Freeman, R. Sultana, N. Reza, H. Woodvine, J. Terry, A. Walton, C. Brady, I. Schmueser, and A. Mount, "Comparison of the performance of an array of nanoband electrodes with a macro electrode with similar overall area," *Physical Chemistry Chemical Physics*, vol. 15, no. 21, pp. 8112–8118, 2013. [Online].

Available: https://www.scopus.com/inward/record.uri?eid=2-s2.0-84877686992&partnerID=40&md5=d92ce1144affd862c2534c30080389c2

Chapter 9

Conclusions and Future Directions

9.1 Summary

This work presents a microfabricated microelectrode sensor for operation in LKE at 450 - 500°C. This microelectrode is based on a proof of concept design, shown in figure 9.1, which demonstrated plating and stripping of Ag, but did not function as a microelectrode and yielded no quantifiable data. The microelectrode suffered from several

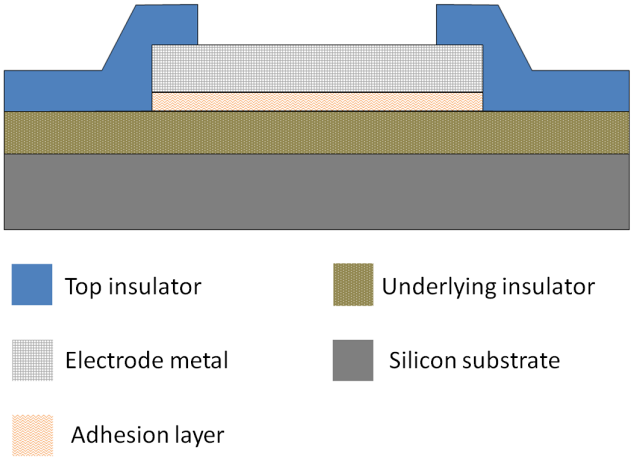

Figure 9.1: Transverse cross-section of the microelectrode architecture.

mechanisms of failure: delamination of the top insulation, loss of electrode metal, permeability of the top insulator, and damage to the top insulator around the electrode metal perimeter. A systematic investigation of each failure mechanism resulted in an optimised microelectrode architecture, which consisted of:

- SiO_2 underlying insulator which acted as a stress relief layer and prevented top insulator delaminations;
- TiN adhesion layer which prevented electrode metal loss over the time courses investigated;
- Si_3N_4 top insulator which was not permeable;
- Etched Pt electrode metal which prevented damage to the top insulator.

These changes culminated in a microelectrode which was capable of delivering quantifiable data for around 1.4 hours.

In order to improve upon the microelectrode lifetime yield (46%), the layout was optimised. This was done to reduce the critical area where defects or pinholes could affect

microelectrode performance and figure 9.2 presents the three microelectrode layouts characterised. This reduction in critical area led to an improved yield of 65% and

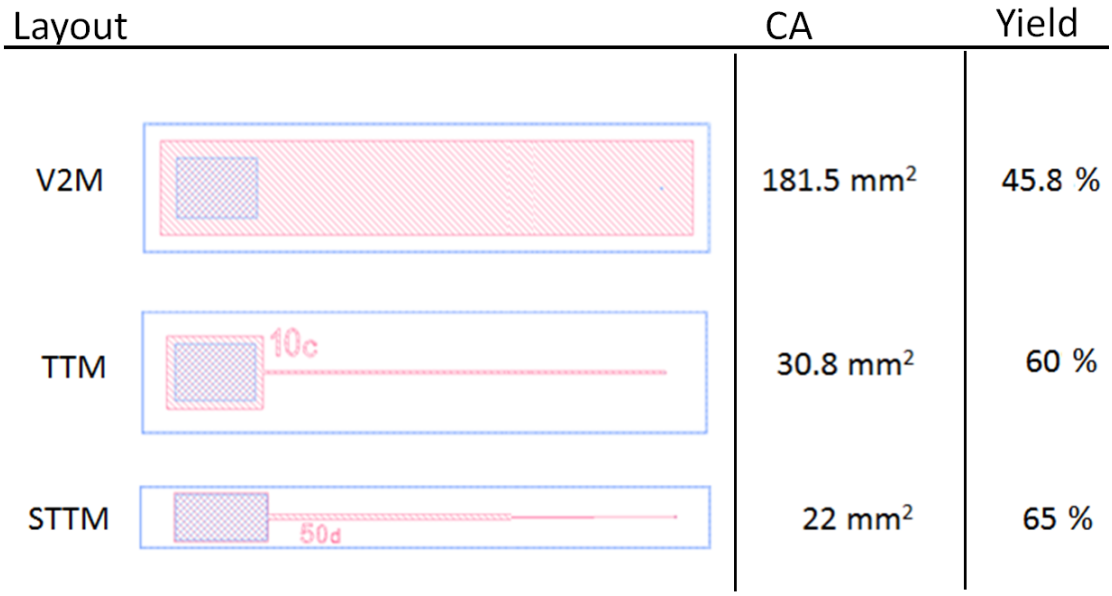

Figure 9.2: The three microelectrode layouts characterised with their respective CA and yield.

lifetimes of around 20 hours. Despite this, the microelectrodes demonstrated very high variability in lifetime and the improvement in yield was not as high as it was hoped. Test structures were designed to investigate the causes of the continued microelectrode failures and identified shorting between the electrode metal and Si substrate. This suggests the existence of defects in the underlying insulator are the cause of the 35% of microelectrodes which never functioned. This effect may also be potential dependent, as microelectrode users observed decreasing lifetime with increasing size of potential window. The microelectrodes which did function failed through loss of electrode metal. Test structures suggested this was caused by the dissolution of the TiN adhesion layer. Ta has been suggested as a replacement electrode metal, as it does not require an adhesion layer. A proof of concept study demonstrated the feasibility of employing thin film Ta as an electrode metal in LKE.

Several proof of concept microelectrode designs have been presented for improved sensing in specific applications:

- Reactive Bi and Al microelectrodes were designed and fabricated, for improved detection of elements that reduce towards the negative end of the LKE potential window such as Pu;

- Microelectrode arrays have been designed, fabricated, and gave the expected increase in Faradaic signal when tested;
- LKE capable nanoelectrodes have also been fabricated and tested;
- Microelectrodes with on-chip CEs have also been designed and fabricated.

The Bi, Al, and nanoelectrodes are undergoing characterisation and further development as parts of separate Ph.D projects.

9.2 Future work

9.2.1 Microelectrode Design

In order to mitigate the impact of possible defects in the underlying insulator, a thin layer of SiN could be included between the electrode metal and underlying insulator. As this layer would not be exposed to the salt, it may be possible to use Si-rich SiN instead of Si_3N_4. In either case, it would be desirable to also increase the thickness of the underlying insulator to balance the increased tensile stress associated with the addition of a new layer of SiN. This approach is currently undergoing testing, with the additional SiN layer appearing to successfully mitigate short circuits to the Si substrate. Another approach that may improve microelectrode robustness is to fabricate the microelectrodes on a non-silicon substrate. Attempts have been made during the project to fabricate microelectrodes on a quartz substrate, however when the top insulator was deposited it was observed to crack. It is possible that with further process development, this approach will be successful and improve microelectrode performance.

Given the removal of the TiN adhesion layer has been suggested as the mechanism limiting microelectrode lifetime, a metal layer that does not require an adhesion layer would be beneficial. In order to test this, Ta microelectrodes have been fabricated and are awaiting characterisation. An on-chip reference electrode is also under development and, combined with the on-chip counter electrode, could result in an integrated three-electrode system.

9.2.2 Industrial Deployment

Work began in collaboration with the National Nuclear Laboratory to develop a method of connecting the microelectrodes into a molten salt dynamic rig (MSDR), which mimics flow of MS in an industrial set up. Unfortunately, the MSDR suffered a catastrophic

salt leak and was not operable. At this stage material compatibility tests had been conducted and a design for the connection had been completed. Should the MSDR be brought back online or a suitable replacement built, this work could be continued in order to test the microelectrodes in an industrial environment.

9.3 Other Applications of the Microelectrodes

Work is underway to utilise the microelectrodes presented here as online monitoring for PUREX-type, aqueous-based processes. These proceed in an environment of concentrated nitric acid and, so far, the microelectrodes have performed well. It is also relevant that MS-based nuclear reactors are gaining interest and a microelectrode sensing system could prove useful for overseeing the state of the MS in such a system. For example, work on the microelectrodes has shown the possibility of monitoring oxygen ingress into the salt, as well as successfully detecting corrosion products from stainless steel. These benefits could conceivably be applied to any MS system, such as those used for manufacturing metals or storing energy from renewable sources.

Further opportunities are presented by a number of other harsh environments such as, oil wells, acids and bases in industrial processes, or possibly corrosive gas. However, the materials would likely have to be tailored to the chemistry and stresses of each specific environment and this work presents a possible methodology to achieve this.

List of Publications

- Corrigan, D.K., Blair, E.O., Terry, J.G., Walton, A.J., and Mount, A.R., "Enhanced electroanalysis in lithium potassium eutectic (LKE) using microfabricated square microelectrodes", *Analytical Chemistry*, vol. 86, no. 22, pp. 11342 - 13348, 2014. [Online]. Available: http://pubs.acs.org/doi/abs/10.1021/ac5030842

- Blair, E.O., Corrigan, D.K., Terry, J.G., Mount, A.R., and Walton, A.J., "Development and Optimization of Durable Microelectrodes for Quantitative Electroanalysis in Molten Salt", *Journal of Microelectromechanical Systems*, vol. 24, no. 3, pp. 1346 - 1354, 2015. [Online]. Available: http://ieeexplore.ieee.org/stamp/stamp.jsp?tp=&arnumber=7046354&isnumber=7283693

- Blair, E.O., Corrigan, D.K., Schmueser, I., Terry, J.G., Smith, S., Mount, A.R., and Walton, A.J., "Test Structures to Support the Development and Process Verification of Microelectrodes for High Temperature Operation in Molten Salts", *IEEE International Conference on Microelectronic Test Structures 2016*, 2016 - May, pp.158 - 162. [Online]. Available: http://ieeexplore.ieee.org/stamp/stamp.jsp?tp=&arnumber=7476198&isnumber=7476153

- Scarfi, S., Smith, S., Tabasnikov, A., Schmuser, I., Blair, E. O, Bunting, A.S., Walton, A.J., Murray, A.F., and Terry, J.G., "Test structures for the characterisation of conductive carbon produced from photoresist", *IEEE International Conference on Microelectronic Test Structures 2016*, 2016 - May, pp.184 - 189. [Online]. Available: http://ieeexplore.ieee.org/stamp/stamp.jsp?tp=&arnumber=7476204&isnumber=7476153

- Corrigan, D. K., Elliott, J. P., Blair, E. O., Reeves, S. J., Schmuser, I., Walton, A. J., and Mount, A. R., "Advances in Electroanalysis, Sensing and Monitoring in Molten Salts", *Faraday Discussions*, vol. 190, pp. 351 - 366, 2016. [Online]. Available: http://pubs.rsc.org/en/content/articlepdf/2016/fd/c6fd00002

- Blair, E.O., Corrigan, D.K., Levene, H.J, Schmueser, I., Terry, J.G., Smith, S., Mount, A.R., and Walton, A.J., “Improving the Yield and Lifetime of Microfabricated Sensors for Harsh Environments", *IEEE Transactions on Semiconductor Manufacturing*, vol. PP, no, 99, 2017 - June. [Online]. Available: http://ieeexplore.ieee.org/document/

Appendix A

Chemicals and Tools used in Microfabrication

Photolithogaphy

- *Photoresist adhesion promoter* - HMDS, 1,1,1,3,3,3 hexamethyldisilazane 97 % purity (Aldritch)
- *Photoresists* - Megaposit SPR 350 - 3 positive photoresist (Michrchem), Megaposit SPR 220 - 4.5 positive photoresist (Microchem), LOR 5B negative resist (Microchem), AZ2070-nLoF negative resist (Microchem)
- *Mask Aligner* - Karl Suss MA8
- *Photoresist developers* - Megaposit MF26A resist developer , AZ 726 resist developer
- *Photoresist Strippers* - Microposit Remover 1165 (Microchem), ACT CMI (Air Products)
- *Solvents* - Acetone (KMG Ultra Pure Chemicals), Isopropyl alcohol (KMG Ultra Pure Chemicals)

Thin Film Etching

- *Reactive ion etching tools* - Mini-Lab RIE 80 etching system (JLS), Multiplex RIE (STS)
- *Wet etches* - H_2O_2 30% (Chestech)

Thin Film Deposition

- *Sputter tools* - Balzers BAS 450PM Sputterer (dunno), Plasmalab System 400 Sputterer (Oxford Plasma Technologies)
- *Evaporation tool* - ANS Cluster Tool (ANS?)
- *Furance Deposition tool* - 8" Oxide Furnace (HITEC), 8" Nitride Furnace (HITEC)

Metrology

- *Optical tools* - Polyvar MET Optical microscope (Reichert-Jung), DM12000 M microscope (Leica), Axiotron Optical microscope (Zeiss), Nanospec 3000 reflectometer (Nanometrics)
- *Profilometry tool* - Dektak 8 Surface profiler (Veeco)
- *Electrical tool* - FPP5000 Four Point Probe (Veeco)

Appendix B

Chemicals and Tools used in High Temperature Measurements

Molten Salt and Redox Couples

- *LKE* -Anhydrous grade LiCl and KCl (Sigma-Aldritch)
- *Redox Couples* - AgCl (Sigma-Aldritch), $SmCl_3$ (Sigma-Aldritch)

High Temperature Set Up

- *Furnace* -Carbolite GVA12/100/3
- *Thermocouple* -

Electrochemical Measurement

- *Potentiostat* - PGSTAT12 (EcoChemie)
- *Electrochemical Analysis Software* - GPES 4.9 (EcoChemie), NOVA 1.1 (EcoChemie), OriginLab 9.1 (OriginLab)